Antenna Development and Calibration for Measurements of Radio Emission from Extensive Air Showers at the Pierre Auger Observatory

Von der Fakultät für Mathematik, Informatik und Naturwissenschaften
der RWTH Aachen University zur Erlangung des akademischen Grades
eines Doktors der Naturwissenschaften genehmigte Dissertation

vorgelegt von
Raphael Krause, M. Sc. RWTH
aus Remscheid

Berichter:

Prof. Dr. Martin Erdmann
Prof. Dr. Christopher Wiebusch

Tag der mündlichen Prüfung: 30.05.2018

Contents

1

Introduction

The universe has always exerted a special fascination on humankind, especially far-away objects such as active galaxy nuclei, star bursts, or super novae. Messengers coming from these objects are produced, propagate through the universe, and reach Earth despite the huge distances. This enables investigating fundamental questions of astro- and astroparticle physics.

Cosmic rays are the most energetic particles in the universe and thus of special interest. They reach energies of more than $10^{20}\,\mathrm{eV}$ which is several orders of magnitude higher than the particle energies produced in human-build accelerators, e.g., the large hadron collider (LHC) [1]. They have firstly been observed by Victor Hess in 1912 [2]. Despite the long elapsed time since their first observation, there are still open questions concerning the comprehension of cosmic rays which are of great interest in physics and are in the focus of current research.

The Earth is constantly bombarded by cosmic rays with a cosmic-ray flux rapidly decreases with the particle energy to only a few cosmic rays per century and square kilometer at highest energies of more than $10^{19}\,\mathrm{eV}$. The small flux is one of the reasons why large ground-based detectors are necessary to observe such high-energy cosmic rays.

When high-energy cosmic rays hit the Earth's atmosphere, they interact with air molecules and millions of secondary particles are produced which form a so-called extensive air shower. The atmosphere acts as a giant calorimeter that is typically readout by stochastic measurements of particles on ground and by direct measurements of fluorescence light emitted by air molecules which are excited by secondary particles. Both detection techniques are established at the Pierre Auger Observatory [3].

Complementary to these baseline detection techniques, the measurement of radio signals from cosmic-ray induced air showers recently gains in importance for reconstructing cosmic-ray properties [4–10]. The Auger Engineering Radio Array (AERA) [6] is the radio detector of the Pierre Auger Observatory and consists of more than 150 radio stations covering about $17\,\mathrm{km}^2$.

The radio emission of air showers primarily stems from its well-understood electromagnetic part. Two mechanisms contribute to the coherent radio emission. Firstly, the dominant geomagnetic emission process originates from the propagation of charged secondary particles through the Earth's magnetic field [4, 11–15]. Secondly, a time-varying negative charge excess is present due to the knock out of electrons in the shower front and due to the fact that positrons of the shower front partly annihilate in the atmosphere [16–20]. The atmosphere is transparent to radio waves which offers a great potential for accurate measurements, e.g, of the primary cosmic-ray energy. That the radio emission is related to the primary cosmic-ray energy has meanwhile been shown by several experiments [21–25]. Moreover, the radiation energy, which is the amount of energy transferred from the primary cosmic ray into the radio emission, has been determined [25]. By combining such accurate measurements with the predictions of the radio emission by calculations based on first principles of classical electrodynamics [26–29] the cosmic-ray energy scale is determinable [25, 30, 31].

For such high-quality measurements of the cosmic-ray properties, the antenna used in the radio sta-

tions and an accurate knowledge of the frequency and directional-dependent antenna sensitivity are essential. The so-called antenna response pattern is obtained in an absolute antenna calibration. In this work, the absolute calibration of the radio stations equipped with logarithmic periodic dipole antennas (LPDAs) using a remotely piloted octocopter is presented. All components involved in the calibration have been quantified with respect to their uncertainties. The antenna calibration uncertainty directly impacts the cosmic-ray energy scale. Thus, a reduction of the uncertainties is most desirable. A new calibration setup has been developed which enables more polarization measurements, a higher sampling of different arrival directions and reduced systematic uncertainties compared to previously performed calibrations. The uncertainties have been reduced to the level of $10\,\%$ which is a significant improvement compared to calibration uncertainties obtained at other radio experiments [32–34].
Radio stations typically consist of two horizontally aligned but perpendicular polarized antennas. The vertical component of the radio emission from air showers is not measured directly but is reconstructed by the measurements in the horizontally aligned antennas. Radio stations consisting of three separated antennas are called 3D radio stations. They enable direct measurements of all three components of the radio signal which potentially reduces the reconstruction uncertainties and furthermore extends the field of view of the radio detector to signals with arrival directions close to the horizon. Air showers coming from that directions are called horizontal air showers (HASs) and are of special interest in radio experiments because the shower information viewed at large distances is only saved in the muonic and radio component and measuring both then enables a reconstruction of the cosmic-ray mass. Furthermore, HASs have a large footprint on ground and thus offer a great potential for future large-scale radio experiments [35, 36]. For AERA, a new 3D radio station has been developed and deployed in the field. The antenna response pattern is discussed and the antenna functionality has been proven. Furthermore, first measurements of cosmic-ray candidates are presented.
This work is structured as follows. In Chap. 2, the current status of knowledge about cosmic rays is briefly summarized, recent measurements are presented, and the air shower development is explained with focus on the radio emission. In Chap. 3, a theoretical overview of antennas and the signal processing in antennas is explained. The vector effective length is introduced as measure of the frequency and directional-dependent antenna sensitivity. Afterwards, the Pierre Auger Observatory and AERA are presented in Chap. 4. The mechanical and electrical properties of the antennas used in the radio stations are discussed. One of the challenges measuring cosmic-ray induced air showers at AERA is the handling of the local environmental conditions, e.g., temperature changes impact the signal gain of the amplifier used in the stations. The temperature drift of the amplifier gain has been investigated and is presented in Chap. 5. Furthermore, a thorough knowledge of ground conditions and their variation, e.g., due to rain fall, is necessary for an accurate description of the antenna response pattern. In Chap. 6, measurements of the permittivity of ground at the AERA site are presented. The influence of several effects on the antenna, e.g., varying ground conditions or antenna misalignment, has been investigated in multiple simulations using the NEC-2 simulation code [37] which are discussed in Chap. 7. The absolute calibration measurements using the octocopter are presented in Chap. 8. This chapter includes a detailed discussion of the calibration uncertainties and its influence on the radio signal reconstruction. In Chap. 9, the development and first measurements of a new 3D radio station are presented. Finally, the results of this work are concluded in Chap. 10.

2

Cosmic Rays

Parts of this chapter have been published in:

A. Aab et al. (Pierre Auger Collaboration)
"Calibration of the Logarithmic-Periodic Dipole Antenna (LPDA) Radio Stations at the Pierre Auger Observatory using an Octocopter"
J. Instrum. **12** (2017) T10005
The work presented in this publication was primarily performed by the author of this thesis. The text of the publication has been written by the author of this thesis and was revised and copy-edited by the co-authors of the publication.

R. Krause for the Pierre Auger Collaboration
"A new method to determine the energy scale for high-energy cosmic rays using radio measurements at the Pierre Auger Observatory"
Proc. of the 35th ICRC 2017, Busan, South Korea (2017)
PoS (ICRC2017) 528

R. Krause for the Pierre Auger Collaboration
"Detection of Ultrahigh-Energy Cosmic Rays with the Auger Engineering Radio Array"
Proc. of the VCI 2016, Vienna, Austria (2016)
Nucl. Instrum. Meth. A, **845C** (2017) 378-382

R. Krause for the Pierre Auger Collaboration
"AERA – The Auger Engineering Radio Array"
Proc. of the VULCANO Conf. 2014, Vulcano Island, Italy (2014)
Frascati Physics Series Vol. **58** (2014) 315-322

Cosmic rays are particles which have their origin in outer space and some of them propagate to Earth. The Earth is constantly bombarded by cosmic rays. The cosmic-ray flux decrease with the cosmic-ray energy from some thousands per square meter and second at small energies of about $10^9\,\mathrm{eV}$ to a few cosmic rays per century and square kilometer at highest energies of about $10^{20}\,\mathrm{eV}$. Cosmic rays have firstly been observed by Victor Hess in 1912 [2]. In seven balloon flights he ascertained an additional ionizing radiation beside the terrestrial radiation increasing with the flight height of the balloon. He concluded that the source of this radiation must have its origin outside of the Earth. This cosmic radiation makes up about half of the natural radiation on the Earth's surface.
The comprehension of cosmic rays is of great interest in physics and in the focus of current research

in several experiments. Due to the large energy range of cosmic rays, different kinds of experimental setups are necessary to investigate the cosmic-ray properties. Balloon-based experiments (e.g. [38–41]) and space-born experiments (e.g. [42–45]) enable to detect cosmic rays with energies below $10^{15}\,\mathrm{eV}$ whereas cosmic rays at highest energies are measured in large ground-based detectors on Earth (e.g. [3, 46–48]).
The fundamental questions physicists worldwide would like to answer are: what is the chemical composition of cosmic rays, where do they come from, how are they accelerated to their extreme energies, and how do they propagate through the universe to Earth.
In this chapter, the recent status of knowledge about cosmic rays is briefly summarized, in particular for cosmic rays at the highest energies. In the first section, the cosmic-ray energy spectrum measured on Earth as well as the cosmic-ray composition are presented. In Sec. 2.2, possible sources and acceleration mechanisms are discussed. The propagation of cosmic rays through the universe is covered in Sec. 2.3. Finally, the cosmic-ray interaction with the Earth's atmosphere and the development of so-called extensive air showers are discussed in Sec. 2.4.

2.1 Energy Spectrum and Chemical Composition

Energy and mass are characteristic properties of cosmic rays and thus are of great interest in current research. The energy of cosmic rays covers a range to more than $10^{20}\,\mathrm{eV}$ for a single particle. The respective cosmic-ray flux decreases rapidly to a few cosmic rays per square kilometer and century at highest energies. For energies of more than some tens of GeV, the cosmic-ray flux F follows a simple inverse power law:

$$F(E) = \frac{dN}{dE} \propto E^{-\gamma}, \tag{2.1}$$

where E is the energy per nucleus and γ the spectral index.
The experimental detection of cosmic rays is divided into two categories of experimental setups. Cosmic rays with energies below $10^{15}\,\mathrm{eV}$ are directly measurable using balloon-based or satellite-based experiments. Such direct measurements of cosmic rays enable reconstructing the cosmic-ray energy as well as the cosmic-ray mass with small uncertainties. In Fig. 2.1, the particle flux of cosmic rays is shown as a function of the energy in the case of different cosmic-ray masses. Cosmic rays with energies below $10^{15}\,\mathrm{eV}$ consist mostly of protons and helium.
Above $10^{15}\,\mathrm{eV}$, cosmic rays are not directly measured anymore for two major reasons: Firstly, the statistics is reduced due to the low particle flux at highest energies. Secondly, the energy of these particles is so high that the particle just fly through the detector as balloon-based or satellite-based experiments are too small to absorb the particle. Therefore, cosmic rays at highest energies have to be measured indirectly in large-scale experiments on Earth. The primary cosmic ray hits the Earth atmosphere creating lots of secondary particles forming a so-called extensive air shower (EAS). The atmosphere acts thereby as a giant calorimeter which is read out by large ground-based detectors. EAS are described in more detail in Sec. 2.4.
In Fig. 2.2, the cosmic-ray flux at highest energies as function of the cosmic-ray energy measured by different experiments is shown. Clear characteristic properties of the flux become visible when multiplying the flux with a factor of $E^{2.6}$. The measurements of the particle flux at high energies

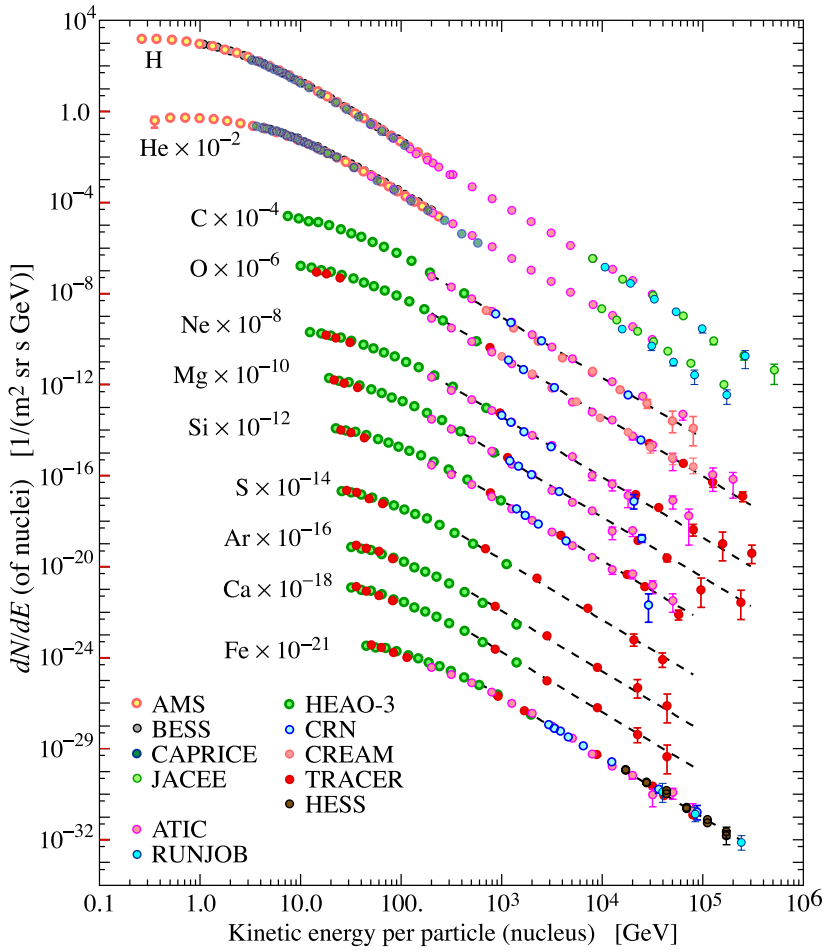

Figure 2.1: *The flux of cosmic rays with different masses as function of their energy obtained by direct measurements. Plot taken from [49] based on data from [50–62].*

exhibit four characteristic energies where the power law is broken and the spectral index is changed. For cosmic rays with energies smaller than $5 \cdot 10^{15}\,\mathrm{eV}$, the spectral index is $\gamma \approx 2.7$. For larger energies, the spectral index changes to $\gamma \approx 3.1$ which is called the *knee region* [75]. The *knee region* was firstly observed in 1958 [83]. A *2nd knee* is found close to $8 \cdot 10^{16}\,\mathrm{eV}$. Here, the spectral index increases to $\gamma \approx 3.24$ [79]. Typically, the particle flux is interpreted in the way that cosmic rays with lower energies have mostly a galactic origin. In the *knee region*, cosmic rays are accelerated to the maximal energy of most galactic accelerators. As the cosmic-ray acceleration scales with the cosmic-ray charge Z, iron nuclei can be accelerated to higher energies than protons. Hence, the *knee* position depends on the particle type [84–86]. At the so-called *ankle* of the cosmic-ray spectrum, the extragalactic component becomes dominant and at about $5 \cdot 10^{18}\,\mathrm{eV}$ the spectral index decreases to $\gamma \approx 2.6$ again which has been measured at the HiRes experiment [76], at the Telescope Array experiment [81], and at the Pierre Auger Observatory [82]. At highest energies, the particle flux decreases rapidly to zero. There are no observations of cosmic rays with energies above some $10^{21}\,\mathrm{eV}$. The cutoff energy $E_{1/2}$ is defined as the position at which the cosmic-ray flux has dropped to half of the cosmic-ray flux if no cutoff would be present. Here, significant differences between the experiments have been observed [87]. The HiRes experiment and the Telescope Array experiment found a

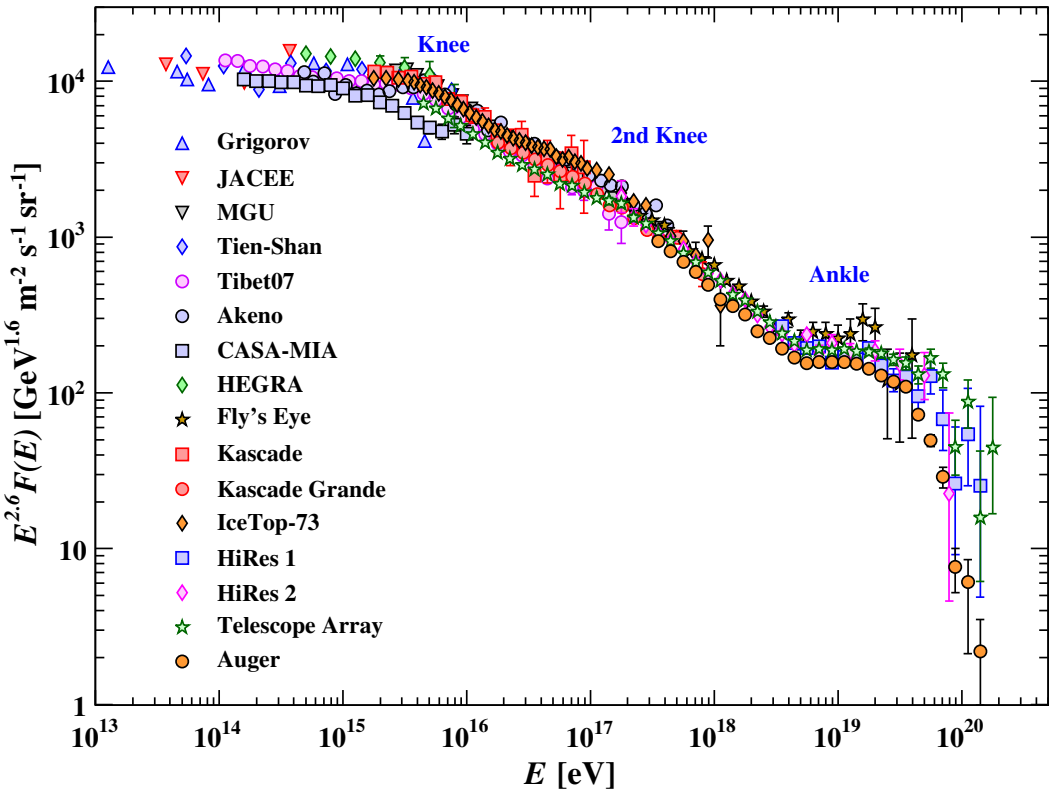

Figure 2.2: *The cosmic-ray flux scaled with the particle energy as function of the energy. It can be described by a power law. Four characteristic features of the energy spectrum are identified where the spectral index changes: the Knee, the 2nd Knee, the Ankle and the cosmic-ray cut off for cosmic rays at highest energies. Plot taken from [49] based on data from [63–82].*

cosmic-ray cutoff energy of $E_{1/2} \approx 6 \cdot 10^{19}\,\mathrm{eV}$ [76, 81]. At the Pierre Auger Observatory a cutoff energy of $E_{1/2} \approx 2.5 \cdot 10^{19}\,\mathrm{eV}$ is observed. A possible explanation of such a cutoff is the interaction of the cosmic rays with photons of the cosmic microwave background (CMB) which was predicted by Kenneth Greisen, Georgiy Zatsepin and Vadim Kuzmin in 1966, called the GZK-cutoff or the GZK-suppression [88, 89]. The GZK-suppression is explained in more detail in Sec. 2.3. A different explanation is a simple die-out of possible sources which are able to accelerate particles to such high energies.

Due to the indirect measurement setup, the cosmic-ray reconstruction of energy and chemical composition is less accurate than those of direct measurements. Nevertheless, indirect cosmic-ray measurements enable determining the cosmic-ray composition. One characteristic parameter correlated to the cosmic-ray mass is the so-called slant depth X. The slant depth measured from the top of the atmosphere to the shower maximum, which is the position within the shower where the maximal

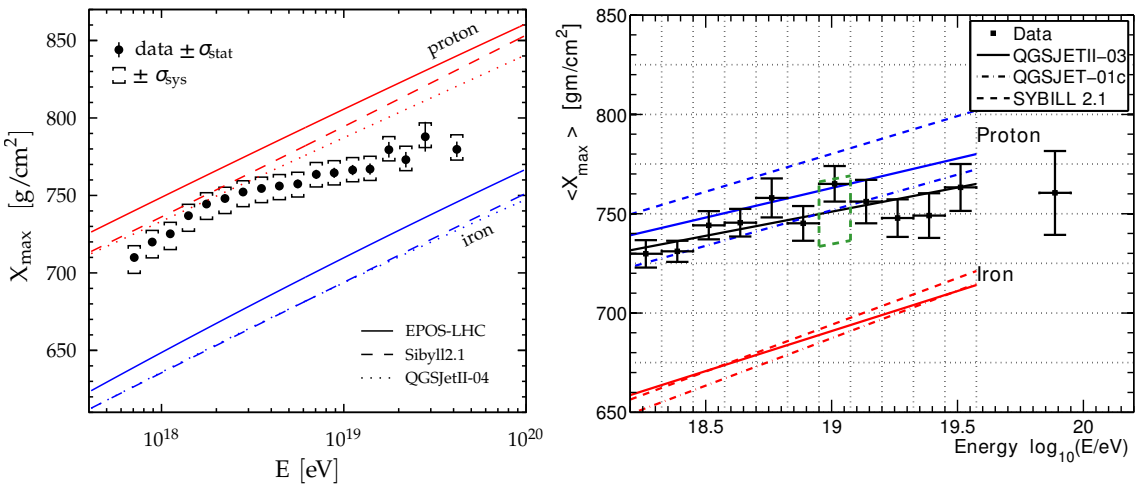

Figure 2.3: *The averaged depth of the shower maximum X_{max} measured at the Pierre Auger Observatory [97]* ***(left)*** *and measured at the Telescope Array [98]* ***(right)*** *compared to different predictions of air-shower simulations indicated by the solid, dashed and dotted lines. The black line in the right diagram marks a straight-line fit to the data. The systematic uncertainties are illustrated by the brackets (left plot) and by the green dashed box (right plot). Plots taken from [96].*

number of particles is achieved, is described by the parameter X_{max}. The average X_{max} of an iron nucleus induced air shower is less deep in the atmosphere than those of a proton induced air shower with the same energy. The slant depth of the shower maximum X_{max} as function of the cosmic-ray energy measured at the Pierre Auger Observatory as well as at the Telescope Array is presented in Fig. 2.3 and is compared to different predictions from air-shower simulations as EPOS-LHC [90], QGSJET [91–94] and Sibyll2.1 [95]. The measurements reveals a mixed composition getting heavier at the largest energies. Both data sets from the Pierre Auger Observatory and from the Telescope Array have been compared to each other and an agreement within their uncertainties has been found [96].

2.2 Origin and Acceleration Processes

The kinetic energy of cosmic rays can exceed the cosmic-ray mass by several orders of magnitudes. A main question is how these particles gain such high energies which corresponds to the question of the origin of cosmic rays. There are two approaches to explain the highest energies of cosmic rays. On the one hand, the cosmic ray could be produced by high-energy processes, e.g., during the early universe. Super-massive particles with masses beyond 10^{20} eV decay into quarks and leptons producing jets. From this decay high energy cosmic rays are produced without any further acceleration processes. Nevertheless, this model is disfavored as also a large number of gamma rays are predicted which is excluded by the low rate of gamma-ray observations [99–101]. More favored is a model where the cosmic ray is accelerated to highest energies by stochastic acceleration processes. Thus, the question for the cosmic-ray source and for possible acceleration processes of galactic and intergalactic objects are coupled to each other. The idea is that the cosmic ray gains energy with each phase of acceleration. The acceleration process takes place as long as the cosmic ray is in the region of influence of the source and is bound by its magnetic field B. The deflection of a particle with a charge Z within a

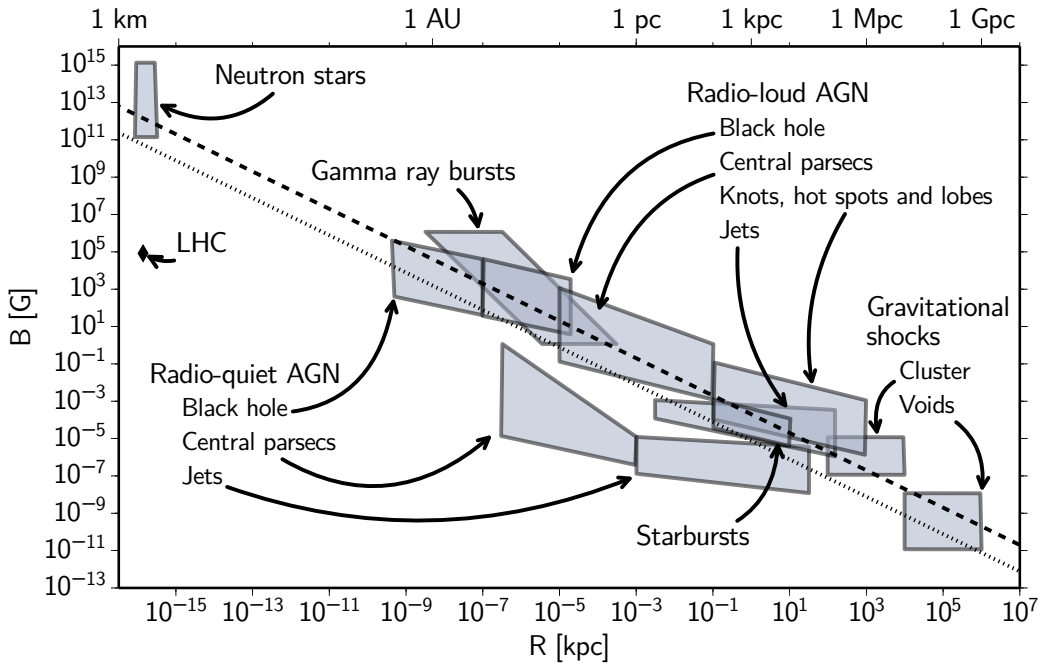

Figure 2.4: *The Hillas plot illustrates the capability of different objects in the universe to accelerate cosmic rays with respect to their size and magnetic field strength. The objects located above the dashed (dotted dashed) line are able to accelerate protons (iron nuclei) to* 10^{20} eV. *Plot taken from [102] (modified from [105]).*

homogeneous magnetic field is called Larmor radius r_L for which the following relation holds:

$$r_L[kpc] = 1.08 \frac{1}{Z} \frac{E[EeV]}{B[\mu G]}. \tag{2.2}$$

The higher the energy, the larger is the Larmor radius of the cosmic-ray. At the point when the Larmor radius exceeds the size of the region of influence of the source, the cosmic ray can escape and is not accelerated any more. The maximal cosmic-ray energy E_{max} of a source constrained by its magnetic field B and the size of its region of influence R is estimated using the following equation:

$$E_{max}[EeV] = 2.16\, Z\, \beta\, B[\mu G]\, R[kpc]. \tag{2.3}$$

where β describes the velocity of the scattering center [102]. Whereas most low-energy cosmic rays have a galactic origin, the magnetic field of the Milky Way is too small to capture cosmic rays at highest energies and thus, they have an extragalactic origin. In 1984, A.M. Hillas illustrated the question of possible source candidates in relation to their magnetic field and their size considering Eq. (2.3) in a graphical way [103]. The so-called Hillas plot is shown in Fig. 2.4. The dotted (dashed) line indicates the source requirement to accelerate a proton (iron nucleus) to at least 10^{20} eV. All sources above this line are possible source candidates of cosmic-rays with highest energies, e.g., neutron stars, gamma-ray bursts, active galactic nuclei, or gravitational shocks [104].

The idea of a stochastic energy gain of the cosmic ray was formulated by E. Fermi in 1949 [106].

He stated that a cosmic ray with initial energy E_0 gains a constant energy ΔE for each acceleration phase. The cosmic-ray energy after n accelerations is then given by:

$$E = E_0(1 + \Delta E)^n. \tag{2.4}$$

Two types of acceleration models are formulated. The first acceleration model is based on elastic scattering of the cosmic ray with interstellar magnetized clouds moving with the speed of β. Whereas the momentum, and the energy of the cloud do not change due to the scattering, the cosmic ray is accelerated and the energy gain is proportional to the square of β: $\Delta E \propto \beta^2$. Due to the squared dependency, this model is called *2nd order Fermi acceleration*.
In a second more efficient model, the cosmic-ray energy gain is explained by diffuse shocks. These shocks are propagating with supersonic speed through a plasma. The space is divided in a shocked region and a region without shock with different densities of the plasma. A cosmic ray is reflected at the shock which results in an energy gain proportional to β: $\Delta E \propto \beta$ where β is the velocity of the center of the scattering [107]. This model is called *1st order Fermi acceleration* due to the linear correlation between energy gain and velocity.

2.3 Propagation and Arrival Directions

The propagation of cosmic rays through the universe until they reach the Earth is influenced by magnetic fields and interactions with background radiations. According to Eq. (2.2), charged cosmic rays are deflected in extragalactic and galactic magnetic fields. The degree of influence depends on the cosmic-ray charge, on the cosmic-ray energy, on the magnetic-field strength and on the coherence length. The magnetic-field strength of extragalactic magnetic fields (EGMF) is poorly known. The magnetic fields in the center of galaxy clusters are measured by Faraday rotation measurements resulting in a magnetic-field strength on the level of $1\,\mu\mathrm{G}$ to $40\,\mu\mathrm{G}$ [104]. The magnetic fields in voids are much smaller. Here, γ-ray observations confine the magnetic-field strength to less than $1\,\mathrm{nG}$ [108]. From models of the EGMF, the cosmic-ray deflection due to the EGMF can be estimated [102, 109]. It is found that the cosmic-ray deflection due to EGMFs is small for cosmic rays at highest energies and with small charge. Thus, the arrival direction still points back to the source [110].
The galactic magnetic field (GMF) is better known than EGMFs. It is constrained by Faraday rotation measures of extragalactic sources [109, 111]. The strength of the GMF is on the order of μG on a coherence length of some kpc. Common GMF models are made by Pshirkov, Tinyakov and Kronberg in 2011 (PTK11) [112] and by Jansson and Farrar in 2012 (JF12) [113–115]. The JF12 is based on large-scale regular fields following the spiral arms of the galaxy, a halo field as well as additional random fields. From these models, the cosmic-ray deflection in the Milky Way can be estimated. The average cosmic-ray deflection $<\beta>$ scales with the cosmic-ray charge Z and correlates inverse with the cosmic-ray energy E: $<\beta>[^\circ] \approx 300 \cdot \mathrm{Z} \cdot (\mathrm{E}[\mathrm{EeV}])^{-1}$ [109] which allows for a correction of the deflection if the cosmic-ray charge and energy is known [116].
Cosmic rays lose energy due to interaction with background radiations, e.g., the cosmic microwave background (CMB) which for this process is the most important extragalactic background radiation. A radiation from the intergalactic space with a temperature of about $T = 2.8\,\mathrm{K}$ was firstly pre-

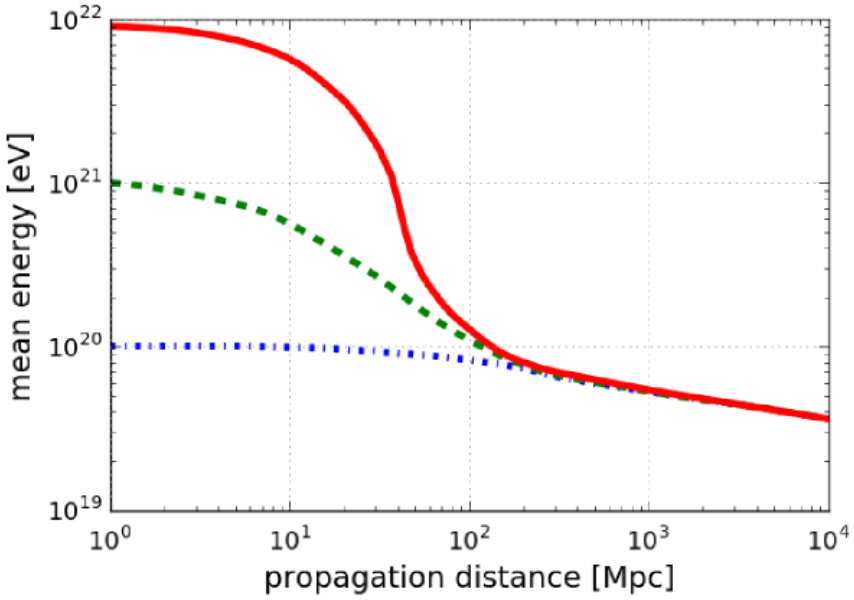

Figure 2.5: *Proton energy as a function of the propagation distance of three protons with different initial energies of* 10^{20} eV, 10^{21} eV, *and* 10^{22} eV. *Plot taken from [30] and adapted from [119].*

dicted by E. Regener in 1933 [117] and then observed by A.A. Penzias and R.W. Wilson in 1965 [118]. The CMB is the radiation left over from the early universe from about 380.000 a after the big bang and is deemed to be the confirmation of the big bang theory. The CMB has a temperature of $T = 2.725(2)\,\mathrm{K}$ [49] which corresponds to a photon energy of about $\epsilon = 0.2\,\mathrm{meV}$. The CMB is mostly opaque for protons at highest energies leading to a cosmic-ray suppression at highest energies. This effect is explained by Kenneth Greisen, Georgi Sazepin and Wadim Kusmin [88, 89] and is called the GZK-suppression: A proton at highest energy interacts with a photon of the CMB and creates a delta-resonance. The delta particle then decays into a pion and a proton or neutron of lower energy. The neutron further decays into protons:

$$\begin{aligned} p + \gamma_{\mathrm{CMB}} \rightarrow \Delta^{+}(1232) &\rightarrow p + \pi^{0} \\ &\rightarrow n + \pi^{+} \rightarrow p + e^{-} + \bar{\nu}_{e} + \pi^{+} \end{aligned} \tag{2.5}$$

The lower energy threshold E_{th} of the proton is calculated by:

$$E_{\mathrm{th}} = \frac{m_{\pi}(2m_{p} + m_{\pi})}{4\epsilon} \approx 10^{20}\,\mathrm{eV} \tag{2.6}$$

where m_{π} is the pion mass, m_{p} is the proton mass, and ϵ the photon energy as given beforehand. In Fig. 2.5, the proton energy loss due to the proton interaction with CMB photons is illustrated. The proton energy of three different initial energies is shown as a function of the propagation distance. In all cases, the proton energy drops below $10^{20}\,\mathrm{eV}$ within a propagation distance of about $100\,\mathrm{Mpc}$.

The energy loss of cosmic-ray nuclei with mass number A and with charge Z is described by the

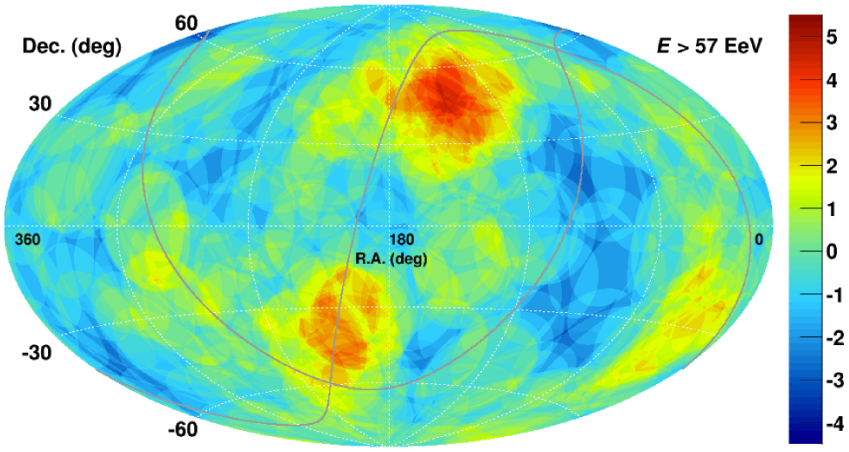

Figure 2.6: *The sky map of cosmic-rays with energies above* $5.7 \cdot 10^{19}$ eV *in equatorial coordinates measured by the Pierre Auger Observatory and the Telescope Array [123]. The color code represents the excess significance above isotropy as described in [120]. In both hemispheres an excess is observed: The northern excess is observed by the Telescope Array. The southern excess points in direction of Centaurus A and is measured by the Pierre Auger Observatory. Plot is taken from [109].*

effect of the photo disintegration which results in an energy loss similar to the proton energy loss:

$$ {}^{A}_{Z}X + \gamma_{\mathrm{CMB}} \rightarrow {}^{A-M}_{Z-N}X + {}^{M}_{N}X \tag{2.7} $$

Thus, cosmic rays observed with energies above about 10^{20} eV must have their origin within a distance of about 100 Mpc from Earth.

The origin of cosmic rays is of great interest in astrophysics research. Due to the small event horizon of cosmic rays at highest energies, anisotropies in the cosmic-ray arrival direction are expected. Analyses of the Pierre Auger Observatory and Telescope Array show indications of anisotropy for cosmic rays at highest energies. In the following, the results of some of the anisotropy analyses are briefly presented. For more information refer to the respective analyses given in the following.

The Telescope Array Collaboration reported a hot spot of 20° radius at $\alpha = 147^\circ$ and $\delta = 43^\circ$ in equatorial coordinates for cosmic rays exceeding $5.7 \cdot 10^{19}$ eV with a post-trial significance of 3.4σ. In the first five years of data taking, 19 events have been measured coming from the hot spot while 4.5 were expected [120, 121]. With a new data set considering nine years of data taking, the number of events coming from the direction of the hot spot has almost doubled [122]. The sky map of event excesses from cosmic rays exceeding $5.7 \cdot 10^{19}$ eV in relation to the expectation from isotropy is shown in Fig. 2.6.

At the Pierre Auger Observatory, an excess for cosmic rays above $5.8 \cdot 10^{19}$ eV into the direction of Centaurus A have been found. In this direction within a distance of 50 Mpc, a large number of galactic clusters are present. The excess has been determined with a post-trial significance of 2.5σ above isotropy [124] (see Fig. 2.6). Recently, the Pierre Auger Collaboration reported an update of the anisotropy analysis of the region close to Centaurus A. The significance increased to almost 3σ [125]. Within an analysis of the Pierre Auger Collaboration the arrival directions of the most energetic cos-

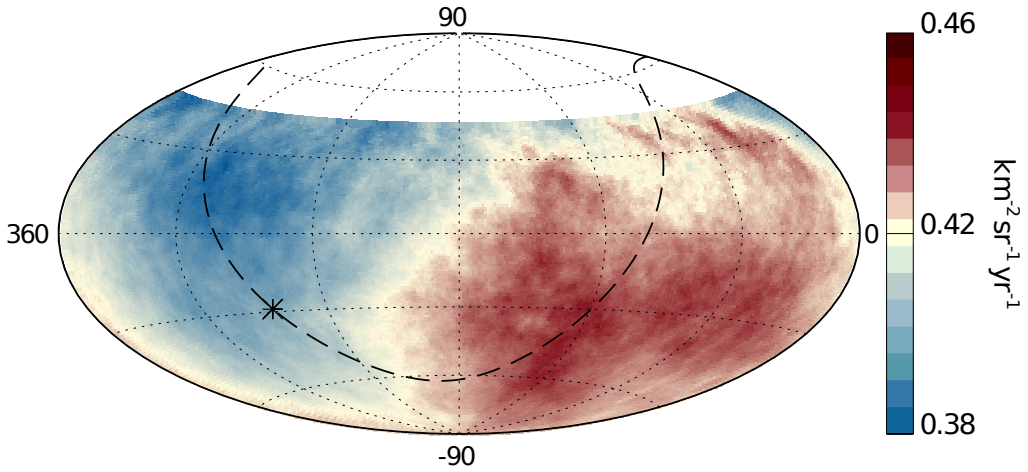

Figure 2.7: *Sky map of the cosmic-ray flux in equatorial coordinates for cosmic rays with energies above* $8 \cdot 10^{18}\,\mathrm{eV}$ *in units of* $(\mathrm{km}^2\,\mathrm{yr}\,\mathrm{sr})^{-1}$ *measured at the Pierre Auger Observatory. The data are smoothed with a radius of* 45°*. The dashed line marks the Galactic plane and the asterisk denotes the Galactic center. Plot is taken from [133].*

mic rays above $5.9 \cdot 10^{19}\,\mathrm{eV}$ have been compared to the positions of active galaxy nuclei (AGN) listed in the VCV catalog [126] with distances smaller than $75\,\mathrm{Mpc}$. After several years of data taking, an agreement of $28.1^{3.8}_{-3.6}\,\%$ has been found which is about 2σ above the expectation from isotropy [127, 128]. Recently, the Pierre Auger Collaboration reported an analysis update comparing the arrival directions of these most energetic cosmic rays with AGN listed in the swift-BAT catalog considering the most luminous AGN with distances smaller than $190\,\mathrm{Mpc}$. The anisotropy in the arrival direction has been confirmed with increased significance of more than 3σ [125]. Furthermore, the measured arrival directions of cosmic rays at highest energies have been compared to the directions of gamma-ray AGN listed in the 2FHL-catalog [129] and star forming galaxies. For the gamma-ray AGN an excess is found with a significance of 2.7σ and for the star forming galaxies an excess at the level of 4σ is reported [125].

Achieved by harmonic analyses of the arrival directions decomposed in multipole moments, the Pierre Auger Observatory found a large-scale anisotropy in the dipole moment when analyzing the arrival direction of cosmic rays with energies above $8 \cdot 10^{18}\,\mathrm{eV}$ at $\alpha = (95 \pm 13)^\circ$ and $\delta = (-39 \pm 13)^\circ$ in equatorial coordinates with a significance of 4σ [130, 131]. The dipole has been confirmed by a needlet-wavelet analysis which is reported in [132]. Recently, the Pierre Auger Collaboration reported a further analysis confirming the presence of the dipole with an amplitude of $6.5^{+1.3}_{-0.9}\,\%$ and a significance of 5.2σ [133]. A sky map of the observed cosmic-ray flux in equatorial coordinates illustrating the large-scale anisotropy is presented in Fig. 2.7. This is the first observation with high significance of anisotropy in the cosmic-ray arrival directions at energies above $8 \cdot 10^{18}\,\mathrm{eV}$.

2.4 Extensive Air Showers

When high-energy cosmic rays hit the Earth's atmosphere, they collide with air nuclei and secondary particles are produced. Due to the high energy of the primary cosmic ray, the secondary particles

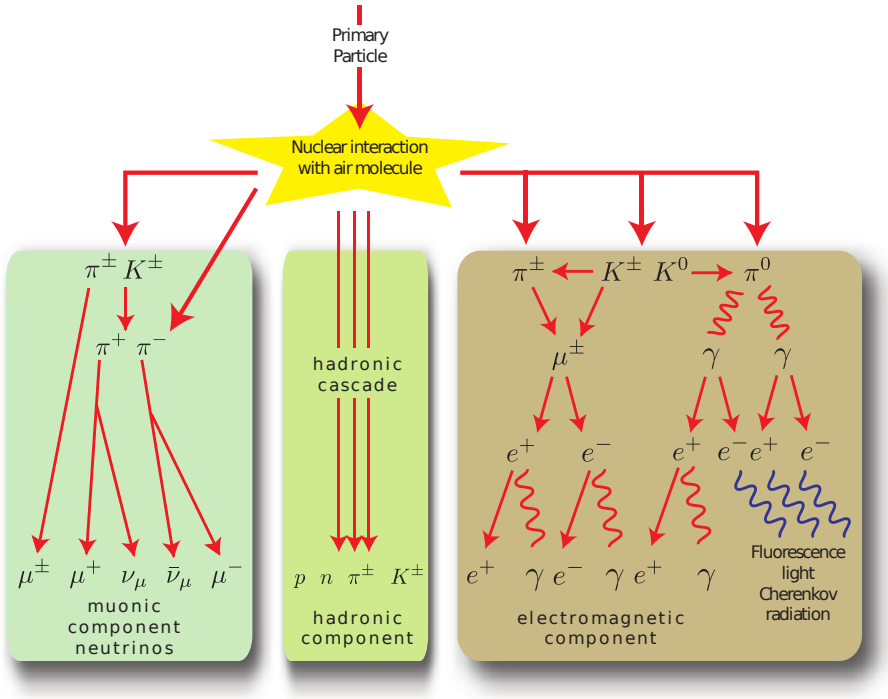

Figure 2.8: *The primary particle enters the Earth's atmosphere and interacts with air molecules producing a cascade of secondary particles forming a so-called extensive air shower (EAS). The EAS is divided into three subcomponents: a muonic component, a hadronic component and an electromagnetic component. Picture taken from [135].*

can thereby interact with air molecules and thus a particle cascade of millions of secondary particles is created, a so-called extensive air shower (EAS). The Earth's atmosphere acts thereby as a giant calorimeter of about $\sim$11 hadronic interaction lengths. The first interaction usually takes place at a height of 15 km to 35 km [134]. The EAS is divided into three subcomponents: a muonic component, a hadronic component and an electromagnetic component. The muonic component is composed of charged muons and muon neutrinos which stems from the decay of pions and kaons. The neutrinos rarely contribute to the shower development due to their small cross section in air but they carry a significant part of the initial energy and thus are important for reconstructing the primary cosmic-ray energy. The hadronic component is composed of long-life baryons. Furthermore, pions and kaons have a lifetime of $\tau_{\pi^{\pm}} = 2.6 \cdot 10^{-8}$ s and $\tau_K = 1.2 \cdot 10^{-8}$ s [49] respectively. Thus, they live long enough to produce new pions and kaons. The electromagnetic component is composed of electrons, positrons, and photons created by bremsstrahlung, pair production as well as the decay of charged pions and kaons into muons which then further decay into electrons and positrons. Furthermore, neutral pions have a small lifetime of $\tau_{\pi^0} = 8.5 \cdot 10^{-17}$ s [49] and thus directly decay into two photons. A scheme of an EAS is shown in Fig. 2.8.

2.4.1 Extensive Air Shower Development

The shower development correlates with the properties of the primary cosmic ray, e.g., the cosmic-ray energy and the cosmic-ray particle type. From the lateral and longitudinal particle density distribution, information about the primary particle can be concluded. In Fig. 2.9, simulations of the shower development for different initial particles with an energy of $10^{14}\,\mathrm{eV}$ using the CORSIKA [26, 136] simulation code are shown. In the case of photons, the shower maximum is reached relatively deep in the atmosphere and the lateral shower distribution is smaller compared to EASs induced by protons or iron nuclei on average. The larger the cosmic-ray mass, the higher is the probability to interact with the atmosphere. Thus, the particle cascade starts earlier and the shower maximum is reached higher up in the atmosphere. Furthermore, the lateral extension of the EAS is getting significantly larger with increased mass of the primary cosmic ray.

The number of particles produced in an EAS can be estimated according to the Heitler model [137, 138]. The Heitler model is a simple shower model and is based on photon pair production: $\gamma \rightarrow e^+ + e^-$ and bremsstrahlung: $e^\pm \rightarrow e^\pm + \gamma$ in the case of the electromagnetic cascade. After each splitting length $d = X_0 \cdot ln(2)$ where $X_0 = 36.7 \frac{\mathrm{g}}{\mathrm{cm}^2}$ is the radiation length of air [49] two new particles are created which carry the same amount of energy. The model of the electromagnetic cascade is illustrated on the left side of Fig. 2.10.

The total number of particles N is doubled after each splitting length:

$$N(n) = 2^n, \tag{2.8}$$

where n is the number of splitting lengths. For the corresponding particle energy E at iteration n the following equation holds:

$$E(n) = \frac{E_0}{N(n)}, \tag{2.9}$$

where E_0 is the initial cosmic-ray energy. The particle cascade stops as soon as a critical energy $E_c = 85\,\mathrm{MeV}$ is reached. The critical energy is defined as the particle energy where the electron energy loss due to bremsstrahlung is equal to those of ionization. According to Eq. (2.8) and Eq. (2.9), the maximal number of iterations is then given by

$$n_c = \frac{ln(\frac{E_0}{E_c})}{ln(2)} \tag{2.10}$$

and the maximal number of particles is determined to be

$$N_{max} = 2^{n_c} = \frac{E_0}{E_c}. \tag{2.11}$$

Considering a correction factor deduced from measurements $g \approx 13$ [140] for electrons, the total number of electrons N_e is then estimated to be

$$N_e = \frac{N_{max}}{g} \approx 9 \cdot 10^5 E_0[\mathrm{PeV}]. \tag{2.12}$$

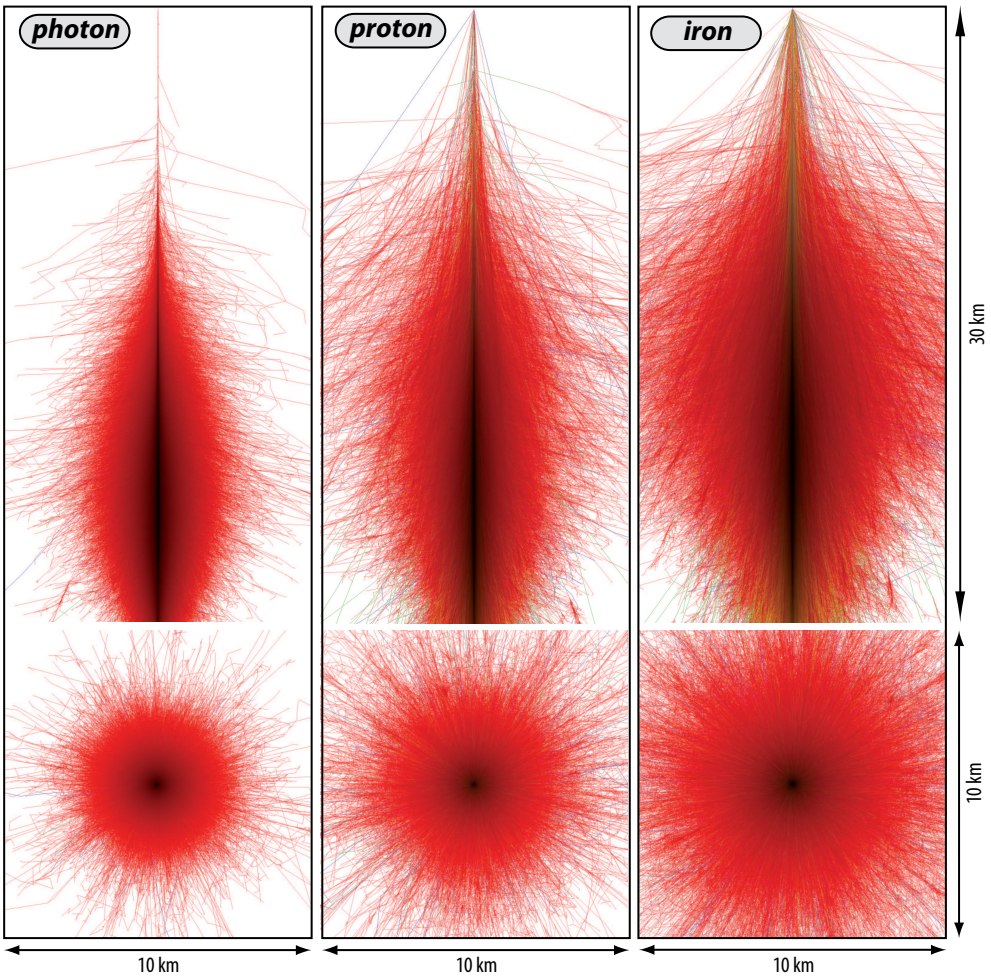

Figure 2.9: *Simulation of the longitudinal* ***(top)*** *and lateral* ***(bottom)*** *shower development of* ***(from left to right)*** *photon, proton and iron induced air showers with a primary cosmic-ray energy of* 10^{14} eV *using the CORSIKA [26, 136] simulation code. The color represents the particle type:* red $= e^{\pm}$, γ, green $= \mu^{\pm}$, blue $=$ hadrons. *The darker the color, the higher is the particle density. The shower development differs for different initial particle types. The heavier the primary cosmic-ray the shower development reaches its maximum higher up in the atmosphere and has a larger lateral extension. Picture taken from [135].*

The Heitler model can be extended so that also the hadronic component of the shower development can be described. In the case of a hadronic cascade, mostly pions are produced followed by kaons which then decay into pions. Similar to the electromagnetic cascade, it is assumed that after the fixed pion interaction length $\lambda_\pi = 120\,\mathrm{g/cm^2}$ in air [141] a new interaction takes place. The pions interact with air molecules in a hadronic interaction producing N_{ch} new charged pions and $0.5N_{\mathrm{ch}}$ new neutral pions. Thus, the total number of particles produced in each interaction is $N_{\mathrm{tot}} = \frac{3}{2}N_{\mathrm{ch}}$. The charged pions live long enough to create new particles whereas the neutral pions decay immediately into two photons and thus contribute to the electromagnetic cascade. The principle is illustrated on the right side of Fig. 2.10. The number of pions after n interactions is determined to be

$$N_\pi(n) = (N_{\mathrm{ch}})^n \tag{2.13}$$

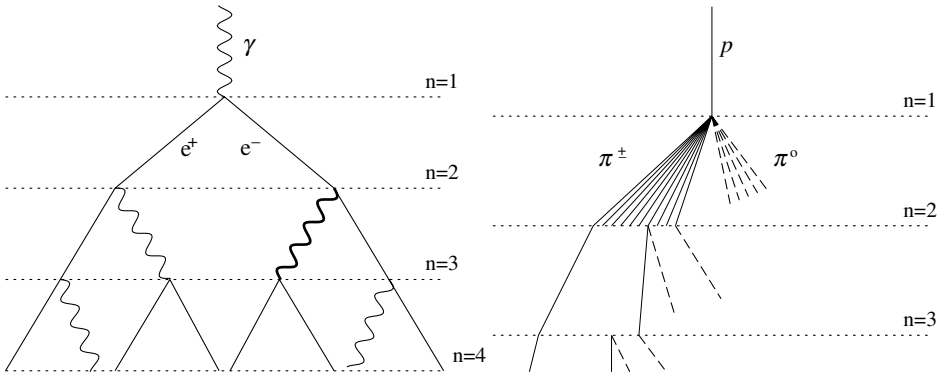

Figure 2.10: *Schematic view of the air shower development by the Heitler model. In the **(left)** panel, the electromagnetic cascade is shown. The curly lines represent photons and the straight lines mark $e^{\pm}$. In the **(right)** panel, the hadronic cascade explained by the extended Heitler model is illustrated. The solid lines represent charged pions ($\pi^{\pm}$) and the dashed lines mark neutral pions (π^0). Pictures taken from [139].*

and each pion carries an energy of

$$E_\pi(n) = \frac{E_0}{(N_{\mathrm{tot}})^n}. \tag{2.14}$$

The critical energy of a pion where the decay is more probable than the interaction is $E_c^\pi = 20\,\mathrm{GeV}$ [139]. Thus, the maximal number of interaction n_c can be calculated for which the following equation holds:

$$n_c = \frac{ln(\frac{E_0}{E_c^\pi})}{ln(N_{\mathrm{tot}})}. \tag{2.15}$$

As charged pions decay mostly into muons [142] and high-energy muons rarely interact in the atmosphere, the number of muons in the hadronic cascade is approximately equal to the number of charged pions: $N_\mu \approx N_\pi$. By plugging Eq. (2.15) in Eq. (2.13), the total number of muons is estimated to be

$$N_\mu = \left(\frac{E_0}{E_c^\pi}\right)^\beta \tag{2.16}$$

with $\beta = \frac{ln(N_{\mathrm{ch}})}{ln(N_{\mathrm{tot}})} \approx 0.9$ for protons as the primary cosmic ray. In the case of a primary cosmic ray with mass number A, the cosmic ray can be assumed as A protons with reduced initial energy E_0/A for each proton. The number of muons created in the hadronic shower cascade is then estimated by:

$$N_\mu = A\left(\frac{E_0}{AE_c^\pi}\right)^\beta \approx 1.7 \cdot 10^4 A^{0.1} (E_0[\mathrm{PeV}])^{0.9} \tag{2.17}$$

The neutral pions produced during the shower development contribute to the electromagnetic cascade, and the energy E_{EM} saved in the electromagnetic cascade is given by:

$$\frac{E_{\mathrm{EM}}}{E_0} = \frac{E_0 - N_\mu E_c^\pi}{E_0} = 1 - (\frac{E_0}{AE_c^\pi})^{\beta-1}. \tag{2.18}$$

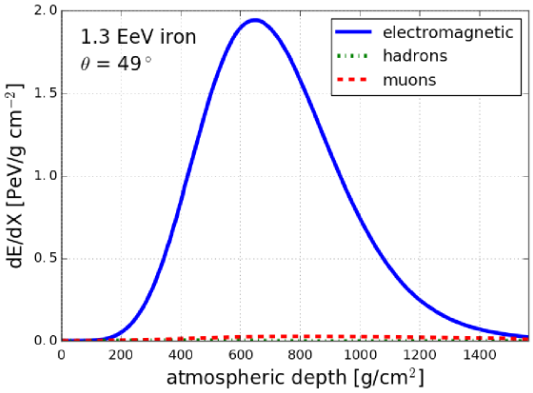

Figure 2.11: *Energy deposition of the electromagnetic (blue line), the hadronic (green dotted line) and the muonic (red dashed line) cascade of an iron induced air shower with a primary cosmic-ray energy of* $1.3 \cdot 10^{18}\,\mathrm{eV}$ *and a zenith angle of* $49\,^{\circ}$ *as a function of the atmospheric depth. Plot taken from [30].*

The total number of electrons N_e is estimated from Eq. (2.18) (refer to [140]):

$$N_e = \frac{E_{\mathrm{EM}}}{g E_c^e} = 6 \cdot 10^5 A^{-0.046} (E_0[\mathrm{PeV}])^{1.046} \tag{2.19}$$

Thus, the ratio of the number of electrons to the number of muons at the shower maximum is a good estimator for the initial cosmic-ray mass. The heavier the primary cosmic rays the earlier the shower maximum is reached. Furthermore, the number of muons is increased whereas the number of electrons is reduced. Even such simple shower models explain the shower development well. Nevertheless, the shower development can significantly vary for the same type of primary cosmic rays due to shower-to-shower fluctuations. Thus, the cosmic-ray mass is typically not determined event-by-event but in average. Hence, the cosmic-ray mass is usually referred to as the cosmic-ray composition.

Usually, the lateral shower distribution is determined by measuring the particles which reach ground level, e.g., using water-Cherenkov detectors (refer to [3]) or scintillation counters (refer to [48]). The longitudinal shower distribution is determined by measuring fluorescence light, which is emitted from air molecules excited by the particle cascade, using fluorescence telescopes [3, 48]. The emitted light intensity is proportional to the shower energy deposition dE/dX in the Earth's atmosphere and thus, enables to observe the longitudinal shower profile. The longitudinal shower profile of an iron induced air shower with a primary cosmic-ray energy of 1.3 EeV is shown in Fig. 2.11 exemplary. The energy deposition is dominated by the electromagnetic cascade of the EAS whereas the hadronic and muonic cascade do not contribute significantly to the energy deposition [30]. Nevertheless, muons and neutrinos can carry a significant fraction of the primary cosmic-ray energy depending on the primary cosmic-ray energy and particle type (cf. Eq. (2.17)). Thus, from the integral of the energy deposition measured by fluorescence telescopes, the energy transferred from the primary cosmic ray into the electromagnetic shower component can be determined.

2.4.2 Radio Emission of EAS

During the shower development also radio emission in the megahertz (MHz) regime is produced [25]. Two mechanisms contribute to coherent radio emission from air showers. Firstly, charged secondary particles are deflected in the Earth's magnetic field. This forms a radiating dipole perpendicular to the shower axis and a signal polarized towards the vector product of the incoming direction $\vec{v}$ and the Earth's magnetic field $\vec{B}$: $\vec{e}_{\text{geo}} \propto \vec{v} \times \vec{B}$. The amplitude scales with $\sin(\alpha)$, where α describes the angle between the arrival direction and the Earth's magnetic field. This emission process is called geomagnetic emission [4, 11–15].
Secondly, secondary particles knock out electrons from air molecules. These electrons move along with the shower front and positively charged air molecules remain. Furthermore, positrons partly annihilate in the atmosphere which leads to a time-varying negative charge excess in the shower front forming a dipole along the shower axis and a radially polarized signal $\vec{e}_{\text{ce}}$. This emission process is called charge excess or Askaryan emission [16–19].
The complete radio signal $\vec{E}$ is a superposition of both processes:

$$\vec{E} \propto \sin(\alpha)\, \vec{e}_{\text{geo}} + a\, \vec{e}_{\text{ce}} \tag{2.20}$$

where a describes the relative strength of the charge-excess emission in relation to the geomagnetic emission process. Both processes are sketched in Fig. 2.12. The radio emission primarily originates from the well-understood electromagnetic part of the air shower. The contribution of muons deflected in the Earth's magnetic field is negligible due to their large mass. Thus, the theoretical aspect of radio measurements is on solid grounds [9, 10]. The radio emission can be calculated from first principles using classical electrodynamics [27–29]. As the atmosphere is transparent to radio waves, the radio technique has a high potential for precision measurements in cosmic-ray physics.
The relative strength of the charge-excess emission has been measured at the radio array of the Pierre Auger Observatory. From signal polarization measurements the average strength of the charge excess has been determined to $a = 0.14 \pm 0.02$ [20]. The measurements are shown on the left side of Fig. 2.13. On the right side of Fig. 2.13, a measurement of the relative charge-excess strength from the LOFAR experiment is shown. The data exhibit a dependency of the relative charge-excess strength on the distance to the shower axis as well as on the incoming zenith angle [19].
Correlation of the strength of the radio signal with the primary cosmic-ray energy has meanwhile been demonstrated by several observatories [21–25]. Furthermore, at the radio detector of the Pierre Auger Observatory the radiation energy, i.e., the energy contained in the radio signal, has been determined [25].

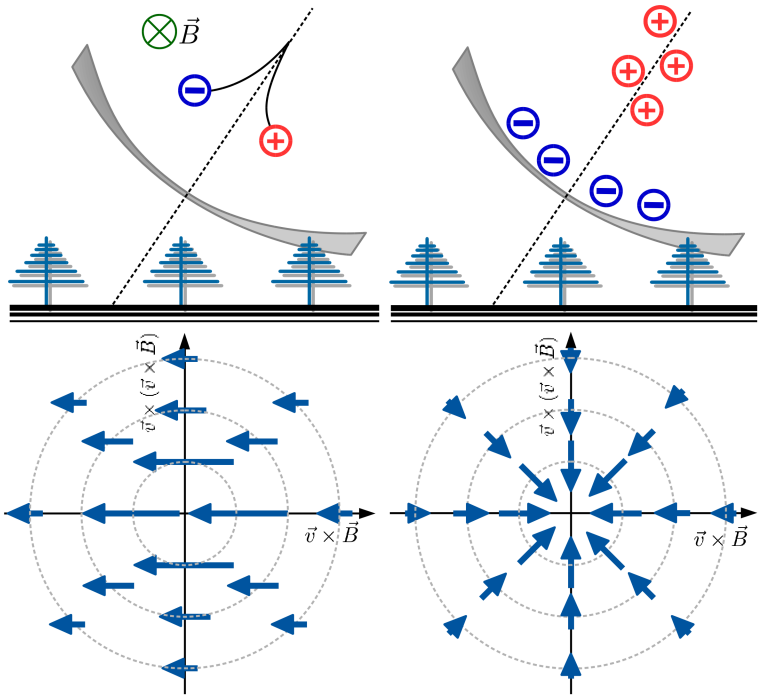

Figure 2.12: *Schematic view of the radio emission processes:* ***(upper left)*** *Geomagnetic emission process. Charged particles are deflected in the Earth's magnetic field forming a moving dipole along the shower axis.* ***(upper right)*** *Charge excess process. A time varying negative charge excess in the shower front forms a dipole oriented along the shower axis resulting in a radially polarized signal.* ***(lower panels)*** *The corresponding signal polarization and signal strength due to the emission processes transformed into the shower plane. Pictures taken from [30].*

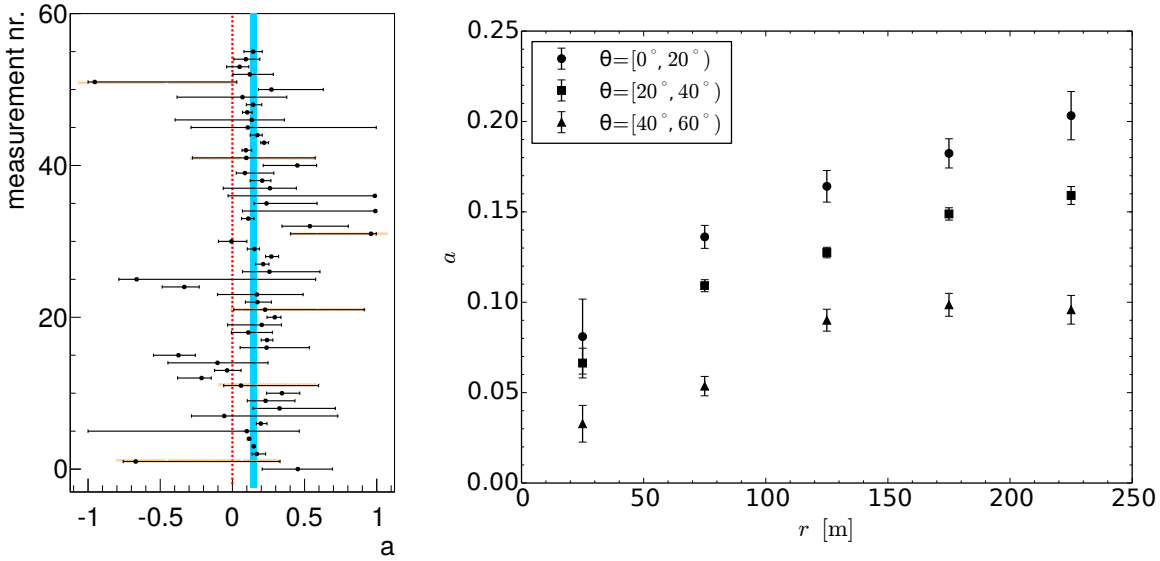

Figure 2.13: *Relative strength of the charge-excess components.* ***(left)*** *Relative charge-excess strength a determined from polarization measurements in different radio stations of the radio array of the Pierre Auger Observatory. Plot taken from [20].* ***(right)*** *Relative charge-excess strength a as a function of the distance to the shower axis r for different zenith angles measured at the Lofar experiment. Plot taken from [19].*

3

Antenna Theory

Parts of this chapter have been published in:

A. Aab et al. (Pierre Auger Collaboration)
"Calibration of the Logarithmic-Periodic Dipole Antenna (LPDA) Radio Stations at the Pierre Auger Observatory using an Octocopter"
J. Instrum. **12** (2017) T10005
The work presented in this publication was primarily performed by the author of this thesis. The text of the publication has been written by the author of this thesis and was revised and copy-edited by the co-authors of the publication.

In this chapter, a theoretical overview about antennas is given. In the first section, antennas are briefly described and the definition of the antenna far-field region is discussed. Then, the absolute antenna gain and the vector effective length (VEL) are introduced as measures of the frequency and directional-dependent antenna sensitivity. It is explained how the VEL is obtained for an uncalibrated antenna in a transmission measurement and in transmission simulations. Furthermore, the influence of electrical components on the VEL is discussed and the influence of ground conditions on the VEL is described.

3.1 Overview

Electromagnetic waves consist of an electrical component $\vec{E}$ and a magnetic component $\vec{B}$ which are oriented transversally to the propagation direction. Hence, the electric field can be expressed in spherical coordinates as a superposition of a horizontal polarization oriented along the $\vec{e}_\phi$ direction and a component oriented perpendicular to the horizontal component along the $\vec{e}_\theta$ direction which is called meridional component:

$$\vec{E} = E_\phi \vec{e}_\phi + E_\theta \vec{e}_\theta \tag{3.1}$$

The energy density and the direction of the energy transfer of electromagnetic waves is described by the so-called Poynting vector $\vec{S}$:

$$\vec{S} = \frac{1}{\mu_0} \vec{E} \times \vec{B} \tag{3.2}$$

where $\mu_0 = 4\pi \cdot 10^{-7} \frac{\mathrm{H}}{\mathrm{m}}$ is the magnetic constant.
Antennas are technical devices which enable to transmit or to receive electromagnetic waves. Thus, they represent the transition of guided and unguided propagating electromagnetic waves and are made of conductive material. Due to incoming electromagnetic waves, a current is produced within the antenna. Vice versa, due to a current within an antenna an electromagnetic wave is radiated. For

antennas, the principle of reciprocity is valid. This means that the antenna behavior is the same for receiving as well as for transmitting [143]. Depending on the issue, it makes sense to switch the perspective between transmitting and receiving antenna to characterize the antenna.
One simple antenna type is a combination of two conductive wires forming a dipole antenna. The wire length then defines the frequency range for which the antenna is most sensitive. Other antenna structures as the combination of several dipole antennas to one single antenna or horn antennas are typical antenna types. In principle, each object made of conductive material can be used as an antenna. The optimal antenna type depends on the application field for which the antenna is used, e.g., if a directive or an isotropic antenna is needed, or if single frequencies or a broad frequency band is measured. The optimal antenna design also depends on further circumstances as antenna complexity, antenna dimensions and production costs which have to be taken into account. For an overview about several different antenna types and their properties refer to [144–147].
The space around the antenna is divided into a near-field and a far-field region. In the following, both regions are explained in the case of a transmitting antenna. There is no effective radiation close to the antenna. Nevertheless, there is an exchange of idle power between the antenna and the environment. This means, the local environment has a direct influence on the antenna response pattern. This local region is called near field of the antenna. Here, the electric and magnetic field are related in a complex way. In contrast, in the so-called far field of the antenna the electric and magnetic component of the electromagnetic wave are coupled by the impedance of free space $Z_0 \approx 120\pi\,\Omega$: $|\vec{B}| = \frac{\mu_0}{Z_0}|\vec{E}|$. The energy density $\vec{S}_\mathrm{k}$ of an electromagnetic wave with an electric-field polarization of $\mathrm{k} = (\phi,\ \theta)$ is then:

$$|\vec{S}_\mathrm{k}| = \frac{|\vec{E}_\mathrm{k}|^2}{Z_0}. \tag{3.3}$$

The electric and the magnetic fields are oriented perpendicular to each other and the field strengths are decreasing with the distance.
There is a smooth transition between the near-field region and the far-field region. The transition limit of the far-field region varies for different definitions and depends on the antenna dimension and the respective wavelength. In the case of large-dimensioned antennas with a maximal antenna dimension L larger than the wavelength λ, a common definition is given by the Kraus definition [148]:

$$R > \frac{2L^2}{\lambda}. \tag{3.4}$$

In the case of small antennas with $L < \lambda$, Eq. (3.4) is not valid anymore. Here, the far-field region is defined according to [149] for distances with

$$R > \frac{\lambda}{2\pi}. \tag{3.5}$$

Further definitions of the far-field region of middle-sized antennas with $L \approx \lambda$ are given in [150] and [146]:

$$\begin{aligned} R &> 5L \\ R &> 1.6\lambda. \end{aligned} \tag{3.6}$$

3.2 The Antenna Gain

For each antenna, an effective area $A_{\mathrm{eff,k}}$ can be associated which describes the power taken from an incoming electromagnetic wave with polarization $\mathrm{k} = (\phi,\ \theta)$ and captured by the antenna. The effective area already accounts for structural and electrical losses within the antenna. For the power $P_{\mathrm{i,k}}$ applied at the antenna, the following equation holds:

$$P_{\mathrm{i,k}} = A_{\mathrm{eff,k}} |\vec{S}_{\mathrm{k}}|. \tag{3.7}$$

The effective area depends on the frequency f and the so-called spatial antenna gain G_{k} of the respective polarization $\mathrm{k} = (\phi,\ \theta)$. The effective area is given by (refer to [147]):

$$A_{\mathrm{eff,k}} = \frac{c^2}{4\pi f^2} G_{\mathrm{k}} \tag{3.8}$$

where c is the speed of light. Both spatial antenna-gain components sum up to the total antenna gain G:

$$G = G_\phi + G_\theta. \tag{3.9}$$

The total antenna gain is a characteristic antenna parameter and differs for different incoming direction with the azimuthal angle Φ and the zenith angle Θ to the antenna: $G = G(\Phi, \Theta, f)$. Thus, the antenna gain is a measure of the frequency and the directional-dependent antenna sensitivity.
The applied power is measured using a read-out system connected to the antenna. Reflection effects arise in the case of differences between the antenna and read-out system impedances which is called impedance mismatch. Only a fraction ϵ of the power $P_{\mathrm{i,k}}$ is transferred to the read-out system while a further fraction, depending on the reflection coefficient Γ, is reflected back to the antenna. The reflection coefficient is discussed in detail in the following section. For the response power $P_{\mathrm{r,k}}$ transferred from the antenna to the read-out system, the following equation holds:

$$P_{\mathrm{r,k}} = \epsilon P_{\mathrm{i,k}} = (1 - |\Gamma|^2) P_{\mathrm{i,k}}. \tag{3.10}$$

In the so-called absolute antenna gain G_{abs} the antenna characteristics given by the antenna gain G and reflection effects due to the impedance mismatch between antenna and read-out system described by the Γ parameter are combined. The absolute antenna gain of the respective polarization $\mathrm{k} = (\phi,\ \theta)$ is then given by:

$$G_{\mathrm{abs,k}} = (1 - |\Gamma|^2) G_k. \tag{3.11}$$

The response power transferred to the read-out system is then obtained by combining Eq. (3.3) and Eq. (3.7) to Eq. (3.11):

$$\begin{aligned} P_{\mathrm{r,k}} &= \frac{c^2}{4\pi f^2} G_{\mathrm{abs,k}} |\vec{S}_{\mathrm{k}}| \\ &= \frac{c^2}{4\pi f^2} G_{\mathrm{abs,k}} \frac{|\vec{E}_{\mathrm{k}}|^2}{Z_0}. \end{aligned} \tag{3.12}$$

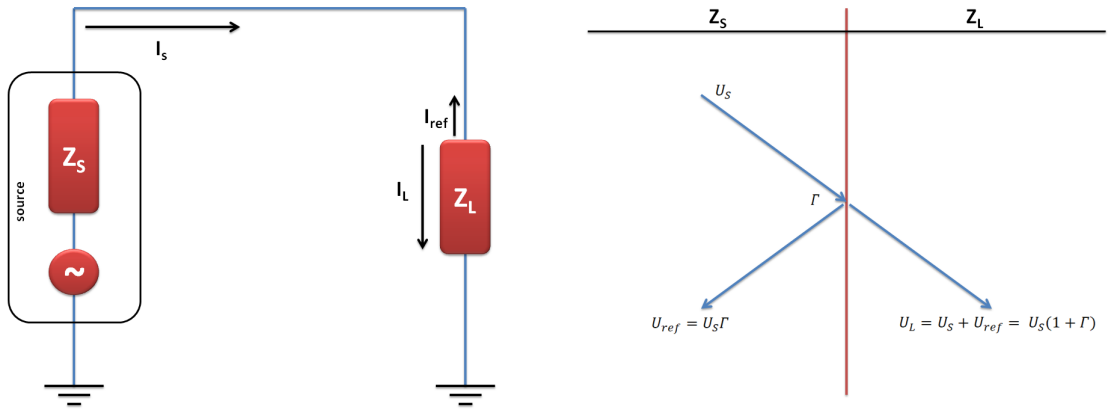

Figure 3.1: *Illustration of the signal reflection between source and load in a reflection measurement.* ***(left)*** *Respective Thévenin circuit diagram of a reflection measurement. A source with impedance Z_S is connected to a load with impedance Z_L. A fraction of the initial current $I_\mathrm{S} = I_\mathrm{L} + I_\mathrm{ref}$ passes the load and a further fraction is reflected back to the source due to impedance mismatch. Picture adapted from [151].* ***(right)*** *Illustration of the applied voltages and the reflection coefficient Γ due to impedance mismatch between source and load.*

The absolute antenna gain relates the response power with the incoming electric field strength for all incoming directions. Thus, it is a characteristic antenna parameter to classify the frequency and directional-dependent antenna sensitivity and accounts for electrical and structural losses within the antenna as well as reflection losses due to impedance mismatches between antenna and read-out systems.

3.3 Impedance Mismatch

In this section, the principle of the impedance mismatch is explained in the case of a source generator with an intrinsic impedance Z_S producing a current I_S and connected to a load with impedance Z_L. The respective Thévenin circuit diagram is shown on the left side of Fig. 3.1. On the right side of Fig. 3.1, the signal reflection due to different impedances is illustrated. The reflection coefficient Γ is defined by the ratio of the reflected voltage U_ref to the initial voltage U_S:

$$\Gamma = \frac{U_\mathrm{ref}}{U_\mathrm{S}}. \tag{3.13}$$

Due to the impedance mismatch, the current from the source I_S is split into a fraction induced into the load I_L and a fraction I_ref reflected to the source:

$$I_\mathrm{S} = I_\mathrm{L} + I_\mathrm{ref}. \tag{3.14}$$

For the voltage at the load U_{L}, the following equation holds:

$$\begin{aligned} U_{\mathrm{L}} &= Z_{\mathrm{L}} I_{\mathrm{L}} \\ &= U_{\mathrm{S}} + U_{\mathrm{ref}}. \end{aligned} \tag{3.15}$$

The reflected voltage U_{ref} is measured at the source generator and measured at the source with impedance Z_{S}:

$$U_{\mathrm{ref}} = Z_S I_{\mathrm{ref}}. \tag{3.16}$$

Plugging Eq. (3.14) to Eq. (3.16) together, the following relation is found:

$$\begin{aligned} U_{\mathrm{S}} + U_{\mathrm{ref}} &= U_{\mathrm{L}} \\ &= Z_{\mathrm{L}} I_{\mathrm{L}} \\ &= Z_{\mathrm{L}} (I_{\mathrm{S}} - I_{\mathrm{ref}}) \\ &= Z_{\mathrm{L}} (\frac{U_{\mathrm{S}}}{Z_S} - \frac{U_{\mathrm{ref}}}{Z_S}). \end{aligned} \tag{3.17}$$

$$\Leftrightarrow (\frac{Z_{\mathrm{L}}}{Z_{\mathrm{S}}} - 1) U_{\mathrm{S}} = (\frac{Z_{\mathrm{L}}}{Z_{\mathrm{S}}} + 1) U_{\mathrm{ref}} \tag{3.18}$$

and the reflection coefficient is given by:

$$\Gamma = \frac{U_{\mathrm{ref}}}{U_{\mathrm{S}}} = \frac{Z_{\mathrm{L}} - Z_{\mathrm{S}}}{Z_{\mathrm{L}} + Z_{\mathrm{S}}}. \tag{3.19}$$

Often, the so-called standing wave ratio (SWR) is calculated to describe the impedance mismatch between a technical device as an antenna and a $50\,\Omega$ read-out system. For the SWR, the following equation holds:

$$SWR = \frac{1 + |\Gamma|}{1 - |\Gamma|} \tag{3.20}$$

where Γ is the reflection coefficient determined according to Eq. (3.19) with $Z_{\mathrm{L}} = 50\,\Omega$. Small values of SWR indicate a good matching and thus, small signal losses due to impedance mismatch. The frequency where SWR is minimal is called the antenna resonance frequency.

3.4 The Vector Effective Length

A further description of the frequency and directional-dependent antenna sensitivity is given by the vector effective length (VEL) $\vec{H}$. In contrast to the absolute antenna gain, the VEL relates the response voltage instead of the response power at the antenna output and the incoming electric field. In Fourier space, the following equation holds:

$$\mathcal{U}(\Phi, \Theta, f) = \vec{H}(\Phi, \Theta, f) \cdot \vec{\mathcal{E}}(f), \tag{3.21}$$

where $\mathcal{U}$ and $\vec{\mathcal{E}}$ are the Fourier transform of the voltage trace U and the electric-field trace E respectively. The VEL $\vec{H}$ is a vector which is oriented in the plane perpendicular to the arrival direction of the signal. As illustrated on the left side of Fig. 3.2, the VEL can be expressed as a superposition

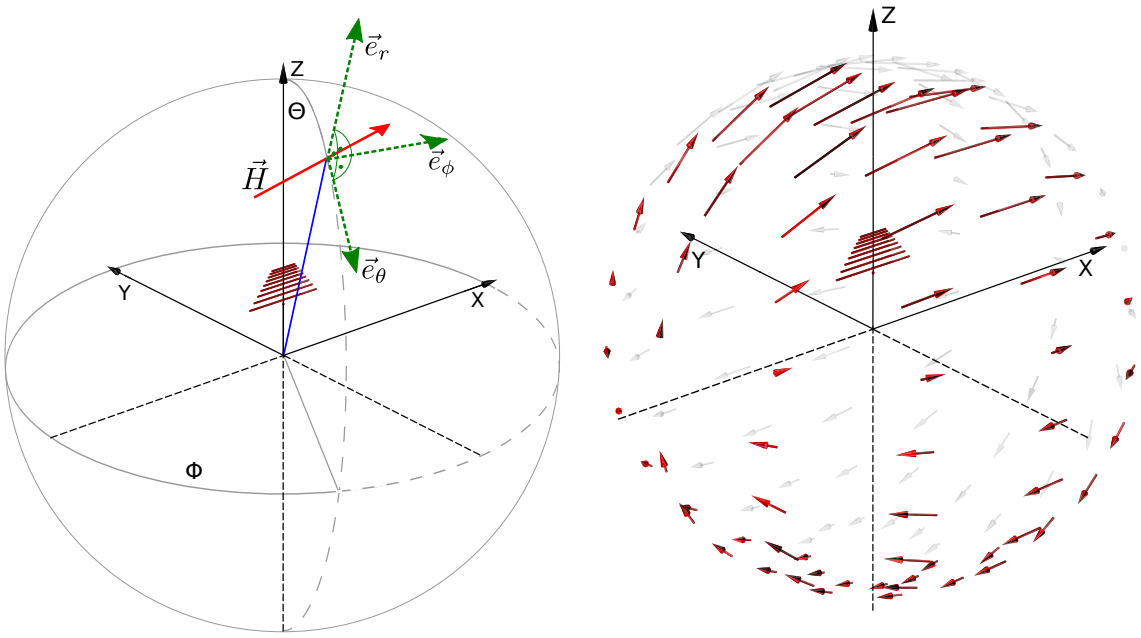

Figure 3.2: ***(left)*** *Illustration of the vector effective length $\vec{H}$ for an arrival direction with an azimuth angle Φ and a zenith angle Θ in a coordinate system where the antenna is centered. The vector effective length is split in two components aligned along the unit vectors $\vec{e}_\phi$ and $\vec{e}_\theta$.* ***(right)*** *The vector effective length of a logarithmic periodic dipole antenna for multiple arrival directions. The vector length indicates the antenna sensitivity and the vector direction illustrates the sensitive signal polarization of the given antenna. Pictures taken from [152].*

of a horizontal component H_ϕ and a component H_θ oriented perpendicular to H_ϕ which is called meridional component:

$$\vec{H} = H_\phi \vec{e}_\phi + H_\theta \vec{e}_\theta. \tag{3.22}$$

The VEL is a complex quantity $H_\mathrm{k} = |H_\mathrm{k}| e^{i\alpha_\mathrm{k}}$ with $\mathrm{k} = \phi,\ \theta$ and accounts for the frequency-dependent electrical losses within the antenna as well as reflection effects which arise in the case of differences between the antenna and read-out system impedances. Both effects lead to dispersion of the signal shape. On the right side of Fig. 3.2, the VEL of a horizontally aligned logarithmic periodic dipole antenna (LPDA) for multiple arrival directions are shown. The vector length indicates the antenna sensitivity and the vector direction illustrates the most sensitive signal polarization of the antenna for the respective arrival direction. Such a horizontally aligned LPDA is most sensitive to the zenith direction and horizontally polarized signals.
With the combination of Eq. (3.12), Eq. (3.21), Eq. (3.22), and the quadratic relation between voltage and power, the absolute antenna gain and the absolute value of the VEL are related by:

$$|H_\mathrm{k}(\Phi, \Theta, f)|^2 = \frac{c^2 Z_\mathrm{R}}{4\pi f^2 Z_0} G_{\mathrm{abs,k}}(\Phi, \Theta, f). \tag{3.23}$$

Here, f is the signal frequency, c is the vacuum speed of light, $Z_\mathrm{R} = 50\,\Omega$ is the read-out impedance, $Z_0 \approx 120\,\pi\,\Omega$ is the impedance of free space, the index $\mathrm{k} = \phi,\ \theta$ indicates the polarization, and Φ and Θ denote the azimuth and zenith angle of the arrival direction.

3.5 Calculating the Absolute Value of the Vector Effective Length from Transmission Measurements

The frequency and directional-dependent antenna sensitivity of an uncalibrated antenna under test (AUT) is determined by measuring the antenna response of the AUT in a transmission setup using a calibrated transmission antenna. The radiated power density $\vec{S}_\mathrm{k}$ of a transmitting antenna in a distance R is then given by:

$$|\vec{S}_\mathrm{k}| = \frac{G_\mathrm{abs,t} P_\mathrm{t}}{4\pi R^2} \tag{3.24}$$

with the transmitted power P_t induced on the transmission antenna and the known absolute antenna gain $G_\mathrm{abs,t}$ of the calibrated transmission antenna. The polarization k depends on the alignment of the transmitting antenna. By plugging Eq. (3.12) in Eq. (3.24), the so-called Friis equation [153] is obtained. With the Friis equation, the ratio of the transmitted power to the response power at the AUT for the respective incoming direction (Φ, Θ) is described and accounts for the free-space path loss in vacuum:

$$\frac{P_\mathrm{r}(\Phi,\Theta,f)}{P_\mathrm{t}(f)} = G_\mathrm{abs,t}(f) G_\mathrm{abs,r}(\Phi,\Theta,f) \left(\frac{c}{4\pi f R}\right)^2, \tag{3.25}$$

with the response power P_r at the AUT, the unknown absolute antenna gain $G_\mathrm{abs,r}$ of the AUT, the distance R between both antennas and the signal frequency f.
By combining Eq. (3.23) and Eq. (3.25), the VEL of the AUT in a transmission setup is then determined by:

$$|H_\mathrm{k}(\Phi,\Theta,f)| = \sqrt{\frac{4\pi Z_\mathrm{R}}{Z_0}} R \sqrt{\frac{P_\mathrm{r,k}(\Phi,\Theta,f)}{P_\mathrm{t}(f) G_\mathrm{abs,t}(f)}}. \tag{3.26}$$

3.6 Calculating the Absolute Value of the Vector Effective Length from Simulations

In this work, the NEC-2 simulation code [37] is used to simulate the response pattern of the passive part of the AUT. With the passive part of the AUT, the antenna without a then following read-out system is meant. These simulations provide information about the response voltage directly at the antenna footpoint (AF) which is the location where the signal is converted from the antenna to the then following $50\,\Omega$ system of the read-out system. Usually, further electronic devices are connected to the AF, e.g., transmission lines (TL) or amplifiers (AMP) which are denoted as active part of the AUT in the following. Then, the voltage at the output of the last additional electronic component is the parameter of interest. In the simulation, the signal transformation within the additional devices as well as impedance mismatch effects have to be considered separately.
In the following subsections, the NEC-2 simulation code is briefly introduced and the transfer functions ρ_i of different active antenna parts are described in detail and finally combined to an overall transfer function ρ. The function ρ transfers the simulated voltage at the output of the passive part of an AUT to the voltage at the output of an amplifier connected to the antenna footpoint via transmission line. Due to the linear correlation between voltage and VEL given in Eq. (3.21), the absolute value of the VEL $|\vec{H}_\rho|$ at the respective position, where the VEL $|\vec{H}_\mathrm{nec}|$ at the antenna footpoint is obtained

from NEC-2 simulations and combined with the transfer function ρ, is determined by:

$$|\vec{H}_\rho| = \rho|\vec{H}_{\mathrm{nec}}|. \tag{3.27}$$

3.6.1 Numerical Electromagnetics Code - NEC

The numerical electromagnetics code (NEC) [37] is a software for the numerical simulation of antennas with wire structures. Surfaces can be realized by a grid of many wires. The code was developed by the Lawrence Livermore Laboratory in the 1970s and further developed in different versions: NEC-2, NEC-3 and NEC-4. The NEC-2 code is an open-source software and available as a Debian package in Linux called NEC2++ [154]. Thus, this version is used for the simulations presented in this thesis.
In NEC-2, an electric-field integral equation [155, 156] is used to model the electric field in a distance $\vec{r}$ to the antenna and solved numerically by the so-called method of moments [157] which is based on segmentation of the antenna. The antenna response is then calculated for each antenna segment and finally superposed.
In the NEC input file, the antenna parameters as wire lengths, wire radii, wire material, and the frequency range are defined. Then, the applied voltage, current, and the impedance of each segment as well as the electric field strength of both polarizations and of each direction is calculated and stored in the NEC output file. Beside the simulation of the antenna response pattern, NEC-2 enables investigating environmental effects on the antenna response pattern, e.g., by adding a ground plane with a given ground permittivity and ground conductivity which impacts the antenna response.
The 4nec2 simulation tool is a NEC-based antenna modeler and optimizer [158]. It delivers a graphical user interface for the NEC-2 software and allows a 3D representation of the antenna and the simulation results. In Fig. 3.3, the antenna gain of a simple dipole in free space with a length of $l = 2.5\,\mathrm{m}$ is shown using the 4nec2 tool. On the upper left side, the horizontal gain and on the upper right side, the meridional gain is color coded (cf. Eq. (3.9)). The total gain is shown in the lower panel. The pinker the color, the larger is the gain and thus, the larger is the antenna sensitivity to the respective direction. The given dipole is mostly sensitive in the directions perpendicular to the antenna alignment.

3.6.2 The Vector Effective Length Extracted from NEC-2 Simulations

The NEC-2 simulation software enables calculating the antenna VEL of an AUT in two different ways: from the original simulation and from a transmission setup.
In the original simulation, only the AUT is considered. The electric field $\vec{E}$ in a distance R emitted by the antenna is determined according to [145] by:

$$\vec{E} = -i\frac{Z_0 f}{2cR} I \vec{H} e^{-i\frac{2\pi f R}{c}} \tag{3.28}$$

with the impedance of free space $Z_0 \approx 120\pi\,\Omega$, the frequency f, the speed of light c, the simulated current at the AF I and the VEL $\vec{H}$. Hence, for the VEL $\vec{H}$ follows:

$$\vec{H} = -i\frac{2cRI}{Z_0 f} \vec{E} e^{i\frac{2\pi f R}{c}}. \tag{3.29}$$

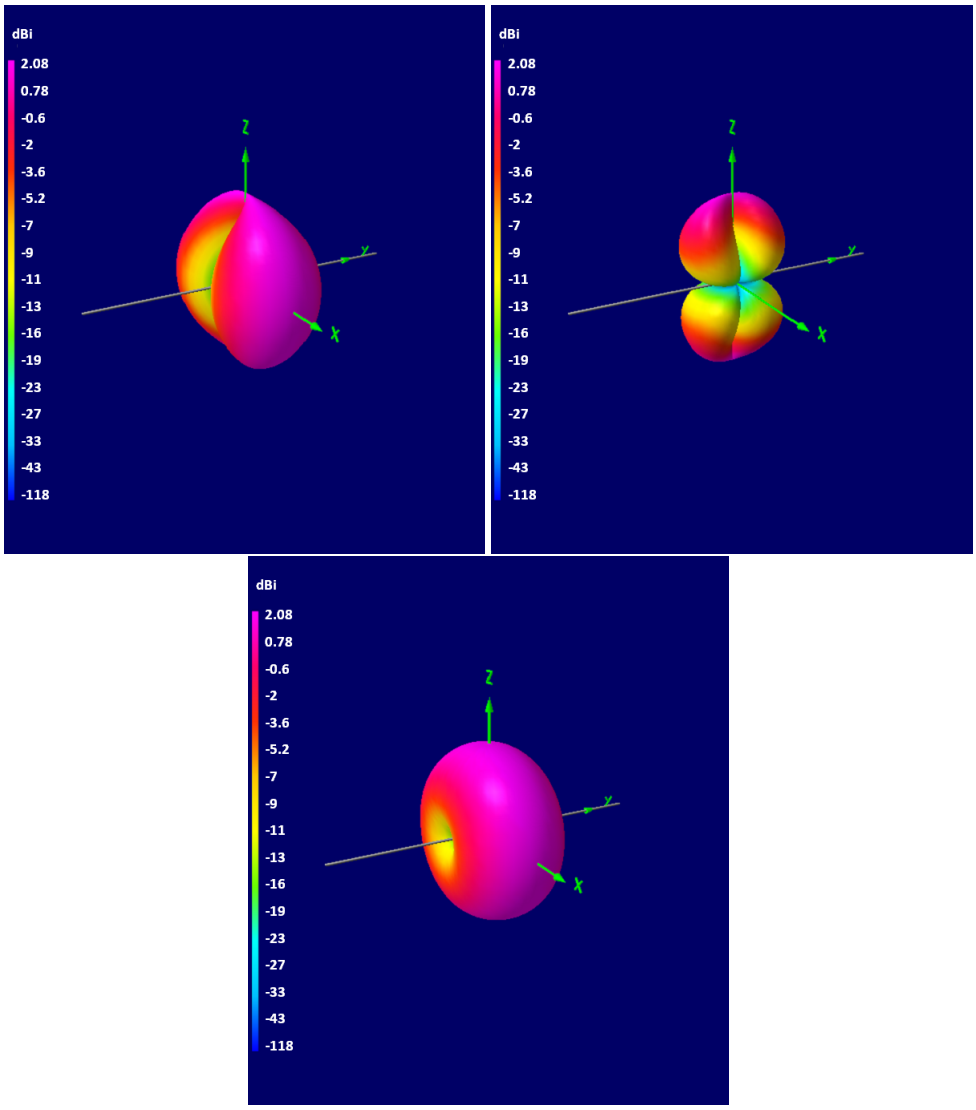

Figure 3.3: *Simulated antenna gain of an one-wire dipole antenna in free space with a wire length of* $2.5\,\mathrm{m}$ *using the 4nec2 simulation tool. In the* ***(upper left)*** *panel, the horizontal antenna gain* G_ϕ*, in the* ***(upper right)*** *panel the meridional antenna gain* G_θ *and in the* ***(lower)*** *panel the total gain* $G = G_\phi + G_\theta$ *are shown. The respective gain is indicated by the color code and is given in logarithmic units. The pinker the color, the larger is the gain and thus, the larger is the antenna sensitivity to the respective direction.*

The electric field $\vec{E}_{\mathrm{nec}}$ calculated within the NEC simulation is normalized to a distance of $R_0 = 1\,\mathrm{m}$ [37]:

$$\vec{E}_{\mathrm{nec}} = Re^{i\frac{2\pi f R}{c}}\vec{E}. \tag{3.30}$$

By plugging Eq. (3.30) into Eq. (3.29), the VEL from the original NEC simulations is obtained by:

$$\vec{H}_{\mathrm{nec}} = i\frac{2c}{Z_0 I f}\vec{E}_{\mathrm{nec}}. \tag{3.31}$$

In this work, an LPDA is calibrated in a transmission measurement using an additional transmission antenna. Further influences due to the presence of the transmitting antenna and its antenna charac-

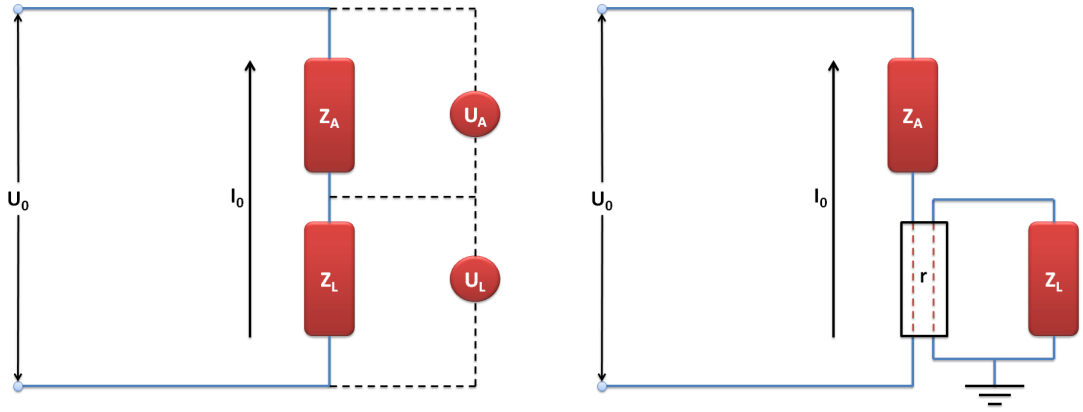

Figure 3.4: ***(left)*** *Thévenin-circuit diagram of a receiving antenna with an antenna impedance Z_A connected to a read-out system with impedance Z_L.* ***(left)*** *Thévenin-circuit diagram when the antenna is read-out by a transformer with a transfer parameter r. Picture adapted from [159].*

teristic have to be taken into account and thus, the transmission antenna has to be included in the simulation. In NEC-2, the signal transmission from the transmitted antenna to the AF of the AUT is calculated. Hence, the absolute value of the VEL from NEC-2 simulations is determined equally to the measurement according to Eq. (3.26):

$$|H_{k,\mathrm{nec}}(\Phi,\Theta,f)| = \sqrt{\frac{4\pi Z_R}{Z_0}} R \sqrt{\frac{P_{r,k}(\Phi,\Theta,f)}{P_t(f) G_{abs,t}(f)}}. \tag{3.32}$$

In both cases, a following read-out system connected to the AF and possible mismatch effects are not taken into account and have to be considered separately. The respective VEL transfer functions are explained in the following subsections.

3.6.3 Antenna Read Out

In the NEC-2 simulations, the AUT is used as receiving antenna and the received signal is read-out at a load connected to the AF. The voltage U_L applied at the load Z_L is calculable by Thévenin's theorem. Typical loads are transmission lines and amplifiers which are explained in later subsections. The antenna impedance Z_A and the load impedance Z_L are connected in series to a voltage source U_0. A sketch of the equivalent Thévenin's circuit is shown on the left side of Fig. 3.4. As antenna and load are connected in series, both impedances are combined to the overall system impedance Z:

$$Z = Z_\mathrm{A} + Z_\mathrm{L} \tag{3.33}$$

and the current stays constant at each position in the circuit:

$$I_0 = I_\mathrm{A} = I_\mathrm{L}. \tag{3.34}$$

From Eq. (3.33) and Eq. (3.34), the voltage applied at the load U_L is determined by:

$$\begin{aligned} U_\mathrm{L} &= Z_\mathrm{L} I_\mathrm{L} \\ &= Z_\mathrm{L} I_0 \\ &= \frac{Z_\mathrm{L}}{Z_\mathrm{A} + Z_\mathrm{L}} U_0. \end{aligned} \tag{3.35}$$

The transfer function ρ_{CM} describes the signal fraction transferred from the received signal at the antenna to a load connected at the AF and is determined by the ratio of the voltage applied at the load U_L and applied at the source U_0:

$$\rho_{CM} = \frac{U_\mathrm{L}}{U_0} = \frac{Z_\mathrm{L}}{Z_\mathrm{A} + Z_\mathrm{L}}. \tag{3.36}$$

The optimal signal transfer from the antenna to the load is given for the case of the so-called conjugate matching [145]. In this case, the load impedance and the antenna impedance are the complex conjugated of each other: $Z_\mathrm{L} = Z_\mathrm{A}^*$. Often, an impedance transformer is used to optimize the signal transfer. The transformer is connected at the AF and thus, the antenna impedance is modified by the transformer parameter r which describes the ratio of the impedance matching. The respective Thévenin circuit diagram is shown on the right side of Fig. 3.4. In the case of an additional transformer, the factor $\frac{1}{\sqrt{r}}$ has to be multiplied to Eq. (3.36) and the antenna impedance has to be divided by r [160]. Then, for the transfer function, the following equation holds:

$$\rho_{CM} = \frac{1}{\sqrt{r}} \frac{Z_\mathrm{L}}{\frac{Z_\mathrm{A}}{r} + Z_\mathrm{L}}. \tag{3.37}$$

3.6.4 Transmission Lines

In this subsection, the influence of a TL with length l_TL connected to the AF on the response voltage is discussed. Typically, TLs have an impedance of $Z_\mathrm{TL} = 50\,\Omega$. One the one hand, a TL attenuates the signal strength of the incoming signal by the attenuation parameter γ. On the other hand, the signal is delayed depending on l_TL, the frequency f, and the transfer rate c_n inside the TL which impacts the signal phase of the complex voltage. For the respective transfer function ρ_TL, the following equation holds:

$$\rho_\mathrm{TL} = e^{-(\gamma + i\frac{2\pi f}{c_\mathrm{n}})l_\mathrm{TL}}. \tag{3.38}$$

3.6.5 Signal Amplification by Amplifiers

In this subsection, the signal amplification within the amplifier itself of a voltage transferred into the amplifier is explained. Amplifiers are characterized by its four S-parameters [161] which are typically given in the case of a $Z = 50\,\Omega$ system:

S11: reflection coefficient at the input port
S21: signal amplification from the input to the output
S12: signal transfer from the output to the input
S22: reflection coefficient at the output port

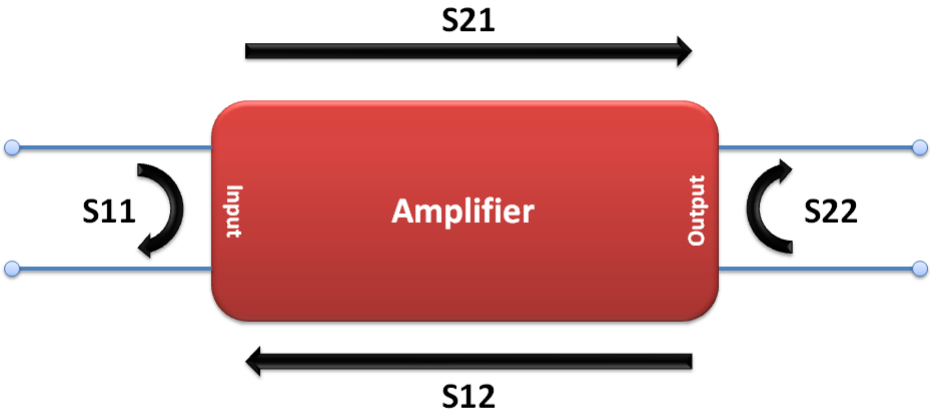

Figure 3.5: *Illustration of the S-parameters of an amplifier. Picture adapted from [151].*

The principle of the amplifier S-parameters is illustrated in the sketch shown in Fig. 3.5. In the case of a receiving antenna, the signal source delivers a voltage U_{S} and is applied to the amplifier input. The S11 parameter describes the relation of the reflected voltage U_{ref} to the source voltage U_{S}:

$$S11 = \frac{U_{\mathrm{ref}}}{U_{\mathrm{S}}}. \tag{3.39}$$

According to Eq. (3.19), the S11 reflection coefficient is related to the amplifier impedance Z_{AMP} and the read-out impedance Z:

$$S11 = \frac{Z_{\mathrm{AMP}} - Z}{Z_{\mathrm{AMP}} + Z}. \tag{3.40}$$

Hence, Z_{AMP} is then determined by:

$$Z_{\mathrm{AMP}} = \frac{1 + S11}{1 - S11} Z \tag{3.41}$$

According to Eq. (3.41), the amplifier impedance differs from the $Z = 50\,\Omega$ system and only a fraction of the source voltage is transferred into the amplifier. The amplifier S21 parameter relates the amplified voltage U_{AMP} at the amplifier output in a $Z = 50\,\Omega$ system to the source voltage U_{S}:

$$S21 = \frac{U_{\mathrm{AMP}}}{U_{\mathrm{S}}}. \tag{3.42}$$

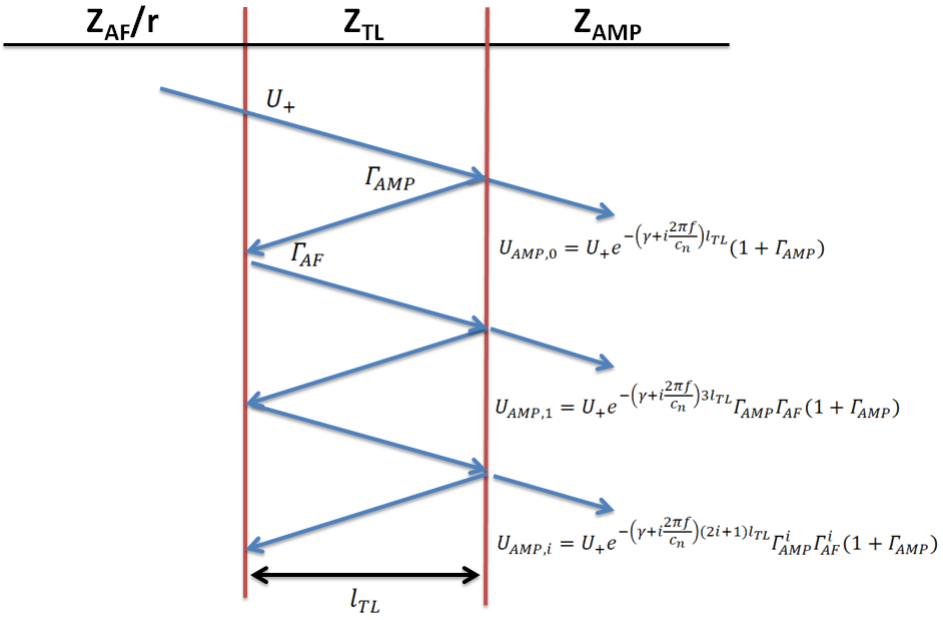

Figure 3.6: *Multiple signal reflections due to impedance mismatches between the antenna footpoint (AF) with an impedance transformer (r) and the amplifier (AMP) connected via a transmission line (TL) with length* l_{TL} *described by the reflection coefficients* Γ_{AMP} *and* Γ_{AF}*. The overall voltage transferred from the AF into the AMP is a superposition of several voltage fractions. Picture adapted from [159].*

The voltage U_{L} transferred into the amplifier is a superposition of the source voltage U_{S} and the reflected voltage U_{ref} at the input of the amplifier:

$$U_{\mathrm{L}} = U_{\mathrm{S}} + U_{\mathrm{ref}}. \tag{3.43}$$

The transfer function describing the relation of the output voltage U_{AMP} to the voltage transferred into the amplifier U_{L} is then determined by combining Eq. (3.39), Eq. (3.42), and Eq. (3.43):

$$\rho_{\mathrm{AMP}} = \frac{U_{\mathrm{AMP}}}{U_{\mathrm{L}}} = \frac{S21}{1 + S11}. \tag{3.44}$$

3.6.6 Combined Transfer Function and Signal Reflections

In this subsection, the transfer function ρ is discussed when connecting an amplifier with impedance Z_{AMP} to the antenna footpoint with impedance Z_{AF}/r via transmission line with impedance Z_{TL}. Besides the influence of each single electronic component on the signal which has been discussed in the previous subsections, also multiple reflections due to impedance mismatch between the components have to be taken into account. The signal transfer between the electronic components is sketched in Fig. 3.6.

In the case of a receiving antenna, a voltage U_0 is induced at the AF. The voltage U_+ transferred into the then following TL due to impedance mismatch between AF and TL is determined according to

Eq. (3.37) by:

$$U_+ = \frac{1}{\sqrt{r}} \frac{U_{\mathrm{TL}}}{U_{\mathrm{TL}} + \frac{U_{\mathrm{AF}}}{r}} U_0. \tag{3.45}$$

In the TL, the signal is attenuated as well as delayed and according to Eq. (3.38) for the voltage U_{TL} at the TL output follows:

$$U_{\mathrm{TL}} = e^{-(\gamma + i\frac{2\pi f}{c_{\mathrm{n}}})l_{\mathrm{TL}}} U_+ \tag{3.46}$$

with the attenuation parameter γ, the frequency f, transfer rate c_{n} and the cable length l_{TL}. Due to impedance mismatch between TL and AMP, only a fraction of the voltage is transferred into the AMP while the other part is reflected back propagating through the TL towards the AUT. Also here a fraction of the voltage is reflected and transferred back through the TL to the AMP. The reflection coefficient $\Gamma_{\mathrm{AMP}} = \frac{Z_{\mathrm{AMP}} - Z_{\mathrm{TL}}}{Z_{\mathrm{AMP}} + Z_{\mathrm{TL}}}$ describing the signal reflection at the AMP and the reflection coefficient $\Gamma_{\mathrm{AF}} = \frac{Z_{\mathrm{AF}}/r - Z_{\mathrm{TL}}}{Z_{\mathrm{AF}}/r + Z_{\mathrm{TL}}}$ describing the signal reflection at the TL are determined according to Eq. (3.19). At the AMP, further reflections take place. Thus, the overall voltage transferred into the AMP is a superposition of several voltage fractions $U_{\mathrm{AMP,m}}$:

$$\begin{aligned} U_{\mathrm{AMP}} &= \sum_{m \in \mathbb{N}_0} U_{\mathrm{AMP,m}} \\ &= \sum_{m \in \mathbb{N}_0} e^{-2m(\gamma + i\frac{2\pi f}{c_{\mathrm{n}}})l_{\mathrm{TL}}} \Gamma_{AMP}^m \Gamma_{\mathrm{TL}}^m (1 + \Gamma_{\mathrm{AMP}}) U_{\mathrm{TL}} \\ &= (1 + \Gamma_{\mathrm{AMP}}) \frac{e^{2(\gamma + i\frac{2\pi f}{c_{\mathrm{n}}})l_{\mathrm{TL}}}}{e^{2(\gamma + i\frac{2\pi f}{c_n})l_{\mathrm{TL}}} - \Gamma_{\mathrm{AMP}}\Gamma_{\mathrm{AF}}} U_{\mathrm{TL}}. \end{aligned} \tag{3.47}$$

Finally, the signal is amplified in the AMP and the voltage U_{L} at the AMP output is determined according to Eq. (3.44):

$$U_{\mathrm{L}} = \frac{S21}{1 + S11} U_{\mathrm{AMP}} \tag{3.48}$$

By plugging Eq (3.45) in Eq (3.48), the combined transfer function $\rho = \frac{U_{\mathrm{L}}}{U_0}$ is determined to be:

$$\rho = \frac{1}{\sqrt{r}} \frac{Z_{TL}}{Z_{TL} + Z_{AF}/r} (1 + \Gamma_{AMP}) \frac{e^{(\gamma + i\frac{2\pi f}{c_n})l_{TL}}}{e^{2(\gamma + i\frac{2\pi f}{c_n})l_{TL}} - \Gamma_{AMP}\Gamma_{AF}} \frac{S21}{1 + S11} \tag{3.49}$$

which is a general description of the signal transferred from the antenna footpoint to an amplifier output through a transmission line. By choosing a cable length of $l_{TL} = 0$, a transformer parameter $r = 1$, or the reflection coefficients $\Gamma_i = 0$ with $i = (\mathrm{AMP, or\ TL})$, the impact of single components on the transferred voltage can be switched off.

3.7 Influence of Ground on the Antenna Response Pattern

The ground acts as a conductive element and thus directly impacts the antenna response pattern. Electromagnetic waves are reflected on the ground surface. Such secondary signals then interfere with the primary signal and therefore impact the total measured signal at the antenna. The mechanism is illustrated in Fig. 3.7. The strength of the signal reflection on ground is described by the Fresnel reflection

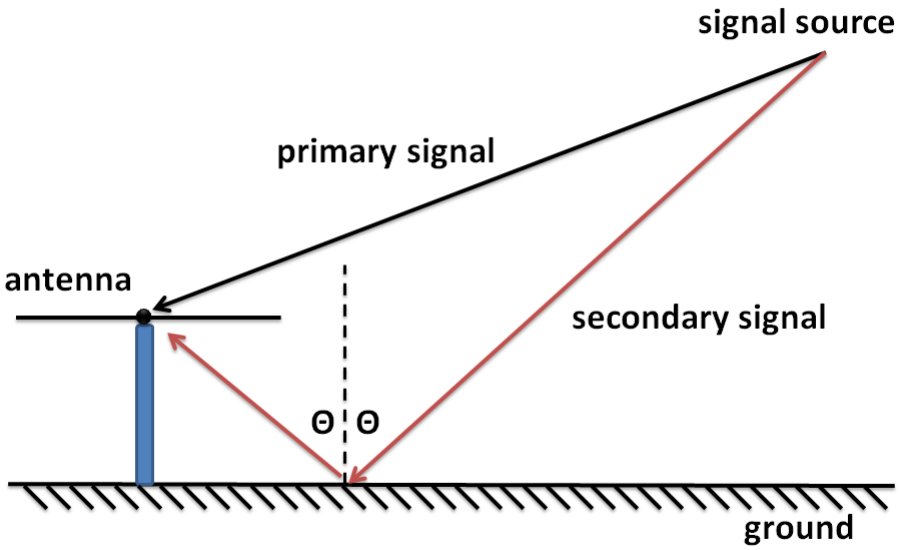

Figure 3.7: The electromagnetic signal of a signal source measured at the antenna is a superposition of a primary signal and a secondary signal due to signal reflections on ground.

coefficient and depends on the ground conditions described by ground permittivity and ground conductivity. In this section, the influence of different ground conditions on the antenna response pattern is discussed and the corresponding theoretical overview is given. In the first subsection, the complex permittivity is introduced which combines the information about ground permittivity and ground conductivity. Then, the signal reflection on ground based on the Fresnel equations is deduced and the reflection coefficients with respect to different ground conditions are determined. In the last subsection, the NEC-2 simulation code is used to investigate the influence of different ground conditions on the antenna VEL which is exemplary presented for the case of a simple dipole antenna.

3.7.1 The Complex Permittivity

The relative permittivity of a specific material indicates the transmittance for electromagnetic waves through this material. If an electric field is applied to a dielectric, the dipoles within the dielectrics align according to the electric field. In contrast to the response of vacuum, the material response - and thus the relative permittivity - depends on the frequency of the applied electric field. As the polarization of the material does not response directly to the applied field, the material response flag in phase. This effect is called polarizability of the material. The complex permittivity $\epsilon_{c,r}$ is a frequency-dependent quantity describing both the transmittance for electromagnetic waves through the material as well as its polarizability:

$$\epsilon_{c,r} = \epsilon_r^{'} + i\epsilon_r^{''}. \tag{3.50}$$

To deduce the complex permittivity of a conductive material, an electric-field ansatz of

$$\vec{E}(\vec{r},t) = \vec{E}_0 e^{(-i2\pi ft + \vec{k}\cdot\vec{r})} \tag{3.51}$$

with amplitude $\vec{E}_0$, the signal frequency f, the time t, the wave vector $\vec{k}$, and the position vector $\vec{r}$ is chosen. The Maxwell equation describing the Ampère's circuital law is given by:

$$\frac{1}{\mu} rot\vec{B} = \epsilon_0 \epsilon_r \frac{d\vec{E}}{dt} + \vec{j} \tag{3.52}$$

where $\vec{B}$ is the magnetic field, μ is the magnetic permeability, ϵ_0 is the vacuum permittivity, and ϵ_r is the relative permittivity. There are no free charges in a conductive material. Thus, the charge density of a conductive material is given by

$$\rho(\vec{r},t) = 0. \tag{3.53}$$

In a conductive material with conductivity σ, the current density $\vec{j}(\vec{r},t)$ induced by an electric field $\vec{E}(\vec{r},t)$ is calculated by:

$$\vec{j}(\vec{r},t) = \sigma \vec{E}(\vec{r},t). \tag{3.54}$$

Plugging Eq. (3.51) and Eq. (3.54) into Eq. (3.52) yields:

$$\frac{1}{\mu} rot\vec{B} = -i2\pi f \epsilon_0 \left(\epsilon_r - i\frac{\sigma}{2\pi f \epsilon_0}\right) \vec{E}. \tag{3.55}$$

The relative permittivity is extended by an imaginary value depending on the material conductivity and the angular frequency. The combination of the relative permittivity and the imaginary extension of the relative permittivity is called the complex permittivity:

$$\epsilon_{c,r} = \epsilon_r - i\frac{\sigma}{2\pi f \epsilon_0}. \tag{3.56}$$

The complex permittivity combines the information about the ground permittivity and ground conductivity in one parameter. From comparing Eq. (3.50) and Eq. (3.56), it follows:

$$\epsilon_r^{'} = \epsilon_r \wedge \epsilon_r^{''} = -\frac{\sigma}{2\pi f \epsilon_0}. \tag{3.57}$$

3.7.2 Fresnel Equations

The Fresnel equations describe the reflected and transmitted signal amplitudes E_r and E_t of electromagnetic waves relative to the incoming signal amplitude E_i on the interface of two materials ($j = 1, 2$) with different refraction indices N_j. The mechanism is illustrated in Fig. 3.8. The refraction index is coupled to the material permittivity $\epsilon_{c,r}$ and thus is a complex quantity as well:

$$N_j = \sqrt{\mu_{r,j}\epsilon_{c,r,j}} \tag{3.58}$$

where $\mu_{r,j}$ is the magnetic permeability of the material. The complex refraction index is a measure of the wavelength reduction as well as the signal absorption within the material. As the signal reflec-

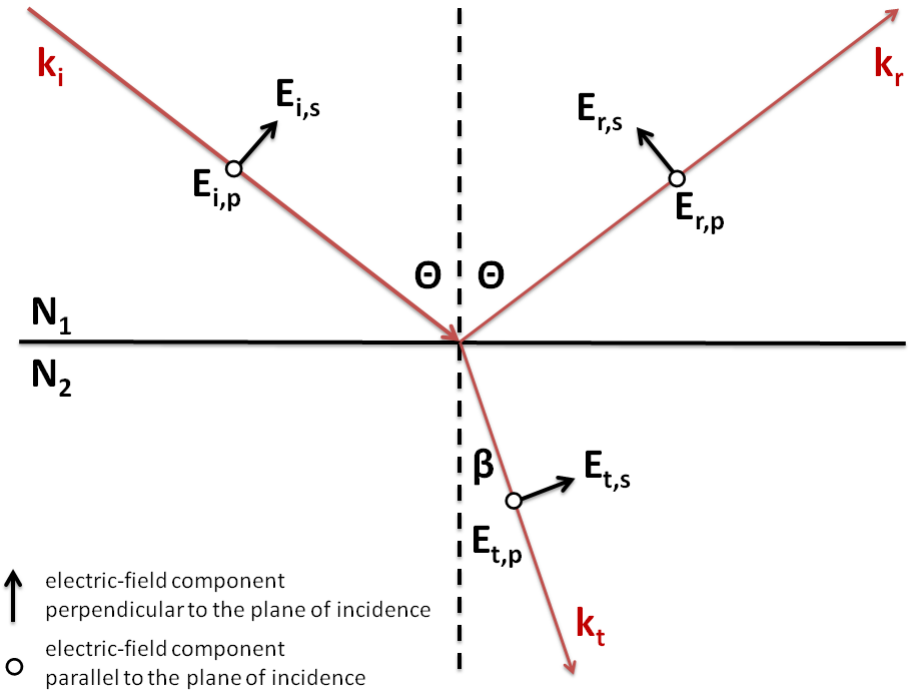

Figure 3.8: Signal reflection and transmission on the interface between two materials with different refraction indices N_j with $j = 1, 2$ of an incoming electromagnetic wave polarized parallel (p) or perpendicular to the plane of incidence (s) at an incoming zenith angle of Θ. Picture adapted from [162].

tion on ground is the parameter of interest, for the following calculations the refraction index of air $N_1 = N_a = 1.000292$ is used as initial material property and for the ground a non-magnetic material is applied describing by $\mu_{r,j=2} \approx 1$.
Considering Snell's law, the reflection coefficient r_p of a signal polarized parallel to the plane of incidence is then calculated by:

$$r_p = \left(\frac{E_r}{E_i}\right)_p = \frac{N_g cos(\Theta) - N_a\sqrt{1 - \frac{N_a^2}{N_g^2}\sin^2(\Theta)}}{N_g cos(\Theta) + N_a\sqrt{1 - \frac{N_a^2}{N_g^2}\sin^2(\Theta)}}. \tag{3.59}$$

Similarly, the reflection coefficient r_s of a signal polarized perpendicular to the plane of incidence is obtained by:

$$r_s = \left(\frac{E_r}{E_i}\right)_s = \frac{N_a cos(\Theta) - N_g\sqrt{1 - \frac{N_a^2}{N_g^2}\sin^2(\Theta)}}{N_a cos(\Theta) + N_g\sqrt{1 - \frac{N_a^2}{N_g^2}\sin^2(\Theta)}} \tag{3.60}$$

where N_g is the complex refraction index of the ground material and Θ denotes the zenith angle of the incoming signal. In the panels of Fig. 3.9, the absolute value of the reflection coefficients r_p and r_s of an incoming signal with a zenith angle of $\Theta = 45°$ at a frequency of $f = 55\text{MHz}$ as a function of the ground conductivity ranging from $0.1\,\text{mS/m}$ to $100\,\text{mS/m}$ and ground permittivity ranging from 1 to 81 (water) are shown. Both reflection coefficients exhibit a dependency on ground

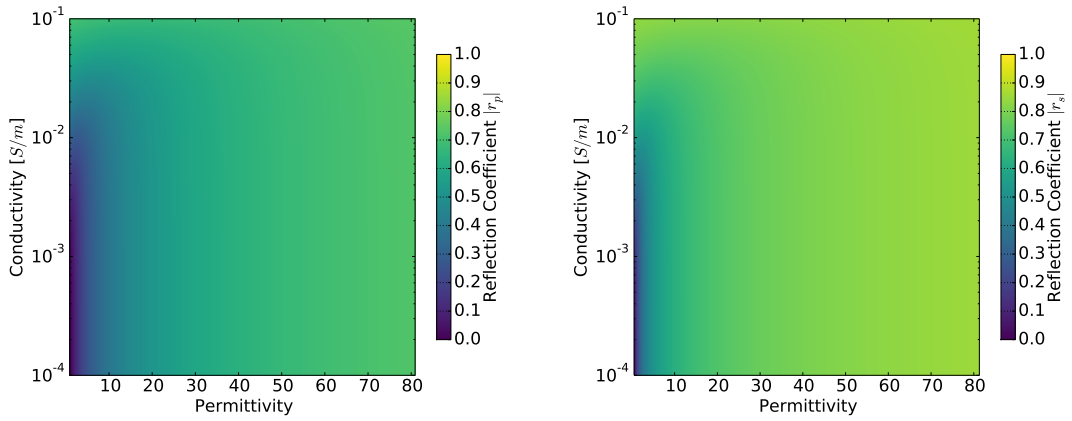

Figure 3.9: Absolute value of the ground reflection coefficients $|r_p|$ **(left)** and $|r_s|$ **(right)** of an electromagnetic signal as a function of the ground conductivity and ground permittivity at a zenith angle of $\Theta = 45^\circ$ and at a frequency of $f = 55\,\mathrm{MHz}$.

conditions especially on the ground permittivity. Whereas the signal reflection is about $10\,\%$ at small permittivites it rapidly increase to more than $80\,\%$. In contrast, the signal reflection on ground is less sensitive on different ground conductivities especially for values smaller than $10\,\mathrm{mS/m}$ which is typically the case for several ground consistencies [158, 163, 164].

3.7.3 Ground Influence on the Antenna Vector Effective Length

In this subsection, the influence of different ground conditions on the antenna VEL in the exemplary case of a dipole antenna is discussed. The NEC-2 simulation code is used to simulate the antenna VEL for different ground conditions. On the left side of Fig. 3.10, a visualization of a horizontally polarized dipole antenna with a dipole length of $l = 2.5\,\mathrm{m}$ used in the NEC-2 program without ground and on the right side the dipole antenna placed $1\,\mathrm{m}$ above ground with a ground conductivity set to be $1.4\,\mathrm{mS/m}$ and a ground permittivity set to be 5.5 is shown. Color coded is the total dipole antenna gain at $55\,\mathrm{MHz}$. The pinker the color, the larger is the antenna sensitivity to the respective direction. The antenna sensitivity decreases with the zenith angle if ground is introduced.

To investigate the influence of different ground conditions on the dipole antenna VEL multiple NEC-2 simulations with ground conductivities ranging from $0.1\,\mathrm{mS/m}$ to $5\,\mathrm{mS/m}$ and ground permittivities ranging from 2.5 to 81 have been performed which are typical values of different ground conditions from dry sand to water. The antenna VEL is calculated according to Eq. (3.31) and then modified with Eq. (3.49) considering the transfer function to a $50\,\Omega$ read-out system without impedance transformer, additional transmission line, or amplifier. To switch off their influences in Eq. (3.49), the transfer parameter r is set to one, the transmission line length l_{tl} is set to zero, and the amplifier parameters are disabled. In Fig. 3.11, the horizontal component of the dipole antenna VEL $|H_\phi|$ at a frequency of $55\,\mathrm{MHz}$ is shown exemplary. The antenna VEL shape changes if ground is introduced: The antenna sensitivity decreases for large zenith angles towards the horizon but increases at small zenith angles. Different ground conductivity marginally influences the dipole antenna VEL whereas the simulations of different ground permittivities exhibit a significant influence on the antenna response pattern especially at small zenith angles. Thus, the simulations confirm that for an accurate description of the

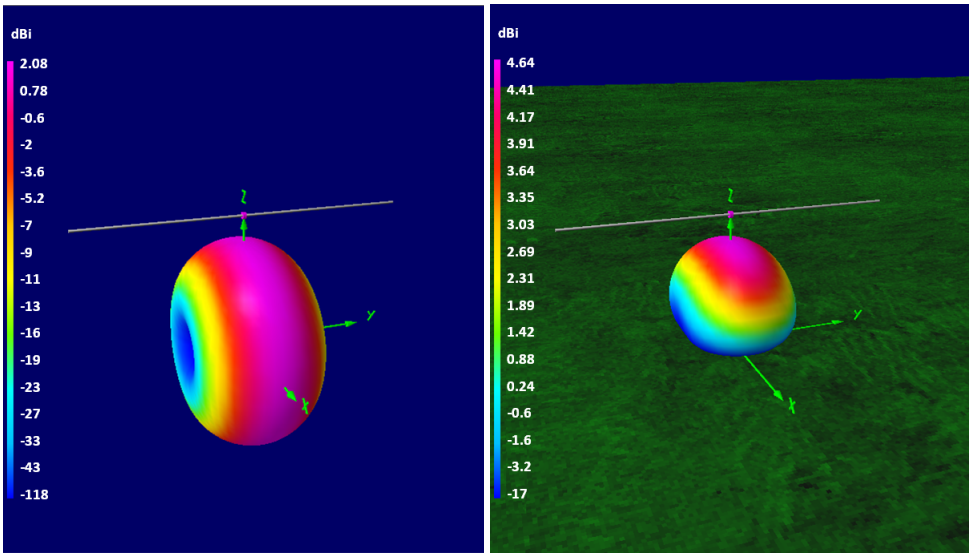

Figure 3.10: NEC-2 realization of a horizontally aligned dipole antenna with a dipole length of $l = 2.5\,\mathrm{m}$ without ground **(left)** and placed $1\,\mathrm{m}$ above ground **(right)**. Color coded is the total antenna gain in logarithmic units. The pinker the color, the larger is the antenna sensitivity to the respective direction. The pink dot in the middle of the dipole marks the antenna footpoint.

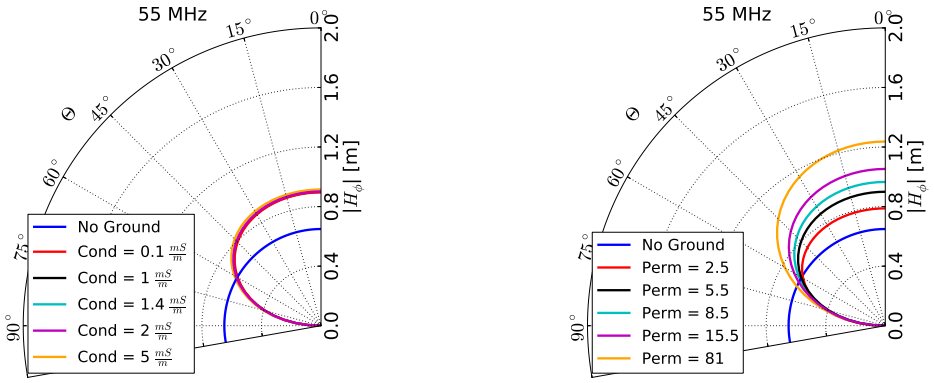

Figure 3.11: Horizontal component of the dipole antenna vector effective length $|H_\phi|$ for different ground conditions obtained from NEC-2 simulations. **(left)** Multiple simulations of different ground conductivities with a constant ground permittivity of 5.5. **(right)** Multiple simulations of different ground permittivities with a constant ground conductivity of $1.4\,\mathrm{mS/m}$.

antenna response pattern especially the ground permittivity has to be known.

3.8 Electric-Field Reconstruction using Calibrated Antennas

An electric field generated by an air shower induces a voltage in antennas. For an accurate reconstruction of the incoming electric field, a thorough knowledge of the frequency and directional-dependent antenna sensitivity described by the horizontal and meridional component of the antenna VEL H_ϕ and H_θ is necessary. The electric-field is then reconstructed in the following way: Referring to Eq. (3.1),

the electric field can be written in spherical coordinates and is split into two polarizations E_ϕ and E_θ aligned along the unit vectors $\vec{e}_\phi$ and $\vec{e}_\theta$ respectively. According to Eq. (3.21) and Eq. (3.22), for the measurable voltage $\mathcal{U}$ in Fourier space follows:

$$\begin{aligned} \mathcal{U} &= \mathcal{U}_\phi + \mathcal{U}_\theta \\ &= H_\phi \mathcal{E}_\phi + H_\theta \mathcal{E}_\theta. \end{aligned} \tag{3.61}$$

where $\mathcal{U}_i$ and $\mathcal{E}_i$ are the Fourier transform of the voltage trace U_i and the electric-field trace E_i with polarization $i = \phi, \theta$ respectively. Typically, the radio emission of air showers is measured in radio stations consisting of two perpendicularly aligned and horizontally polarized antennas ($j = (1,\ 2)$) which result in a system of two equations for the voltage $\mathcal{U}_j$:

$$\begin{aligned} \mathcal{U}_1 &= H_{\phi,1} \mathcal{E}_\phi + H_{\theta,1} \mathcal{E}_\theta \\ \mathcal{U}_2 &= H_{\phi,2} \mathcal{E}_\phi + H_{\theta,2} \mathcal{E}_\theta. \end{aligned} \tag{3.62}$$

With a known arrival direction described by the zenith angle Θ and the azimuth angle Φ, both VEL components are read out at the respective arrival direction and the electric-field components are then calculable by solving the given system of equations. The arrival direction can be taken from external measurements or by a time analysis of the signal time of at least three radio stations triggered in coincidence. For the reconstructed electric field follows:

$$\begin{aligned} \mathcal{E}_\theta &= \frac{H_{\phi,2}\,\mathcal{U}_1 - H_{\phi,1}\,\mathcal{U}_2}{H_{\phi,2}\,H_{\theta,1} - H_{\phi,1}\,H_{\theta,2}} \\ \mathcal{E}_\phi &= \frac{H_{\theta,2}\,\mathcal{U}_1 - H_{\theta,1}\,\mathcal{U}_2}{H_{\phi,1}\,H_{\theta,2} - H_{\phi,2}\,H_{\theta,1}}. \end{aligned} \tag{3.63}$$

As the electric field is a transversally aligned wave, it can be combined with the information about the arrival direction, and be transformed into Cartesian coordinates.

4

The Pierre Auger Observatory

Parts of this chapter have been published in:

A. Aab et al. (Pierre Auger Collaboration)
"Calibration of the Logarithmic-Periodic Dipole Antenna (LPDA) Radio Stations at the Pierre Auger Observatory using an Octocopter"
J. Instrum. **12** (2017) T10005
The work presented in this publication was primarily performed by the author of this thesis. The text of the publication has been written by the author of this thesis and was revised and copy-edited by the co-authors of the publication.

R. Krause for the Pierre Auger Collaboration
"A new method to determine the energy scale for high-energy cosmic rays using radio measurements at the Pierre Auger Observatory"
Proc. of the 35th ICRC 2017, Busan, South Korea (2017)
PoS (ICRC2017) 528

R. Krause for the Pierre Auger Collaboration
"Detection of Ultrahigh-Energy Cosmic Rays with the Auger Engineering Radio Array"
Proc. of the VCI 2016, Vienna, Austria (2016)
Nucl. Instrum. Meth. A, **845C** (2017) 378-382

R. Krause for the Pierre Auger Collaboration
"AERA – The Auger Engineering Radio Array"
Proc. of the VULCANO Conf. 2014, Vulcano Island, Italy (2014)
Frascati Physics Series Vol. **58** (2014) 315-322

The Pierre Auger Observatory [3] is a physics large-scale experiment to detect high-energy cosmic rays. The observatory is located on a high plateau in the Argentinian Pampa close to the city Malargüe with an average height over sea level of about $1400\,\mathrm{m}$ which corresponds to an atmospheric depth of about $875\,\mathrm{g/cm^2}$ [3]. Hence, the observatory is ideally placed for ground-based observations of secondary particles shortly after the shower maximum in the case of vertical incoming cosmic-rays (cf. Fig. 2.11 in Sec. 2.4.1).
In Fig. 4.1, a map of the Pierre Auger Observatory is shown. At the observatory, two baseline detection techniques are used to measure cosmic-ray induced extensive air showers (EAS). These are a surface detector (SD) [165] and a fluorescence detector (FD) [166]. The SD consists of 1660 water-

Cherenkov detector stations which enable stochastic measurements of particles at ground level with a duty cycle close to $100\,\%$. These detector stations are set up in a hexagonal grid with a spacing of $1500\,\mathrm{m}$ covering an area of more than $3000\,\mathrm{km}^2$. Thus, the Pierre Auger Observatory is currently the largest cosmic-ray experiment world wide. The SD array is overlooked by 27 fluorescence telescopes which are located at four different positions at its edge. The telescopes enable measuring the ultraviolet fluorescence light emitted by air molecules excited by the particle cascade of the EAS and thus provide information about the longitudinal shower development. The FD is restricted to operate in clear and moonless nights resulting in a duty cycle of about $12\,\%$ in early years [167] which has meanwhile been increased to $15\,\%$ [3]. Both detection techniques provide independent measurements of cosmic-ray induced air showers and are used for cross checks and redundant measurements [3, 168, 169].

Both baseline detectors are extended with a low-energy enhancement. The Auger Muons and Infill for the Ground Array (AMIGA) [170, 171] and the High-Elevation Auger Telescopes (HEAT) [172].

AMIGA: In a smaller array of $23.5\,\mathrm{km}^2$ located in the north-west corner of the regular SD array, the grid spacing of 61 detector stations is reduced to $750\,\mathrm{m}$. The smaller grid spacing lowers the minimum energy threshold from about $10^{18.5}\,\mathrm{eV}$ [173] to about $10^{17.5}\,\mathrm{eV}$ [170]. These infill stations are accompanied with buried scintillator modules which enable detecting the muon component of EAS [174].

HEAT: Three out of the 27 fluorescence telescopes are mounted in tiltable containers. These containers can be inclined so that the telescopes cover an elevation of $30\,^\circ$ to $58\,^\circ$ (cf. Sec.4.1) which enables observing EASs higher in the atmosphere compared to the regular telescopes of the FD. This reduces the lower energy threshold to about $10^{17}\,\mathrm{eV}$ [172]. HEAT is located close to the FD telescopes of Coihueco and thus also overlooks AMIGA.

The Auger Engineering Radio Array (AERA) is the radio detector of the Pierre Auger Observatory located in the north-west corner of the SD array within the low-energy enhancements and consists of 153 radio stations which are used to measure the radio signal of EAS. Covering an area of about $17\,\mathrm{km}^2$, AERA is the largest cosmic-ray radio detector world wide. It is sensitive on measuring both the lateral and longitudinal shower development with a duty cycle close to $100\,\%$. Thus, the radio detection technique exhibits great potential for cosmic-ray physics.

This chapter is structured as follows: First, in Sec. 4.1 and Sec. 4.2, the two baseline detectors are described in more detail. Afterwards, in Sec. 4.3 special focus is put on the description of AERA. The layout of AERA as well as the mechanical setup and electrical properties of the used radio stations are given. Furthermore, the triggering systems as well as the data acquisition are described.

4.1 The Fluorescence Detector of the Pierre Auger Observatory

The FD including the low-energy enhancement HEAT [3, 166, 172] comprises 27 fluorescence telescopes overlooking the SD array from four sites at its edge: Coihueco, Loma Amarilla, Los Leones and Los Morados. With the FD, the fluorescence light emitted by air molecules excited by the particle cascade of EAS is measured. The FD requires low background light and thus is restricted to operate in clear and moonless nights.

Each site of the regular FD consists of six telescopes assembled in a climate-controlled building [175]. Each telescope provides a field of view of $30\,^\circ \times 30\,^\circ$ with a minimal elevation of $1.5\,^\circ$ above the hori-

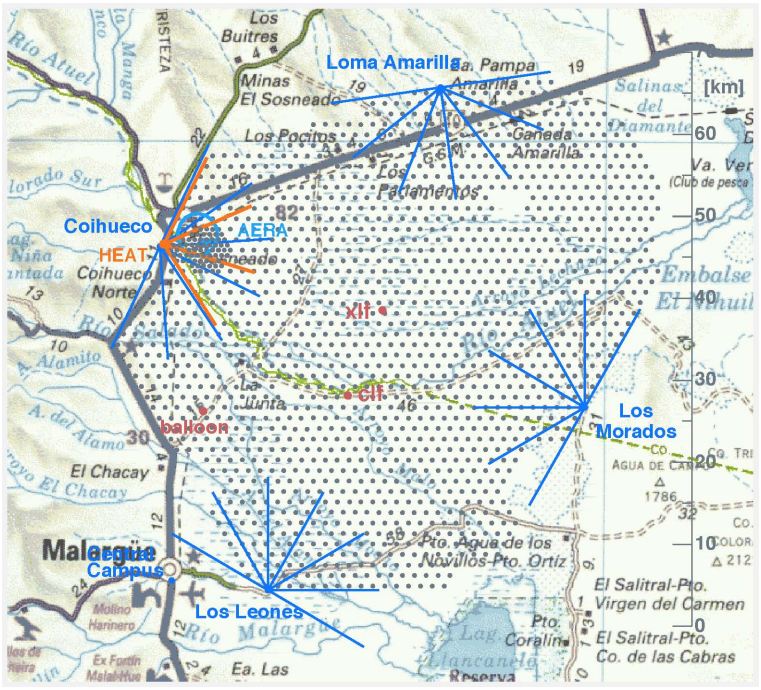

Figure 4.1: *Layout of the Pierre Auger Observatory. The gray dots represent the water-Cherenkov detector stations of the surface detector (SD). The telescopes of the fluorescence detector (FD) are located at the four sites Coihueco, Loma Amarilla, Los Leones, and Los Morados. The field of view of the telescopes is illustrated by the blue lines. The low-energy enhancements AMIGA and HEAT are located close to Coihueco. The field of view of HEAT is marked by the orange lines. The position of AERA is indicated by the light-blue circle in the north-west corner of the SD array.*

zon. In Fig. 4.2, a picture of an FD building at day as well as a schematic view of the main parts of a telescope are shown. The telescope design is based on the Schmidt optic [176] to maximize the detector field of view with small coma aberration. A diaphragm of $1.1\,\mathrm{m}$ radius is covered by an UV-filter glass which reduces background light and is transparent for light with wavelengths in between $310\,\mathrm{nm}$ to $390\,\mathrm{nm}$ with a transmission coefficient above $50\,\%$. An annular lens is used to correct for spherical aberration and eliminates coma aberration. More details are given in [175, 177]. Once passing filter and lens, the incident light is reflected by a segmented spherical mirror with a size of $13\,\mathrm{m}^2$ which has an average reflectivity of more than $90\,\%$ for light with a wavelength of $370\,\mathrm{nm}$ and finally recorded by a curved camera. The camera is placed in the focal plane of the spherical mirror and is composed of 440 pixels arranged in 22 rows and 20 columns. These pixels are read out by photomultiplier tubes (PMTs) with a hexagonal shape equipped with a Winston cone to minimize the dead space between the PMTs. Finally, a shutter protects the telescopes from dangerous environmental conditions such as rain, strong wind, as well as daylight.

The electronics of the PMTs are located directly behind the camera body. The FD data are digitized with $15\,\mathrm{bits}$ and a sampling rate of $10\,\mathrm{MHz}$ [3]. Three trigger stages are implemented on firmware and software of each telescope. In the first trigger level, the trigger rate of each pixel in a camera is reduced to about $100\,\mathrm{Hz}$ by adjusting the pixel threshold level. Events with tracks of at least five pixels in length fulfill the second trigger level. The trigger rate of the second trigger level is typically between

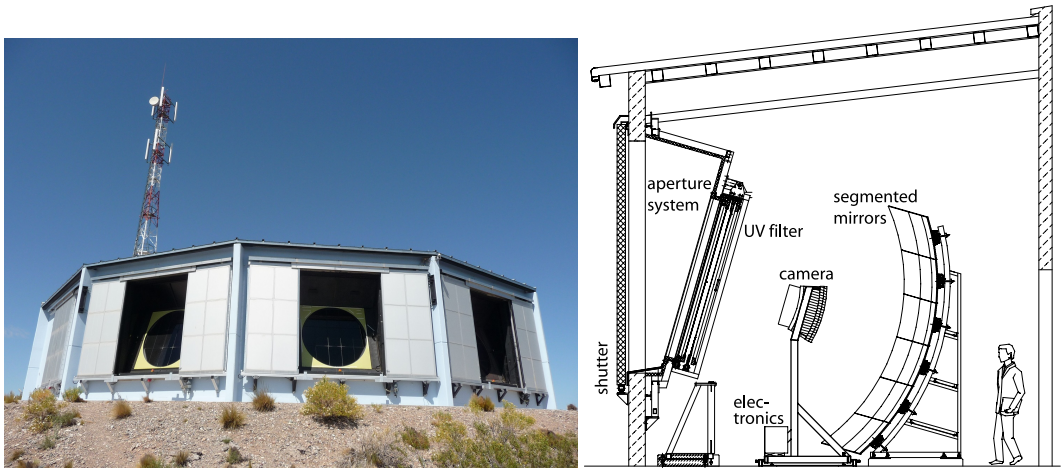

Figure 4.2: ***(left)*** *Picture of the fluorescence detector (FD) building at Loma Amarilla.* ***(right)*** *Schematic view of the main components of an FD telescope. Pictures taken from [3].*

0.1 Hz and 10 Hz. The third trigger level is a software algorithm which filters out noise events, e.g., caused by lightnings, cosmic-ray muons or randomly triggered pixels [3]. The data of events fulfilling the third trigger level requirements are send to the Central Data Acquisition System (CDAS) and then merged with data measured by the SD. The global trigger rate of each FD building is about 0.012 Hz. The recorded signal from the PMTs are measured in counts of the analog-to-digital converter (ADC) which has been calibrated to a light flux in multiple calibration campaigns. In a so-called drum calibration [166] a pulsed light source has been used to determine the ratio of photons per ADC count. The source provides an uniform illumination of each pixel resulting in a calibration factor of 4.5 photons per ADC count. The calibration precision is better than 4 % [178] and the systematic uncertainty of the drum calibration is stated to be 9.9 % [179]. In a further calibration campaign, a well-calibrated isotropic emitting light source has been mounted beneath a drone and flown into the field of view of the telescopes [180, 181]. Compared to the drum calibration this drone calibration has the advantage of reproducing realistic conditions of signals coming from cosmic-ray induced air showers. Furthermore, a smaller systematic uncertainty of 4.6 % has been achieved. Finally, further light sources are installed directly in each telescope for relative calibration [166] which enables monitoring the long-time variations of the calibration factor.

In case of an EAS, multiple pixels of a telescope are triggered forming a track. From the timing of each pixel with signal the shower axis is reconstructed. An example event measured in two telescopes of one FD building is shown on the right side of Fig. 4.3. From the information provided by the SD, the shower core on ground is determined resulting in a full geometry reconstruction of the shower. An example of such a so-called hybrid event measured in all four FD sites as well as with the SD is shown on the left side of Fig. 4.3.

For the event reconstruction, the calibrated signal of each contributing pixel is summed up to the photon flux as function of time. Together with the shower geometry, the complete signal is converted to the energy deposition dE/dX as function of the slant depth X. Here, parasitic light sources as Cherenkov light [183, 184] and multiple scattered light [185–187] as well as the light attenuation in the atmosphere and the fluorescence yield [188–190] are considered. An example of a measured en-

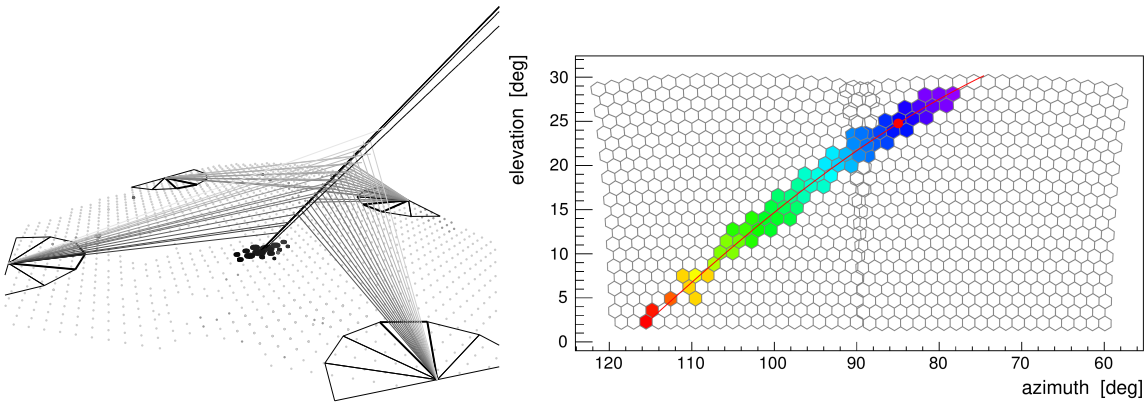

Figure 4.3: ***(left)*** *Hybrid event measured with the surface detector (SD) and telescopes from all fluorescence detector (FD) sites. The data combination enables reconstructing the shower geometry meaning the shower core on ground and shower axis. Picture taken from [3].* ***(right)*** *Example EAS event measured in two telescopes at the Coihueco site. The colored pixels mark the pixel with signal and the respective signal time is indicated by the color. Red corresponds to a later and purple to an earlier signal. The red line illustrates the shower axis projected into the telescopes. Plot taken from [182].*

ergy deposition as function of the slant depth is presented in Fig. 4.4. A Gaisser-Hillas function [191] is fitted to the data:

$$f_{\mathrm{GH}}(X) = \left(\frac{dE}{dX}\right)_{\mathrm{max}} \left(\frac{X - X_0}{X_{\mathrm{max}} - X_0}\right)^{(X_{\mathrm{max}} - X_0)/\lambda} e^{(X_{\mathrm{max}} - X)/\lambda} \tag{4.1}$$

with the maximal energy deposition $\left(\frac{dE}{dX}\right)_{\mathrm{max}}$ at the shower maximum $X = X_{\mathrm{max}}$ and the two shape parameters X_0 and λ of the Gaisser-Hillas function. If large parts of the shower are not observed, e.g., if the shower maximum is located outside the field-of-view of the detector, an accurate reconstruction of all fit parameters is not possible anymore. To handle this issue, the two shape parameters are then constrained to their average values [3, 192]. From the integral of $f_{\mathrm{GH}}(X)$ over X the energy transferred from the primary cosmic ray into the electromagnetic shower component can be determined. The total cosmic-ray energy is then obtained by correcting for the invisible energy which is carried away by neutrinos and high-energy muons [3, 142] as they rarely interact in the atmosphere and thus do nearly not contribute to the energy deposit of EAS in the atmosphere. The FD provides an energy resolution of better than $10\,\%$ and an energy scale uncertainty of $14\,\%$ [179].

4.2 The Surface Detector of the Pierre Auger Observatory

The SD [3, 165] comprises 1660 water-Cherenkov detector stations deployed on a hexagonal grid with a spacing of $1500\,\mathrm{m}$ which covers an area of $3000\,\mathrm{km}^2$. In a smaller array of $23.5\,\mathrm{km}^2$ located in the north-west corner of the regular SD array the grid spacing of 61 detector stations is reduced to $750\,\mathrm{m}$. Each detector station consists of a cylindric tank made of polyethylene with a diameter of $3.6\,\mathrm{m}$ and a height of less than $1.6\,\mathrm{m}$. The tank contains a sealed liner with a reflective inner surface [3] which is filled to a height of $1.2\,\mathrm{m}$ with about $12.000\,\mathrm{l}$ ultra-pure water. If charged particles of an EAS

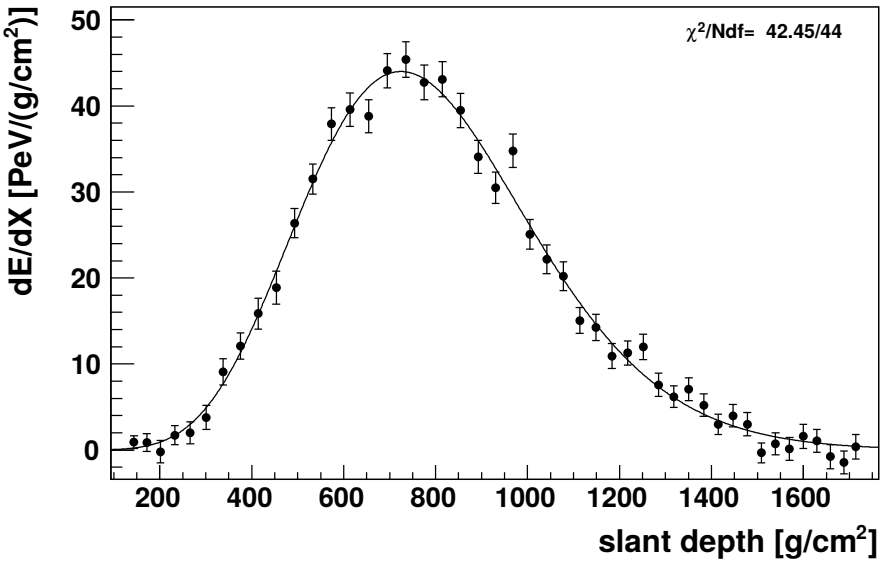

Figure 4.4: *Example measurement of the energy deposition dE/dX as function of the slant depth X. The data (dots) are fitted by a Gaisser-Hillas function (line). Plot taken from [3].*

cascade propagate faster than light through the water, Cherenkov light is emitted. The intensity of the Cherenkov light and the detector-station timing allows for reconstructing the primary cosmic-ray properties. Three 9-inch diameter photomultiplier tubes (PMTs) are used to detect the Cherenkov light and are symmetrically installed with a distance of $1.2\,\mathrm{m}$ to the center axis of the tank. Compared to conventional flat scintillator modules, the detector stations exhibit an increased sensitivity to inclined showers due to the large height of water inside the tank. Furthermore, they are sensitive to photons which produce an electron-positron pair within the water. Besides the PMTs, each station consists of a GPS receiver, a $12\,\mathrm{V}$ battery, a charge controller as well as solar panels which provide a $10\,\mathrm{W}$ power supply in average. Thus, each detector station is autonomously working. The data are sent to the CDAS via radio in the $902\,\mathrm{MHz}$ to $928\,\mathrm{MHz}$ frequency band. On the left side of Fig. 4.5, a picture and on the right side, a sketch of an SD station is shown.

The recorded signal from the PMTs is given in units of a vertical equivalent muon (VEM) which normalizes the signal strength to a signal produced by a muon propagating on a vertical trajectory through the detector station [194]. For the data taking, different trigger levels are applied to increase the event purity of air showers. The first two trigger levels T1 and T2 are directly implemented in the station electronics. The T1 trigger comprises a simple threshold trigger (TH) which requires a signal in all of the three PMTs of more than $1.75\,\mathrm{VEM}$ which reduces the rate of atmospheric muons from about $3\,\mathrm{kHz}$ to $100\,\mathrm{Hz}$. Additionally, a time-over-threshold (ToT) trigger is implemented which requires a signal strength of more than $0.2\,\mathrm{VEM}$ in at least 13 bins within a time window of $3\,\mu\mathrm{s}$ (120 samples) measured in two of the three PMTs [3]. The ToT trigger selects sequences of small signals spread in time resulting in a trigger rate on the level of a few Hz [3].

If the T1 trigger is a ToT trigger or a TH trigger with a signal strength of more than $3.2\,\mathrm{VEM}$ the T2 requirements are fulfilled. The T2 trigger decreases the global rate of T1 triggers to about $22\,\mathrm{Hz}$. If the T2 trigger requirements are fulfilled, the event time stamp is then send to the CDAS. At the CDAS,

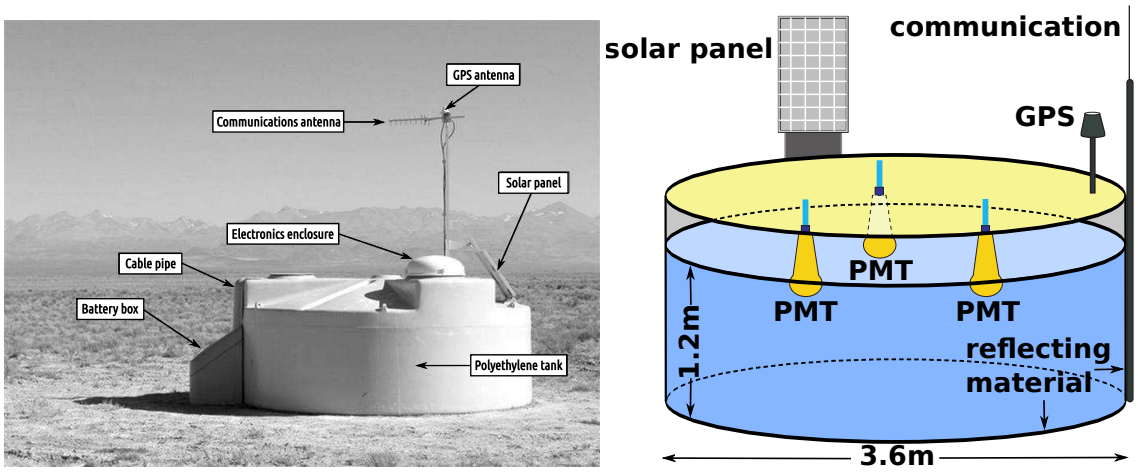

Figure 4.5: ***(left)*** *Picture of a surface detector (SD) station in the field. The main components are labeled. Picture taken from [3]. Schematic view of the SD station illustrating the inner components of the station. Picture taken from [102] and modified from [193].*

a third trigger level (T3) is initiated which is based on the received timing of the T2 triggers.
The T3 trigger requires a clustering of the triggered stations and is divided into two modes. The neighbors of each detector station is segmented in different sets of neighbors considering the hexagonal grid layout of the array. The first T3 mode requires at least three ToT triggers with minimum compactness. The T3-ToT trigger requirements are fulfilled if one station of the first set and one further station of the first two sets of neighbors are triggered in time coincidence with the reference station. The second T3 mode requires at least four stations with a T2 trigger in time coincidence with the reference station while at least one of the first, another of the first two, and one further of the first four sets of neighbors are triggered. The time coincidence is verified if the time stamp of each station with T2 trigger is within $(6 + 5n)\,\mu$s of the reference station while n is the respective set of neighbors. Possible configurations of triggered stations for both T3 modes are illustrated in Fig. 4.6. The trigger rate of the global T3 trigger level is about $0.03\,$Hz. If the T3 trigger requirements are fulfilled, the data from those stations fulfilling at least the T1 trigger requirements within $30\,\mu$s of the T3 time stamp are communicated to the CDAS.
The first physics trigger applied on the data is called T4 and requires that the signal time of the stations of a T3 event fits to a plane shower front moving with the speed of light. From this fit, the incoming arrival direction is reconstructed with a resolution of better than 1.6° for events with at least three triggered stations and better than 0.9° for events with at least six triggered stations [195] in the case of the regular SD array. In the case of SD-infill array, the resolution is better than 1.3° [170].
The air shower direction and the cosmic-ray energy can be incorrectly reconstructed if a part of the shower is missing, e.g., if the shower position is located at the border of the SD array. The so-called 6T5 trigger requires that the detector station with largest signal is surrounded by 6 active stations. The 6T5 trigger allows for an accurate reconstruction of the shower core and estimation of the shower energy. More details about the SD-triggers can be found in [3, 173].
The shower core is reconstructed by fitting a model of the lateral shower distribution (LDF) $S(r)$ described by a Nishimura-Kamata-Greisen function [196, 197] to the signal strength of the detector

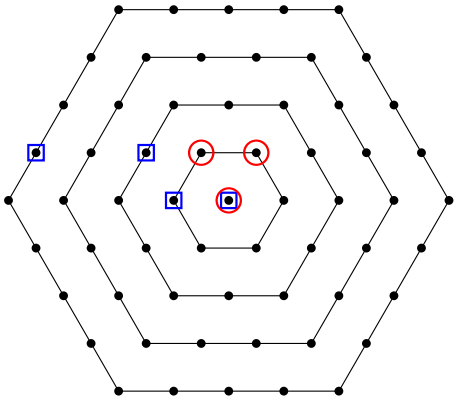

Figure 4.6: *Examples of possible station configurations which are triggered in time coincidence with the centered reference station for both T3 modes. The first T3 mode (red circles) requires at least three stations triggered in coincidence while one station of the first set of neighbors and a second station of the first two sets of neighbors are triggered. The second T3 mode (blue squares) requires four stations triggered in coincidence while at least one of the first, another of the first two, and one further of the first four set of neighbors are triggered. Each set of neighbors is marked by the black lines and counted from the reference stations. Picture taken from [3].*

stations with signal:

$$S(r) = S_{r_{\mathrm{opt}}} \left(\frac{r}{r_{\mathrm{opt}}} \right)^{\beta} \left(\frac{r + r_1}{r_{\mathrm{opt}} + r_1} \right)^{\beta+\gamma} \tag{4.2}$$

with the distance to the shower axis r and $r_1 = 700\,\mathrm{m}$. The parameter r_{opt} is the distance for which the model dependency on the lateral shower distribution is minimal and thus $S_{r_{\mathrm{opt}}}$ is an estimator of the shower size which is used to estimate the cosmic-ray energy. In the case of the regular SD array, it is $r_{\mathrm{opt}} = 1000\,\mathrm{m}$ [198] while in the case of the SD-infill array, it is $r_{\mathrm{opt}} = 450\,\mathrm{m}$ [170]. In Fig. 4.7, an example event of an air shower is shown with a zenith angle of $(25.1 \pm 0.1)^\circ$ and a cosmic-ray energy of $(104 \pm 11) \cdot 10^{18}\,\mathrm{eV}$ measured in several stations and the respective LDF.

The shower size $S_{r_{\mathrm{opt}}}$ depends on the cosmic-ray energy as well as on the incoming zenith angle. As the length of the shower path through the atmosphere increases with the zenith angle, the shower is stronger attenuated. The shower size S_{1000} (S_{450}) is normalized to a median zenith angle of 38° (35°) using the constant intensity cut method [199] and is then called S_{38} (S_{35}) which has an energy dependency only. Thus, they are used as cosmic-ray energy estimator of the SD.

Inclined events with zenith angles above 60° exhibit a large asymmetry in the shower footprint and thus are reconstructed in a different way which is explained in [200]. Here, the number of muons on ground is modeled by introducing a parameter N_{19} which scales the measured signals to a reference muon distribution of a proton induced air shower with an energy of $10^{19}\,\mathrm{eV}$ obtained from air shower simulations. The parameter N_{19} has an energy dependency only and thus is used as energy estimator. The SD energy estimators $\hat{S} = S_{35}, S_{38}, N_{19}$ are absolutely calibrated using high-quality hybrid events which include additional information provided by the FD. The relation between the SD energy estimators and the cosmic-ray energy measured by the FD is described by a power law:

$$E_{\mathrm{FD}} = A \cdot \hat{S}^B \tag{4.3}$$

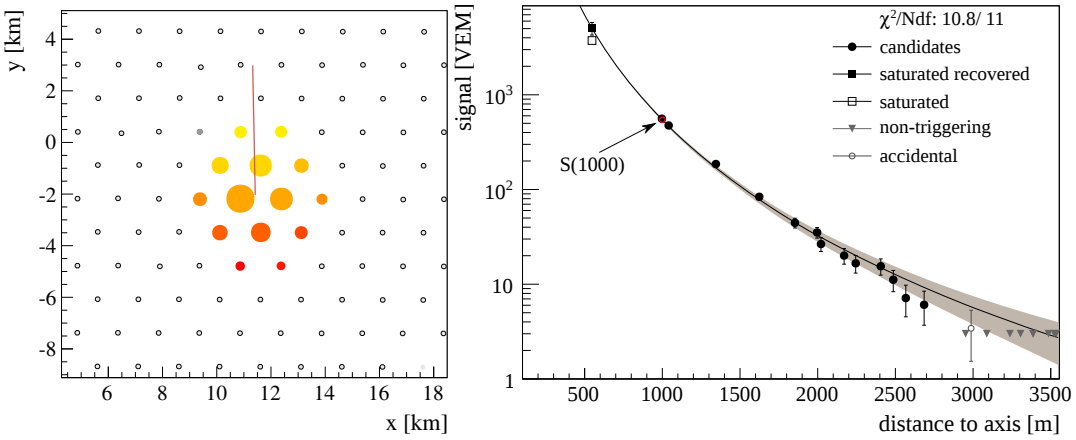

Figure 4.7: *Example event of an air shower with a reconstructed zenith angle of* $(25.1 \pm 0.1)^\circ$ *and a reconstructed cosmic-ray energy of* $(104 \pm 11) \cdot 10^{18}$ eV *measured in multiple stations of the regular surface detector (SD) array.* ***(left)*** *Footprint of the event. Each circle represents an SD station. While the color indicates the arriving time from early (yellow) to late (red) the marker size illustrates the signal strength. The red line marks the shower axis.* ***(right)*** *The respective signal strength measured in the SD stations as function of the distance to the shower axis. The optimal shower size estimator* S_{1000} *is marked as a red dot. Both plots are taken from [3].*

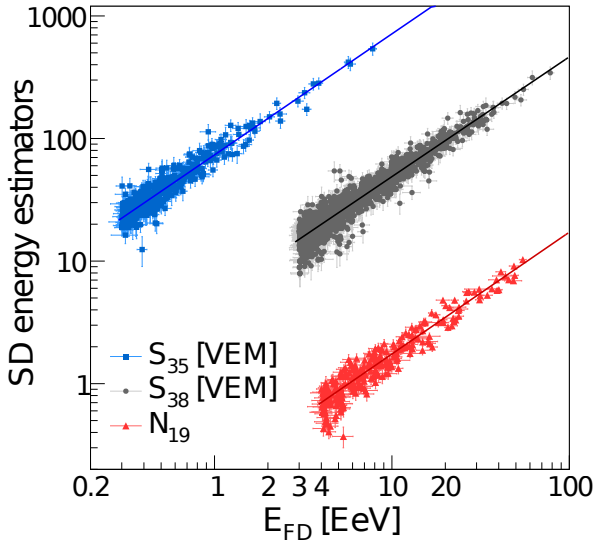

Figure 4.8: *The surface detector (SD) energy estimators* S_{35}*,* S_{38}*, and* N_{19} *cross calibrated with information from the fluorescence detector (FD). The* S_{35} *and* S_{38} *parameters are measured in units of a vertical equivalent muon (VEM). In contrast, the* N_{19} *SD energy estimator is a scaling factor and thus dimensionless. The plot is taken from [82].*

that is fitted to the data using a tailored maximum-likelihood method [201] as presented in Fig. 4.8. In the case of the regular SD-array, the energy resolution is 15.3 % for vertical events and 19 % in the case of inclined events [82]. The SD-infill array exhibits an energy resolution of 13 % [82]. As the fit uncertainties are small compared to those of the FD energy scale, the SD energy scale uncertainty is equal to the FD scale uncertainty of 14 % [82].

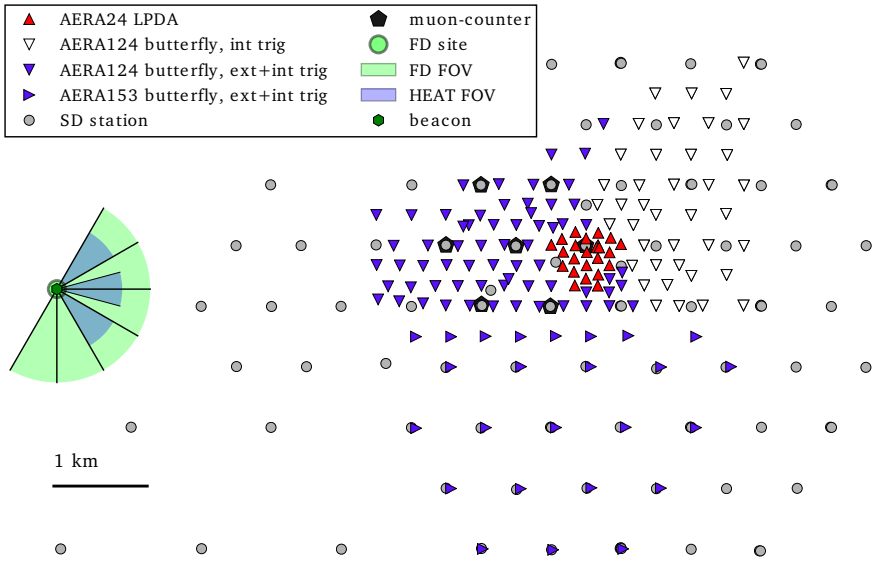

Figure 4.9: *Layout of AERA within the surface detector (SD) array (gray dots) and the buried muon array (black pentagons) [170, 171]. The radio stations (red, white and blue triangles) are set up on a regular grid in spacings of* 144 m, 250 m, 375 m *and* 750 m. *The field of view of the fluorescence detector (FD) telescopes of Coihueco including the high-elevation FD extension HEAT [172] is indicated by the green and blue area. The beacon antenna [202] for time calibration is located at the FD site. Figure taken from [6].*

4.3 The Auger Engineering Radio Array

In this section, the radio detector of the Pierre Auger Observatory, the Auger Engineering Radio Array (AERA), is described in detail. AERA is located in the north-west corner of the SD array close to the low-energy enhancements of the two baseline detectors. Currently, AERA is the largest cosmic-ray radio detector world wide and comprises 153 radio stations to detect radio emission of cosmic-ray induced air showers in the frequency range from 30 MHz to 80 MHz. The layout of AERA is shown in Fig. 4.9.

AERA is an engineering array which means that different types of radio stations with different kind of hard- and software are developed and tested in the field which contributes to several different physical purposes. The radio stations of AERA are deployed in three stages with different grid spacings. In September 2011, the first 24 radio stations were installed (AERA24) on a triangular grid with a grid spacing of 144 m covering about $0.4\,\mathrm{km}^2$. Using AERA24, the radio emission mechanisms have been investigated and the radio-signal correlation of the cosmic-ray energy has been determined [20, 24, 25]. In May 2013, the AERA24 array was extended with 100 additional radio stations (AERA124). These radio stations were deployed with a grid spacing of 250 m and 375 m resulting in a covered area of about $6\,\mathrm{km}^2$. The larger instrumented area enhanced the detector sensitivity to higher cosmic-ray energies. In the third and currently last stage of expansion, AERA was extended with 29 additional radio stations with 375 m and 750 m spacing so that AERA covers an area of about $17\,\mathrm{km}^2$. The increased distance between the stations allows for a better investigation of horizontal air showers (HASs)

which have large footprints on ground [35, 36]. The flight path of HASs through the Earth's atmosphere is increased resulting in a die-out of the hadronic and electromagnetic shower components before they are detectable at ground level. The shower information is then saved in the muonic and radio component of the shower only. These information are directly connected to the primary cosmic-ray mass (cf. Sec. 2.4.1).

The AERA objectives are to improve the comprehension of cosmic-ray induced air showers using the radio detection technique in coincidence with the well-established baseline detection techniques and for future stand-alone radio detectors, investigating the radio emission mechanisms in the Earth's atmosphere, and to measure the properties of primary cosmic-rays. Radio measurements are less dependent on atmospheric conditions compared to those made with the well-established fluorescence technique. Only strong atmospheric electric fields (e.g. produced in thunderstorms) limit the radio data acquisition. This results in a duty cycle close to $100\,\%$. Thus, the radio detection technique offers a high potential for cosmic-ray physics, e.g., an energy determination of cosmic rays with reduced systematic uncertainties [30].

The section is structured as follows. At first, the detector design and the hardware of the AERA radio stations is described in Sec. 4.3.1. In Sec. 4.3.2 and Sec. 4.3.3, the two main antenna types used in the radio stations of AERA are presented. Afterwards, the data trigger systems and data acquisition are described in Sec. 4.3.4. Then, the calibration efforts are discussed in Sec. 4.3.5 and finally, the event reconstruction is explained in Sec. 4.3.6.

4.3.1 Detector Design

Each station consists of two perpendicular polarized antennas which are aligned to magnetic north and east with a precision better than 1° [159]. Two different main antenna types are used at AERA. The 24 radio stations of AERA24 are equipped with logarithmic-periodic dipole antennas (LPDAs). A photo of a station equipped with LPDAs and a schematic view of the LPDAs are shown in Fig. 4.10. The radio stations of the second and third stage of AERA are equipped with Butterfly antennas. In Fig. 4.11, a photo and a schematic view of the Butterfly antenna-equipped radio station are shown.

Each antenna is connected through a low-noise amplifier (LNA) and a filter amplifier to a digitizer which is located in an RFI-shielded electronics box made of aluminum placed beneath the antennas of each station. The system consisting of the LNA and the filter amplifier of each radio station forms a band-pass filter for frequencies from $30\,\mathrm{MHz}$ to $80\,\mathrm{MHz}$ and thus suppresses short-wave and FM-band transmitters. The digitizer contains a field programmable gate array (FPGA). The FPGA enables first analysis of the recorded radio data, e.g., data filtering of noise signals and executing of trigger algorithms [204] (cf. Sec. 4.3.4). Two different kinds of digitizers, one with and one without a large ring buffer, are used which enable using different kinds of trigger systems for data taking such as self trigger, external triggers and internal scintillator triggers. In principle, four different setups of the signal chain from antenna to digitizer are used which are sketched in Fig. 4.12 and are described in the following.

In the case of the LPDA-equipped radio stations, the LNA has a power gain of $|S21|^2 \approx 18\,\mathrm{dB}$ [205]. A filter amplifier restricts the frequency bandwidth of the antenna stations to between $30\,\mathrm{MHz}$ and $80\,\mathrm{MHz}$. For increasing the dynamic range, the signal is split in a low-gain channel with a further

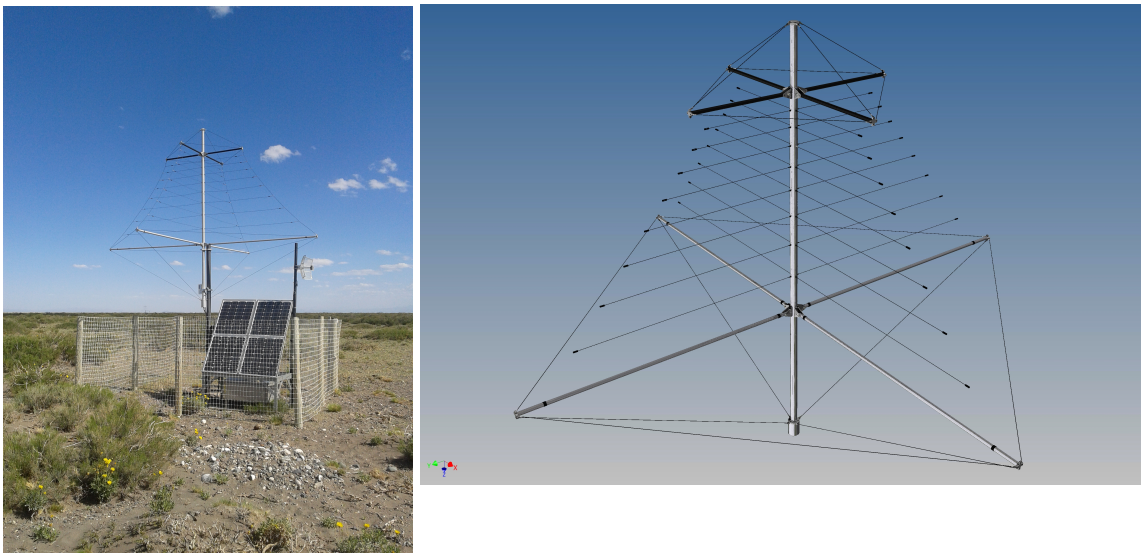

Figure 4.10: *LPDA-equipped radio station used at AERA.* ***(left)*** *Photo of the radio station in the field.* ***(right)*** *Schematic drawing of both LPDAs used in each LPDA-equipped radio station. Drawing taken from [203].*

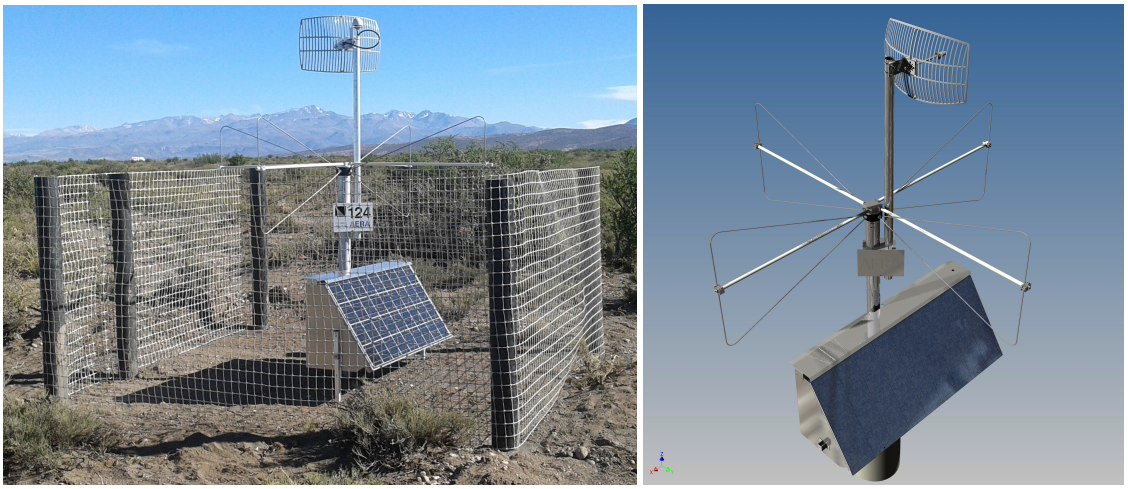

Figure 4.11: *An AERA radio station equipped with Butterfly antennas.* ***(left)*** *Photo of the radio station in the field.* ***(right)*** *Schematic drawing of the radio station. Drawing taken from [203].*

amplification of 10 dB and a high-gain channel with a further amplification of 30 dB [206]. The received signal is then sampled by a digitizer. The first type of digitizers contains a 4 GB ring buffer which enables storing the measured data of the high-gain channel of both antenna polarizations for about 7 s. This is necessary for external triggers from the Auger baseline detectors which have a time delay up to 7 s. The data are sampled with a rate of 180 MHz using 12-bit flash analog-to-digital converters (FADC). The second digitizer type does not have a large ring buffer but is optimized for data taking with self triggers. These digitizers have a sampling rate of 200 MHz using 12-bit FADCs. In the case of the radio stations equipped with Butterfly antennas, the LNA has a power gain of $|S21|^2 \approx 30\,\mathrm{dB}$ [207] in the sensitive frequency range of AERA. The frequency bandwidth of the

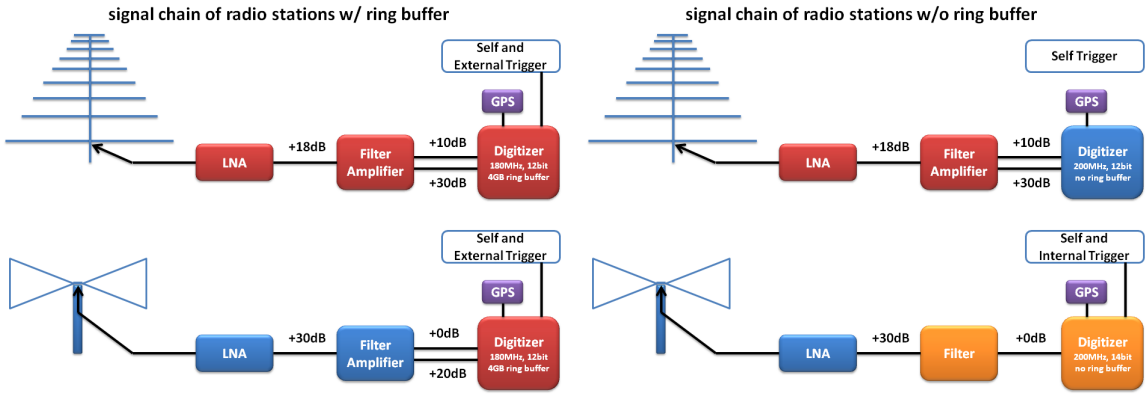

Figure 4.12: *Signal chain of the LPDA-equipped **(top)** and Butterfly antenna-equipped radio stations **(bottom)**. Each antenna is connected through a low-noise amplifier (LNA), and a filter amplifier or a filter to a digitizer. Two different types of digitizers are used: with **(left)** and without **(right)** large ring buffer, which are optimized for self triggers, and external triggers or internal scintillator triggers respectively. The event time is obtained by a GPS receiver. The black arrow marks the position of the LNA. The colors represent different types of the respective electronic device.*

antenna stations is restricted to between 30 MHz and 80 MHz in a filter amplifier or a passive filter. For the stations connected to the digitizer with ring buffer, in the low-gain channel the signal is not further amplified and in the high-gain channel the signal is amplified by 20 dB in the filter amplifier [206]. For the stations of the third stage of AERA, only the high-gain channel is implemented in the digitizer. One of the reason is that due to the limited buffer size, the trace length which can then be stored in the buffer if all four channels are digitized is reduced to about 3.5 s which is to short for the external triggers. For the stations connected to the digitizer without ring buffer, a passive filter instead of the filter amplifier is utilized. This means that no further signal amplification is implemented. The increased dynamic range is obtained by using 14-bit FADCs instead of using 12-bit FADCs and splitting the signal in a low-gain and high-gain channel. These stations contain one or two small scintillator counters of size $45.7\,\mathrm{cm} \times 17.2\mathrm{cm} \times 2.4\,\mathrm{cm}$ which enable detecting particles of air showers directly at the radio station and are used for internal scintillator triggers. For more information about the digitizers, passive filter, and the scintillators refer to [182, 206, 208].

Each radio station is equipped with a GPS antenna which enables accurate measurements of the signal timing. The stations are powered by solar panels and are equipped with battery so that they are autonomously operated.

In the first two years of data taking, the central radio station (CRS) was used for the data acquisition (DAQ) of AERA. The CRS is a modified shipping container which is powered by solar panels and is located close to the stations of AERA24. A picture of the CRS is shown in Fig. 4.13. The 24 stations of AERA24 are connected by optical fibers to the CRS [209]. Together with the first expansion of AERA and the extended distances between the radio stations and the CRS, the DAQ was moved to the buildings of the FD station Coihueco. Now, a commercial wireless communication link is used to connect the radio stations with the DAQ. Each station of the second and third stage of AERA comprises a hyperbolic wifi antenna mounted on a hollow tube made of aluminum with a length of

Figure 4.13: *Photo of the central radio station.*

1.5 m which is called wifi mast. The wifi mast is vertically aligned and mounted with a distance of about 10 cm to the station pole using conductive clamps made of aluminum and thus is grounded. The wifi antenna is connected by an optical fiber through the wifi mast and the station pole to the digitizer of the radio station. The recorded data are transmitted to access points installed at the CRS or directly to the access points located at Coihueco using a 5 GHz connection. A further wireless connection between the CRS and Coihueco is applied so that the connection of all radio stations to the DAQ is realized. For more information concerning the wireless communication used at AERA refer to [182].

4.3.2 The Logarithmic-Periodic Dipole Antenna

An LPDA consists of several $\lambda/2$-dipoles of different lengths l_i which are combined to one single antenna with the largest dipole located at the bottom and the shortest dipole at the top of the LPDA. The dipoles are arranged so that an opening angle α is spanned from the virtual array vertex (VAV) as defined in Fig. 4.14 and are connected to a waveguide with the footpoint (which is called *feeder* in Fig. 4.14) at the top of the antenna. Each dipole is sensitive to a different wavelength resulting in a broad sensitive frequency estimated by the length of the smallest l_{min} and largest l_{max} dipole:

$$\begin{aligned} f_{\mathrm{min}} &\approx \frac{c}{2l_{\mathrm{max}}} \\ f_{\mathrm{max}} &\approx \frac{c}{3l_{\mathrm{min}}}. \end{aligned} \tag{4.4}$$

It has to be mentioned that f_{max} deviates from the assumption of a half-wave dipole due to a complex interplay with the waveguide [151] but the real upper frequency limit is typically larger than obtained from this estimation. The signal measured in the dipoles should interfere constructively at the LPDA footpoint which is realized by a constant ratio of the distance R_i between the VAV and the i-th dipole, and the respective dipole length l_i:

$$\frac{R_i}{l_i} \propto \frac{R_i}{\lambda_i} = const. \tag{4.5}$$

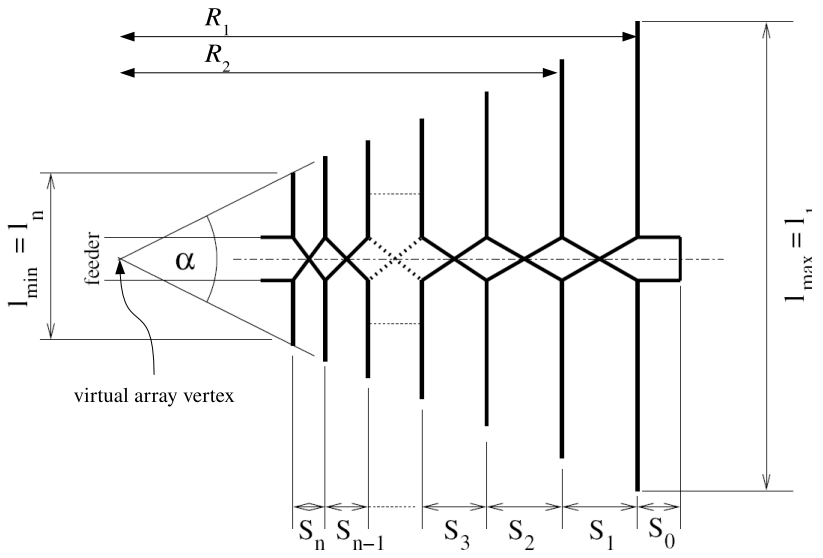

Figure 4.14: *Schematic view of an LPDA. Picture taken from [210] and modified from [144].*

From Eq. (4.5), a relation between the dipole length l_i and l_{i-1} of two neighboring dipoles is derived which is denoted by τ:

$$\tau = \frac{l_i}{l_{i-1}} = const. \tag{4.6}$$

The spacing S_i between two neighboring dipoles relates to R_i and τ: $S_i = R_i - R_{i+1} = R_i(1-\tau)$. The ratio of S_i and the corresponding dipole length l_i is constant and is denoted by σ:

$$\sigma = \frac{S_i}{2l_i} = const. \tag{4.7}$$

The parameters τ and σ combined with the length of the smallest and largest dipole define the LPDA design parameters. From these parameters the full antenna structure is determined.

The four design parameters of the LPDAs used at AERA are $\tau = 0.875$, $\sigma = 0.038$, $l_{min} = 1470\,\mathrm{mm}$ and $l_{max} = 4250\,\mathrm{mm}$. These values were chosen to cover the frequency range from around $30\,\mathrm{MHz}$ to $80\,\mathrm{MHz}$ and to combine a high antenna sensitivity in a broad field of view using a limited number of dipoles and reasonable dimensions. They lead to an LPDA with nine separate dipoles and an overall antenna dimension of $4.5 \times 3.5\,\mathrm{m}^2$. The upper eight of the nine dipoles are made of thin coated copper wires which reduce the antenna weight (to about $18\,\mathrm{kg}$) and make the LPDA less affected by the wind. Coil springs are used to span and align these dipoles horizontally. The lowest dipole is included in the antenna support structure at the bottom of the LPDA which spans the antenna and is made of aluminum. A full drawing of the LPDA including all sizes is presented in Fig. 4.15. The dipoles are connected to a waveguide with the footpoint at the top of the antenna. An LNA is used to amplify the recorded signal. The optimal place of the LNA is directly at the antenna footpoint so that signal loss and background noise injected to the signal chain are reduced. In the case of the LPDA used at AERA, the footpoint is at a height of about $5\,\mathrm{m}$. Thus, for maintenance reasons the LNA is moved to the bottom of the LPDA. The footpoint is connected through a $4:1$ impedance transformer to an RG58 [211] coaxial transmission line with a length of $2.9\,\mathrm{m}$. Due to the impedance transformer,

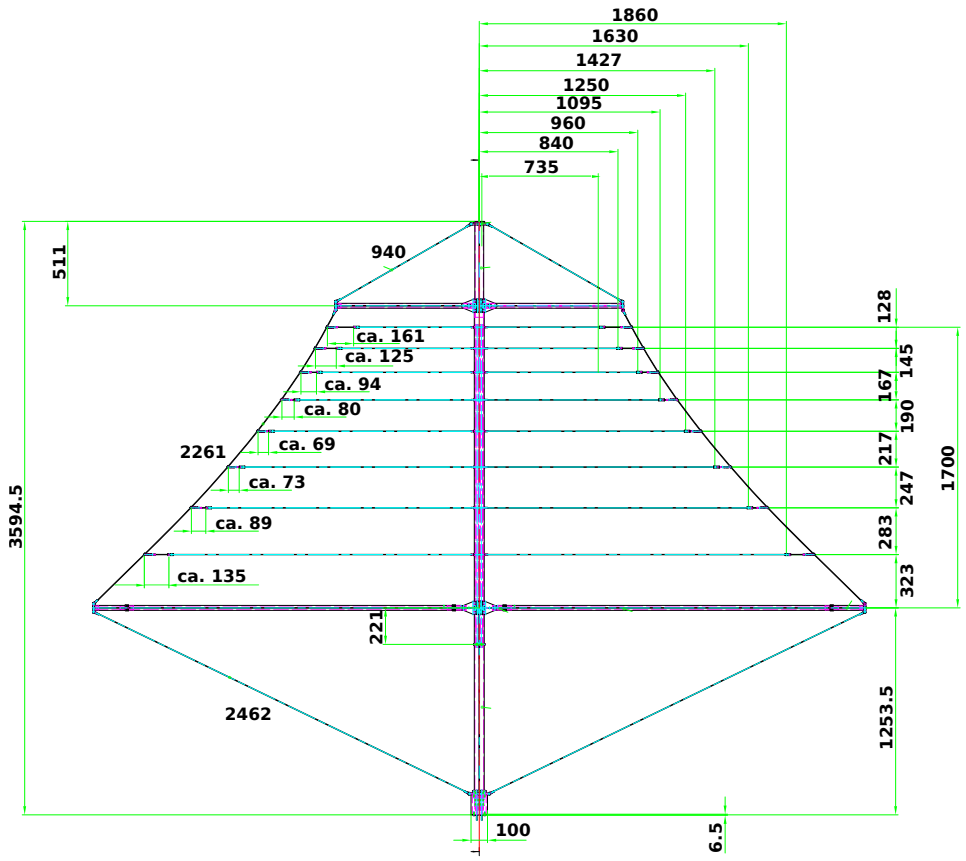

Figure 4.15: *Drawing of the LPDA used at AERA, units are millimeter.*

the antenna impedance is reduced from about $200\,\Omega$ to about $50\,\Omega$ in the sensitive frequency range and thus matches the $50\,\Omega$ system of the RG58 cable. The LPDA impedance has been measured in a reflection measurement [159]. On the left side of Fig. 4.16, the LPDA resistance and reactance are shown as a function of the frequency which corresponds to the real and imaginary part of the antenna impedance respectively. The measurement exhibits a resistance which varies around $50\,\Omega$ and a reactance which is close to zero in a frequency range from $30\,\mathrm{MHz}$ to $80\,\mathrm{MHz}$. On the right side of Fig. 4.16, the LPDA standing wave ratio (SWR) as function of the frequency calculated according to Eq. (3.20) is presented. The SWR reveals values of about 2 for the sensitive frequency range of AERA which corresponds to reflection efficiencies of more than $90\,\%$ [159, 203]. The LPDAs are mechanically and electrically identical at the percent level [159, 203].

A dedicated LNA was developed [205] which is shown in Fig. 4.17. The LNA is placed in an aluminum housing at the bottom of the LPDA and thus is protected from environmental conditions such as rain, wind, and direct sunlight. The LPDA and the LNA form a technical unit and thus the LNA properties are included in the antenna response pattern. The LNA characteristics are described by the four amplifier S-parameters, most importantly by the power gain $|S21|^2$ and the power reflection at the LNA input port $|S11|^2$ which are related to the LNA impedance (cf. Sec. 3.6.5). The LNA is optimized to match to the $50\,\Omega$ system of the coaxial cable connected to the antenna footpoint in the frequency range from $30\,\mathrm{MHz}$ to $80\,\mathrm{MHz}$. The corresponding LNA resistance and reactance are shown on the left side of Fig. 4.18. In general, the resistance varies slightly around $50\,\Omega$ and the

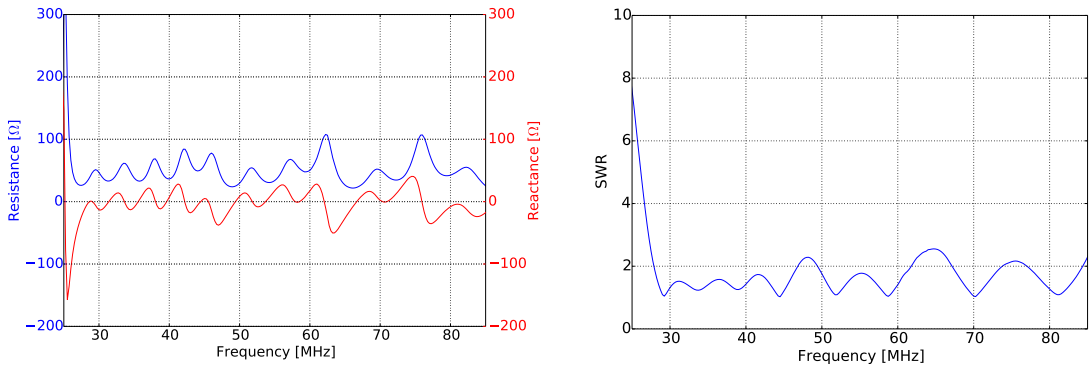

Figure 4.16: ***(left)*** *The LPDA impedance described by the antenna resistance (blue) and the antenna reactance (red) as well as* ***(right)*** *the resulting antenna standing wave ratio (SWR) as functions of the frequency. Plots adapted from [159].*

reactance is small within the frequency range of AERA. The LNA power gain and the LNA power reflection at the input port are presented on the right side of Fig. 4.18. The LNA amplifies the signal typically by $18\,\mathrm{dB}$. The LNA is connected via a coaxial cable to the station electronics. For more technical details about the LPDA and the LNA refer to [152] and [205] respectively.

4.3.3 The Butterfly Antenna

The Butterfly antenna is a so-called bow-tie antenna and a full-wave dipole. A broad sensitive frequency range is achieved by an area broadening of the dipole arms which have then a triangular form with an opening angle α. Typically, the triangular dipole arms are made of thin conductive patches. In the case of the Butterfly antennas used at AERA, thin aluminum wires with a diameter of $3\,\mathrm{mm}$ along the shape of the triangular area are used which result in a lower weight and makes the Butterfly antenna less affected by the wind while the electric properties of the typical Butterfly antenna are only minimal affected [145]. An opening angle of the dipole arms of $\alpha \approx 42^\circ$ is chosen. The Butterfly antennas have an overall dimension of $2.28 \times 0.8\,\mathrm{m}^2$ and the middle of the dipole arms is installed in a height of $1.65\,\mathrm{m}$ where the antenna footpoint is located. The dipole arms are aligned in the vertical plane and connected to a nut made of non-conductive material located in the middle of the antenna. The nut is made of UV-resistant plastic and has a diameter of $0.12\,\mathrm{m}$. Thus, it provides enough space for the antenna LNA. In contrast to the LPDA, the Butterfly antenna LNA is located directly at the antenna footpoint. A support structure has been developed to improve the wind stability of the Butterfly antenna. Tubes made of fiber glass are connected to the dipole arms by aluminum clamps and are held by an aluminum cap mounted on top of the nut. This support structure significantly improves the wind stability of the Butterfly antenna which has been tested in a wind tunnel [203, 212]. It is designed to have only a small influence on the electric property of the Butterfly antenna which has been determined to be on the percent level [203]. A schematic view of the Butterfly antenna used at AERA including the antenna dimensions is presented in Fig. 4.19.

On the left side of Fig. 4.20, the antenna impedance described by the antenna resistance and antenna

Figure 4.17: *Photo of the low-noise amplifier used in the LPDA-equipped radio stations at AERA.*

reactance is shown as function of the frequency. The antenna impedance exhibits large fluctuations in the relevant range. A matching to a $50\,\Omega$ system is achieved around $45\,\mathrm{MHz}$ which becomes visible in the antenna SWR presented as a function of the frequency on the right side of Fig. 4.20. Here, The SWR is minimal with a value of around 1.1. Note that the Butterfly antenna is designed as active antenna. The sensitive frequency range of the antenna is realized by an interplay between the antenna and the antenna LNA. Thus, the antenna and the LNA form a technical unit and the LNA properties are included in the antenna response pattern.

A photo of the LNA is shown in Fig. 4.21. The LNA characteristics are described by the four amplifier S-parameters, most importantly by the power gain $|S21|^2$ and the power reflection at the LNA input port $|S11|^2$ which is related to the LNA impedance (cf. Sec. 3.6.5). The LNA is designed to match to the Butterfly antenna impedance in the frequency range from $30\,\mathrm{MHz}$ to $80\,\mathrm{MHz}$. The corresponding LNA resistance and reactance are shown on the left side of Fig. 4.22. The LNA power gain and the LNA power reflection at the input port are presented on the right side of Fig. 4.22. It amplifies the

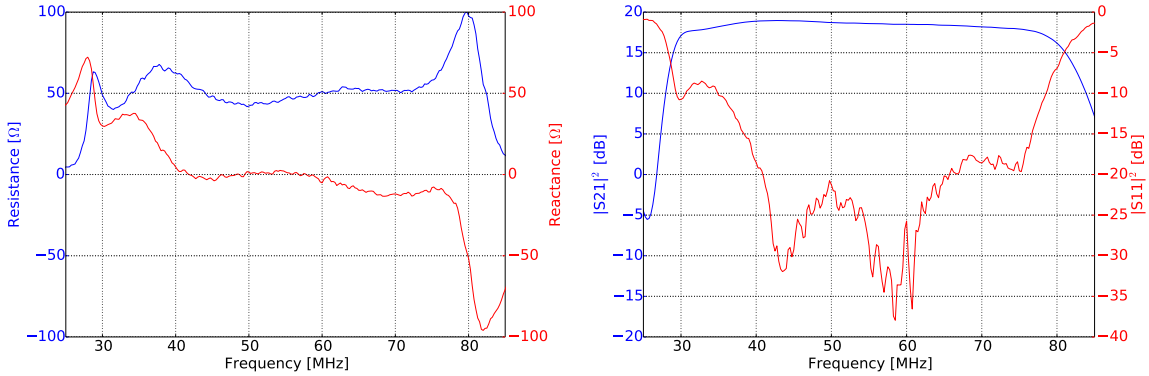

Figure 4.18: ***(left)*** *The impedance of the low-noise amplifier (LNA) used in the LPDA-equipped radio stations which is described by the LNA resistance (blue) and the LNA reactance (red).* ***(right)*** *The power gain $|S21|^2$ (blue) and the power reflection at the LNA input port $|S11|^2$ (red) as functions of the frequency. Plots adapted from [203].*

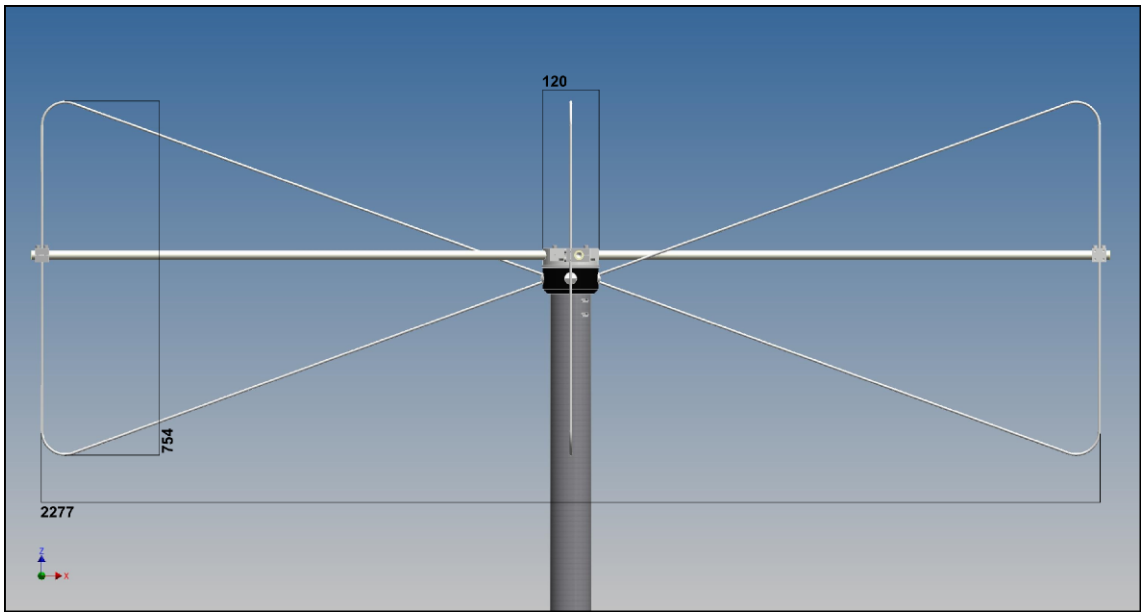

Figure 4.19: *Drawing of the Butterfly antenna, units are millimeter. Picture adapted from [203].*

signal typically by 30 dB. Note that the LNA power reflection is relative high compared to that of the LPDA LNA. This behavior is explained by the fact that the $|S11|^2$ parameter describes the power reflection in a 50 Ω system and the Butterfly antenna LNA is not designed for an operation in a 50 Ω system. For more details concerning the Butterfly antenna and its LNA used at AERA refer to [152, 207]. The LNA is connected to the station electronics via a coaxial cable which is guided through the bottom of the nut and then through the station pole.

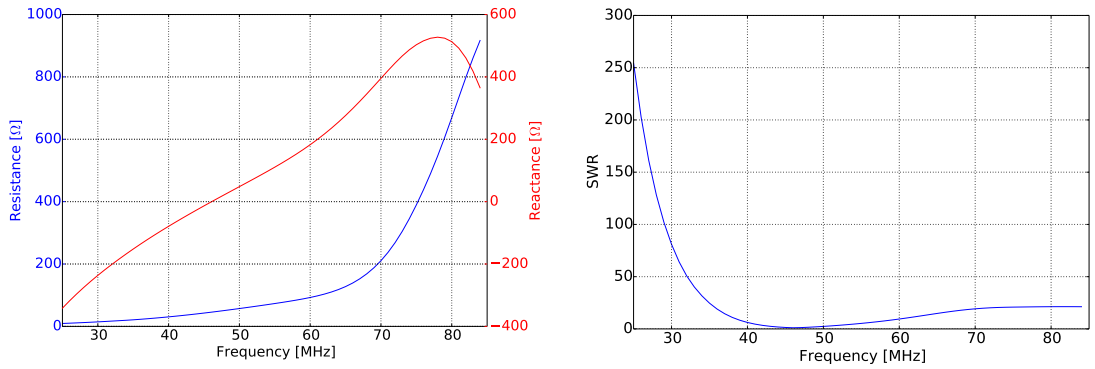

Figure 4.20: ***(left)*** *The Butterfly antenna impedance described by the antenna resistance (blue) and the antenna reactance (red) as well as* ***(right)*** *the resulting antenna standing wave ratio (SWR) as functions of the frequency obtained by simulations using the NEC-2 simulation code. In the simulation, the full radio station including both antennas as well as the conductive elements (e.g. the station pole and the electronics box) of the radio station are taken into account.*

4.3.4 Trigger Systems and Data Acquisition

As AERA is an engineering array, different kinds of triggers are tested for the observation of radio emission from cosmic-ray induced air showers. Different physical triggering systems such as a self trigger, an internal scintillator trigger as well as an external trigger are implemented. Furthermore, monitoring triggers are implemented delivering important information about the detector status as well as allowing detector calibrations using background noise.

The principle of the self trigger is simple as it is just searched for signals over a certain threshold level. However, the threshold level strongly depends on the noise background which complicates the triggering. The background noise stems from diffuse radio emission of the galactic plane which moves over the sky and furthermore from man-made sources, e.g., radio transmitters or airplanes. Thus, it varies in time which complicates to differentiate between radio signals induced by air showers and background noise. Hence, it makes sense to improve the signal-to-noise (SNR) ratio before triggering on the recorded radio trace in a first step. In a second step, the present noise situation from the monitoring triggers should be taken into account to set the trigger threshold level.

Narrow-band transmitters are filtered out by notch filters implemented on the FPGA of each radio station resulting in a significant reduction of the noise level of the recorded radio trace [204]. Moreover, a fast-Fourier transform of the radio trace is performed by the FPGA and the frequency spectrum is smoothed by replacing the amplitude at each frequency with the median value of the amplitude in a certain frequency window [204]. The filtered trace is then obtained by an inverse fast-Fourier transform.

The self trigger is applied on the filtered trace and is an advanced signal threshold trigger which is based on the present noise situation at AERA [204]. A level 1 trigger (L1) is formed by the FPGA if a bandwidth-limited pulse in at least one polarization is observed in the recorded voltage trace. Several radio stations of AERA are equipped with one or two additional scintillator counters. In these stations, alternatively to the L1 trigger from the self trigger, an L1 trigger is formed if the scintillator counters

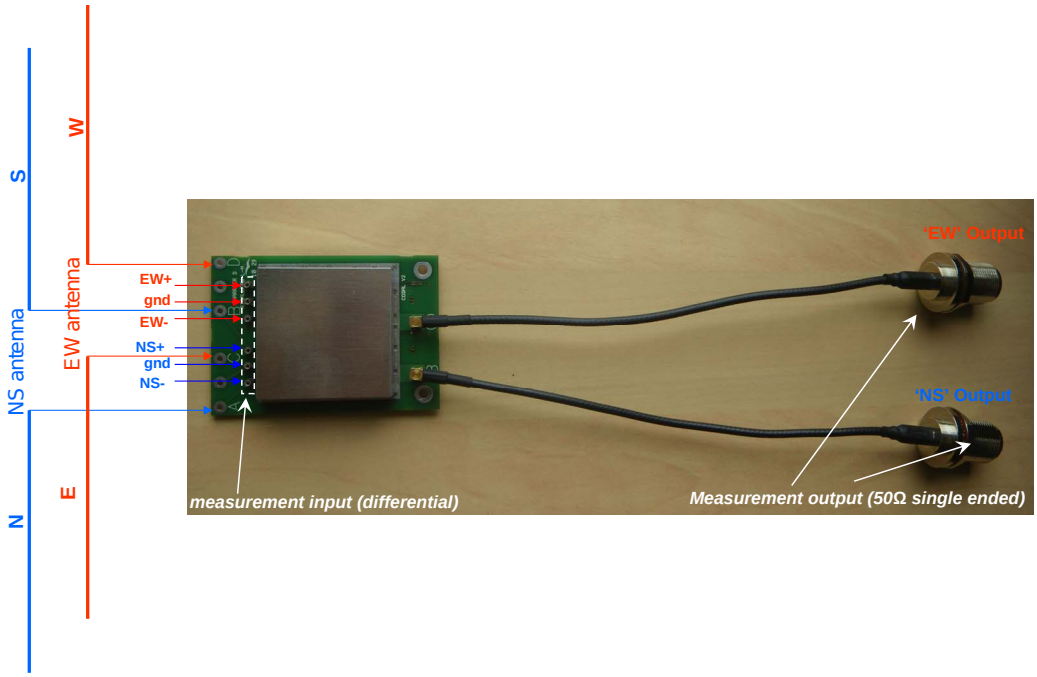

Figure 4.21: *Photo of the low-noise amplifier (LNA) used in the radio stations equipped with Butterfly antennas. Both antenna polarizations of the radio station are connected to one LNA board. The connections of the north-south (east-west) antenna are indicated by the blue (red) marks. Photo from [213].*

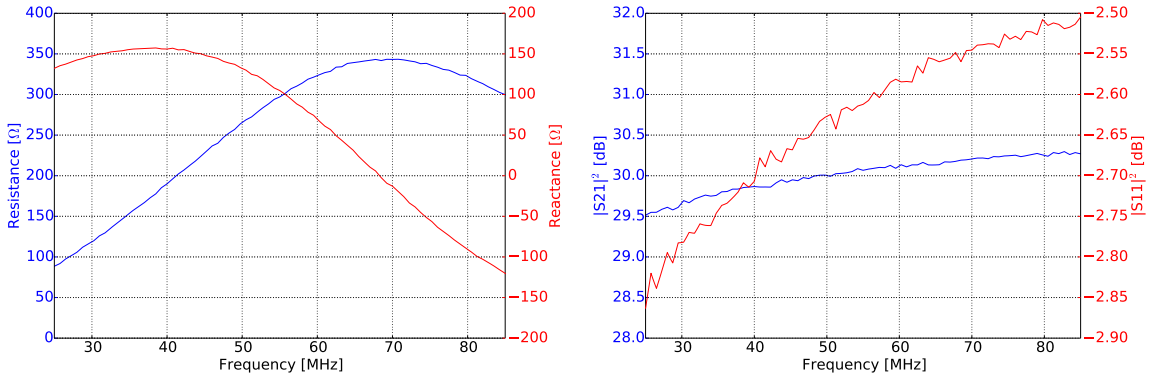

Figure 4.22: ***(left)*** *The low-noise amplifier (LNA) impedance described by the LNA resistance (blue) and the LNA reactance (red) as well as* ***(right)*** *the power gain $|S21|^2$ (blue) and the power reflection at the LNA input port $|S11|^2$ (red) as functions of the frequency. Plots adapted from [203].*

are triggered. Afterwards, the radio trace is time stamped with the information from the GPS receiver at the station by a CPU and is stored in the digitizer memory. A level 2 trigger (L2) is formed containing the time of the recorded trace and the position of the radio station which are then sent to the central DAQ. The typical rate of L2 triggers is in between 1 Hz and 500 Hz [204]. At the DAQ, an algorithm searches for time and spatial coincidences of signals measured in multiple stations. If a coincidence

is found in at least three radio stations, the event time stamp is determined and a level 3 trigger (L3) request is sent back to the radio station containing the event time stamp. Finally, the measured data from each station in a specific time interval around the given event time stamp is sent to the central DAQ, combined to one event, and stored on disk. The typical L3 trigger rate is in between $0.1\,\mathrm{Hz}$ and $50\,\mathrm{Hz}$ [204].

More than 100 radio stations of AERA are utilized with a digitizer containing a $4\,\mathrm{GB}$ ring buffer. The large ring buffer enables saving the recorded trace for about $7\,\mathrm{s}$ and thus allows for an additional external trigger coming from the baseline detectors of the Pierre Auger Observatory. The trigger delay from the SD is about $3\,\mathrm{s}$ and from the FD the delay is at maximum $7\,\mathrm{s}$. In the case of an external trigger, the event decision is performed by the triggers of the baseline detectors so that the position of the radio signal is not accurately known in general. Hence, the full array of stations with ring buffer is then read out. This has the advantage that even events with small signal strength are recorded which are to small too fulfill the self-trigger requirements. However, it has an increased data volume as well as the danger to include stations with noise.

About 40 radio stations of AERA are equipped with one or two additional scintillator counters instead of having a large ring buffer. The scintillator counters enable detecting secondary particles directly at the radio station. Thus, the time delay between the particle and radio detection technique is reduced and a large ring buffer is not needed for an external trigger. Radio stations equipped with scintillator counters are a possible design of future stand-alone radio arrays. However, the scintillator counters have a limited field of view. In the radio stations of AERA, they are horizontally aligned which leads to a reduced detector efficiency for horizontal air showers.

Despite the prefiltering of noise, there are still a significant number of noise events in the recorded data. Several methods have been developed to reject such noise events. One class of noise pulses is created by the Argentinian power grid. These noise pulses show a periodicity of $100\,\mathrm{Hz}$ which is twice the power grid frequency and are removed from the trace [204].

Typically, man-made noise originates from the horizon. To veto events originate from known noise sources, a first reconstruction of the arrival direction is performed by the DAQ using the information of the GPS time stamps and the positions of the involved stations. A planar wave moving with the speed of light is fitted to the data which enables reconstructing the arrival direction in a fast manner to keep up with the event rate but still is accurate enough for the veto purpose. The event is rejected if the reconstructed arrival direction matches to directions of known noise sources [204].

A further method to identify noise sources is performed by a simple algorithm analyzing the trigger time between two stations. The time difference is expected to be constant for noise sources. Dynamic histograms of a certain number of past entries are created by the DAQ and the obtained distribution is compared to the expected distribution from cosmic rays [204, 214].

Moreover, noise signals are identified by a so-called cone algorithm [159, 215]. The event is rejected if signals arrive repeatedly from a constant direction with an opening angle of $5\,^{\circ}$ within a $10\,\mathrm{min}$ time window [214].

At AERA, two different kinds of monitoring triggers are implemented. Firstly, a periodic trigger is formed each $100\,\mathrm{s}$ and the full array is read out. Secondly, for the radio stations containing a ring buffer every 999^{th} L1 trigger and for the stations without ring buffer every $40\,000^{\mathrm{th}}$ L1 trigger is stored. From these monitoring data, important information about the detector status is obtained, e.g.,

the current noise level at each station as well as the detector uptime. Furthermore, the data from the monitoring triggers can be used for a relative calibration between the radio stations [216] as well as for an absolute calibration of the radio stations by analyzing the radio emission from the Galaxy [34, 217, 218].

4.3.5 Detector Calibration

A relative time calibration between the radio stations is obtained by using a beacon reference transmitter which is installed at the FD building Coihueco. The beacon transmitter continuously emits four sharp sine waves at $58.887\,\mathrm{MHz}$, $61.523\,\mathrm{MHz}$, $68.555\,\mathrm{MHz}$, and $71.191\,\mathrm{MHz}$ which are mainly detectable in the north-south polarized antenna of each radio station. From the known distance between each station to the beacon transmitter and the recorded phase differences between the beacon signals, the timing of the radio stations can be corrected for GPS drifts which results in a timing precision of better than $2\,\mathrm{ns}$. The beacon method has been crosschecked by a second time-calibration method. The radio stations are calibrated using information emitted by commercial airplanes flying above the AERA array. On the one hand, airplanes emit radio emission in the AERA frequency range. On the other hand, their position is transmitted by an ADS-B signal at around $1000\,\mathrm{MHz}$ which enables comparing the reconstructed position from radio data with the real airplane position. For that purpose, the cone algorithm to avoid repeated signals from constant directions has been optimized. For more information about the beacon transmitter and the airplane calibration method refer to [202].
For analyzing data of cosmic-ray induced air showers, the frequency and directional-dependent detector sensitivity has to be known which can be calculated by simulations and is obtained in an absolute calibration. Several calibration campaigns have been performed using different calibration methods [152, 203, 212, 218]. A new improved absolute calibration of the LPDA-equipped radio stations is part of this thesis. A new setup was used which enables a much more dense sampling of the arrival directions, more field polarization measurements, and an extended control of systematic effects including the full repetition of calibration series. The simulated LPDA response pattern is described in Chap. 7 and the calibration campaign is presented in Chap. 8.

4.3.6 Radio Event Reconstruction

For the reconstruction of radio data, the Auger software framework $\overline{\text{Off}}\,\underline{\text{line}}$ [219] is used. $\overline{\text{Off}}\,\underline{\text{line}}$ is a modular software framework written in C++ and originally developed for data analysis of the Auger baseline detectors. Additional functionalities have been implemented to enable data analysis of the muon detectors of AMIGA as well as of AERA [220]. Thus, $\overline{\text{Off}}\,\underline{\text{line}}$ allows comprehensive data analyses of cosmic-ray induced air showers measured with different detection techniques. Furthermore, information about the time-varying detector status, e.g., due to hardware replacements or bad periods, are automatically taken into account, environmental conditions measured by several atmospheric monitoring systems are considered, and the Earth's magnetic field for each position and time is implemented according to the International Geomagnetic Reference Field [221] which is important for radio analyses as the radio emission of air showers highly depends on the Earth's magnetic field.
The measurement of radio emission of air showers enables investigating radio physics of EAS as well as determining primary cosmic-ray properties, e.g., arrival direction and energy. The reconstruction

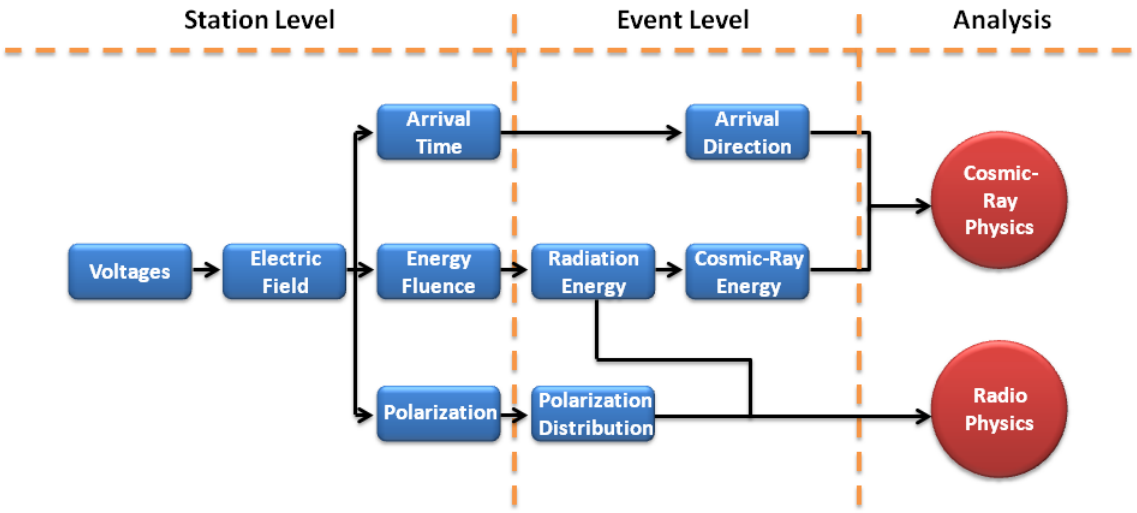

Figure 4.23: *Principle sketch of radio and cosmic-ray physics using radio antennas for air shower experiments.*

steps on station level as well as on the combined information of multiple stations forming the event level are sketched in Fig. 4.23 and are explained in the following.

Due to radio emission generated by an air shower, a voltage trace is induced in both antennas in each radio station which is then recorded at the digitizer and measured in ADC counts. The recorded ADC counts per time are calibrated to a voltage trace $U(t)$ [206]. Afterwards, the voltage trace is corrected for the frequency-dependent influence of the full signal chain of the radio station from the digitizer to the antenna footpoint so that the voltage that has been induced into the antenna is obtained. Then, the station timing depending on the GPS clocks of the stations is corrected by using the information from the reference beacon transmitter (cf. Sec. 4.3.5) [202]. As the noise varies in time, a complex method to suppress mono-frequent noise is applied by fitting sine waves to the voltage trace [222, 223]. From these fits, amplitudes, frequencies, and phases of noise sources are obtained and the noise can be removed from the trace. A Fourier transformation is performed and continuous noise signals from known sources such as the beacon frequencies are filtered out.

From the corrected voltage in the Fourier space, the electric-field as function of the frequency is reconstructed by using the information about the antenna response pattern in terms of the VEL as described in Sec. 3.8. By performing an inverse Fourier transformation, the electric field trace is obtained. In Fig. 4.24, the corrected voltage traces and the reconstructed electric-field traces are shown for an example event. For each electric-field trace of each polarization, the Hilbert envelope is calculated and quadratically summed. From the Hilbert envelope of the electric field several physical quantities are obtained enabling investigating radio physics of the EAS as well as reconstructing properties of the primary cosmic ray which are briefly described in the following.

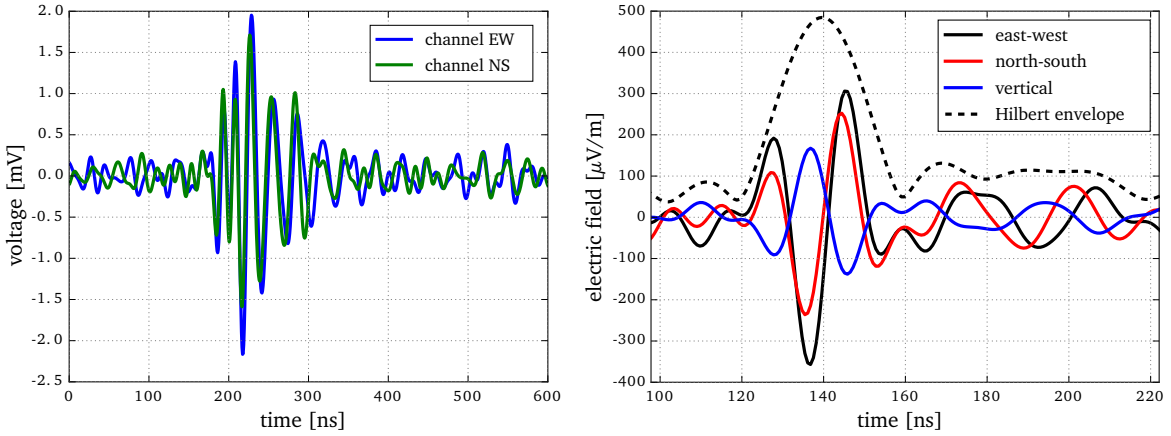

Figure 4.24: *Radio signal of a cosmic-ray induced air shower having an energy of* $1.14 \cdot 10^{18}$ eV*, with a zenith angle of* 30° *and an azimuth angle of* 14° *south of east measured in one of the radio stations equipped with LPDAs.* ***(left)*** *Voltage traces measured in both horizontal polarizations. The ADC calibration factor as well as signal chain and background noise corrections are already considered.* ***(right)*** *Reconstructed electric field in Cartesian coordinates and the corresponding Hilbert envelope. Plots adapted from [30].*

Arrival Direction

The position of the maximum of the combined Hilbert envelope marks the arrival time of the signal. Combining the information about the arrival time of multiple stations with signal, the arrival direction of the primary cosmic ray can be reconstructed. It depends on the shape of the radio signal [159, 224, 225]. Different model types of the shower front such as a planar, a spherical and a conical wavefront are sketched in Fig. 4.25. A good estimation of the shower shape is a hyperbola which means that it is described by a spherical wavefront close to the shower axis and at larger distances the shape is described by a conical wavefront [226, 227]. From the assumptions of the different shower fronts, the expected arrival time t_i of the signal at each station i is calculable:

$$\begin{aligned} t_i^{\text{planar}} &= -\frac{\vec{n}(\theta,\phi)\cdot\vec{d_i}}{c} \\ t_i^{\text{spherical}} &= \frac{|\vec{R}(R,\theta,\phi)-\vec{d_i}|}{c} \\ t_i^{\text{conical}} &= \frac{|\vec{h}(\rho,\theta,\phi,\vec{d_i})|-\vec{n}(\theta,\phi)\cdot\vec{d_i}}{c} \end{aligned} \tag{4.8}$$

with the incoming direction $\vec{n}(\theta,\phi)$ described by the zenith angle θ and the azimuth angle ϕ, the distance of the i-th radio station to the shower core $\vec{d_i}$, the speed of light c, the position of the signal source $\vec{R}(R,\theta,\phi)$ and the offset of the conical shower front compared to the planar shower front $|\vec{h}(\rho,\theta,\phi,\vec{d_i})|$ which depends on the opening angle ρ of the cone. The easiest model is to assume a planar wave front moving with the speed of light. Then, the signal source is placed in infinite distance. In this case, the arrival time only depends on the azimuth and zenith angle and at least three stations with signal are needed to reconstruct the arrival direction. The assumption of a planar shower shape is just a rough estimation and the arrival direction is reconstructible with a resolution on the degree

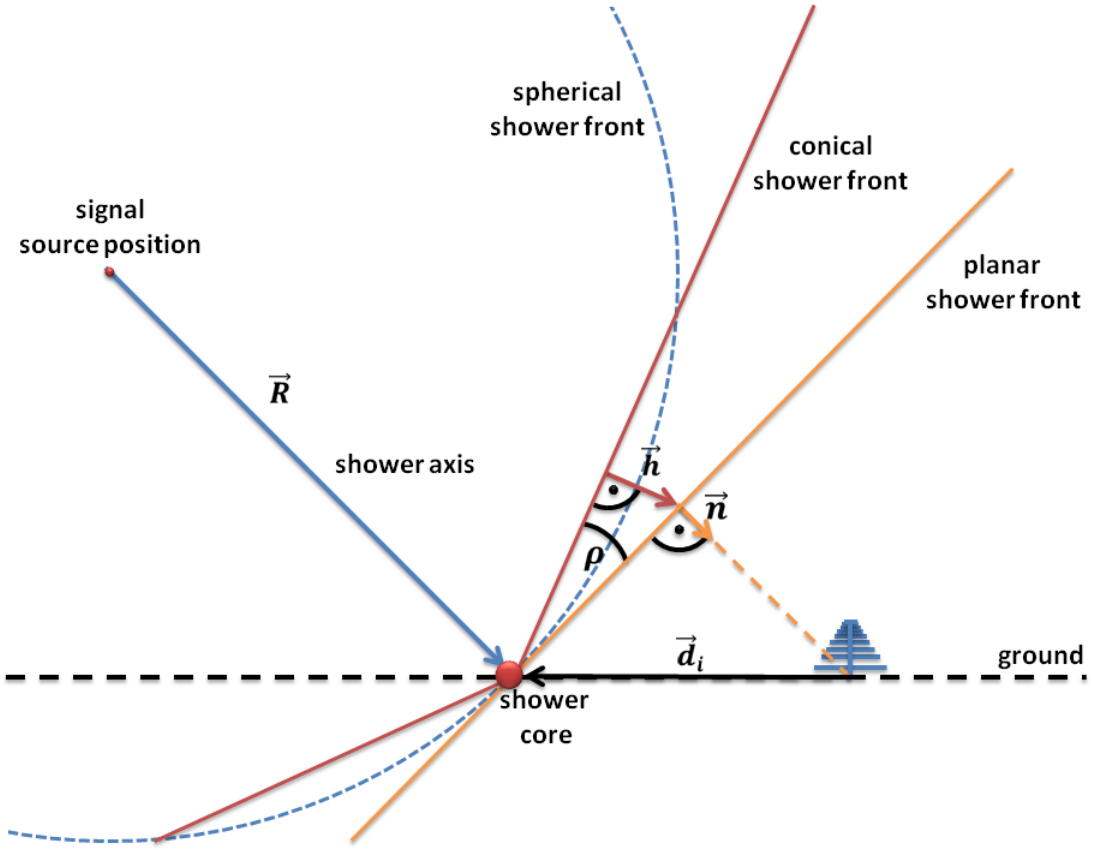

Figure 4.25: *Sketch of different models of the shower front such as a planar (orange solid line), a spherical (blue dashed line) and a conical (red solid line) wavefront. Picture adapted from [30].*

level. A more complex model such as the spherical or conical wave front exhibits a better description of the shower shape. Nevertheless, the fit of the arrival direction using a complex shower-front model gets more difficult compared to those using a planar shower front. In the case of the spherical shower front at least four and in the case of a conical shower front a large number of radio stations with signal are needed to perform the reconstruction. In $\overline{\text{Off}}$ $\underline{\text{line}}$, these different shower fronts are implemented and are usable for data analyses. The reconstruction starts with fitting the simplest model of a planar wave front and then the fit is enhanced by adding the additional parameters of the more complex shower front model. If the more complex fit fails, the simpler shower front model is used for the reconstruction. In Fig. 4.26, the arrival directions of 126 events measured with the radio stations of AERA24 are presented. A clear north-south asymmetry is visible. The asymmetry stems from the fact that the signal strength of the dominant geomagnetic emission process scales with $\sin(\alpha)$ where α is the angle between the arrival direction and the Earth's magnetic field and thus is maximal if arrival and magnetic-field direction, are perpendicularly aligned.

Polarization Distribution

Besides the arrival direction, the electric-field polarization is reconstructed from the Hilbert envelope. It is found that the electric-field polarization in the full width half maximum (FWHM) of the Hilbert

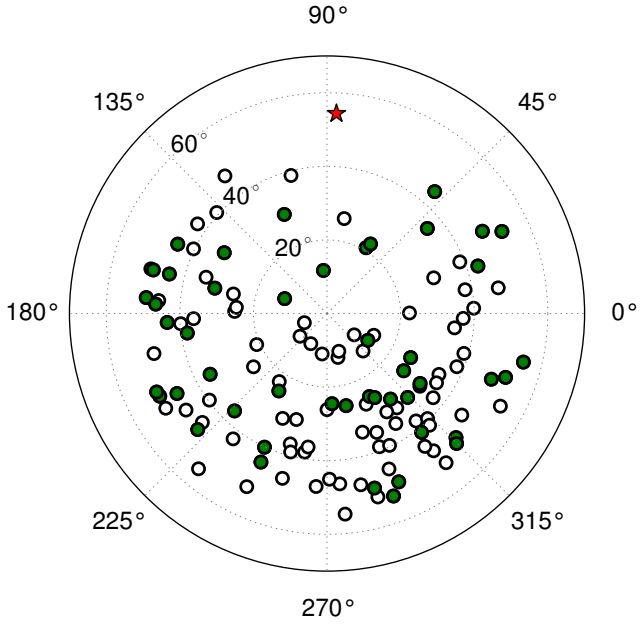

Figure 4.26: *Arrival directions of* 126 *events measured with the radio stations of AERA24. The radial axis denotes the zenith angle and the polar axis indicates the azimuth angle respectively. The green circles mark events with at least five station with signal and the red star indicates the magnetic-field direction at AERA. Plot taken from [25].*

envelope from EAS is nearly constant in contrast to those from noise [203]. To improve the precision of the electric-field polarization, the electric-field vector $\vec{E}(t)$ is determined for each time bin t in the FWHM of the Hilbert envelope and is then averaged to the combined electric-field vector to describe the electric-field polarization. The determination of the polarization distribution from measurements in multiple radio stations enables probing the radio emission processes (cf. Sec. 2.4.2). In the geomagnetic emission process, charged particles are deflected in the Earth's magnetic field forming a moving dipole and a signal polarized according to the Lorentz force described by $\vec{e}_{\mathrm{geo}}$. Thus, polarization due to the geomagnetic emission process only depends on the arrival direction and is constant for all radio stations. In contrast, in the charge-excess emission process secondary particles knock out electrons of the air molecules. Furthermore, positrons partly annihilate in the atmosphere which leads to a time-varying negative charge excess in the shower front forming a dipole along the shower axis and a radially polarized signal described by $\vec{e}_{\mathrm{ce}}$. Thus, the electric-field polarization due to the charge-excess emission process depends on the observer position. The complete radio signal $\vec{E}$ is a superposition of both processes:

$$\vec{E} \propto \sin(\alpha)\, \vec{e}_{\mathrm{geo}} + a\, \vec{e}_{\mathrm{ce}} \tag{4.9}$$

with the angle α between the arrival direction and the Earth's magnetic field, and the relative strength of the charge-excess emission process a. The relative strength of the charge-excess emission process has been measured using the radio stations of AERA24. From signal polarization measurements the average strength of the charge-excess emission process has been determined to $a = 0.14 \pm 0.02$ [20] which has already been presented in Fig. 2.13 of Sec. 2.4.2.

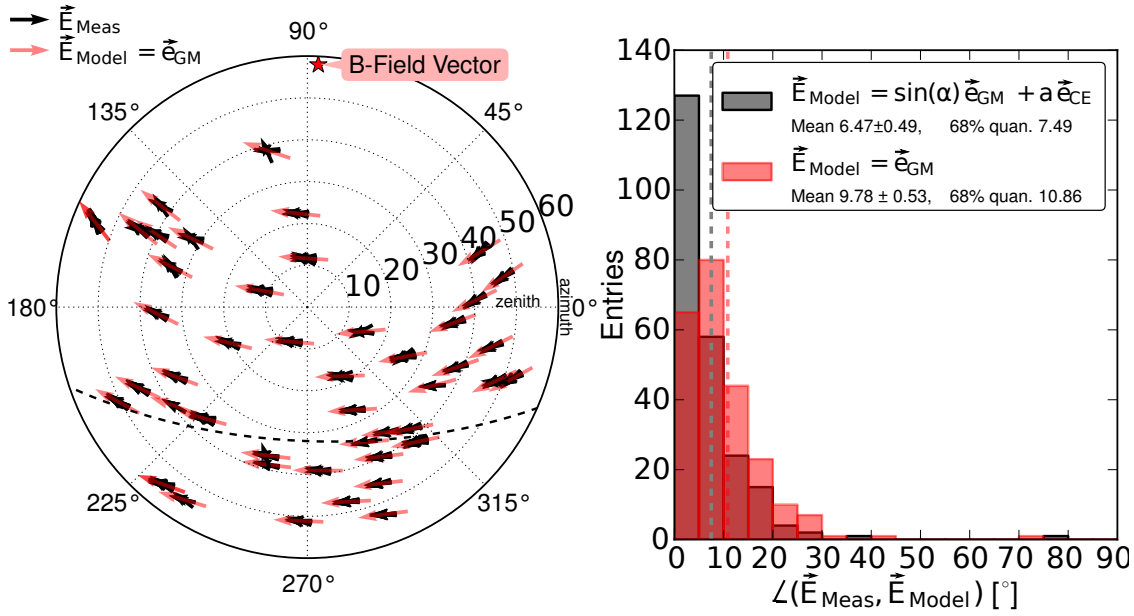

Figure 4.27: ***(left)*** *Sky map of the arrival directions of* 47 *events measured with the radio stations of AERA24. The black arrows indicate the horizontal component of the measured electric-field polarization in an underlying Cartesian coordinate system. Note that there are at least three measurements per event. The red arrows indicate the expectation from the geomagnetic emission process. The red star marks the Earth's magnetic field at AERA.* ***(right)*** *Histogram of the angle between the measured and expected electric-field vector from a model with (black) and without (red) the charge-excess component included. Plots taken from [203].*

In a further analysis, the polarization of 47 events measured in the radio stations of AERA24 has been investigated and compared to an electric-field model based on the geomagnetic emission process first before adding the charge-excess component [203]. On the left side of Fig. 4.27, a sky map of the event arrival directions is shown where the measured polarization is compared to the expectation from the geomagnetic emission process while both are projected to the horizontal component. Both the measured and the predicted polarization agree in a first approximation which confirm that the geomagnetic emission process is the dominant emission process. On the right side of Fig. 4.27, the angles between the measured and modeled electric-field vector with and without adding an average charge-excess component of 14 % are histogramed. A better agreement between measurement and model is achieved if the charge-excess component is included in the model which confirms the presence of the charge-excess emission process.

Radiation and Cosmic-Ray Energy

From the Hilbert envelope of the reconstructed electric field of the air shower $\vec{E}(t)$, the radio energy fluence f_i at station i is determined which describes the amount of energy transferred from the cosmic-ray energy into the radio emission per area. It is determined by calculating the time integral of the absolute value of the Poynting vector. The integral is calculated in the signal windows defined in a range of $\pm 200\,\mathrm{ns}$ around the arrival time t_i which edges are denoted by t_1 and t_2. Background noise is taken into account by subtracting a time integral in a noise window $[t_3, t_4]$ which is normalized to

the same size as the signal window from the signal [30]:

$$f_i = \epsilon_0 c \left(\Delta t \sum_{t_1}^{t_2} |\vec{E}(t)|^2 - \Delta t \frac{t_2 - t_1}{t_4 - t_3} \sum_{t_3}^{t_4} |\vec{E}(t)|^2 \right) \tag{4.10}$$

with the vacuum permittivity ϵ_0, the speed of light c, and the size of the time bin Δt. From the combination of the energy fluence measured in multiple stations, the lateral energy-fluence distribution of the air shower is obtained. The superposition of the signal strength from the geomagnetic component and from the charge-excess component leads to destructive and constructive interference effects (cf. Sec. 2.4.2) and therefore to an azimuthal asymmetry in the lateral distribution of the radio energy fluence. The energy fluence distribution is described by a two-dimensional lateral distribution function (LDF) [228, 229] taking into account asymmetries resulting from the two emission processes. The LDF shape is best understood within the shower plane with one axis perpendicular to the shower direction $\vec{v}$ and the Earth's magnetic field $\vec{B}$: $\vec{v} \times \vec{B}$, and the perpendicular axis: $\vec{v} \times (\vec{v} \times \vec{B})$. On the left side of Fig. 4.28, the energy fluence distribution of a measured cosmic-ray induced air shower and the corresponding LDF fit are presented. From the integral of the LDF over the area, the radio energy estimator of the primary cosmic ray is obtained which is called the radiation energy. The radiation energy describes the amount of energy which is transferred from the primary cosmic ray into the radio emission of the air shower. The radiation energy is corrected for the geometric dependence of the geomagnetic emission by dividing by $\sin^2(\alpha)$ where α is the angle between $\vec{v}$ and $\vec{B}$ so that different emission strengths due to different angels α are taken into account. On the right side of Fig. 4.28, the corrected radiation energies of 126 air showers are shown, measured with the radio stations of AERA24 and cross-calibrated with the well-understood data of the surface detector of the Pierre Auger Observatory. It is found that from a $10^{18}\,\mathrm{eV}$ cosmic ray an energy of about $(15.8 \pm 0.07) \cdot 10^6\,\mathrm{eV}$ is transferred into radio emission and the observed radiation energy scales quadratically with the cosmic-ray energy [24, 25]:

$$E^{\mathrm{Auger}}_{30-80\,\mathrm{MHz}} / \sin^2(\alpha) = (15.8 \pm 0.7) \cdot 10^6\,\mathrm{eV} \left(\frac{\mathrm{E_{CR}}}{10^{18}\,\mathrm{eV}} \right)^{1.98 \pm 0.04} . \tag{4.11}$$

The AERA energy resolution has been determined to 22 % which improves to 17 % for events with at least five stations with signal. The systematic uncertainty of the cosmic-ray energy reconstruction is 14 %.

In the previous discussion, the radiation energy is calibrated using the information of the baseline detectors of the Pierre Auger Observatory. Instead, the energy calibration can be done by using the theoretical prediction of the radiation energy which allows to determine the cosmic-ray energy scale using the AERA detector. The idea is illustrated on the left side of Fig. 4.29. The procedure to determine the radiation energy is divided into an experimental part, as explained beforehand, and a theoretical part. The radio emission primary originates from the electromagnetic part of the air shower and thus can be calculated from first principles using classical electrodynamics (cf. Sec. 2.4.2). As soon as the creation of radio emission stops at the end of the air-shower development, the radiation energy stays constant because the Earth's atmosphere is essentially transparent for radio waves in the very-high-frequency (VHF) band. Thus, measurement and theoretical prediction of the radiation en-

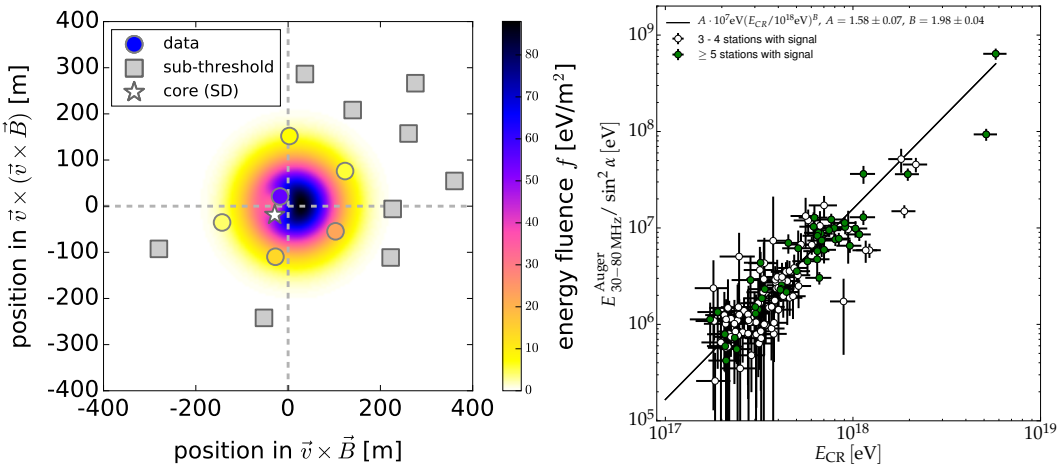

Figure 4.28: ***(left)*** *Energy fluence for an extensive air shower with an energy of* $4.4\cdot10^{17}$ eV *and a zenith angle of* 25° *measured with multiple radio stations of AERA (colored circles). The center indicates the shower core reconstructed with the radio data. The colored background illustrates the energy fluence obtained by a fit of a two-dimensional lateral distribution function (LDF). The white star marks the shower core reconstructed using the surface detector (SD) data of the Pierre Auger Observatory.* ***(right)*** *The corrected radiation energy in relation to the cosmic-ray energy measured with the SD. Events with* 3 *and* 4 *radio stations with signal are marked as white circles and in case of more than* 5 *radio stations with signal are marked as green circles. Plots taken from [24, 25].*

ergy are directly comparable. For a detailed discussion about the theoretical part refer to [29].
The CoREAS simulation code [28] is used to simulate air showers and their radio emission. CoREAS is a microscopic simulation code, where the radiation of each single particle is calculated by first principles of classical electrodynamics, and then superposed to the full radio emission. As the emission originates from the electromagnetic part of the air shower, the radiation energy correlates best with the energy of the electromagnetic cascade. In addition to the geometric dependence of the geomagnetic emission process, a second dependence on the air density at the shower maximum was identified and parametrized. This corrected radiation energy is presented as a function of the energy in the electromagnetic cascade on the right side of Fig. 4.29. A quadratic relation with a scatter of less than 3 % is observed [29]. To obtain the cosmic-ray energy from the electromagnetic shower energy, the invisible energy needs to be taken into account, e.g., neutrinos and high-energy muons rarely contributing to the radiation energy. This can be done using a parametrization that was obtained from measurements [142].
The currently estimated systematic uncertainties with respect to the cosmic-ray energy are briefly discussed in [30]. The uncertainty from the antenna calibration of the radio detector is identified as the dominant uncertainty of the cosmic-ray energy measurement. The antenna calibration and a thorough description of its uncertainties are part of this thesis and discussed in the following chapters.

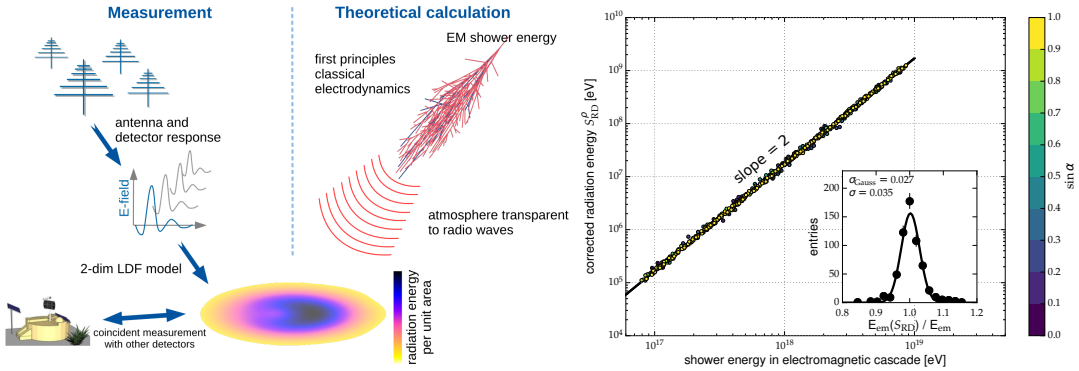

Figure 4.29: ***(left)*** *Idea of the determination of the energy scale from first-principles calculations using radio measurements. Picture taken from [30].* ***(right)*** *The corrected radiation energy estimator vs. the energy in the electromagnetic cascade from CoREAS simulations. Color coded is* $\sin\alpha$ *where* α *is the angle between the incoming direction and the Earth's magnetic field. Plot adapted from [29].*

5

Measurement of the LPDA Low-Noise Amplifier Temperature Dependency

One of the challenges measuring cosmic-ray induced air showers at AERA are the varying local weather conditions. AERA is located in a region with large temperature variations also during the day. Changes in temperature of more than $20\,^{\circ}\mathrm{C}$ are not uncommon. Fluctuations in temperature have a direct influence on the radio station electronics, e.g., the electric properties of the low-noise amplifier (LNA), filters, and amplifiers. This directly impacts the recorded signal strength of the corresponding radio signals and thus the reconstructed cosmic-ray properties. As the LNA is included in the absolute detector calibration, its temperature dependency is of great interest (refer to Chap. 8) with respect to the calibration uncertainties. The temperature dependency of the LPDA LNA power gain $|S21|^2$ has been determined which is presented in this chapter. The chapter is structured as follows. In Sec. 5.1, the measurement setup is explained, an example measurement is presented in Sec. 5.2 and the measurement results are finally presented in Sec. 5.3.

5.1 Measurement Setup

The temperature dependency of the LNA gain has been determined using a temperature-adjustable and PC-controlled fridge. The fridge has originally been developed at the RWTH Aachen University to perform temperature dependent measurements of silicon photomultiplier. For detailed technical information concerning the fridge refer to [230]. A schematic view of the setup is shown in Fig. 5.1. The LNA was placed in the fridge and connected via coaxial cables to a vector network analyzer (VNA). Transmission measurements were performed while different temperatures are adjusted. The VNA is located outside the fridge to avoid temperature drifts stemming from the VNA itself. An FSH4 vector network analyzer from the company Rohde&Schwarz [231] is used for the measurements providing a signal of $0\,\mathrm{dBm}$ strength sweeping each second through the whole frequency range and a readout impedance of $50\,\Omega$. The manufacturer states an uncertainty of $0.05\,\mathrm{dB}$ for transmission measurements. The full signal chain from FSH4 to the LNA is calibrated out so that only the LNA power gain $|S21|^2$ is measured. The temperature within the fridge is set using a PC and is measured using eight SHT10 temperature sensors from the manufacturer Sensirion [232]. The manufacturer states a typical temperature uncertainty of $0.5\,^{\circ}\mathrm{C}$. The temperature is sampled with a rate of about $0.2\,\mathrm{Hz}$. The data of the temperature sensors and of the FSH4 are stored on the PC. One of the temperature sensors is located close to the LNA which is used to determine the ambient temperature at the LNA. The fridge enables performing the measurements in a wide temperature range. Pictures of the setup are shown in Fig. 5.2.

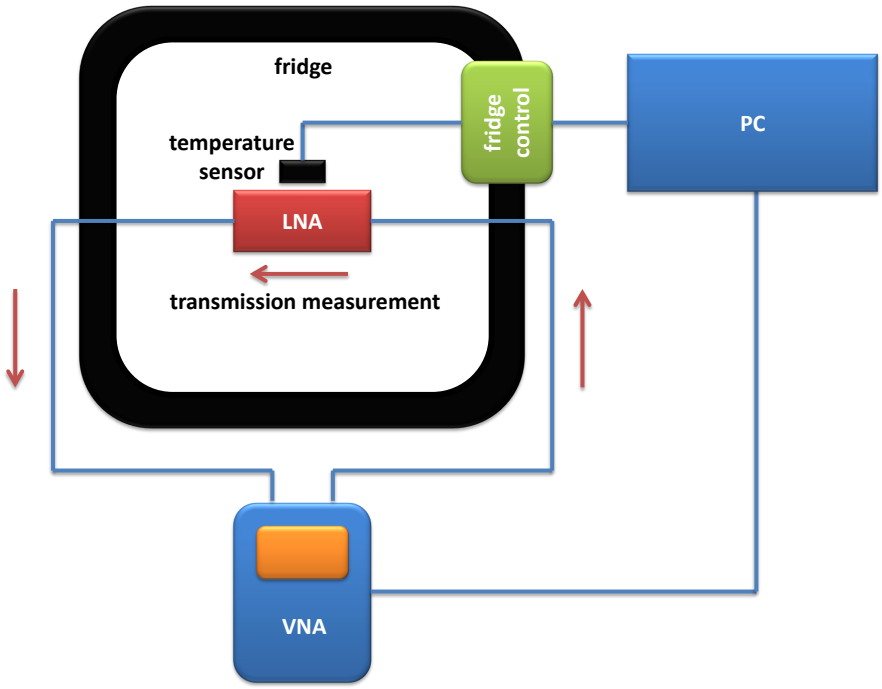

Figure 5.1: *Schematic view of the setup to measure the temperature dependency of the low-noise amplifier (LNA) gain using a PC-controllable fridge. The LNA is placed in the fridge and connected via coaxial cables to a vector network analyzer (VNA). Transmission measurements are performed while different temperatures are set. The temperature is measured by a temperature sensor placed close to the LNA. A PC is used to control the temperature in the fridge and to store the data from the temperature sensor and the VNA.*

5.2 Example Measurement

In the following, one example measurement of one LNA is presented. The measurement of the LNA power gain $|S21|^2$ has been done for temperatures ranging from about $8\,^\circ\mathrm{C}$ to about $45\,^\circ\mathrm{C}$ and was performed over more than two days. The fridge has been heated to approximately $45\,^\circ\mathrm{C}$ first. Then, the measurement has been started and the temperature has been reduced in steps of $2\,^\circ\mathrm{C}$ to approximately $8\,^\circ\mathrm{C}$. Afterwards, the temperature has been increased in steps of $2\,^\circ\mathrm{C}$ to approximately $41\,^\circ\mathrm{C}$ again. Thus, a positive as well as a negative temperature gradient have been taken into account. The temperature measured close to the LNA as a function of time is shown on the left side of Fig. 5.3. At each $2\,^\circ\mathrm{C}$-step in temperature, a small oscillation around the new set temperature is visible until the temperature stays constant. This effect can negatively influence the measurement resolution if the time window of the temperature oscillation is small compared to the reaction time of the LNA. On the right side of Fig. 5.3, the LNA power gain $|S21|^2$ as a function of the frequency for three different temperatures of $T = 8.0\,^\circ$, $T = 18.6\,^\circ$, and $T = 38.5\,^\circ$ is shown exemplary. The LNA exhibits a typical power gain of $|S21|^2 = 18\,\mathrm{dB}$ in the frequency range from $30\,\mathrm{MHz}$ to $80\,\mathrm{MHz}$ (cf. Sec. 4.3.2). Additionally, from these measurements a temperature dependency of the LNA gain is suggested: The higher the temperature, the lower is the LNA gain.

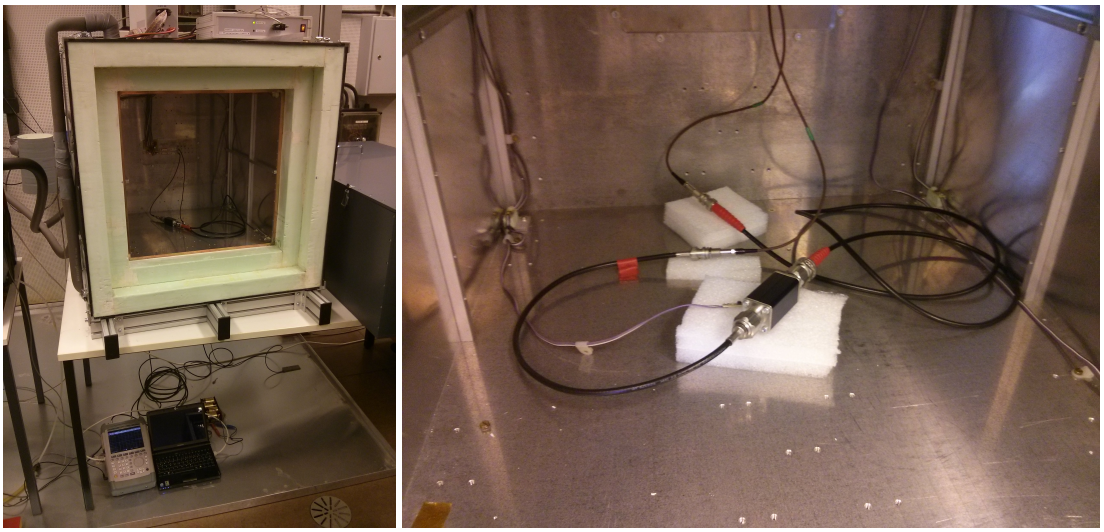

Figure 5.2: *Pictures of the low-noise amplifier placed inside the fridge.*

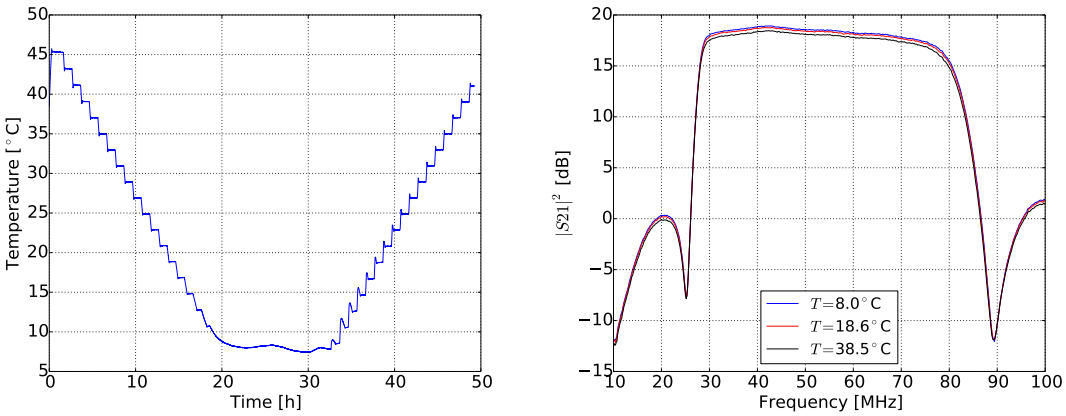

Figure 5.3: ***(left)*** *Temperature measured using the temperature sensor located close to the low-noise amplifier (LNA) as a function of time.* ***(right)*** *LNA power gain $|S21|^2$ as a function of the frequency for three different temperatures of $T = 8.0\,^{\circ}\mathrm{C}$, $T = 18.6\,^{\circ}\mathrm{C}$, and $T = 38.5\,^{\circ}\mathrm{C}$.*

5.3 Results of the Measurement

A deeper quantification of the temperature dependency has been performed. The temperature drift of the LNA power gain is analyzed for each measured frequency. In Fig. 5.4, the LNA power gain $|S21|^2$ as function of the temperature measured at 55 MHz is shown exemplary. The power gain decreases with the temperature. A function $y = a \cdot x + b$ with two fit parameters a and b is fit to the data. The temperature drift of the LNA power gain is described by the slope a of the fit which is $a = -0.017\,\mathrm{dB/K}$ at 55 MHz.

The slope a has been determined for all measured frequencies and is presented on the left side of Fig. 5.5. In general, the fits exhibit a nearly constant slope for frequencies ranging from 30 MHz to 80 MHz. On the right side of Fig. 5.5, all fit slopes in the mentioned frequency region are histogramed.

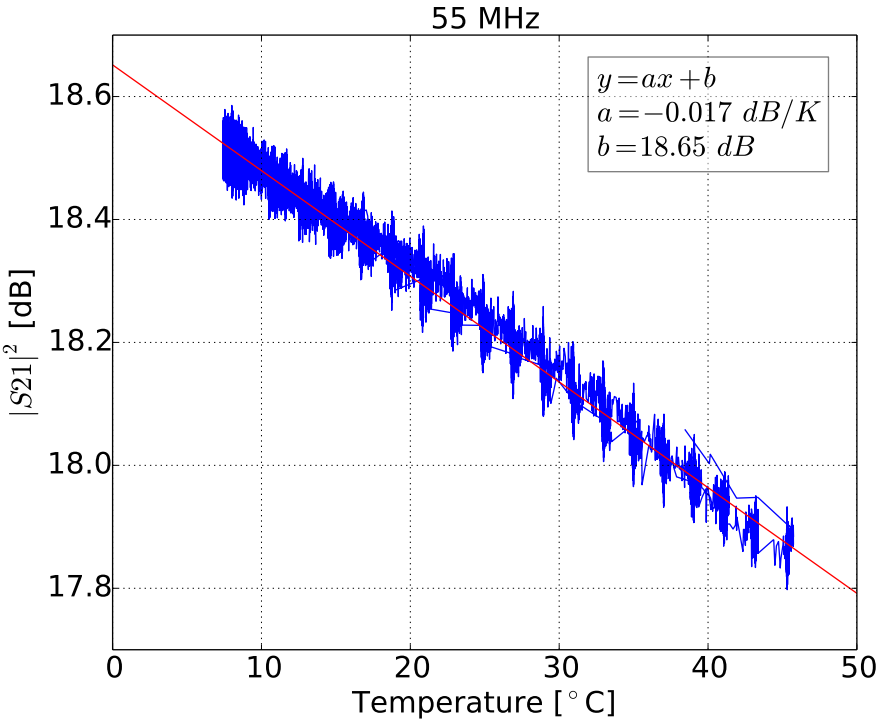

Figure 5.4: *Power gain $|S21|^2$ of the low-noise amplifier as a function of the temperature at $55\,\mathrm{MHz}$ (blue line). The red line indicates the linear fit to the measured data.*

The temperature dependency of the LNA power gain $|S21|^2$ is determined to be $a = -0.017\,\mathrm{dB/K}$ in the median. The measurements show fluctuations of the LNA power gain of typically less than $0.1\,\mathrm{dB}$. The measurement has been repeated for another LNA in an independent measurement and similar results have been determined which are presented in the appendix A.

As an additional cross check, the influence of the temperature gradient on the temperature dependency of the LNA power gain has been investigated. The measurement discussed beforehand is split in two samples of same size resulting in two data samples one with a falling and one with a rising temperature gradient (compare to left plot of Fig. 5.3). The analysis is repeated for both data samples. The new slopes are histogramed for all frequencies from $30\,\mathrm{MHz}$ to $80\,\mathrm{MHz}$ for both data samples respectively. The resulting histograms of a are presented in Fig. 5.6. The median values are in good agreement with the result from the whole measurement presented in Fig. 5.5. From this, it is concluded that hysteresis effects are negligible small.

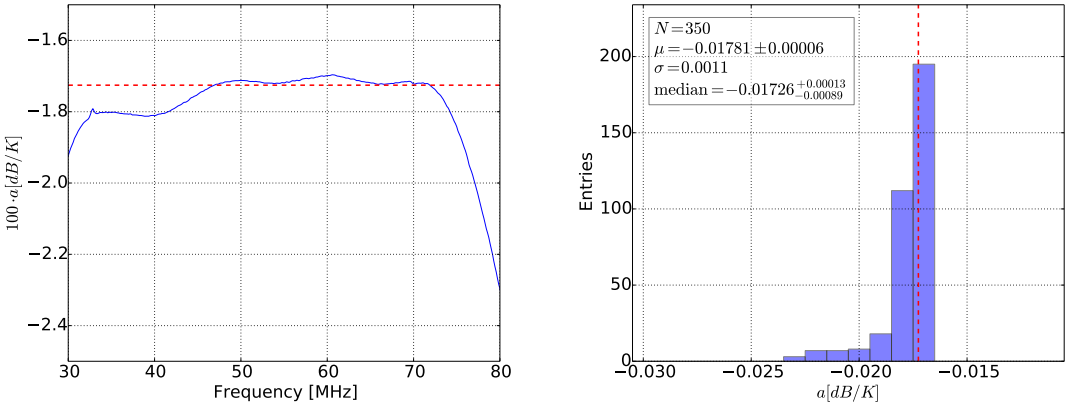

Figure 5.5: ***(left)*** *Temperature dependency slope a of the low-noise amplifier power gain as a function of the frequency.* ***(right)*** *Histogram of a in the frequency range from* 30 MHz *to* 80 MHz*. The red dashed line marks the median value in both plots.*

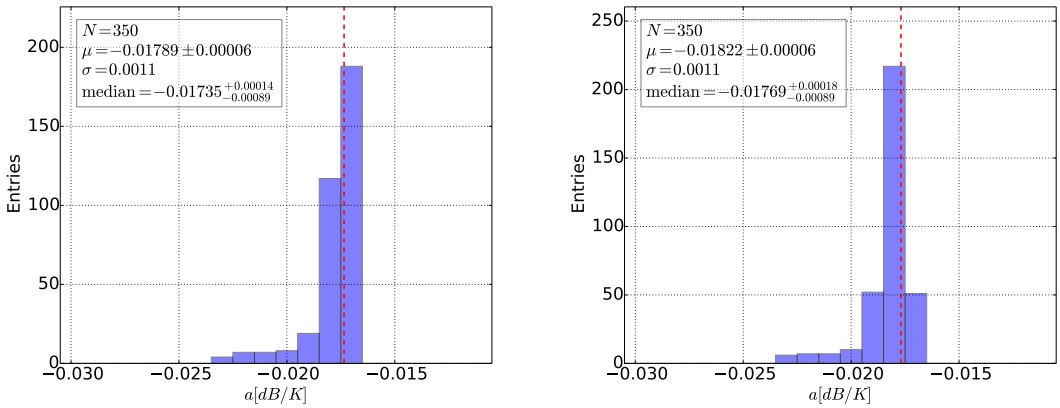

Figure 5.6: *Histograms of the slope a of the temperature dependency of the low-noise amplifier power gain in the frequency range from* 30 MHz *to* 80 MHz *for the subsample with a falling temperature gradient* ***(left)*** *and with a rising temperature gradient* ***(right)****. The red dashed line marks the median value in both plots.*

6 Relative Permittivity Measurements of Soil from the AERA Site

Both ground permittivity and ground conductivity have a direct influence on the signal reflection on ground. Thus, different ground conditions impact the antenna response pattern depending on the antenna sensitivity to the ground direction. A thorough knowledge of ground permittivity and ground conductivity with respect to the signal frequency as well as their variations, e.g., due to rain fall, is necessary for an accurate description of the frequency-dependent antenna response pattern. From Sec. 3.7, it is known that the signal reflection on ground with typical ground conditions at AERA is most dependent on the ground permittivity. Thus, a focus is put on the investigation of the ground permittivity of soil from the AERA site in this chapter. A measurement setup has been developed to measure the frequency-dependent permittivity of soil from the AERA site using a capacitor. In a measurement campaign, soil samples from the AERA site have been collected and the ground permittivity has been measured in the laboratory with respect to the soil humidity. In a second measurement campaign, the ground permittivity at different positions has been measured directly at AERA to investigate the ground homogeneity at the site.
The chapter is structured as follows: In the first section, the measurement principle is presented and a theoretical overview is given. In Sec. 6.2, calibration measurements are shown in which the relative permittivity of known materials are determined and compared to its literature values. Afterwards, the results of the measurement campaigns are presented in Sec. 6.3. From the combination of the results of both measurement campaigns, typical values of the soil permittivity at the AERA site are achieved.

6.1 Principle of the Permittivity Measurement

In this section, the principle to determine the frequency-dependent relative permittivity of soil is explained. As the electric field within a capacitor is influenced by the dielectric described by its relative permittivity, a capacitor is an ideal instrument to measure the relative permittivity ϵ_r of a dielectric. The dielectric is placed in between the capacitor plates with a plate area A with a distance d between the capacitor plates. To avoid shorting effects, the capacitor plates are enveloped in a thin layer of non-conductive film. Applying an alternating electric field to the capacitor plates then enables to measure the frequency-dependent relative permittivity ϵ_r of the dielectric. A sketch of the setup is shown in Fig. 6.1.
The capacity C of a capacitor is calculated by:

$$C = \epsilon_0 \epsilon_r \frac{A}{d} \tag{6.1}$$

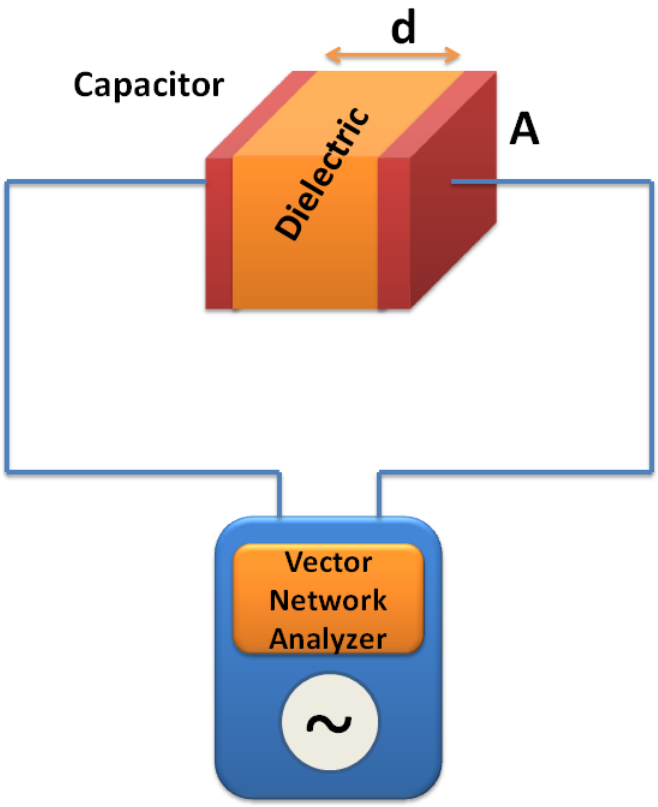

Figure 6.1: *Setup to determine the frequency-dependent relative permittivity of a dielectric using a capacitor with plate size A and a plate distance d applying an alternating electric field produced by a vector network analyzer in a reflection measurement.*

where $\epsilon_0 = 8.854 \cdot 10^{-12} \frac{\mathrm{F}}{\mathrm{m}}$ is the vacuum permittivity. By applying an alternating electric field with a frequency f, the capacitor acts as resistor with a complex impedance $Z_C = R_C + iX_C$. The so-called capacitive reactance X_C is correlated with the capacity of the capacitor:

$$X_C = -\frac{1}{2\pi f C}. \tag{6.2}$$

From a reflection measurement using a vector network analyzer (VNA) the electrical reactance X of the setup is obtained. The setup itself consists of cables and connectors and thus has a constant inductance L resulting in a parasitic inductive reactance X_L:

$$X_L = 2\pi f L. \tag{6.3}$$

Further parasitic conductive terms are expected to be small compared to the capacitive reactance of the capacitor especially at small frequencies. Thus, the electrical reactance X of the setup measured in the reflection measurement is a superposition of the reactance of the capacitor X_C and the parasitic reactance X_L:

$$X = X_C + X_L \tag{6.4}$$

The parasitic inductivity L is obtained from multiple calibration measurements using air as dielectric. The relative permittivity of air $\epsilon_{r,air}$ is close to one and thus close to that of vacuum. Hence, no frequency dependency of $\epsilon_{r,air}$ is expected and thus also no dependency of the capacity C_{air} on the frequency is expected. From these calibration measurements, the resonance frequency of the respective measurements f_{res} is determined. The resonance frequency denotes the frequency where the setup reactance X is equal to zero:

$$X = X_{C_{air}}(f_{\mathrm{res}}) + X_L(f_{\mathrm{res}}) = 0. \tag{6.5}$$

By plugging Eq. (6.2) and Eq. (6.3) in Eq. (6.5), the setup inductance is then obtained by:

$$L = \frac{1}{(2\pi f_{\mathrm{res}})^2 C_{air}} \tag{6.6}$$

For a given plate distance d_{meas}, the capacity C_{air} of the setup using air as dielectric is calculated according to Eq. (6.1) resulting in a setup inductivity of:

$$L = \frac{d_{meas}}{(2\pi f_{\mathrm{res}})^2 \epsilon_0 \epsilon_{r,air} A}. \tag{6.7}$$

The obtained inductivities of the multiple calibration measurements are averaged to the combined inductivity $\overline{L}$ of the setup. The frequency-dependent relative permittivity ϵ_r of different dielectrics is then obtained by combining Eq. (6.1) to Eq. (6.4) resulting in:

$$\epsilon_r = \frac{d}{2\pi f \epsilon_0 A (2\pi f \overline{L} - X)} \tag{6.8}$$

with the distance between the capacitor plates d, the capacitor plate area A, the combined setup inductivity $\overline{L}$, the setup reactance X, and the respective frequency f.

6.2 Test Measurements to Benchmark the Capacitor System

In this section, the principle of determining the frequency-dependent relative permittivity using a capacitor is proven by measuring the relative permittivity of specific materials which is then compared to the respective literature value. Furthermore, the measurement uncertainties are discussed on basis of these calibration measurements. First, the measurement devices and the calibration measurements using air as dielectric as well as its uncertainties are presented and afterwards the determined relative permittivities of different specific materials are shown.

A capacitor with a plate area of $A = 0.09\,\mathrm{m}^2$ is used and the setup reactance is determined from a reflection measurement using an MS46522A VNA from the manufacturer Anritsu [233] with an intrinsic impedance of $Z_S = 50\,\Omega$. The complex reflection coefficient Γ is measured and the setup impedance Z_L is then obtained from Eq. (3.19). The setup reactance X is given by the imaginary part of Z_L. The manufacturer states an uncertainty of better than $0.3\,\mathrm{dB}$ on the reflection coefficient magnitude and denotes an uncertainty of better than $3\,^\circ$ on the reflection coefficient phase. The uncertainty of the frequency is stated to be $2.25\,\mathrm{ppm}$ which is negligible compared to the uncertainties arising due to the

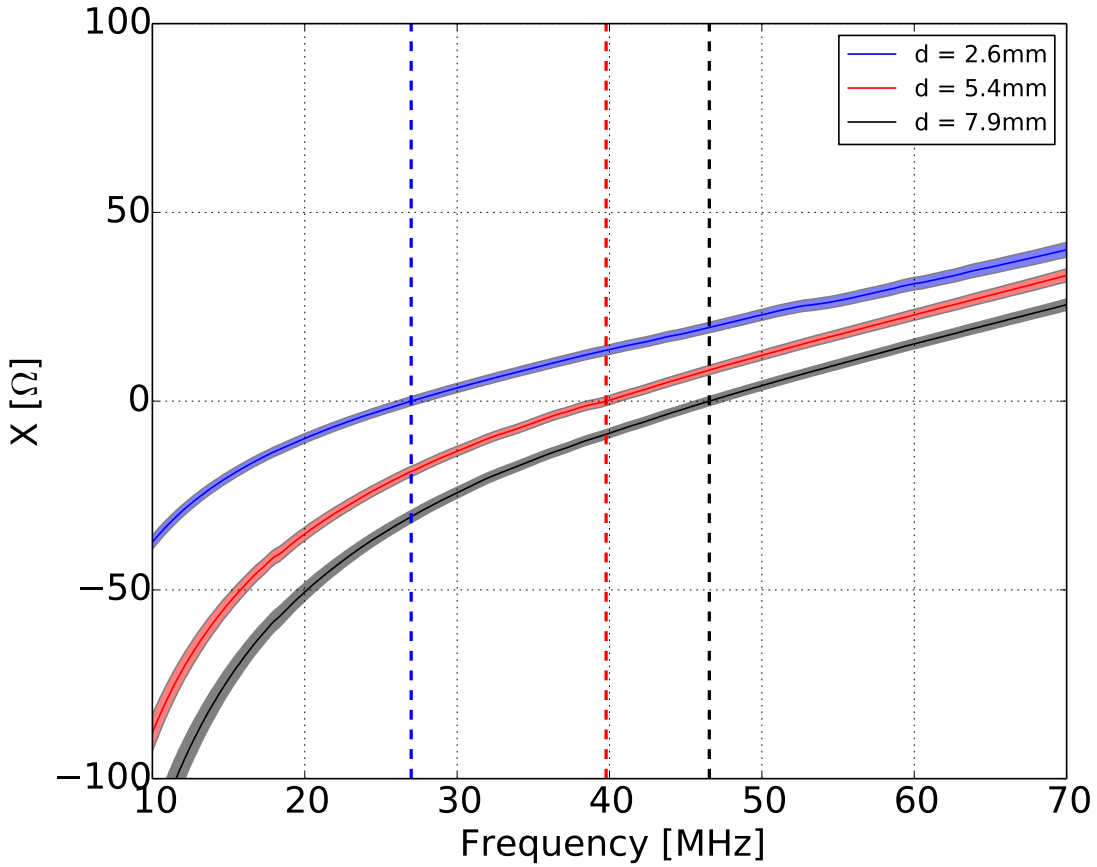

Figure 6.2: *The reactance X as function of the frequency using a capacitor and using air as dielectric for different capacitor plate distances. The colored bands indicate the respective measurement uncertainty from the vector network analyzer. The dashed lines mark the respective resonance frequency with $X = 0\,\Omega$.*

magnitude and phase.

The distance between the capacitor plates d is measured using a caliper gauge with an accuracy of about $0.05\,\mathrm{mm}$ which is negligible compared to the uncertainties arising from the VNA.

The parasitic inductivity of the setup resulting in the parasitic reactance X_L is determined in multiple calibration measurements using air as dielectric. The reactance X of three different measurements as function of the frequency and the respective resonance frequencies are shown in Fig. 6.2. In Tab. 6.1, the resulting inductivities are listed and then combined to the averaged inductivity $\overline{L}$ of the setup including the influence of the used cables and connectors. The fluctuation between the inductivities is used as uncertainty of the combined inductivity $\overline{L}$.

According to Eq. (6.8), the frequency-dependent relative permittivity ϵ_r of different materials with different material thicknesses has been determined and is then compared to the respective literature values. A picture of the capacitor with PVC in between the capacitor plates is shown in Fig. 6.3.

The obtained relative permittivities of acrylic glass, paper, pressboard, and PVC as function of the frequency in a frequency range from $10\,\mathrm{MHz}$ to $70\,\mathrm{MHz}$ are presented in Fig. 6.4. The colored bands denote the respective uncertainties where the influence from the VNA, from the calibration measure-

Measurement	d [mm]	f_{res} [MHz]	L [nH]
1	2.6	27.0	113
2	5.4	39.8	108
3	7.9	46.6	116
4	7.9	46.6	116
5	7.9	45.9	119
combination	–	–	115 ± 4

Table 6.1: *The parasitic setup inductivity of five calibration measurements. The measurements are combined to the averaged inductivity.*

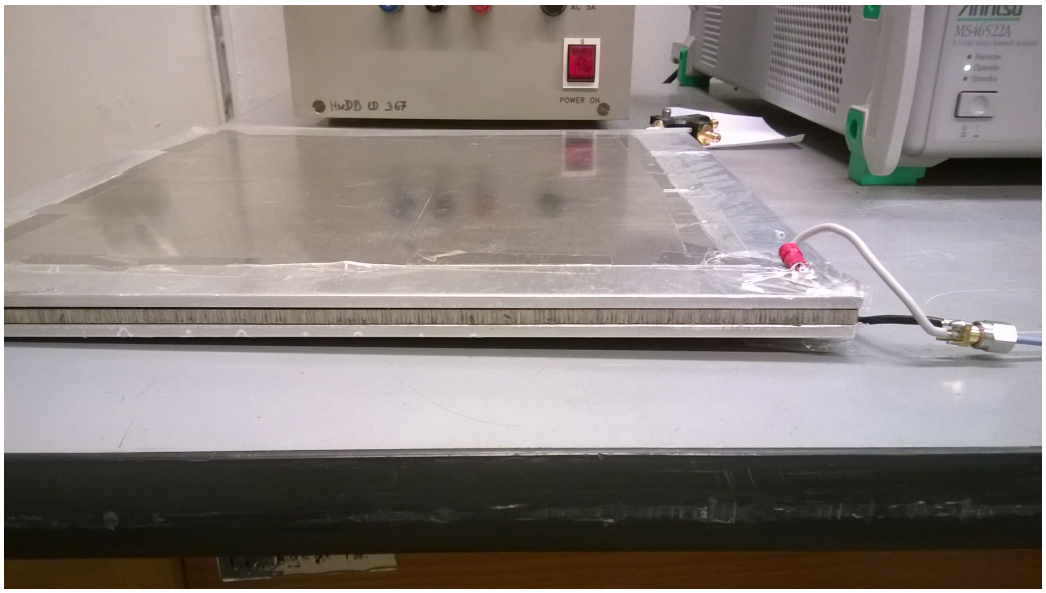

Figure 6.3: *The capacitor used for the relative permittivity measurements. The capacitor plates are enveloped in a thin layer of non-conductive film. In between the capacitor plates, a PVC plate is placed to measure its relative permittivity and thus, to proof the measurement principle of using a capacitor to determine the relative permittivity.*

ments to obtain the combined inductivity, and from the distance between the capacitor plates are combined. For frequencies outside the chosen range, the measurement uncertainties strongly increase and thus inhibit valid conclusions about ϵ_r. In general, the relative permittivity decreases with the frequency for the given materials. At large frequencies ϵ_r increases again, but also the uncertainties are getting larger especially in the case of acrylic glass and PVC. All measurements exhibit relative permittivites which are compatible with the respective literature values. Typical values of the respective material for direct current are illustrated by the markers and the error bars at small frequencies. For visualization reasons the literature values are shifted.

6.3 Soil Measurement Campaigns

In this section, the frequency-dependent relative permittivity of soil from the AERA site is determined. For this purpose, two kind of measurement campaigns have been performed. Firstly, the relative per-

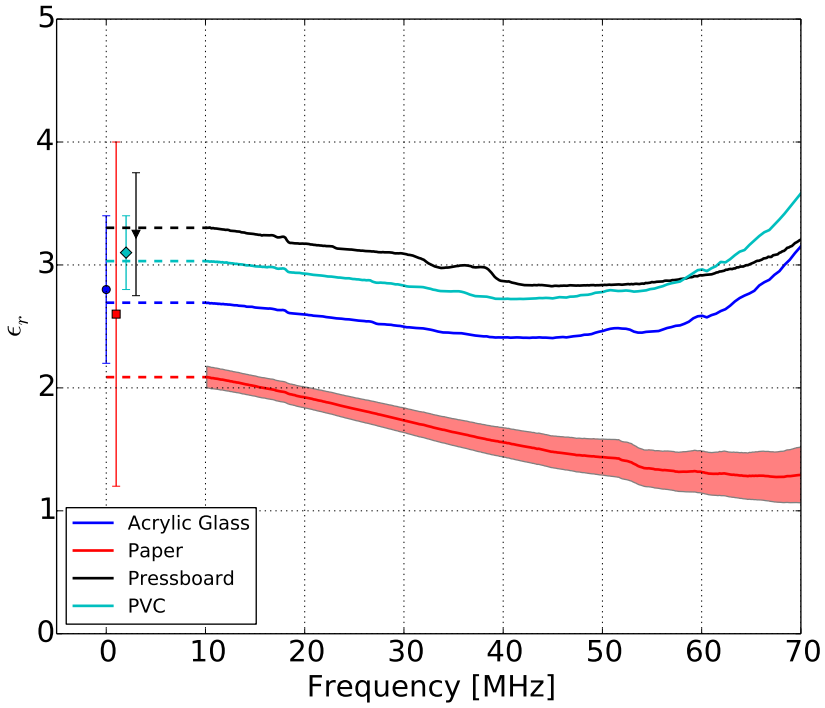

Figure 6.4: *Frequency-dependent measurement of the relative permittivity of acrylic glass (blue line), paper (red line), pressboard (black line) and PVC (turquoise line). The colored markers with the error bars represent typical literature values of the respective material for direct current. For visualization reasons the literature values are shifted. Typical values of the respective materials are listed in [234–237].*

mittivity of soil collected from one position has been measured in the laboratory. Here, reproducibility of the measurements with stable environmental conditions as well as the dependence of the relative permittivity on the soil humidity is investigated. Secondly, measurements of the relative soil permittivity at different locations at AERA measured directly at the site are presented. These measurements give an impression of the homogeneity of the soil conditions at the AERA site. From both measurement campaigns, typical values of the relative permittivity from the soil at the AERA site are obtained. In the following, the laboratory measurements of the permittivity of soil from AERA are discussed first and afterwards the measurements performed directly at the site are presented.

6.3.1 Permittivity Measurements in the Laboratory of Soil collected at the AERA site

With the measurements of the relative permittivity of soil from AERA the reproducibility of the measurement as well as the influence of soil humidity on the relative permittivity are investigated. A sample of soil from the surface at one station of AERA has been collected and the relative permittivity has been determined in multiple measurements in the laboratory. For the measurement, the same setup is used as mentioned in the calibration measurements. In contrast to the specific materials used in the calibration measurements, the soil is not a rigid plate and thus it is expected that the distance between the capacitor plates is not constant. Hence, the distance between the plates is measured at multiple positions and then averaged to a combined distance which is used in the analysis. Pictures of the soil

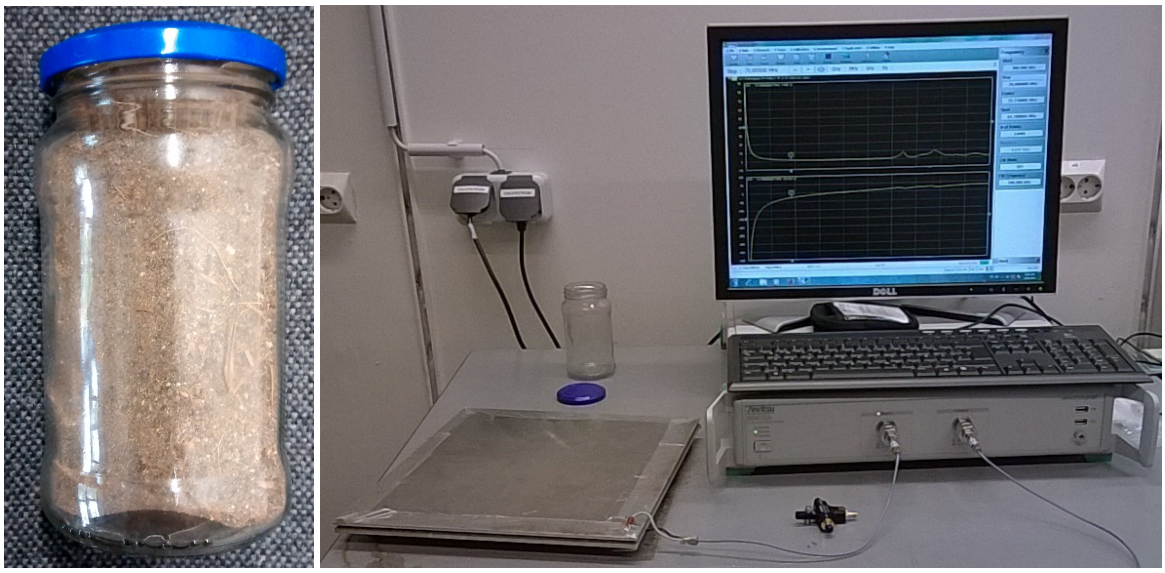

Figure 6.5: ***(left)*** *The sample of soil collected from the surface at the AERA site.* ***(right)*** *Setup of the laboratory measurement campaign to determine the relative permittivity of the soil sample using the capacitor connected to a vector network analyzer.*

sample as well as of the setup are shown in Fig. 6.5.

Reproducibility Measurements

To investigate the measurement reproducibility multiple measurements of the soil sample have been performed. The measurements have been repeated four times at different days so that independent measurements with nearly constant environmental conditions of the laboratory are guaranteed. Before performing the measurements, the soil sample has been dried. The recorded setup reactance X of the four measurements is shown as function of the frequency in the upper left diagram of Fig. 6.6. From these measurements, the relative permittivity of the soil sample is then determined according to Eq. (6.8) which is presented as function of the frequency in the upper right diagram of Fig. 6.6. The relative permittivity increases with the frequency starting at a relative permittivity around 2.5 at $10\,\mathrm{MHz}$ up to about 6 at $70\,\mathrm{MHz}$. In the lower left diagram of Fig. 6.6, the average permittivity $\overline{\epsilon_r}$ of these four measurements is shown as function of the frequency. The fluctuation σ between the measurements is marked by the blue area which increases with the frequency. Compared to the average $\overline{\epsilon_r}$ from four measurements, the median value of the ratio $\sigma/\overline{\epsilon_r}$ is about $6\,\%$ which is presented in the lower right diagram of Fig. 6.6.

Influence of the Soil Humidity

The influence of the soil humidity on the relative permittivity has been investigated by using soil with different content of water as dielectric. The soil sample is humidified by spraying water ranging from $10\,\mathrm{ml}$ to $100\,\mathrm{ml}$ on the sample as shown in Fig. 6.7. The measurements of the different degrees of soil humidity have been performed in a row starting with dry soil. Thus, for the measurements the same environmental conditions and the same plate distance were present. The measurements differ in the

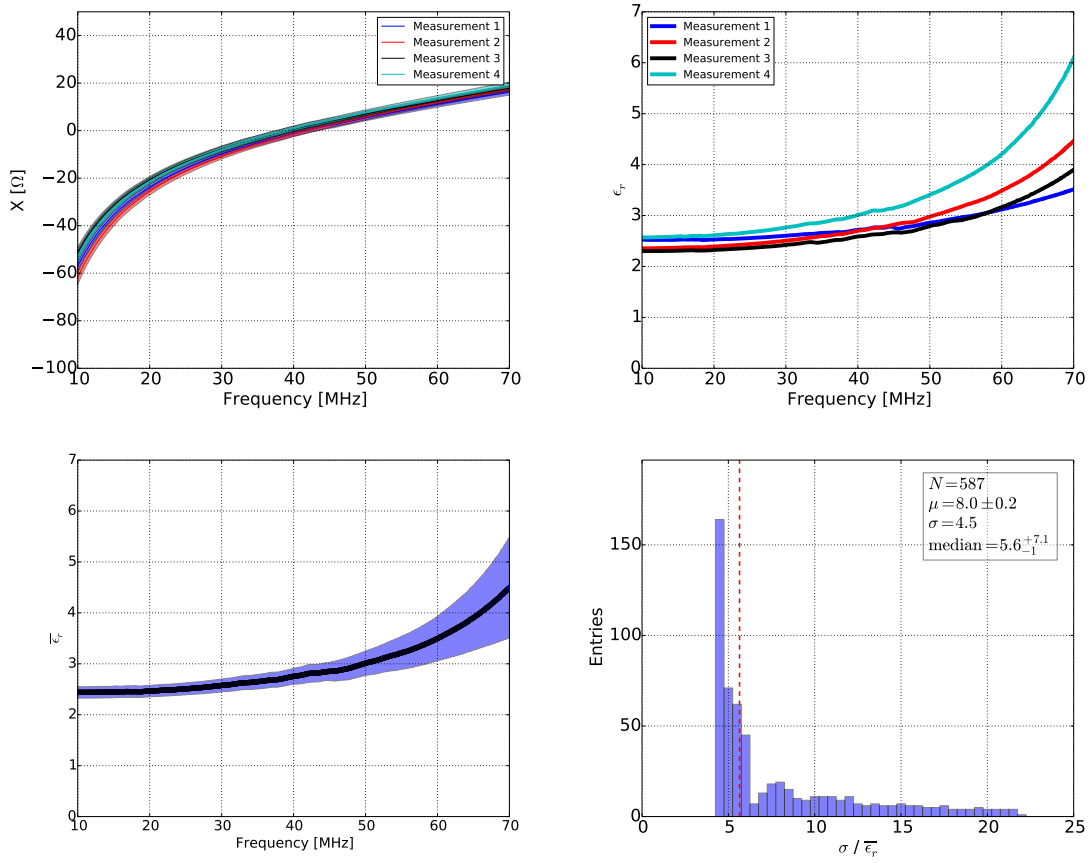

Figure 6.6: ***(upper left)*** *The setup reactance X (colored lines) as function of the frequency for four independent measurements. The colored bands mark the respective measurement uncertainty due to the vector network analyzer.* ***(upper right)*** *The resulting relative permittivity of the respective measurement as function of the frequency.* ***(lower left)*** *The average relative permittivity $\overline{\epsilon_r}$ from the four measurements. The fluctuation between the measurements is indicated by the blue region.* ***(lower right)*** *Histogram of the ratio $\sigma/\overline{\epsilon_r}$ from four measurements. The median value is indicated by the red dashed line.*

soil humidity only. Compared to the capacitor plate size $A = 0.09\,\mathrm{m}^2$, the used amounts of water are equivalent to a column of water ranging from $0.1\,\mathrm{mm}$ to $1.1\,\mathrm{mm}$ per square meter and indicate typical values of rainfall of light rainy days [238].

In the left diagram of Fig. 6.8, the recorded setup reactance is shown exemplary for dry soil and for wet soil with two different contents of water as dielectric. From these measurements, the relative permittivities are determined according to Eq. (6.8) and are presented as function of the frequency and the soil humidity on the right side of Fig. 6.8. The measurements confirm that the soil humidity impacts the relative permittivity of the soil. The wetter the soil, the higher is the relative permittivity. Whereas the relative permittivity is about 3 over the whole frequency range in the case of dry soil, the measurements exhibit values of the relative permittivity in between 4 and 9 in the case of wet soil. Compared to the conditions at AERA, the capacitor plates prohibit that the water seeps away. Therefore, the soil sample used in these laboratory measurements is wetter than the soil at the AERA site would be compared to the same amount of water. Hence, the changes of the relative permittivity compared to the relative permittivity of dry soil give an upper limit for the respective water content.

Figure 6.7: *Picture of the soil sample placed in the capacitor. Different soil humidities are achieved by spraying water with different amounts of water on the soil sample.*

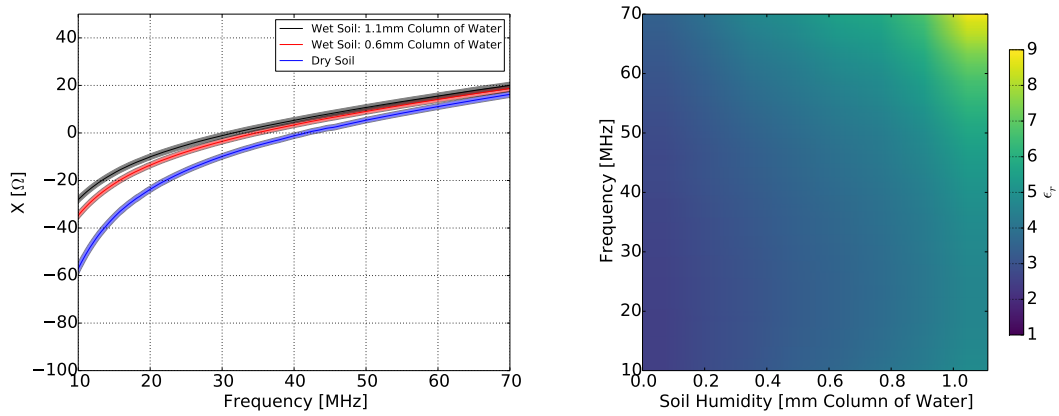

Figure 6.8: ***(left)*** *The setup reactance X (colored lines) as function of the frequency for dry soil as well as for two wet soils with different soil humidity. The colored bands indicate the respective uncertainty due to the vector network analyzer.* ***(right)*** *The resulting relative permittivity as function of the frequency and the soil humidity. The relative permittivity increases with the soil humidity.*

6.3.2 Permittivity Measurements of Soil at the AERA Site

In this subsection, the measurements of the soil permittivity performed at different positions at the AERA site are presented. These measurements give indications of the relative permittivity of the soil under realistic conditions as well as of the homogeneity of the soil consistency at the AERA site. For the measurements, a hand-held FSH4 VNA from the company Rohde&Schwarz [231] is used. For the FSH4, the manufacturer states an uncertainty of $0.06\,\mathrm{dB}$ on the reflection coefficient magnitude and denotes an uncertainty of $3\,^\circ$ on the reflection coefficient phase. The uncertainty of the frequency is stated to be about $10\,\mathrm{ppm}$ which is negligible compared to the uncertainties arising due to the magnitude and phase.

Figure 6.9: *For the measurements at the AERA site, the capacitor has been placed on a wooden plate to reduce disturbing effects from the underlying soil as well as to avoid a grounding of the capacitor plates. Soil from the surface is collected and placed in between the capacitor plates. The distance between the plates is measured at multiple positions using a tapeline.*

During the measurements at AERA, the capacitor was placed on a non-conductive wooden plate to avoid a disturbing influence of the underlying soil as well as to avoid a grounding of the capacitor. At each position, a sample of soil was collected from the surface and was placed in between the capacitor plates. The distance between the capacitor plates is measured at multiple positions using a tapeline which are then combined to an averaged distance. The fluctuation of different distances is used as uncertainty of the averaged distance. Pictures of the setup at AERA are shown in Fig. 6.9 and Fig. 6.10.

The measurements have been performed at ten different positions within the second phase of AERA. A map of AERA including the positions of the permittivity measurements which are marked as red pentagons is shown in Fig. 6.11. The numbers close to the pentagons mark the respective weighted median of the relative permittivity distribution in the frequency range from 30 MHz to 60 MHz which is explained in the following.

In Fig. 6.12, the recorded setup reactance as function of the frequency at four different positions counted from west to east (cf. Fig. 6.11) are presented. From these measurements, the relative permittivity is then determined according to Eq. (6.8). In Fig. 6.13, the frequency-dependent relative permittivities ϵ_r from soil collected from the four positions are shown as function of the frequency. The resulting relative permittivities from the other positions are shown in the appendix B.

The measurement of the relative permittivity at the position located in the west of AERA is nearly constant at 5 for all frequencies whereas at the other positions the relative permittivity is higher, especially at large frequencies. The uncertainties increase with the frequency for all measurements. In case of the measurement in the east of AERA the systematic uncertainty strongly increases at around 65 MHz and thus allows unphysical values of the relative permittivity below 1. Therefore, this method to determine the frequency-dependent relative permittivity is limited to smaller frequencies. To guarantee comparability between all performed measurements the upper frequency limit is set to 60 MHz. Considering this limitation as well as considering the sensitive frequency range of AERA, the analyzed frequency range is set from 30 MHz to 60 MHz. In Fig. 6.14, the relative permittivities measured at the ten different positions are compared to each other. In the left diagram, the relative permittivity at each position for three different frequencies of 35 MHz, 45 MHz, and 55 MHz is presented. The error

Figure 6.10: *Picture of the full setup to measure the relative permittivity of soil at the AERA site using a capacitor connected to the FSH4 vector network analyzer.*

bars indicate the measurement uncertainties due to the uncertainties from the the VNA, from the parasitic inductance measurement as well as from the measurement of the distance between the capacitor plates. In the right diagram, the median weighted by the measurement uncertainties and the weighted 68-percent quantile of the relative permittivity distribution in the frequency range from $30\,\mathrm{MHz}$ to $60\,\mathrm{MHz}$ for each measurement is shown. The measurements are ordered from west to east in both diagrams. The measurements at the AERA site have been performed at one day. The days before the measurement campaign it was rainy at AERA and therefore a wet soil was present. For the majority of the positions, the measurements exhibit values from 6 to 7. Only in the very west of AERA, the measurements of the relative permittivites exhibit values of 5 and in the very east of AERA exhibit larger relative permittivites of about 10. These differences can be attributed to the fact that in the west of AERA the soil consistency is sandy whereas in the east the soil consistency is more earth like.

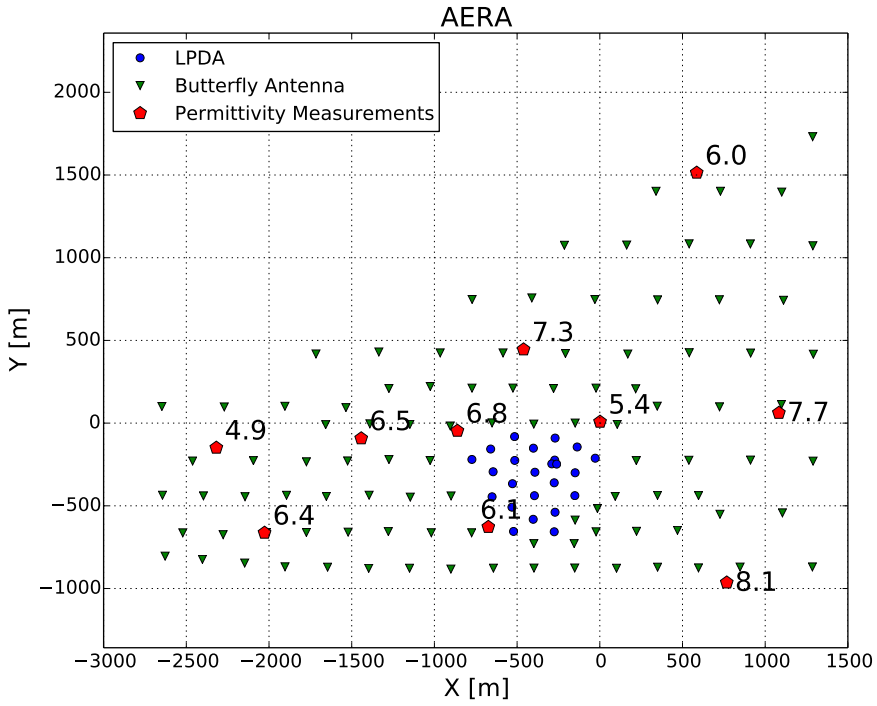

Figure 6.11: *Map of AERA. The LPDA-equipped radio stations are indicated by the blue dots and the Butterfly-equipped radio station of phase* 2 *are marked by the green triangles. The positions of the permittivity measurements are indicated as red pentagons. At each position, the weighted median of the relative permittivity distribution in a frequency range from* 30 MHz *to* 60 MHz *is given.*

6.3.3 Conclusions from the Measurement Campaigns

To define typical values of the relative permittivity of soil at AERA, the results of both measurement campaigns performed in the laboratory and at the site are combined. For the laboratory measurements, the soil was dried first and the relative permittivity of the soil with different content of water has been investigated. It was found that the ground permittivity is typically larger than 2 and increases with the soil humidity.

The ground permittivity has been measured directly at different positions within AERA to investigate the ground homogeneity at the site. The soil used in the laboratory measurements exhibit smaller relative permittivites than those performed at the AERA site. This indicates a larger soil humidity during the measurement campaign at the AERA site than in the measurement performed in the laboratory which is explained by the rainy days before the measurement campaign at AERA. For the majority of the positions, the measurements exhibit values from 6 to 7. Only in the very west and in the very east of AERA the permittivity differs which can be attributed to the fact that in the west of AERA the soil consistency is sandy whereas in the east the soil consistency is more earth like. It was found that the ground permittivity is typically smaller than 10.

The combination of the measurement campaigns exhibits typical values of the relative permittivity between 2 and 10 depending on the soil humidity.

As the ground permittivity changes the reflectivity of an electromagnetic signal on ground, variations

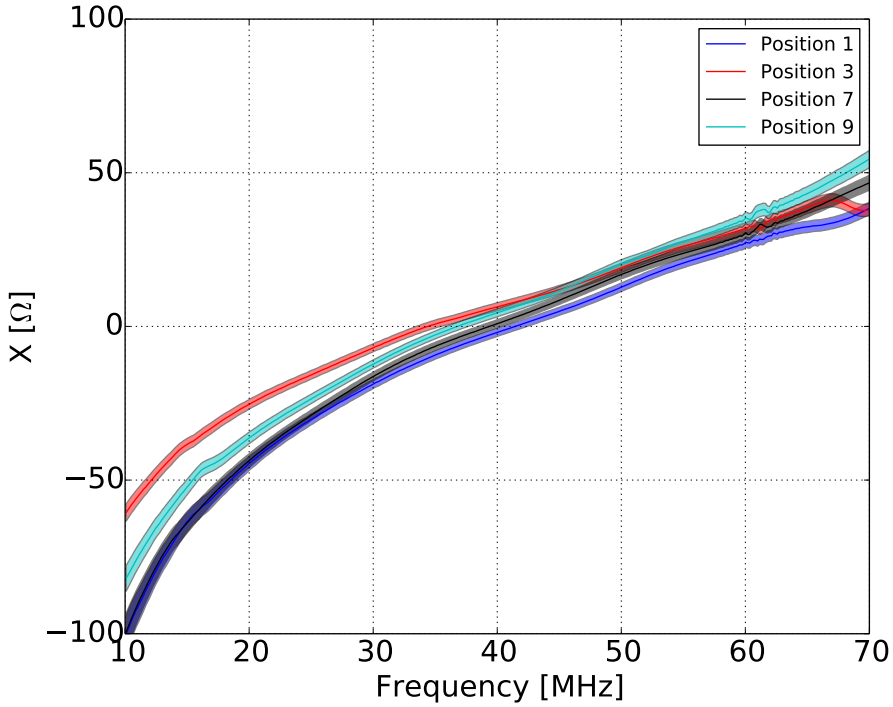

Figure 6.12: *The setup reactance X as function of the frequency of four measurements at the AERA site counted from west to east (cf. Fig. 6.11). The colored bands indicate the respective measurement uncertainty due to the uncertainty from the vector network analyzer.*

of the ground permittivity influence the directional-dependent antenna sensitivity. The larger the sensitivity of the antenna towards the ground direction, the larger is the influence of a changing ground permittivity on the antenna vector effective length. In the case of the LPDA, the influence of variating ground conditions on the response pattern based on the measurements presented in this chapter is discussed in detail in the next chapter.

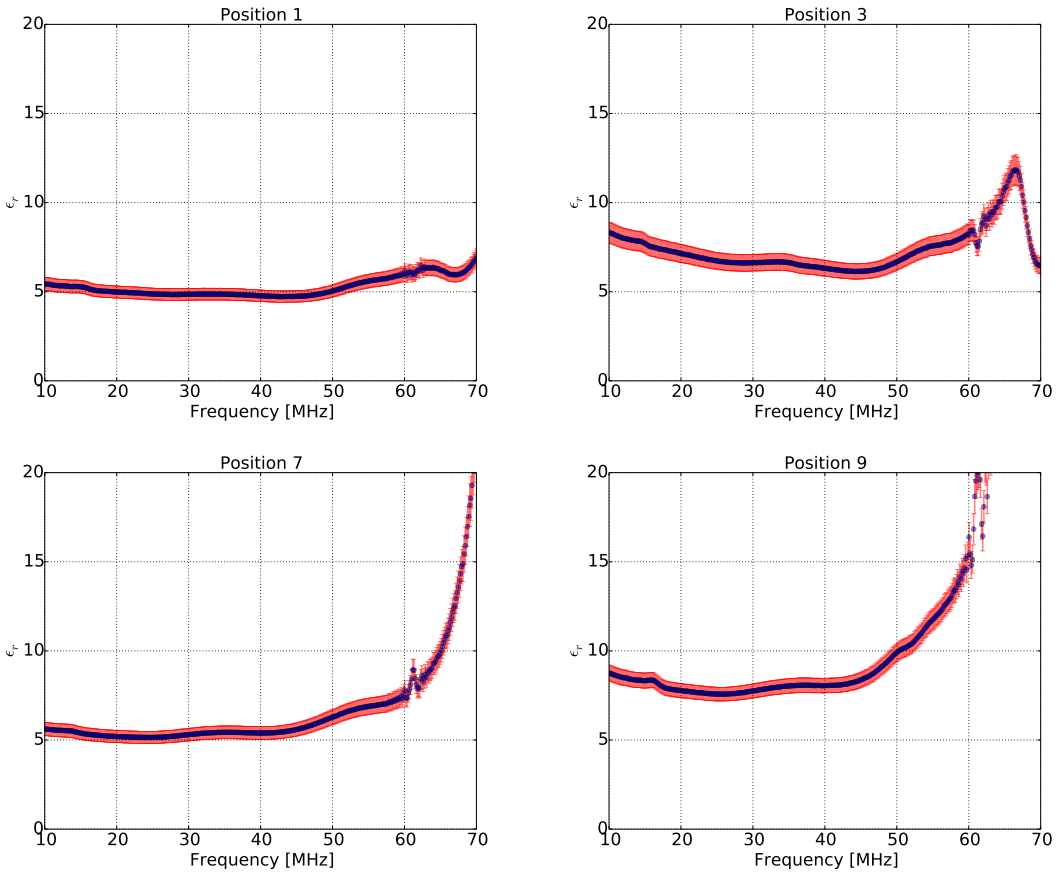

Figure 6.13: *The relative permittivity (blue dots) as a function of the frequency measured at different positions at the AERA site counted from west to east (cf. Fig. 6.11). The red error bars indicate the uncertainty arising from the distance measurements between the capacitor plates and the black area marks the combined uncertainty arising from the vector network analyzer and arising from the measurements of the parasitic inductance of the setup.*

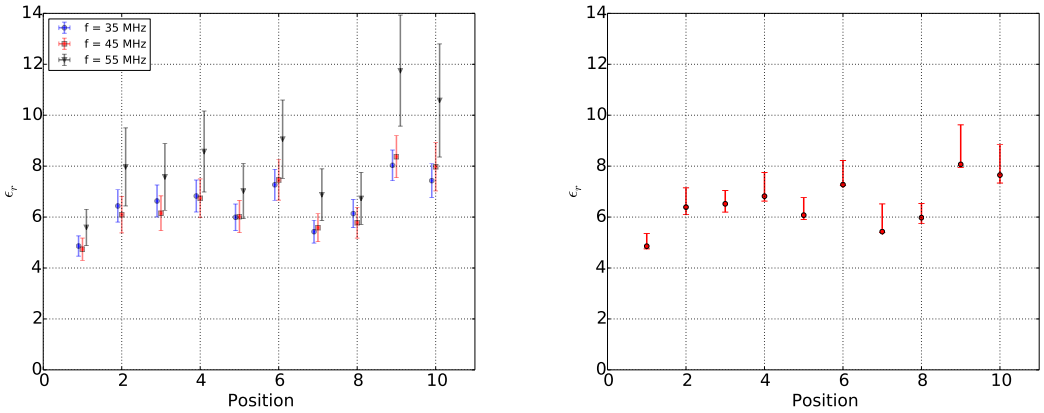

Figure 6.14: ***(left)*** *Relative permittivity at each position for three different frequencies of* 35 MHz*,* 45 MHz*, and* 55 MHz*. The error bars indicate the combined uncertainties arising from the vector network analyzer, arising from the parasitic inductance measurements as well as arising from the measurement of the distance between the capacitor plates.* ***(right)*** *Weighted median of the relative permittivity distribution in the frequency range from* 30 MHz *to* 60 MHz*. The relative permittivity is weighted by its uncertainties. The weighted 68-percent quantile is indicated by the error bars. The measurement positions are ordered from west to east in both diagrams.*

7

Simulation of the LPDA Response Pattern

Parts of this chapter have been published in:

A. Aab et al. (Pierre Auger Collaboration)
"Calibration of the Logarithmic-Periodic Dipole Antenna (LPDA) Radio Stations at the Pierre Auger Observatory using an Octocopter"
J. Instrum. **12** (2017) T10005
The work presented in this publication was primarily performed by the author of this thesis. The text of the publication has been written by the author of this thesis and was revised and copy-edited by the co-authors of the publication.

For analyzing radio emission from extensive air showers, a precise description of the frequency and directional-dependent antenna sensitivity is needed. The measurement of the antenna response pattern is very complex and enables determining the antenna response pattern for discrete arrival directions and frequencies only. A response pattern simulation delivers an overall description for all arrival directions and frequencies. In this chapter, the simulation of the LPDA response pattern in terms of the vector effective length (VEL) is discussed. Nevertheless, the simulation has to be confirmed by measurements which is explained in detail in the next chapter for the case of the LPDA.
The chapter is structured as follows: Firstly, the standard simulation model is described considering the LPDA structure and the standard environmental conditions. Furthermore, the resulting frequency and directional-dependent antenna sensitivity in terms of the VEL decomposed in a horizontal $|H_\phi|$ and a meridional component $|H_\theta|$ is presented. Secondly, the simulation stability is discussed by varying single parameters and investigating their influence on the standard simulation for the most sensitive axis of the respective component with constant azimuth angle. Ground conductivity and ground permittivity influences the signal reflection properties of the ground and thus impact the LPDA response pattern. The influence of different ground conditions are investigated in Sec. 7.2. The antenna electronics are located within an electronics box beneath the LPDA. As the electronics box is made of conductive material and is located close to the antenna within the antenna near field, it impacts the LPDA response pattern. The influence of such an additional box is discussed in Sec. 7.3. Furthermore, in Sec. 7.4, the influence of an antenna misalignment is discussed. Finally, the simulation results are concluded in Sec. 7.5.

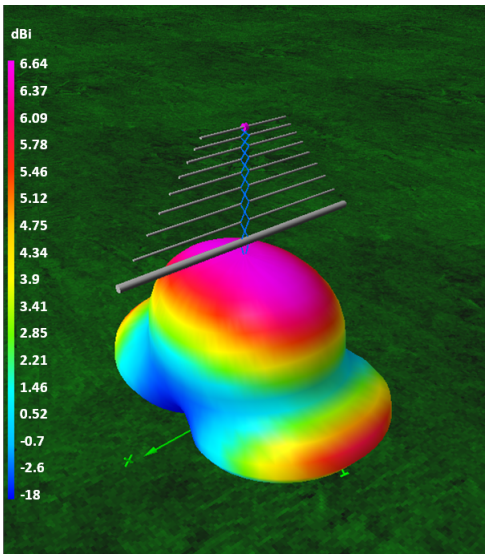

Figure 7.1: *Standard model of the LPDA used in the NEC-2 simulations. The total directional-dependent antenna gain at* $55\,\mathrm{MHz}$ *is color coded in logarithmic units. The pinker the color, the higher is the antenna sensitivity to this direction. The pink dot on top of the antenna marks the antenna footpoint.*

7.1 The Standard LPDA Simulation Model

In this section, the standard antenna model of the LPDA is discussed which is used to simulate the LPDA response pattern. In the original simulation of the LPDA response pattern, the antenna itself as well as the following amplifier stage connected by a transmission line is taken into account.

The LPDA consists of nine $\lambda/2$-dipoles of different lengths which are combined to one single antenna with the largest dipole located at the bottom and the shortest dipole at the top of the LPDA. The antenna model follows the real antenna specifications as discussed in Sec. 4.3.2. The dipoles are connected to a waveguide with the antenna footpoint at the top of the LPDA. The simulation of the LPDA response pattern at the antenna footpoint, which is denoted as passive part of the LPDA, is performed using the NEC-2 simulation code.

For the simulation, realistic ground properties are taken into account. At standard ground conditions the ground conductivity is set to be $1.4\,\mathrm{mS/m}$. Values of the conductivity of dry sand, which is the typical ground consistency at AERA, are reported here [15, 164]. Measurements of the ground permittivity at the AERA site yield values between 2 and 10 depending on the soil humidity (refer to Chap. 6). The standard ground permittivity is set to be 5.5 in the simulation.

The NEC-2 realization of the LPDA is shown in Fig. 7.1. The footpoint is illustrated by the pink dot in the middle of the highest dipole. Color coded is the total LPDA gain at $55\,\mathrm{MHz}$. The pinker the color, the higher is the antenna sensitivity to the respective direction. The main sensitive region of the LPDA at $55\,\mathrm{MHz}$ is the zenith direction above the LPDA.

The footpoint is connected by an RG58 [211] coaxial transmission line with a length of $l_{\mathrm{tl}} = 2.9\,\mathrm{m}$ to a low-noise amplifier (LNA) which amplifies the signal power typically by $(18.1 \pm 0.2)\,\mathrm{dB}$ in the frequency range from $30\,\mathrm{MHz}$ to $80\,\mathrm{MHz}$. Both, the transmission line and the amplifier, then constitute the active part of the LPDA and their own influence on the antenna response pattern as well as reflection effects due to impedance mismatch between the components have to be considered

separately. Mismatch and reflection effects between the antenna footpoint, the transmission line and the LNA are explained in detail in Sec. 3.6. The respective LPDA and LNA impedances as well as the LNA S-parameters are presented in Sec. 4.3.2.

The horizontal component $|H_\phi|$ and the meridional component $|H_\theta|$ of the LPDA VEL are calculated using Eq. (3.31) and the simulation is performed in a frequency range from 30 MHz to 80 MHz in steps of 1 MHz, for zenith angles from $0\,^\circ$ to $90\,^\circ$ in steps of $3\,^\circ$, and for azimuth angles from $0\,^\circ$ to $360\,^\circ$ in steps of $7.5\,^\circ$. Then, the LPDA VEL is modified with Eq. (3.49) considering the transfer function from the LPDA footpoint to the system consisting of the transmission line connecting the LPDA footpoint to the amplifier and the amplifier itself.

In Fig. 7.2, the horizontal component $|H_\phi|$ and the meridional component $|H_\theta|$ as a function of the arrival direction for three different frequencies of 35 MHz, 55 MHz, and 75 MHz of a north-south polarized LPDA are presented. In the case of the horizontal component $|H_\phi|$, an azimuthal pattern appears at $\theta = 0^\circ$ and $\theta = 180^\circ$, which correspond to the east and west direction, with decreasing VEL amplitudes in between. In contrast, for the meridional component $|H_\theta|$ the azimuthal pattern appears at $\theta = 90^\circ$ and $\theta = 270^\circ$, which correspond to the north and south direction. Both axis, the east-west axis and the north-south axis, are called the main axes of the LPDA marking the most sensitive axes of the respective VEL component. In the following discussions, the frequency and zenith dependency of the LPDA response pattern is determined for the respective main axis of highest antenna sensitivity. Both VEL components as function of the zenith angle for three different frequencies of 35 MHz, 55 MHz and 75 MHz of a north-south polarized LPDA are presented in Fig. 7.3. Furthermore, both components as a function of the frequency at a zenith angle of $15\,^\circ$, $45\,^\circ$, and $75\,^\circ$ are shown in Fig. 7.4.

In general, the horizontally polarized LPDA is most sensitive to the zenith direction and the LPDA VEL decreases with the zenith angle close to $90\,^\circ$ for both polarizations and all frequencies. The horizontal component $|H_\phi|$ exhibits a larger sensitivity as the meridional component $|H_\theta|$. Only at small zenith angles of $0\,^\circ$ both components offer an equal antenna sensitivity. As a rule of thumb: the larger the frequency, the smaller is the LPDA VEL. The pattern at 35 MHz is smooth whereas side lobes appear at larger frequencies in the case of the horizontal component $|H_\phi|$.

7.2 Influence of Ground Conditions

As described in Sec. 3.7, the ground conductivity and the ground permittivity impact the signal reflection on ground and therefore, impact the antenna VEL. In this section, the influence of different ground conditions as ground conductivity and ground permittivity on the LPDA VEL is investigated using simulations. The simulations are performed for ground conductivities ranging from 0.5 $\frac{\mathrm{mS}}{\mathrm{m}}$ to 3 $\frac{\mathrm{mS}}{\mathrm{m}}$ and ground permittivities ranging from 2 to 10. Within these ranges, the conductivity and permittivity independently influence the signal reflection properties of the ground. The ground permittivity values used in the simulations are based on permittivity measurements of soil collected from the AERA site (refer to Chap. 6). The ground permittivity at each radio station is not continuously measured. Hence, the modified simulations with a permittivity of 2 and of 10 are combined to obtain the combined influence of the ground permittivity on the LPDA response pattern. In the following, the influence of different ground conditions on the horizontal component of the LPDA VEL $|H_\phi|$ is discussed first and then the influence on the meridional component of the LPDA VEL $|H_\theta|$ is presented.

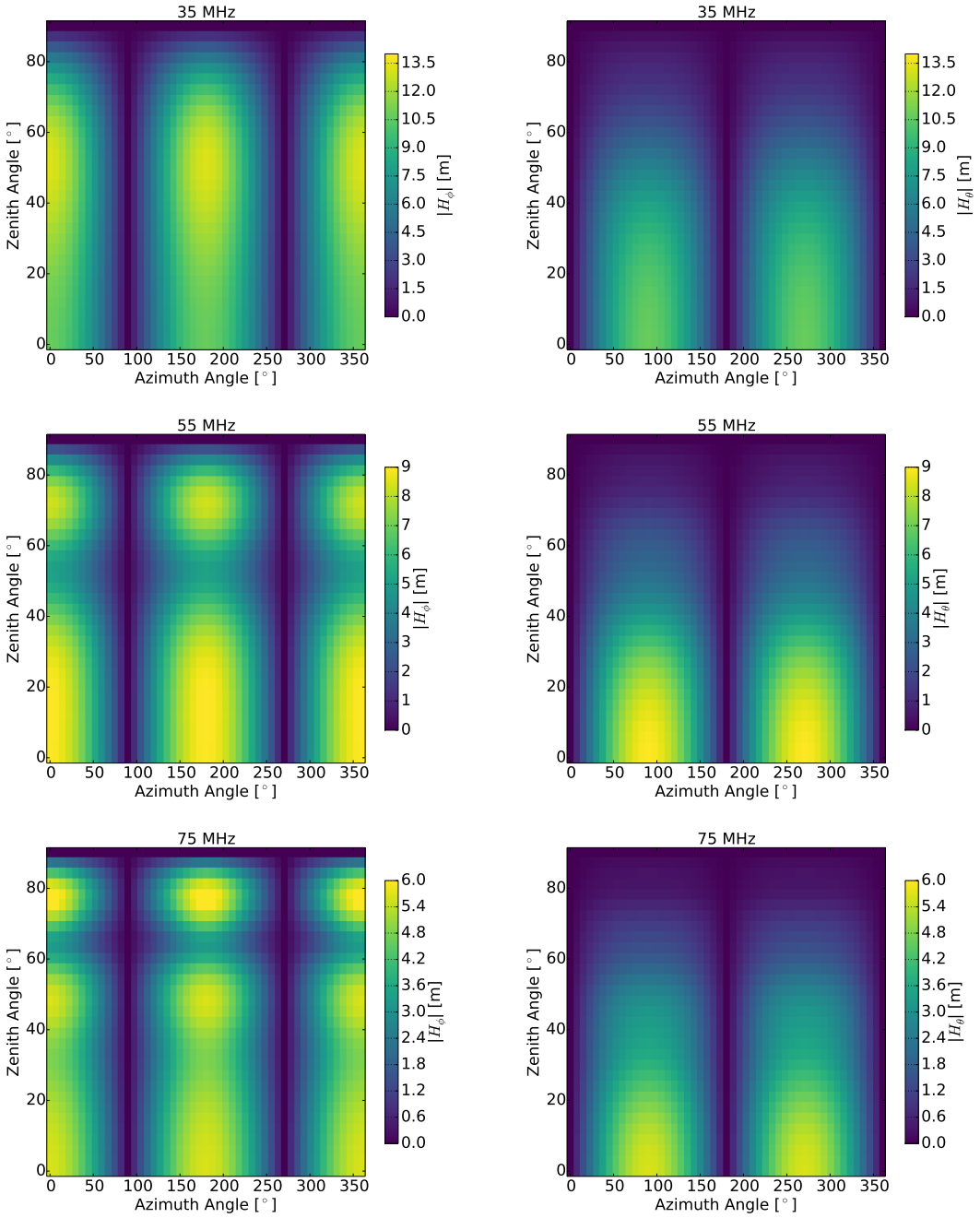

Figure 7.2: *Antenna response pattern of a north-south polarized LPDA.* ***(left)*** *Horizontal component of the LPDA vector effective length (VEL)* $|H_\phi|$ *and* ***(right)*** *meridional component of the LPDA VEL* $|H_\theta|$ *obtained from the standard simulation as a function of the zenith angle* Θ *and the azimuth angle* Φ *counted from east anti clock wise at three different frequencies of* ***(from top to bottom)*** $35\,\mathrm{MHz}$*,* $55\,\mathrm{MHz}$*, and* $75\,\mathrm{MHz}$*. Note that the range of the color bar changes with the frequency for a better visualization of the respective VEL characteristics.*

7.2.1 Horizontal Component of the Vector Effective Length

Here, the influence of different ground conditions on the horizontal component of the LPDA VEL $|H_\phi|$ is discussed. In Fig. 7.5, $|H_\phi|$ for different ground conductivities and different ground permittivities as function of the zenith angle at three different frequencies of $35\,\mathrm{MHz}$, $55\,\mathrm{MHz}$, and $75\,\mathrm{MHz}$ is

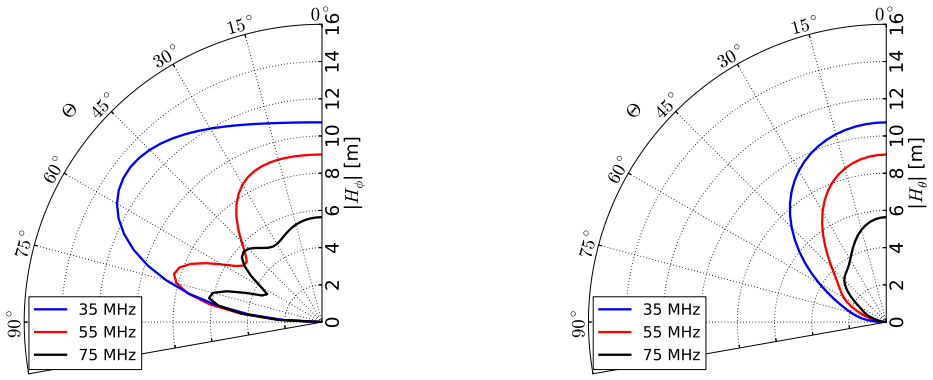

Figure 7.3: *Horizontal component of the LPDA vector effective length (VEL)* $|H_\phi|$ ***(left)*** *and meridional component of the LPDA VEL* $|H_\theta|$ ***(right)*** *obtained from the standard simulation as a function of the zenith angle* Θ *at three different frequencies of* 35 MHz*,* 55 MHz*, and* 75 MHz*.*

compared to the LPDA VEL obtained from the standard simulation. Furthermore, in Fig. 7.6 the respective LPDA VELs are shown as a function of the frequency at a zenith angle of $15\,^\circ$, $45\,^\circ$, and $75\,^\circ$.

Different ground conductivities change the LPDA response pattern on the level of $0.1\,\%$. In contrast, the influence of the ground permittivity on the antenna response is higher. The influence of the ground permittivity varies with the frequency and the zenith angle forming a wave-like pattern. The agreement between the modified simulation with a ground permittivity of 2 (10) and the standard simulation of the horizontal component of the LPDA VEL $|H_\phi|$ is illustrated in the diagram of their ratio versus zenith angle Θ and frequency f in the upper left panel of Fig. 7.7 (Fig. 7.8). In the upper right panel of Fig. 7.7 (Fig. 7.8), all ratios are filled into a histogram with entries weighted by $\sin(\Theta)$ in consideration of the decrease in field of view at small zenith angles. The modified simulation and the standard simulation agree to within $1.6\,\%$ ($1.1\,\%$) in the median. The fluctuation described by the $68\,\%$ quantile is at the level of $\frac{0.087+0.064}{2} = 7.6\,\%$ ($\frac{0.019+0.032}{2} = 2.6\,\%$). In the two lower panels of Fig. 7.7 (Fig. 7.8), the median ratio as a function of the frequency (left) and as a function of the zenith angle (right) are shown. In both cases, the red error bars mark the $68\,\%$ quantile of the distributions. The comparisons of the modified simulations with different ground conductivity and the standard simulation are shown in the appendix C.1.

While a modified simulation with a smaller permittivity lowers the horizontal LPDA VEL component $|H_\phi|$ compared to those of the standard simulation, a larger permittivity increases $|H_\phi|$ and vice versa. Thus, both modified simulations can be interpreted as upper and lower limits of $|H_\phi|$. The combined influence I of the ground permittivity on $|H_\phi|$ is then determined by half the ratio of the difference between both modified simulations to the standard simulation:

$$I = \frac{1}{2}\frac{|H_{\phi,perm=10}| - |H_{\phi,perm=2}|}{|H_{\phi,Standard}|} \tag{7.1}$$

which is histogramed in Fig 7.9 for all frequencies and all zenith angles. In the case of an applied ground permittivity of 2 and of 10, the influence on the horizontal LPDA VEL component $|H_\phi|$ is at

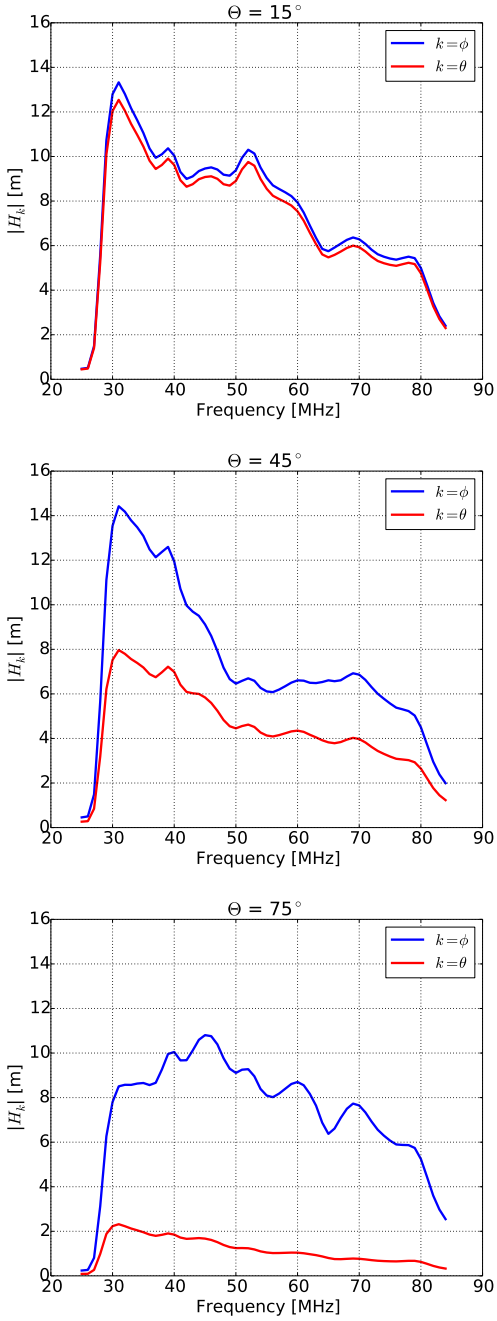

Figure 7.4: *Horizontal component of the LPDA vector effective length (VEL) $|H_\phi|$ (blue line) and meridional component of the LPDA VEL $|H_\theta|$ (red line) obtained from the standard LPDA model as a function of the frequency at a zenith angle of* ***(from top to bottom)*** $15\,^\circ$, $45\,^\circ$, *and* $75\,^\circ$.

the level of $1.3\,\%$ in the median for all frequencies and zenith angles with a scatter of less then $6\,\%$.

7.2.2 Meridional Component of the Vector Effective Length

In this subsection, the influence of different ground conditions on the meridional component of the LPDA VEL $|H_\theta|$ is discussed. In Fig. 7.10, $|H_\theta|$ for different ground conductivities and different ground permittivities as function of the zenith angle at three different frequencies of $35\,\mathrm{MHz}$, $55\,\mathrm{MHz}$,

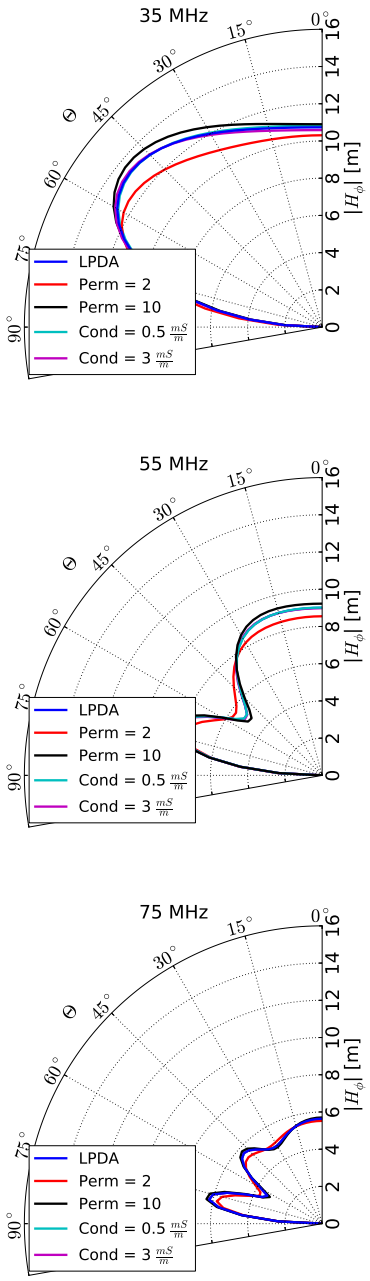

Figure 7.5: *Horizontal component of the LPDA vector effective length $|H_\phi|$ as a function of the zenith angle Θ at a frequency of* ***(from top to bottom)*** $35\,\mathrm{MHz}$*,* $55\,\mathrm{MHz}$*, and* $75\,\mathrm{MHz}$ *obtained from the original simulation (blue line) and compared to those obtained from the modified simulation with different ground conditions: permittivity* $= 2$ *(red line), permittivity* $= 10$ *(black line), conductivity* $= 0.5\,\frac{\mathrm{mS}}{\mathrm{m}}$ *(light blue line), conductivity* $= 3\,\frac{\mathrm{mS}}{\mathrm{m}}$ *(magenta line).*

and $75\,\mathrm{MHz}$ is compared to the LPDA VEL obtained from the standard simulation. Furthermore, in Fig. 7.11, the respective LPDA VEL are shown as a function of the frequency at a zenith angle of $15\,^\circ$, $45\,^\circ$, and $75\,^\circ$.

Different ground conductivities change the LPDA response pattern on the level of $0.1\,\%$. In contrast,

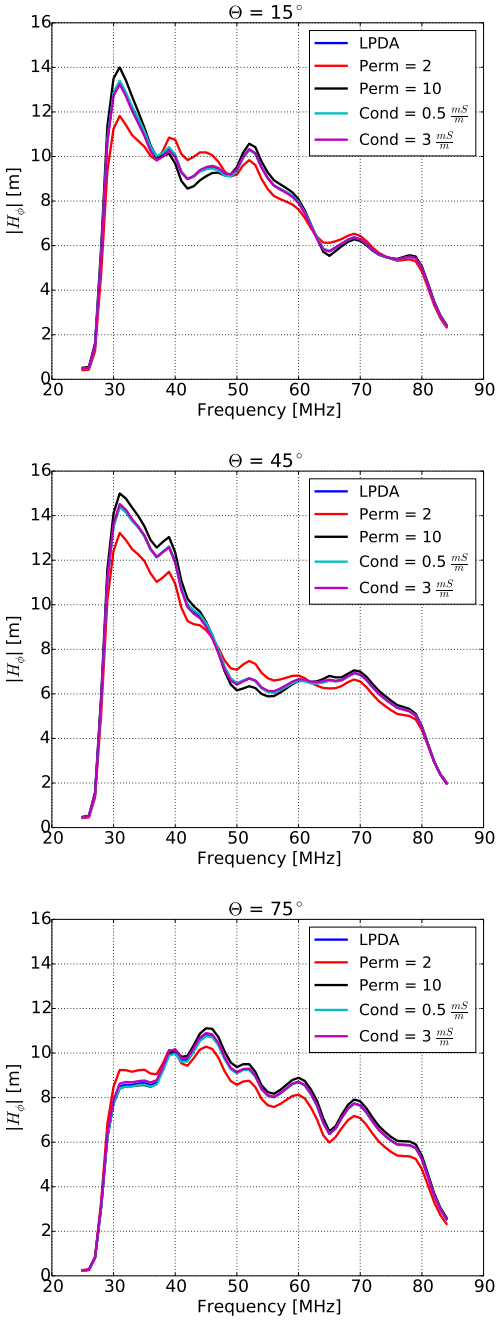

Figure 7.6: *Horizontal component of the LPDA vector effective length $|H_\phi|$ as a function of the frequency at a zenith angle of* ***(from top to bottom)*** $15\,^\circ$, $45\,^\circ$, *and* $75\,^\circ$ *obtained from the original simulation (blue line) and compared to those obtained from the modified simulation with different ground conditions: permittivity* = 2 *(red line), permittivity* = 10 *(black line), conductivity* = $0.5\ \frac{\mathrm{mS}}{\mathrm{m}}$ *(light blue line), conductivity* = $3\ \frac{\mathrm{mS}}{\mathrm{m}}$ *(magenta line).*

the influence of the ground permittivity on the antenna response is higher. The influence varies with the frequency and the zenith angle forming a wave-like pattern. The agreement between the modified simulation with a ground permittivity of 2 (10) and the standard simulation of the meridional component of the LPDA VEL $|H_\theta|$ is illustrated in the diagram of their ratio versus zenith angle Θ and frequency f in the upper left panel of Fig. 7.12 (Fig. 7.13). In the upper right panel of Fig. 7.12

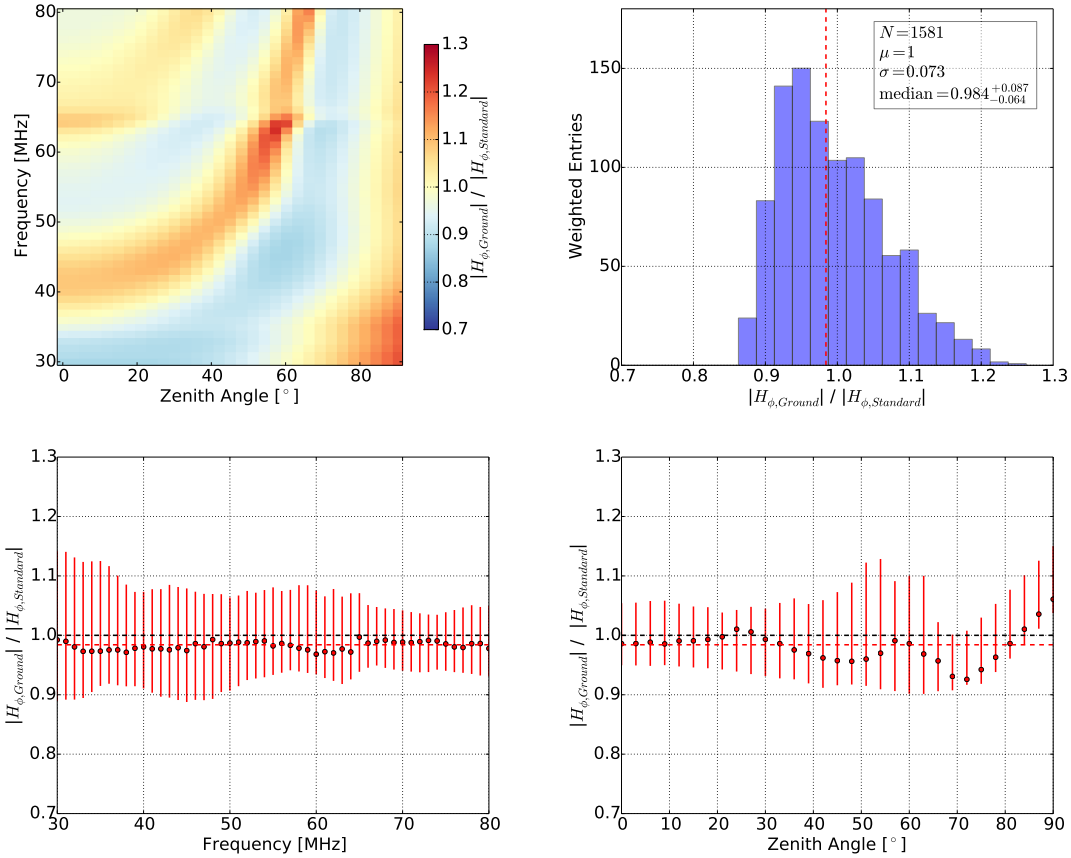

Figure 7.7: *Horizontal component of the LPDA vector effective length $|H_\phi|$ obtained from the modified simulation with a ground permittivity of 2 compared to those obtained from the standard simulation.* ***(top left)*** *Ratio of the modified simulation and standard simulation for all frequencies as a function of the zenith angle Θ.* ***(top right)*** *Histogram of all ratios of the modified simulation and standard simulation for all frequencies and all zenith angles weighted with $\sin(\Theta)$. The median value is marked as the red dashed line.* ***(bottom left)*** *Median (red dots) and the 68 % quantile (red error bars) of the zenith angle weighted ratio distribution as a function of the frequency.* ***(bottom right)*** *Median (red dots) and the 68 % quantile (red error bars) of the ratio distribution as a function of Θ. The red dashed lines mark the overall zenith angle weighted median in both lower diagrams.*

(Fig. 7.13), all ratios are filled into a histogram with entries weighted by $\sin(\Theta)$ in consideration of the decrease in field of view at small zenith angles. The modified simulation and the standard simulation agree to within 0.2 % (0.3 %) in the median. The fluctuation described by the 68 % quantile is at the level of $\frac{0.067+0.077}{2} = 7.2\,\%$ ($\frac{0.052+0.049}{2} = 5.1\,\%$). In the two lower panels of Fig. 7.12 (Fig. 7.13), the median ratio as a function of the frequency (left) and as a function of the zenith angle (right) are shown. In both cases, the red error bars mark the 68 % quantile of the distributions. The comparisons of the modified simulations with different ground conductivity and the standard simulation are shown in the appendix C.1.

While a modified simulation with a smaller permittivity lowers the meridional LPDA VEL component $|H_\theta|$ compared to those of the standard simulation, a larger permittivity increases $|H_\theta|$ and vice versa. Thus, both modified simulations can be interpreted as upper and lower limits of $|H_\theta|$. The

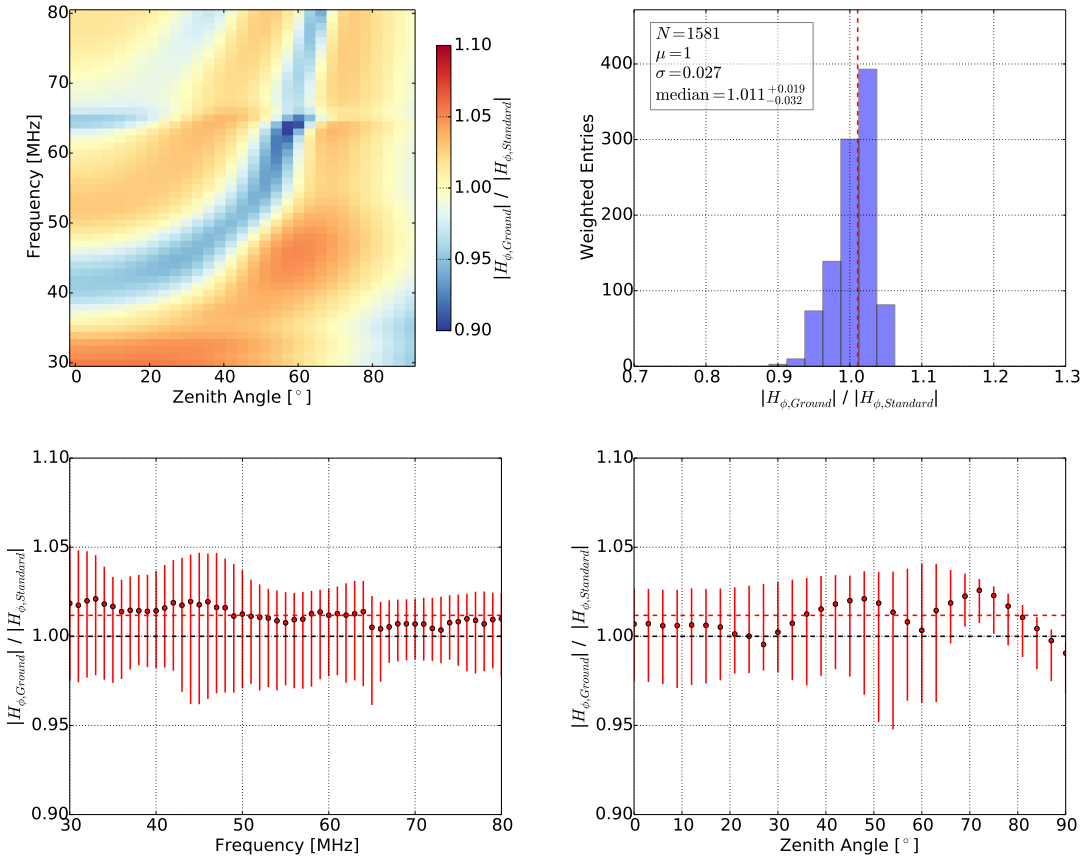

Figure 7.8: *Horizontal component of the LPDA vector effective length $|H_\phi|$ obtained from the modified simulation with a ground permittivity of 10 compared to those obtained from the standard simulation.* ***(top left)*** *Ratio of the modified simulation and standard simulation for all frequencies as a function of the zenith angle Θ.* ***(top right)*** *Histogram of all ratios of the modified simulation and standard simulation for all frequencies and all zenith angles weighted with $\sin(\Theta)$. The median value is marked as the red dashed line.* ***(bottom left)*** *Median (red dots) and the 68 % quantile (red error bars) of the zenith angle weighted ratio distribution as a function of the frequency.* ***(bottom right)*** *Median (red dots) and the 68 % quantile (red error bars) of the ratio distribution as a function of Θ. The red dashed lines mark the overall zenith angle weighted median in both lower diagrams.*

relative influence I of the ground permittivity on $|H_\theta|$ is then determined by half the ratio of the difference between both modified simulations to the standard simulation according to Eq. (7.1) which is histogramed in Fig 7.14 for all frequencies and all zenith angles. In the case of an applied ground permittivity of 2 and of 10, the influence on the meridional LPDA VEL component $|H_\theta|$ is at the level of 0.5 % in the median for all frequencies and zenith angles with a scatter of less then 6 %.

7.3 Influence of the Electronics Box

In this section, the influence of an electronics box located underneath the LPDA on the LPDA VEL is discussed. The electronics box is located in the north-west direction in a horizontal distance of about 1.5 m to the LPDA which is in the near-field region of the LPDA. This box contains the whole

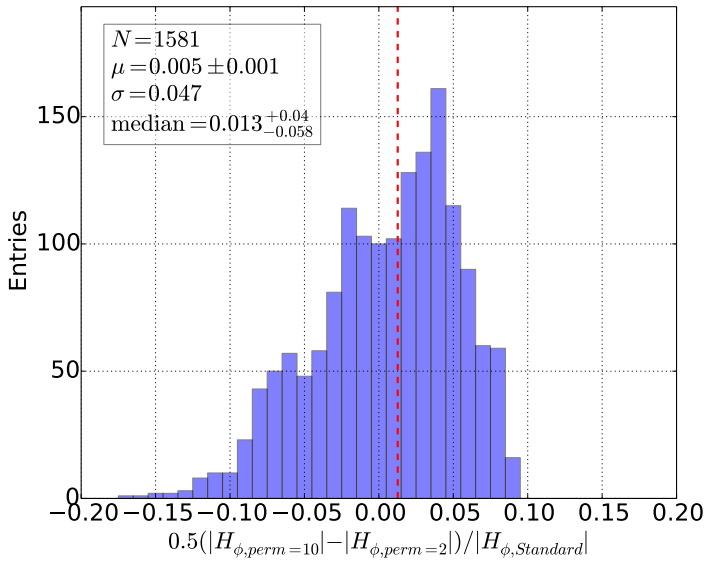

Figure 7.9: *Histogram of the relative influence of the ground permittivity on $|H_\phi|$ which is determined by half the ratio of the difference between both modified simulations with an applied permittivity of 2 and of 10 to the standard simulation $|H_{\phi,Standard}|$ for all frequencies and all zenith angles. The median value is marked by the red dashed line.*

electronics to operate the LPDA radio station. The electronics box is made of conductive material. Furthermore, solar panels as the power supply of the station are mounted on top of the box (cf. Fig. 4.10 in Sec. 4.3.1). These electrical and conductive parts have a direct impact on the antenna VEL of the LPDA. Disturbing influences on the LPDA VEL of the electric devices located inside the box are not expected as the electronics box acts as a Faraday cage and electric field coming from these devices are shielded.

The NEC-2 realization of the LPDA model modified by an electronics box is shown in Fig. 7.15. The model of the electronics box consider all specifications as dimensions and location of the real electronics box. Due to the position and the structure of the electronics box, a different influence of the box on a north-south and on an east-west polarized LPDA is expected. Furthermore, an asymmetric antenna response pattern is expected for both polarizations. To investigate the influence of the electronics box on the LPDA VEL multiple simulations have been performed for the case of a north-south and east-west polarized antenna in both azimuthal direction with highest antenna sensitivity of the respective VEL component. In the following, the influence of the electronics box on the horizontal VEL $|H_\phi|$ is discussed first and afterwards the influence on the meridional VEL $|H_\theta|$ is presented.

7.3.1 Horizontal Component of the Vector Effective Length

Here, the influence of the electronics box on the horizontal component of the LPDA VEL $|H_\phi|$ is discussed. In Fig. 7.16, the LPDA VEL of a north-south and east-west polarized antenna for three different frequencies of 35 MHz, 55 MHz, and 75 MHz in comparison to the standard LPDA simulation is presented. To investigate the asymmetric influence of the electronics box, the LPDA VEL of

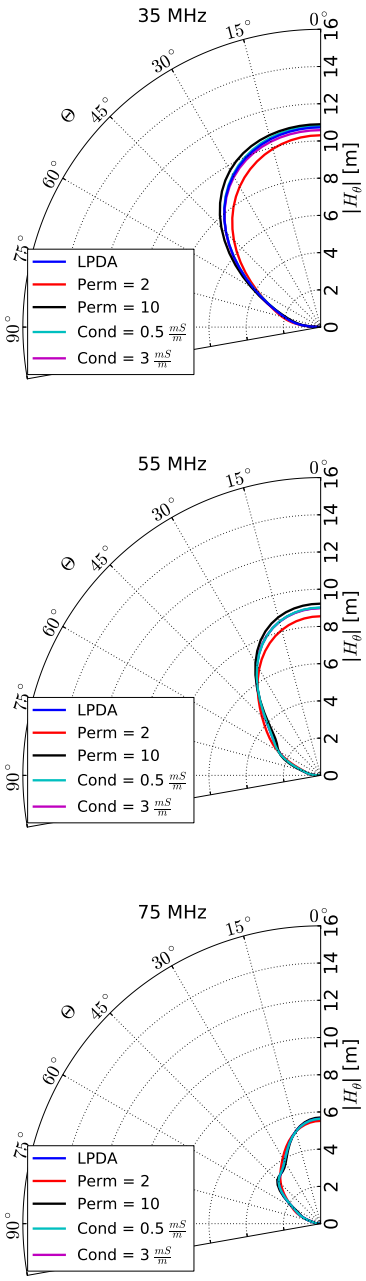

Figure 7.10: *Meridional component of the LPDA vector effective length* $|H_\theta|$ *as a function of the zenith angle* Θ *at a frequency of* ***(from top to bottom)*** $35\,\mathrm{MHz}$, $55\,\mathrm{MHz}$, *and* $75\,\mathrm{MHz}$ *obtained from the original simulation (blue line) and compared to those obtained from the modified simulation with different ground conditions: permittivity* = 2 *(red line), permittivity* = 10 *(black line), conductivity* = $0.5\,\frac{\mathrm{mS}}{\mathrm{m}}$ *(light blue line), conductivity* = $3\,\frac{\mathrm{mS}}{\mathrm{m}}$ *(magenta line).*

the four azimuthal directions with highest antenna sensitivity corresponding to the north direction, the south direction, the east direction and the west direction are simulated. Furthermore, in Fig. 7.17, the respective LPDA VEL are shown as a function of the frequency at a zenith angle of $15\,^\circ$, $45\,^\circ$, and $75\,^\circ$.

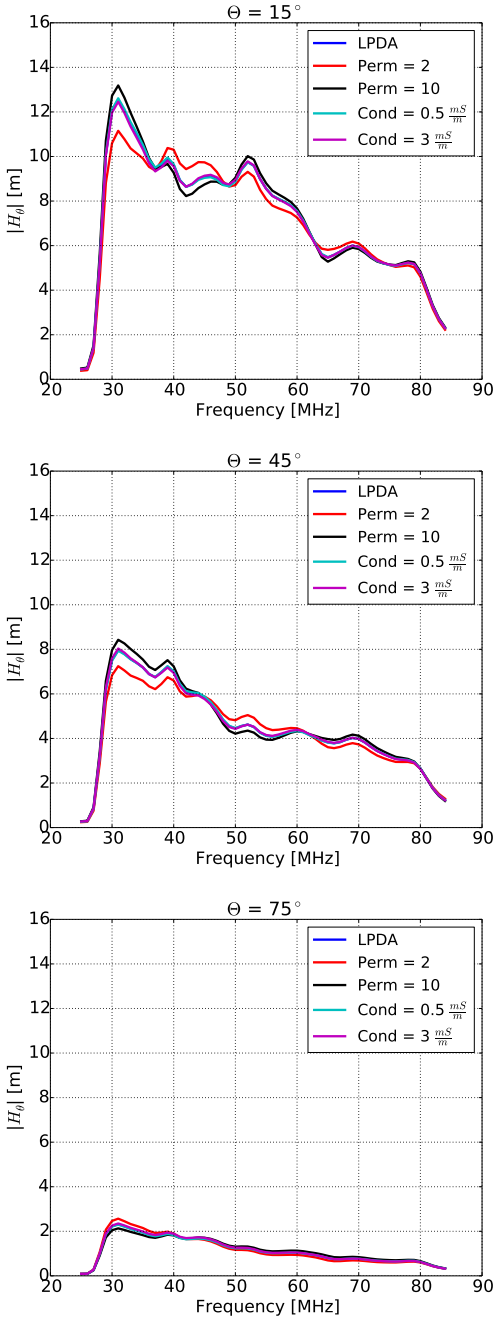

Figure 7.11: *Meridional component of the LPDA vector effective length $|H_\theta|$ as a function of the frequency at a zenith angle of* ***(from top to bottom)*** $15\,^\circ$, $45\,^\circ$, *and* $75\,^\circ$ *obtained from the original simulation (blue line) and compared to those obtained from the modified simulation with different ground conditions: permittivity* = 2 *(red line), permittivity* = 10 *(black line), conductivity* = $0.5\ \frac{\mathrm{mS}}{\mathrm{m}}$ *(light blue line), conductivity* = $3\ \frac{\mathrm{mS}}{\mathrm{m}}$ *(magenta line).*

The simulations exhibit small influences of the electronics box on the horizontal component of the LPDA VEL $|H_\phi|$ in the case of both antenna polarizations and in both main sensitive azimuthal directions. The main influence is found at small frequencies and small zenith angles. The larger the frequency, the smaller are the variations between the simulations. The agreement between the modified simulation of an east-west polarized LPDA in the north direction and the standard simula-

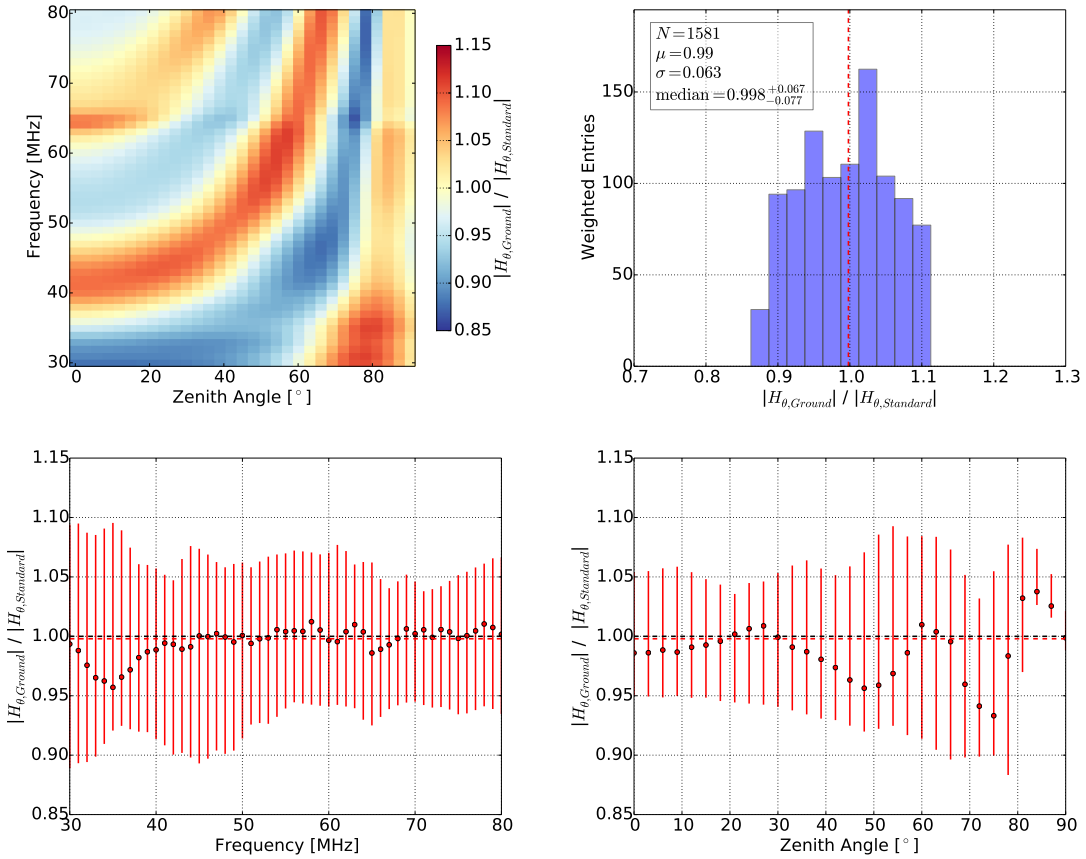

Figure 7.12: *Meridional component of the LPDA vector effective length $|H_\theta|$ obtained from the modified simulation with a ground permittivity of 2 compared to those obtained from the standard simulation.* ***(top left)*** *Ratio of the modified simulation and standard simulation for all frequencies as a function of the zenith angle Θ.* ***(top right)*** *Histogram of all ratios of the modified simulation and standard simulation for all frequencies and all zenith angles weighted with $\sin(\Theta)$. The median value is marked as the red dashed line.* ***(bottom left)*** *Median (red dots) and the 68 % quantile (red error bars) of the zenith angle weighted ratio distribution as a function of the frequency.* ***(bottom right)*** *Median (red dots) and the 68 % quantile (red error bars) of the ratio distribution as a function of Θ. The red dashed lines mark the overall zenith angle weighted median in both lower diagrams.*

tion of the horizontal component of the LPDA VEL $|H_\phi|$ is illustrated in the diagram of their ratio versus zenith angle Θ and frequency f in the upper left panel of Fig. 7.18. In the upper right panel of Fig. 7.18, all ratios are filled into a histogram with entries weighted by $\sin(\Theta)$ in consideration of the decrease in field of view at small zenith angles. The modified simulation and the standard simulation agree to within 0.3 % in the median. The fluctuation described by the 68 % quantile is at the level of $\frac{0.021+0.03}{2} = 2.6\,\%$. In the two lower panels of Fig. 7.18, the median ratio as a function of the frequency (left) and as a function of the zenith angle (right) is shown. In both cases, the red error bars mark the 68 % quantile of the distributions. The comparisons of the other modified simulations and the standard simulation are shown in the appendix C.2.

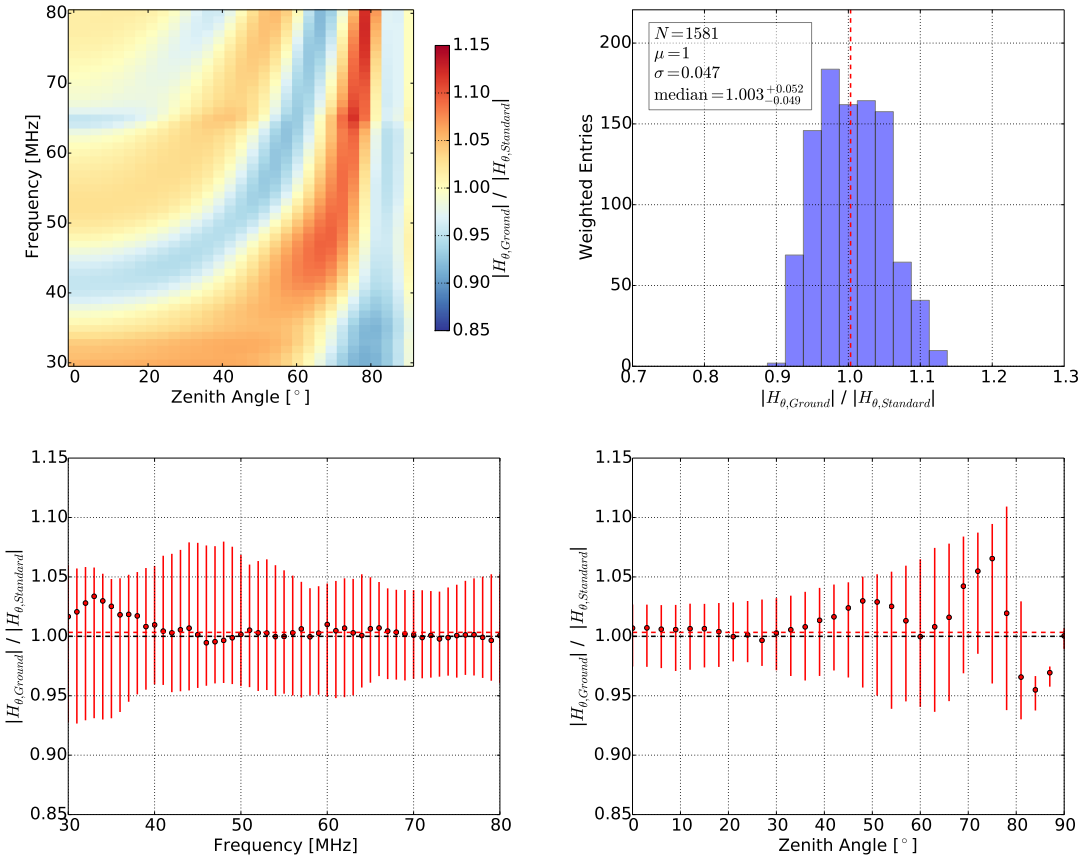

Figure 7.13: *Meridional component of the LPDA vector effective length $|H_\theta|$ obtained from the modified simulation with a ground permittivity of 10 compared to those obtained from the standard simulation.* ***(top left)*** *Ratio of the modified simulation and standard simulation for all frequencies as a function of the zenith angle Θ.* ***(top right)*** *Histogram of all ratios of the modified simulation and standard simulation for all frequencies and all zenith angles weighted with $\sin(\Theta)$. The median value is marked as the red dashed line.* ***(bottom left)*** *Median (red dots) and the 68 % quantile (red error bars) of the zenith angle weighted ratio distribution as a function of the frequency.* ***(bottom right)*** *Median (red dots) and the 68 % quantile (red error bars) of the ratio distribution as a function of Θ. The red dashed lines mark the overall zenith angle weighted median in both lower diagrams.*

7.3.2 Meridional Component of the Vector Effective Length

In this subsection, the influence of the electronics box on the meridional component of the LPDA VEL $|H_\theta|$ is discussed. In Fig. 7.19, the LPDA VEL of a north-south and east-west polarized antenna for three different frequencies of 35 MHz, 55 MHz, and 75 MHz in comparison to the standard LPDA simulation are presented. To investigate the asymmetric influence of the electronics box, the LPDA VEL of the four azimuthal directions with highest antenna sensitivity corresponding to the north direction, the south direction, the east direction and the west direction is simulated. Furthermore, in Fig. 7.20, the respective LPDA VEL is shown as a function of the frequency for a constant zenith angle of 15 °, 45 °, and 75 °.

The simulations exhibit larger influences of the electronics box on the meridional component of the LPDA VEL $|H_\theta|$ than on the horizontal component of the LPDA VEL $|H_\phi|$. The main influence is

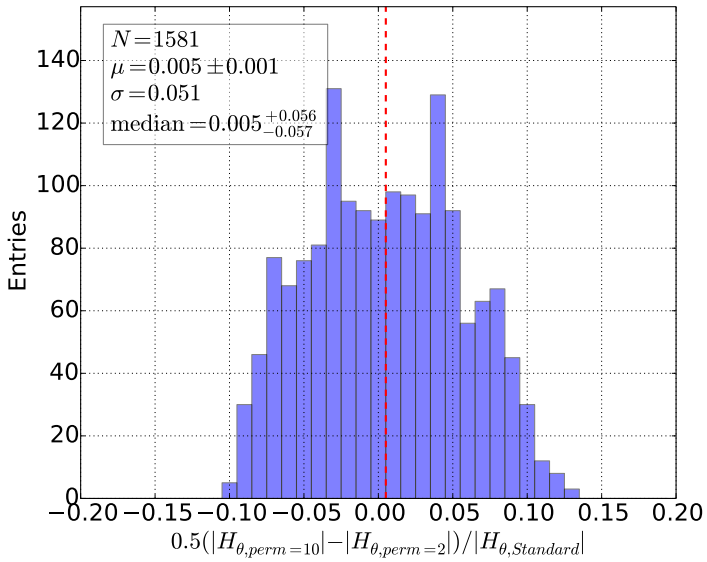

Figure 7.14: *Histogram of the relative influence of the ground permittivity on $|H_\theta|$ which is determined by half the ratio of the difference between both modified simulations with an applied permittivity of 2 and of 10 to the standard simulation $|H_{\theta,Standard}|$ for all frequencies and all zenith angles. The median value is marked by the red dashed line.*

found at zenith angles larger than $60\,^\circ$. The agreement between the modified simulation of an east-west polarized LPDA in the east direction and the standard simulation of the meridional component of the LPDA VEL $|H_\theta|$ is illustrated in the diagram of their ratio versus zenith angle Θ and frequency f in the upper left panel of Fig. 7.21. In the upper right panel of Fig. 7.21, all ratios are filled into a histogram with entries weighted by $\sin(\Theta)$ in consideration of the decrease in field of view at small zenith angles. The modified simulation and the standard simulation agree to within $1\,\%$ in the median. The fluctuation described by the $68\,\%$ quantile is at the level of $\frac{0.11+0.098}{2} = 10.4\,\%$ dominated by the entries at large zenith angles with small antenna sensitivities. In the two lower panels of Fig. 7.21, the median ratio as a function of the frequency (left) and as a function of the zenith angle (right) is shown. In both cases, the red error bars mark the $68\,\%$ quantile of the distributions. The comparisons of the other modified simulations and the standard simulation are shown in the appendix C.2.

7.4 Influence of an Antenna Misalignment

In this section, the influence of an antenna misalignment is investigated. The LPDA is aligned with a precision better than $1\,^\circ$ to magnetic north and east [159]. In the upper diagrams of Fig. 7.22, the horizontal component and meridional component of the LPDA VEL of a rotated antenna are compared to the LPDA VEL of the standard simulation. The relative VEL difference is shown in the lower diagrams respectively. An antenna rotation lowers the LPDA VEL in both antenna components. Nevertheless, the influence of an LPDA rotation on the LPDA VEL is far below $0.1\,\%$. Thus, the simulation confirms that the LPDA alignment is good enough and does not influence analysis of the

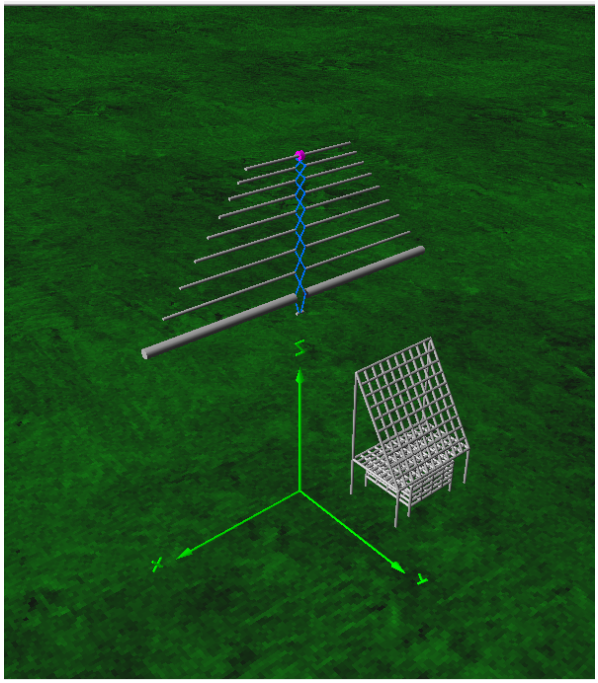

Figure 7.15: *NEC-2 simulation model of an east-west polarized LPDA including an electronic box beneath the antenna. The y-axis marks the north direction.*

radio emission from extensive air showers recorded with the LPDA.

7.5 Discussion

In this section, the simulation results of the LPDA VEL are summarized and discussed. The simulation yields that a misalignment of the LPDA of 1° as well as different ground conductivities do not change the LPDA response pattern neither in the horizontal component $|H_\phi|$ nor in the meridional component $|H_\theta|$. The situation is different in the case of different ground permittivities and as well as in the case of an electronics box beneath the LPDA. In the case of an applied ground permittivity of 2 and of 10, the influence on the horizontal LPDA VEL component $|H_\phi|$ is at the level of $1.3\,\%$ in the median (cf. Fig. 7.9). Simulations of an electronics box beneath an east-west polarized LPDA and in north direction show influences on $|H_\phi|$ of $0.3\,\%$ (cf. upper right panel of Fig. 7.18) in the median which is negligible compared to the influence of the ground permittivity.
In the case of the meridional LPDA VEL component $|H_\theta|$, the influence of different ground permittivities is at the level of $0.5\,\%$ in the median (cf. Fig. 7.14) and impact the whole phase space defined by the frequency and zenith angle as shown in the upper left panels of Fig. 7.12 and Fig. 7.13. The influence of the electronics box is at the level of $1\,\%$ but especially in regions with large zenith angles where the LPDA is less sensitive (cf. Fig. 7.21).
While the electronics box has a constant effect on the LPDA response pattern as the box is located at a fixed position and does not move, the ground permittivity has a time-varying effect. The relative permittivity of soil at the AERA site changes due to different weather conditions and soil humidities. The ground permittivity is not continuously measured at each radio station. Thus, the influence on

the LPDA response pattern changes and is considered as a simulation uncertainty in the comparison between standard simulation and measurement as well as in the analysis of the electric-field reconstruction which is discussed in the next chapter.

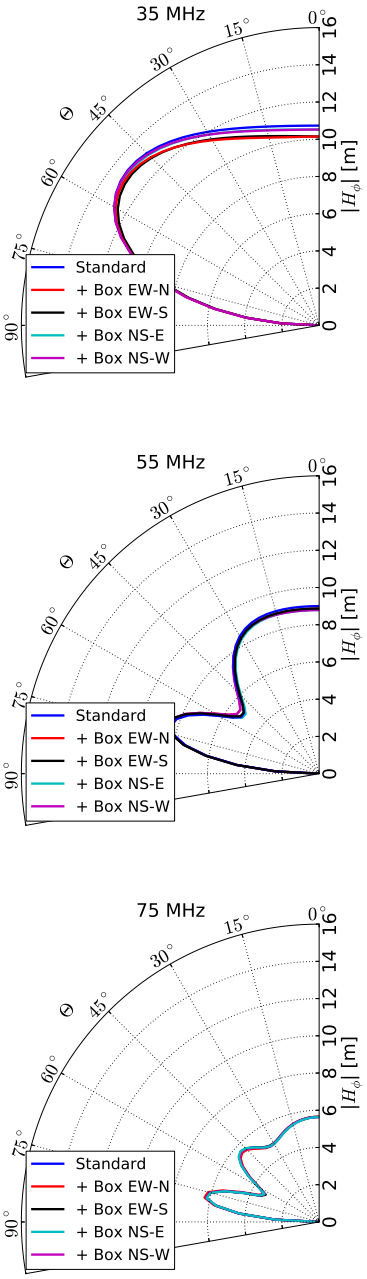

Figure 7.16: *Horizontal component of the LPDA vector effective length (VEL) $|H_\phi|$ obtained from the standard simulation (blue line) and obtained from the simulation modified with an electronics box located in the north-west of the LPDA. The VEL is presented as a function of the zenith angle Θ at a frequency of* ***(from top to bottom)*** $35\,\mathrm{MHz}$, $55\,\mathrm{MHz}$, *and* $75\,\mathrm{MHz}$ *of the east-west (EW) and north-south (NS) polarized LPDA for the main sensitive axis which corresponds to the four different azimuthal directions: north (N), south (S), east (E) and west (W) respectively.*

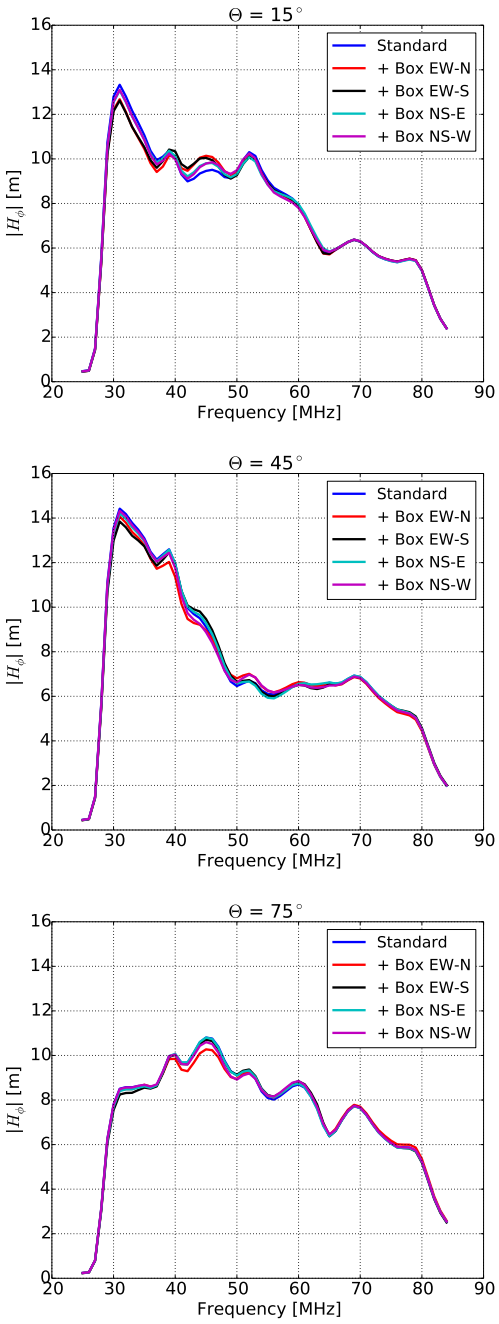

Figure 7.17: *Horizontal component of the LPDA vector effective length (VEL) $|H_\phi|$ obtained from the standard simulation (blue line) and obtained from the simulation modified with an electronics box located in the north-west of the LPDA. The VEL is presented as a function of the frequency at a zenith angle of* ***(from top to bottom)*** $15\,^\circ$, $45\,^\circ$, *and* $75\,^\circ$ *of the east-west (EW) and north-south (NS) polarized LPDA for the main sensitive axis which corresponds to the four different azimuthal directions: north (N), south (S), east (E) and west (W) respectively.*

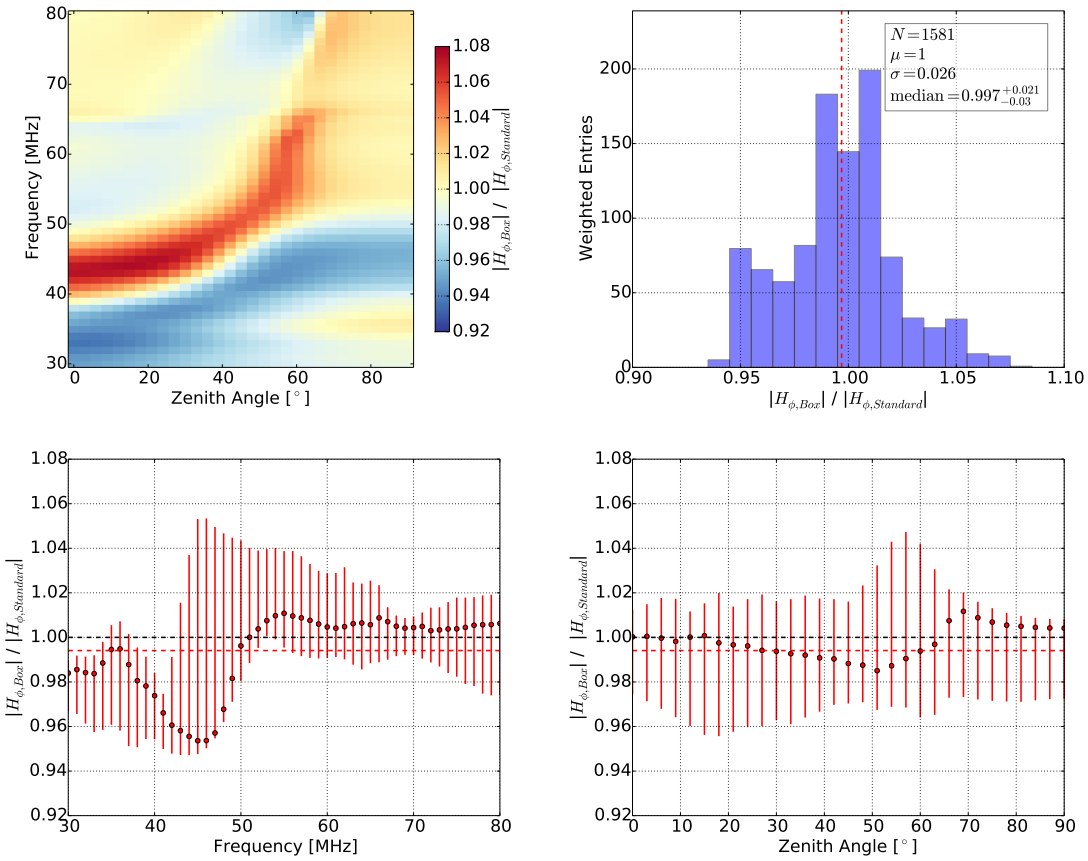

Figure 7.18: *Horizontal component of the LPDA vector effective length $|H_\phi|$ obtained from the modified simulation with an electronics box of an east-west polarized LPDA in the north direction compared to those obtained from the standard simulation.* ***(top left)*** *Ratio of the modified simulation and standard simulation for all frequencies as a function of the zenith angle Θ.* ***(top right)*** *Histogram of all ratios of the modified simulation and standard simulation for all frequencies and all zenith angles weighted with $\sin(\Theta)$. The median value is marked as the red dashed line.* ***(bottom left)*** *Median (red dots) and the $68\,\%$ quantile (red error bars) of the zenith angle weighted ratio distribution as a function of the frequency.* ***(bottom right)*** *Median (red dots) and the $68\,\%$ quantile (red error bars) of the ratio distribution as a function of Θ. The red dashed lines mark the overall zenith angle weighted median in both lower diagrams.*

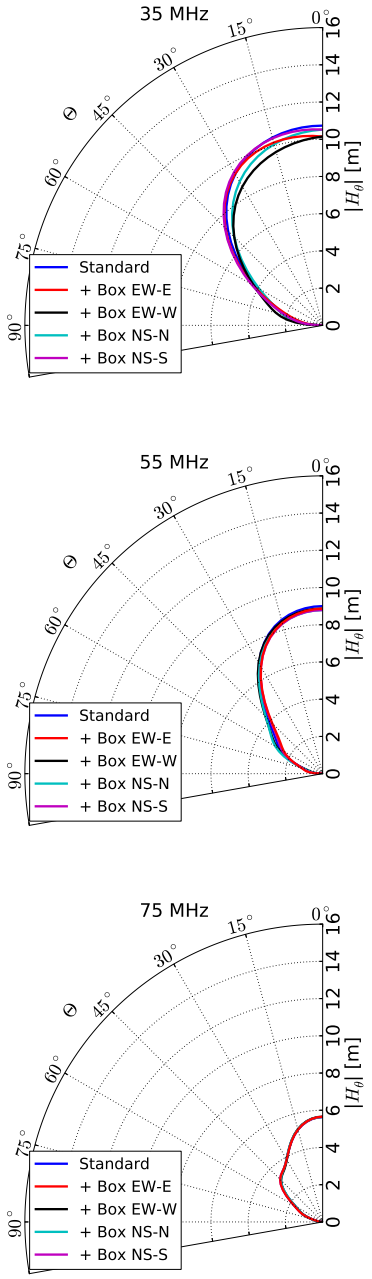

Figure 7.19: *Meridional component of the LPDA vector effective length (VEL) $|H_\theta|$ obtained from the standard simulation (blue line) and obtained from the simulation modified with an electronics box located in the north-west of the LPDA. The VEL is presented as a function of the zenith angle Θ at a frequency of* ***(from top to bottom)*** $35\,\mathrm{MHz}$, $55\,\mathrm{MHz}$, *and* $75\,\mathrm{MHz}$ *of the east-west (EW) and north-south (NS) polarized LPDA for the main sensitive axis which corresponds to the four different azimuthal directions: north (N), south (S), east (E) and west (W) respectively.*

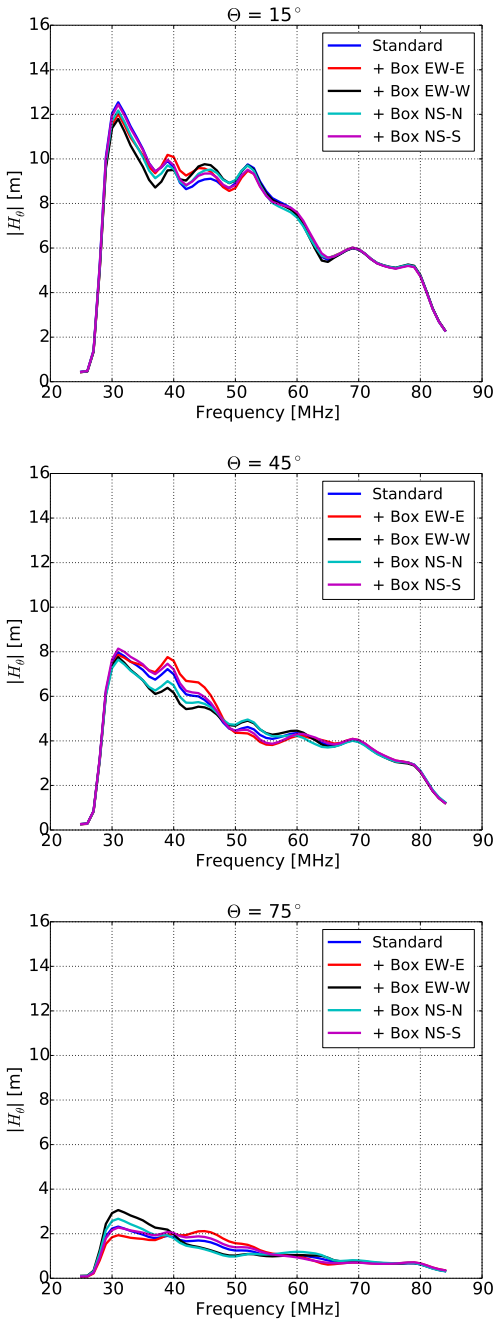

Figure 7.20: *Meridional component of the LPDA vector effective length (VEL) $|H_\theta|$ obtained from the standard simulation (blue line) and obtained from the simulation modified with an electronics box located in the north-west of the LPDA. The VEL is presented as a function of the frequency at a zenith angle of* ***(from top to bottom)*** $15\,^\circ$, $45\,^\circ$, *and* $75\,^\circ$ *of the east-west (EW) and north-south (NS) polarized LPDA for the main sensitive axis which corresponds to the four different azimuthal directions: north (N), south (S), east (E) and west (W) respectively.*

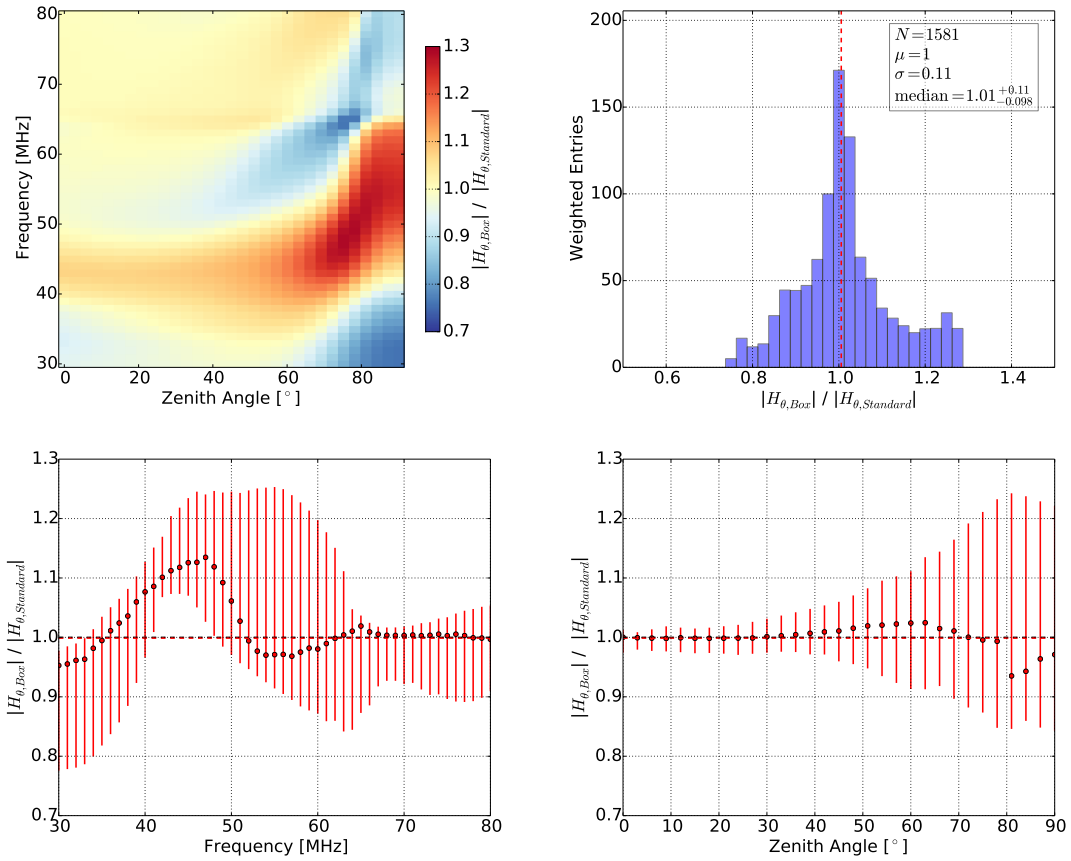

Figure 7.21: *Meridional component of the LPDA vector effective length $|H_\theta|$ obtained from the modified simulation with an electronics box of an east-west polarized LPDA in the east direction with those obtained from the standard simulation.* ***(top left)*** *Ratio of the modified simulation and standard simulation for all frequencies as a function of the zenith angle Θ.* ***(top right)*** *Histogram of all ratios of the modified simulation and standard simulation for all frequencies and all zenith angles weighted with $\sin(\Theta)$. The median value is marked as the red dashed line.* ***(bottom left)*** *Median (red dots) and the $68\,\%$ quantile (red error bars) of the zenith angle weighted ratio distribution as a function of the frequency.* ***(bottom right)*** *Median (red dots) and the $68\,\%$ quantile (red error bars) of the ratio distribution as a function of Θ. The red dashed lines mark the overall zenith angle weighted median in both lower diagrams.*

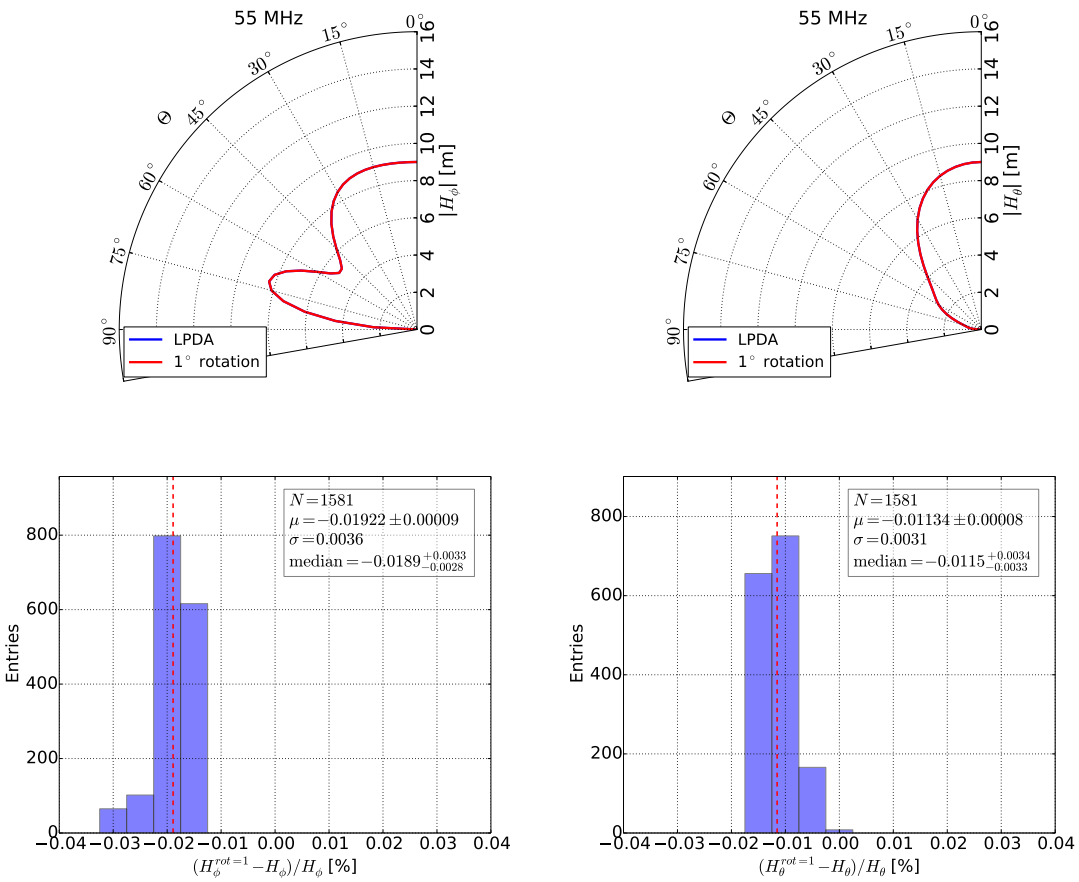

Figure 7.22: *Influence of an LPDA rotated by* 1° *on the horizontal component of the LPDA vector effective length (VEL)* $|H_\phi|$ ***(left)*** *and on the meridional component* $|H_\theta|$ ***(right)***. ***(top)*** *The LPDA VEL as a function of the zenith angle* Θ *at* 55 MHz. *The VEL obtained from the standard simulation (modified simulation with rotated antenna) is indicated by the blue (red) line.* ***(bottom)*** *Histogram of the relative difference between standard simulation and the simulation of the rotated antenna for all zenith angles in steps of* 3° *and a frequency range from* 30 MHz *to* 80 MHz *in steps of* 1 MHz.

8

Measurement of the LPDA Response Pattern

Most parts of this chapter have been published in:

A. Aab et al. (Pierre Auger Collaboration)
"Calibration of the Logarithmic-Periodic Dipole Antenna (LPDA) Radio Stations at the Pierre Auger Observatory using an Octocopter"
J. Instrum. **12** (2017) T10005
The work presented in this publication was primarily performed by the author of this thesis. The text of the publication has been written by the author of this thesis and was revised and copy-edited by the co-authors of the publication.

The antenna to detect the electric field and a thorough description of its frequency and directional-dependent sensitivity is of central importance for analysis of radio emission from extensive air showers. Accurate and precise knowledge of the antenna response pattern is essential to reconstruct the electric field (refer to Sec 3.8) and then enables high quality measurements of the cosmic-ray properties. For a complete description of the antenna response pattern, an absolute antenna calibration needs to be performed. The uncertainties of the absolute calibration directly impact the energy scale for air shower measurements from radio detectors. Therefore, a central challenge of the absolute antenna calibration is to reduce the uncertainties of the antenna response pattern to the level of $10\,\%$ which is a significant improvement in comparison with the uncertainties obtained in calibration campaigns at other radio detectors [32–34].

In this chapter, the reconstruction quality of the electric-field signal from the measured voltage trace is investigated as the voltage trace includes the directional characteristics of the antenna and the dispersion of the signal owing to the antenna size. All information are described with the vector effective length (VEL) $\vec{H}$, a measure that relates the voltage to the incoming electric field as explained in Sec. 3.4.

One antenna of the subset of 24 radio stations equipped with logarithmic periodic dipole antennas (LPDAs) is investigated here exemplarily. This antenna is representative of all the LPDAs which are mechanically and electrically identical at the percent level [203]. The LPDA is explained in detail in Sec. 4.3.2. While the low-noise amplifier (LNA) attached to the antenna was included in the signal chain during the calibration, amplifiers and the subsequent electronics of all radio stations have been characterized individually. The LNA of the radio station amplifies the signal by $18.1\,\mathrm{dB}$. The amplification is nearly constant in the frequency range $30\,\mathrm{MHz}$ to $80\,\mathrm{MHz}$ and varies at the level of $0.5\,\mathrm{dB}$. The LPDA antennas have the advantage of low sensitivity to radio waves reflecting from the ground

far-field region	$\frac{2L^2}{\lambda}$ **[m]**	$\frac{\lambda}{2\pi}$ **[m]**	$5L$ **[m]**	1.6λ **[m]**
$f = 30\,\mathrm{MHz}$	3.6	1.6	21	16
$f = 80\,\mathrm{MHz}$	9.6	0.6	21	6

Table 8.1: Definitions of the far-field region of the LPDA with a largest dimension of $L = 4.25\,\mathrm{m}$ and the frequency range of 30 MHz to 80 MHz.

which makes them largely independent of potentially changing ground conditions (refer to Sec. 7.2). The LPDA antennas have been studied before and a first absolute calibration of one signal polarization was performed in 2012 giving an overall systematic uncertainty of 12.5 % [152]. In comparison to the first absolute calibration of AERA, in this chapter a new absolute calibration is presented using a new setup enabling a much more dense sampling of the arrival directions, more field polarization measurements, and an extended control of systematic effects including the full repetition of calibration series. To ensure far-field measurements, instead of the previously used balloon, a drone was employed which carries a separate signal generator and a calibrated transmitting antenna.
This chapter is structured as follows. Firstly, the LPDA antenna and the calibration setup are specified. Then, the calibration strategy is presented using one example flight where $|\vec{H}|$ is measured on site at the Pierre Auger Observatory at one of the radio stations. The main section contains detailed comparisons of all the measurements with the calculated vector effective length and the determination of the uncertainties in the current understanding of the antenna. Finally, the influence of the calibration results are discussed in applications.

8.1 Setup

The antenna VEL of the LPDA is determined by transmitting a defined signal from a calibrated signal source from different arrival directions and measuring the LPDA response. The signal source consists of a signal generator, producing known signals, and a calibrating transmitting antenna with known emission characteristics. The transmission measurement needs to be done in the far-field region. In Tab. 8.1, the far-field conditions of the LPDA with a largest dimension of $L = 4.25\,\mathrm{m}$ and the frequency range of 30 MHz to 80 MHz according to Eq. 3.4 to Eq. 3.6 are presented. Far-field conditions are fulfilled to a reasonable approximation at a distance of $R > 21\,\mathrm{m}$.
In a first calibration campaign [152], a large weather balloon was used to lift the transmitting antenna and a cable to the signal source placed on ground. As a vector network analyzer was used to provide the source and to measure the antenna under test (AUT) output, this transmission measurement allowed to determine both, the VEL magnitude and phase. This setup has the disadvantages that it requires calm weather conditions and the cost per flight including the balloon and gas are high. Moreover, the cable potentially impacts the measurements if not properly shielded. In this first calibration campaign only the horizontal VEL was investigated. A new calibration campaign was necessary and a new setup was developed.
Now, a signal generator as well as a transmission antenna were both mounted beneath a flying drone, a so-called remotely piloted aircraft (RPA), to position the calibration source. Hence, the cable from

ground to the transmitting antenna is not needed anymore. Furthermore, the RPA is much less dependent on wind, and thus it is easier to perform the measurement compared to the balloon-based calibration. The new calibration is performed with a higher repetition rate and with more positions per measurement.
During the measurement, the RPA flies straight up to a height of typically $25\,\mathrm{m}$ to $35\,\mathrm{m}$ and then towards the AUT until it is directly above it. Finally, it flies back and lands again at the starting position. A sketch of the setup is shown at the top of Fig. 8.1.

The RPA used here was an octocopter obtained from the company MikroKopter [239]. The octocopter with the transmitting antenna mounted beneath the octocopter is shown in Fig. 8.2. The octocopter consists of a center plate and of eight fiber rods where the eight octocopter engines are mounted. The center plate holds the accumulator which provides a $16\,\mathrm{V}$ power supply. The accumulator has a capacity of $6600\,\mathrm{mAh}$ resulting in a flight time of about $10\,\mathrm{min}$ per calibration flight with a maximal payload of about $2.5\,\mathrm{kg}$. The octocopter electronics consists of four printed circuit boards which are arranged in an electronics tower as shown on the left side of Fig. 8.2 and are briefly explained in the following from the bottom to the top. The power supply, the engines, and the control electronics are connected by a power distribution board. The control electronics are located in the flight-control board which lies on top of the power distribution board. The control electronics ensure smooth and stable flights using the information delivered by important flight control sensors as acceleration sensors, three gyroscope sensors, and a barometer, which provides information about the octocopter height above ground. On the top, the navi-control board delivers an interface to a GPS module and enables measuring the horizontal octocopter position. Additionally, the octocopter alignment with respect to the Earth's magnetic field is measured by a compass. Gyroscopes and compass provide information about the octocopter rotation angles (yaw, pitch, roll as defined in Fig. 8.1) which are later used to determine the orientation of the transmission antenna with respect to the AUT. On top of the navi-control board, the GPS-receiver is located. All flight data are autonomously recorded nearly each second, which enables measuring the VEL with good resolution in zenith angle Θ, and are stored on an SD-card. Such an octocopter also has been used for the fluorescence detector [180] and CROME [240] calibrations.
To obtain further improvements of the octocopter position determination, an optical method using two cameras taking pictures of the flight was developed. The cameras are placed on orthogonal axes with a distance of around $100\,\mathrm{m}$ to the AUT. Canon Ixus 132 cameras [241] with a resolution of $16\,\mathrm{MegaPixel}$ are utilized. They are set to an autonomous mode where they take pictures every three seconds. From these pictures, the full flight path of the octocopter can be reconstructed. The method is explained in detail in [242, 243].
The position of the LPDA station was measured by a differential GPS (DGPS) (Hiper V system [244]) and is therefore known with centimeter accuracy.
The reference spectrum generator, model RSG1000 produced by the company TESEQ [245], is used as the signal generator. It continuously produces a frequency comb spectrum between $5\,\mathrm{MHz}$ and $1000\,\mathrm{MHz}$ with a spacing of $5\,\mathrm{MHz}$. This signal is further amplified in order to accomplish power well above background for the measurement. The output signal injected into the transmission antenna has been determined twice in the lab using an FSH4 spectrum analyzer from the company Rohde&Schwarz [231] and using an Agilent N9030A ESA spectrum analyzer [246] both with a read-

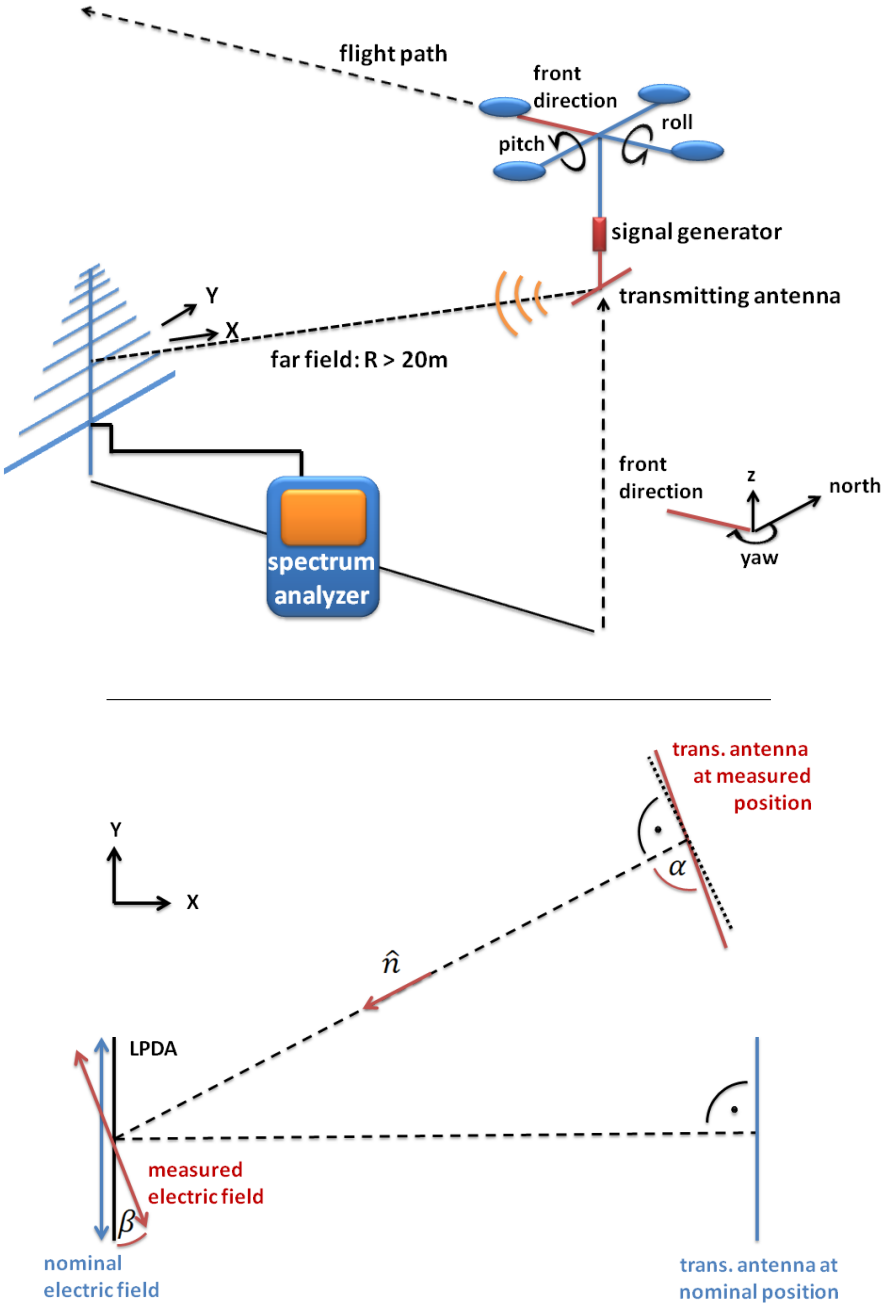

Figure 8.1: ***(top)*** *LPDA calibration setup. The calibration signal is produced by a signal generator and radiated by a transmitting antenna. Both the signal generator and the transmitting antenna are attached underneath a flying drone, a so-called RPA, to realize far-field conditions during the measurement. On arrival of the signal at the LPDA, the antenna response is measured using a spectrum analyzer. The orientation of the RPA is described by the yaw (twist of front measured from north in the mathematically negative direction), and the tilt by the pitch and the roll angles.* ***(bottom)*** *Sketch of the expected (blue arrow) and measured (red arrow) electric-field polarization at the LPDA emitted by the transmitting antenna from the nominal (blue line) and measured (red line) position. The real transmitting antenna position is shifted from the nominal position, e.g., due to GPS accuracy. This misplacement changes the electric-field strength and polarization measured at the LPDA and, therefore, influences the measurement.*

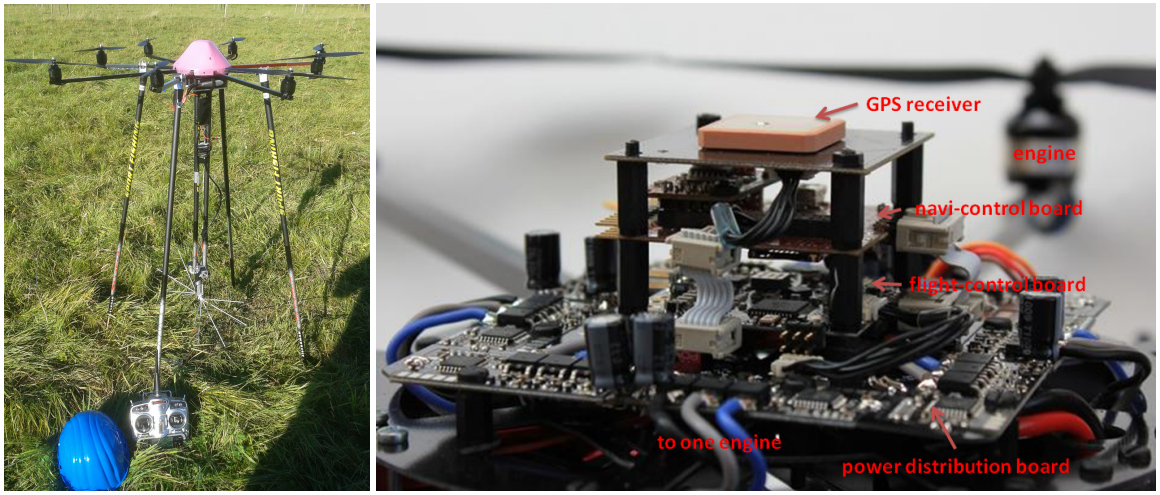

Figure 8.2: *A remotely piloted aircraft (RPA) is used to position the transmitting antenna.* ***(left)*** *The RPA used in the calibration measurement was an octocopter obtained from the company MikroKopter. The transmitting antenna is mounted beneath the octocopter.* ***(right)*** *Electronics tower of the octocopter consisting of several printed circuit boards (from the bottom to the top): a power distribution board, a flight-control board, a navi-control board and a GPS-receiver [239].*

out impedance of $50\,\Omega$.

In an effort to maintain the strict $2.5\,\mathrm{kg}$ octocopter payload limit, a small biconical antenna from Schwarzbeck (model BBOC 9217 [247]) is mounted $0.7\,\mathrm{m}$ beneath the octocopter. This antenna has been calibrated by the manufacturer in the frequency range from $30\,\mathrm{MHz}$ to $1000\,\mathrm{MHz}$ with an accuracy of $0.5\,\mathrm{dB}$. The transmission antenna and its NEC-2 realization is shown in Fig. 8.3. This response pattern and its uncertainty comprise all mismatch effects when connecting a $50\,\Omega$ signal source to such a transmitting antenna. The power received at the LPDA during the calibration procedure is measured using the same FSH4 spectrum analyzer as above.

The absolute value of the different VEL components mentioned in Eq. (3.22) are determined by performing multiple flights in which the orientation of the transmitting antenna is varied with respect to the AUT. Sketches of the antenna orientations during the flights are shown on the left side of Fig. 8.4. The horizontal component $|H_\phi|$ of the LPDA VEL is measured in the LPDA main axis perpendicular to the LPDA orientation. Then, both antennas are aligned in parallel for the entire flight. The meridional component $|H_\theta|$ is split into two subcomponents: The other horizontally but perpendicular to $\vec{e}_\phi$ oriented component $|H_{\theta,\mathrm{hor}}|$ and the vertical component $|H_{\theta,\mathrm{vert}}|$. As the orientation of the transmission antennas is the main difference between both measurements, the phase α_k with $k = (\theta, \mathrm{hor}), (\theta, \mathrm{vert})$ is the same. Then, these two subcomponents are combined to the meridional component $|H_\theta|$:

$$|H_\theta| = \cos(\Theta)|H_{\theta,\mathrm{hor}}| + \sin(\Theta)|H_{\theta,\mathrm{vert}}|. \tag{8.1}$$

Both meridional subcomponents are measured in the axis perpendicular to the LPDA main axis. Therefore, the transmission antenna needs to be rotated by 90° and the flight path needs to start at the 90° rotated position in comparison to the measurement of $|H_\phi|$. For the case of the $|H_{\theta,\mathrm{vert}}|$ measurement, the transmitting antenna is vertically aligned.

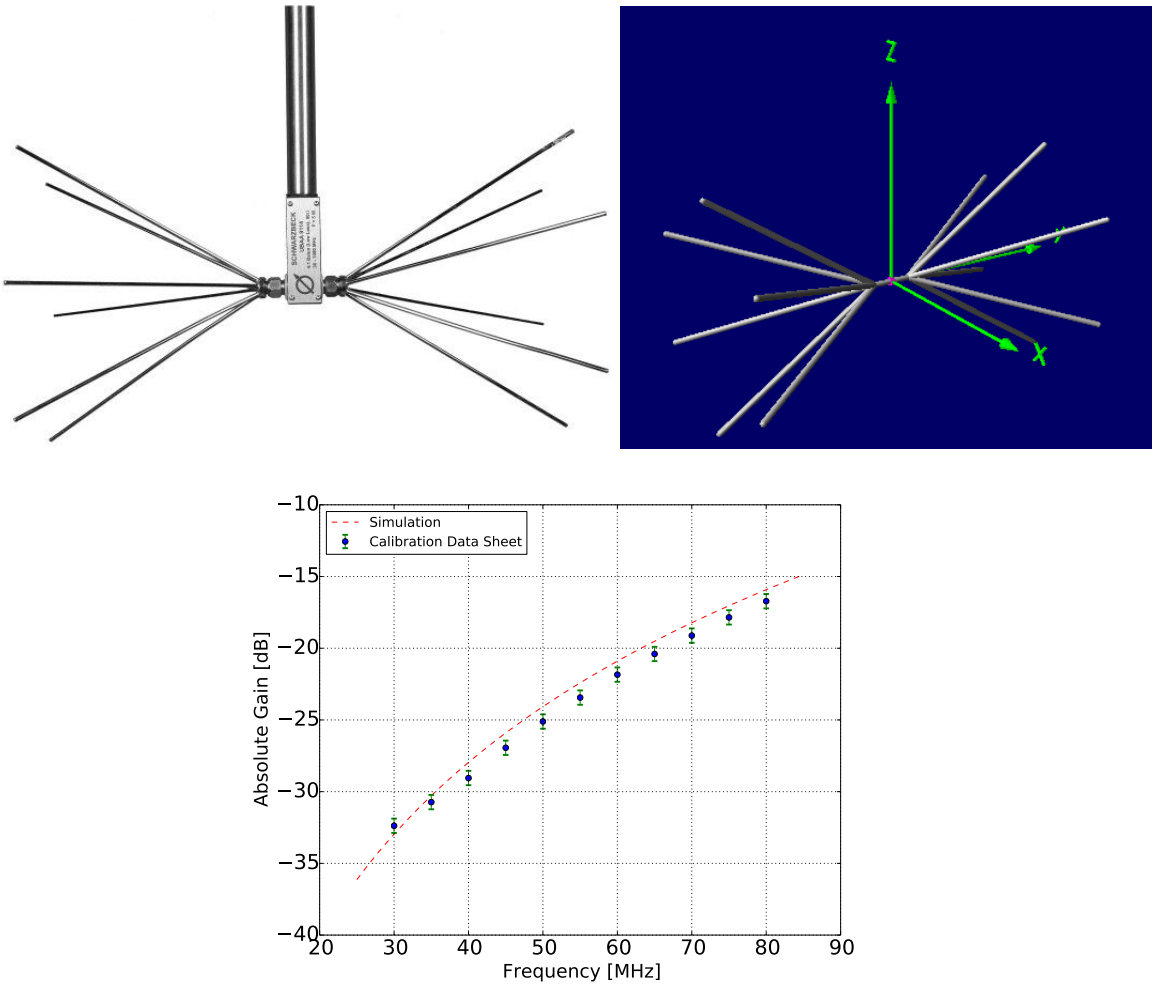

Figure 8.3: ***(top left)*** *Picture of the open biconical antenna which is used as the calibrated transmitting antenna for the LPDA calibration measurement.* ***(top right)*** *Biconical antenna realization included in the NEC-2 simulations. The pink dot marks the antenna footpoint.* ***(bottom)*** *Comparison of the simulated (red dashed line) and the absolute antenna gain stated by the manufacturer (blue dots) as a function of the frequency. The green error bars indicate the calibration uncertainty of* $0.5\,\mathrm{dB}$.

As the receiving power is measured directly at the output of the LPDA amplifier, all matching effects from connecting a transmission line to the LPDA footpoint and the LPDA LNA are taken into account. The VEL is calculated using Eq. (3.26).

8.2 Calibration Strategy

To explain the LPDA calibration strategy, a measurement of each of the three VEL components is presented. Several flights at different days with different environmental conditions were performed and finally combined to give an average LPDA VEL. Here, one of the measurements of each VEL component is presented to show the reconstruction procedure as well as the statistical precision of the measurements. Furthermore, the corrections taking into account cable damping, background measurements, misalignments of the transmitting antenna and shift of the octocopter position are discussed in

corrections	$\Delta\lvert H_\phi\rvert$ **[%]**	$\Delta\lvert H_{\theta,\mathrm{hor}}\rvert$ **[%]**	$\Delta\lvert H_{\theta,\mathrm{vert}}\rvert$ **[%]**
background noise	-0.1	-0.5	-0.9
cable attenuations	$+44.4$	$+44.4$	$+53.2$
background noise + cable attenuation	$+44.3$	$+43.7$	$+51.8$
octocopter influence	$+0.6$	$+0.6$	-0.2
octocopter misalignment and misplacement	$+0.3$	–	–
height at take off and landing	$+1.8$	$+15.8$	$+5.8$
height barometric formula	-5.2	-10.2	-2.5
combined height	-3.6	-5.4	$+1.3$
shift to optical method	-14.5	-4.8	$+0.2$
combined height + shift to optical method	-14.6	-5.5	-0.3
all	$+24.6$	$+36.4$	$+51.1$

Table 8.2: Vector effective length (VEL) corrections taking into account different kinds of corrections for the three measured VEL components $|H_\phi|$, $|H_{\theta,\mathrm{hor}}|$ and $|H_{\theta,\mathrm{vert}}|$ of the example flights at a zenith angle of $(42.5 \pm 2.5)^\circ$ and a frequency of 55 MHz with $\Delta|H_k| = \frac{|H_k|-|H_{k,0}|}{|H_{k,0}|}$ and $k = \phi, (\theta, \mathrm{hor}), (\theta, \mathrm{vert})$.

detail. Afterwards, an overview of the measurement uncertainties is given.

8.2.1 Example Measurement

In the right diagrams of Fig. 8.4, the measured VEL components $|H_\phi|$, $|H_{\theta,\mathrm{hor}}|$ and $|H_{\theta,\mathrm{vert}}|$ at the output of the LPDA LNA as a function of the zenith angle Θ at 55 MHz are shown. In the left drawings, the respective antenna orientations are visible. The antenna response pattern reveals the following features. For the VEL component $|H_\phi|$, the LPDA is most sensitive in the zenith direction. The pattern shows a side lobe at around 65°. For $|H_{\theta,\mathrm{hor}}|$ the most sensitive direction is the zenith while at larger zenith angles the sensitivity is strongly reduced. At the zenith, the components $|H_\phi|$ and $|H_{\theta,\mathrm{hor}}|$ are equal which is expected as the antenna orientations are identical. The fluctuations in $|H_{\theta,\mathrm{hor}}|$ are larger than those in $|H_\phi|$ due to the larger dependencies on the octocopter rotations. When flying towards the antenna, any acceleration causes a rotation around the pitch angle (Fig. 8.1) which does not influence $|H_\phi|$. However, for both meridional subcomponents the pitch angle already changes the transmitting antenna orientation (Fig. 8.4) and therefore, influences both measurements. In comparison to the other components, the meridional subcomponent $|H_{\theta,\mathrm{vert}}|$ is much smaller. Therefore, the LPDA is marginally sensitive to such a signal polarization, especially at vertical incoming directions. All these results exhibit a dependence on the frequency.

8.2.2 Corrections

For the raw VEL determined according to Eq. (3.26), corrections for the experimental conditions have to be applied. The VEL is averaged in zenith angle intervals of 5°. This is motivated by the observed variations in the repeated measurements which were recorded on different days (see e.g. below Fig. 8.14). All corrections to the VEL are expressed relative to the measured raw VEL at a zenith angle of $(42.5 \pm 2.5)^\circ$ and a frequency of 55 MHz and are listed in Tab. 8.2. The corrections are partly zenith angle and / or frequency dependent. The following paragraphs describe the corrections

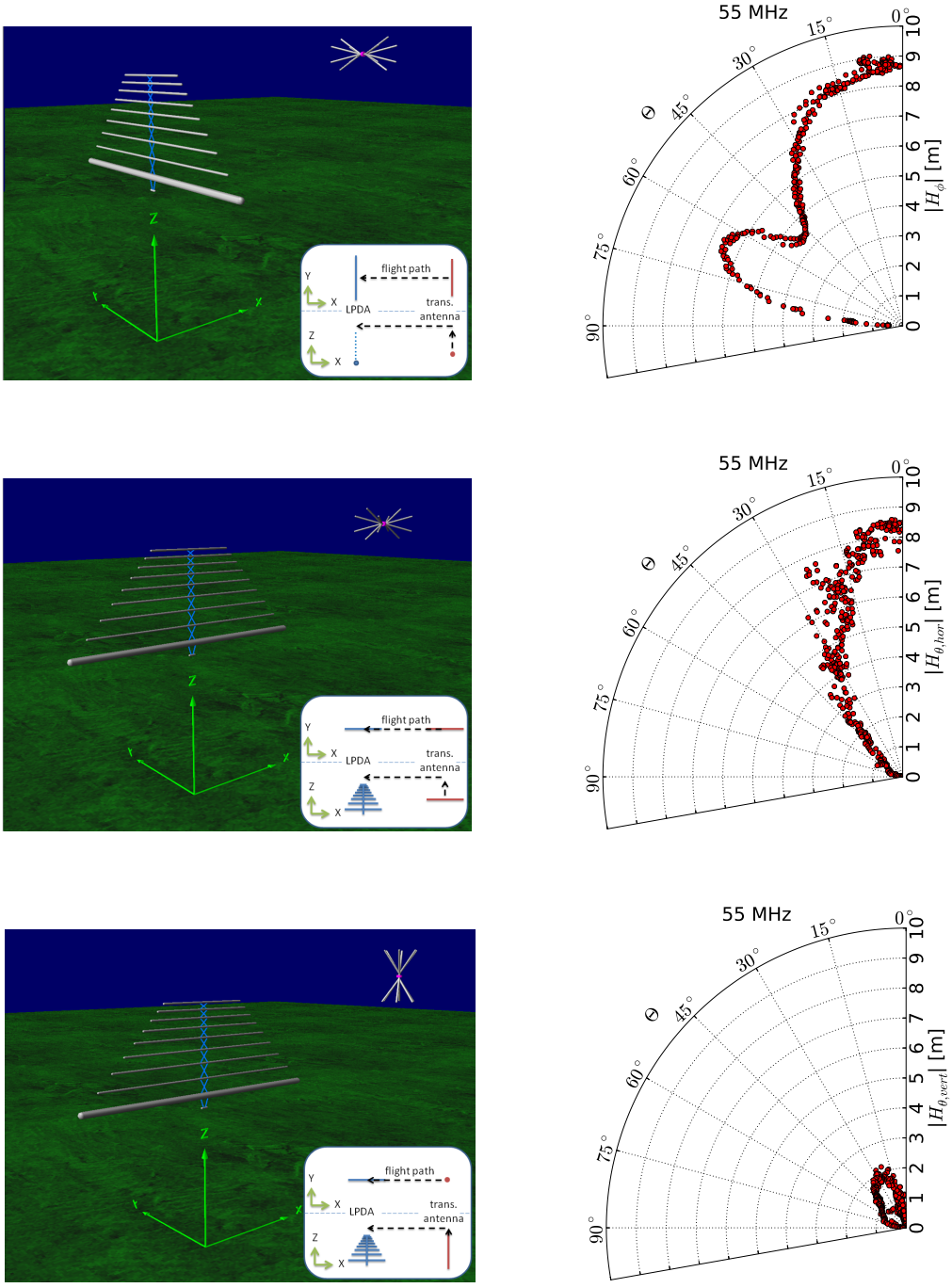

Figure 8.4: ***(left)*** *NEC-2 realization of the setup to simulate the three components of the vector effective length (VEL)* ***(from top to bottom)*** $|H_\phi|$, $|H_{\theta,\mathrm{hor}}|$ *and* $|H_{\theta,\mathrm{vert}}|$. *The meridional component* $|H_\theta|$ *is a combination of* $|H_{\theta,\mathrm{hor}}|$ *and* $|H_{\theta,\mathrm{vert}}|$. *The distance between transmitting and receiving antenna is reduced and the transmitting antenna is scaled by a factor of* 3 *to make both antennas visible. For clarity, the LPDA and the transmitting antenna (assumed as a simple dipole) orientations are sketched in the lower right corner of each picture in the XY-plane as well as in the XZ-plane.* ***(right)*** *Measured VEL as function of the zenith angle (red dots) of three example flights for the three VEL components at* 55 MHz.

of the raw VEL at the LPDA LNA output from the measurement.

Background Noise

During the calibration, the background noise is also recorded. In a separate measurement, the frequency spectrum of the background has been determined and is then subtracted from the calibration signal spectrum. In Fig. 8.5, the LPDA response power for different octocopter zenith angles as function of the frequency recorded during the three example flights are shown exemplary and compared to the background noise. Typically, the background noise is several orders of magnitude below the signal strength. This is even the case for the component $|H_{\theta,\mathrm{vert}}|$ with lowest LPDA sensitivity. For large zenith angles close to 90° and in the case of the component $|H_{\theta,\mathrm{vert}}|$ also for small zenith angles directly above the radio station, however, the background noise and the signal can be of the same order of magnitude. In this case, the calibration signal spectrum constitutes an upper limit of the LPDA sensitivity. If more than $50\,\%$ of the events in a zenith angle bin of 5° are affected, no background is subtracted but half of the measured total signal is used for calculating the VEL and a 100% systematic uncertainty on the VEL is assigned.

Cable Attenuation

To avoid crosstalk in the LPDA read-out system, the read-out system was placed at a distance of about $25\,\mathrm{m}$ from the LPDA. The RG58 coaxial cable [211], used to connect the LPDA to the read-out system, has a frequency-dependent ohmic resistance that attenuates the receiving power by a frequency-dependent factor δ. To obtain the VEL at the LNA output, the cable attenuation is corrected from lab measurements using the FSH4 spectrum analyzer. The cable attenuation factor δ of the additional cables used in the $|H_\phi|$ example flight as function of the frequency is shown in Fig. 8.6 exemplary.

Octocopter Influence

During the LPDA VEL measurement, the transmitting antenna is mounted underneath the octocopter which contains conductive elements and is powered electrically. Therefore, the octocopter itself may change the antenna response pattern of the transmitting antenna with respect to the zenith angle. To find a compromise between signal reflections at the octocopter and stability during take off, flight, and landing, the distance between transmitting antenna and octocopter has been chosen to be $0.7\,\mathrm{m}$. The influence has been investigated by simulating the antenna response pattern of the transmitting antenna with and without mounting underneath an octocopter. A visualization of the NEC-2 realizations is shown in Fig. 8.7. It is found that the average absolute gain of the transmission antenna changes by $0.05\,\mathrm{dB}$ in the case of a horizontally aligned transmitting antenna and changes by $0.02\,\mathrm{dB}$ in the case of a vertically aligned transmitting antenna as shown in Fig. 8.8. At a zenith angle of $(42.5 \pm 2.5)^\circ$ and a frequency of $55\,\mathrm{MHz}$, the octocopter influences the transmitting antenna VEL with $0.6\,\%$.

Octocopter Misalignments and Misplacements

Misalignments and misplacements of the octocopter during the calibration flight have a direct impact on the transmitting antenna position and orientation changing the signal polarization at the position of the AUT. For this investigation, the orientation of the transmission antenna is assumed to correspond to a dipole, which holds to a good approximation. The electric field $\vec{E}_t$ emitted from a dipole antenna

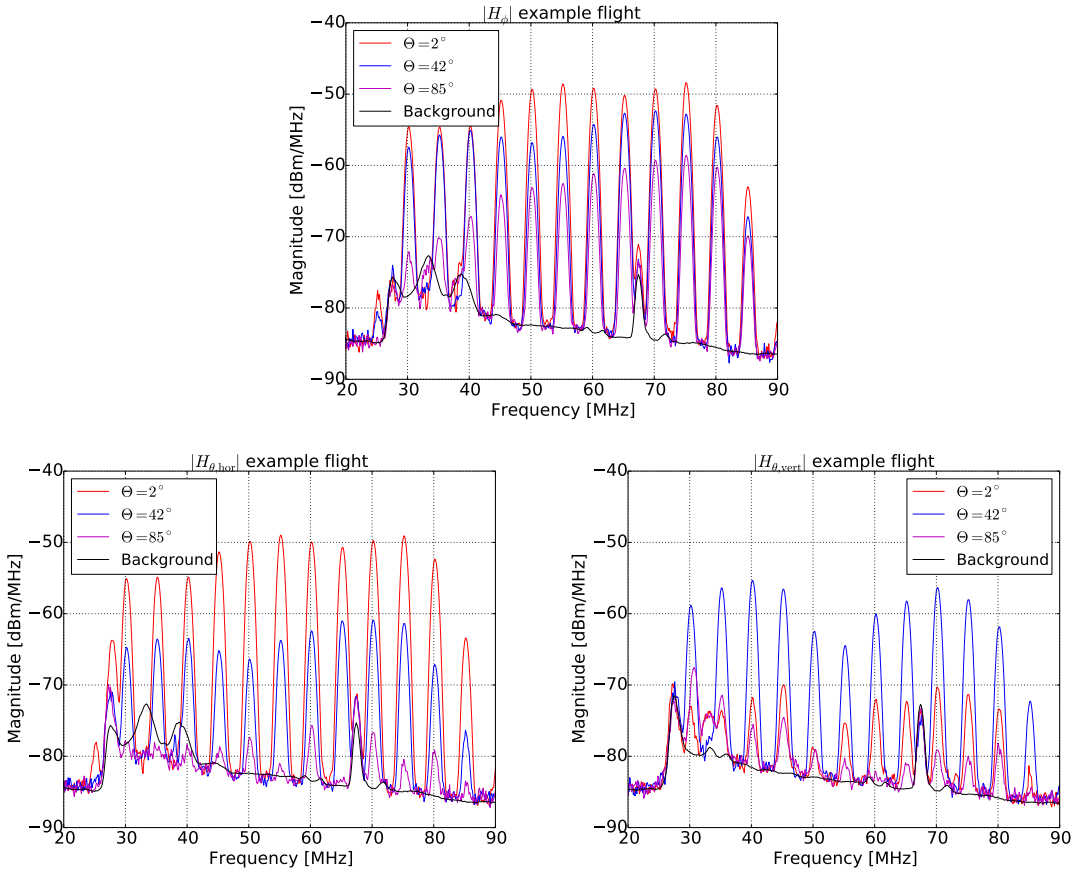

Figure 8.5: *LPDA response power recorded at different octocopter zenith angles (colored lines) as function of the frequency compared with the background noise (black line). In the* ***(upper)*** *diagram, the received power measured in the* $|H_\phi|$ *example flight whereas in the* ***(lower left)*** *diagram the received power measured in the* $|H_{\theta,hor}|$ *example flight and in the* ***(lower right)*** *diagram the received power measured in the* $|H_{\theta,vert}|$ *example flight are shown. Typically, the background noise is several orders of magnitude below the signal strength.*

with orientation $\hat{A}_t$ in the direction $\hat{n}$ in the far-field region is proportional to $\vec{E}_t \sim (\hat{n} \times \hat{A}_t) \times \hat{n}$, and the amplitude is given by $|\vec{E}_t| = \sin(\alpha)$. Here, α describes the smallest angle between the transmitting antenna alignment $\hat{A}_t$ and the direction from the transmitting antenna to the AUT denoted as $\hat{n}$ (see lower sketch of Fig. 8.1). The orientation of the transmitting antenna $\hat{A}_t$ is calculated by an intrinsic rotation of the initial orientation of the transmitting antenna rotating first by the yaw angle G, then by the pitch angle P and finally, by the roll angle R. The AUT sensitivity η to the emitted electric field is then calculated by the absolute value of the scalar product of the electric field and the AUT orientation $\hat{A}_r$: $\eta = |\vec{E}_t \cdot \hat{A}_r| = \sin(\alpha)\cos(\beta)$ with β describing the smallest angle between $\vec{E}_t$ and $\hat{A}_r$ (see lower sketch of Fig. 8.1). Finally, the correction factor ϵ of the power measured at the AUT is determined by the square of the quotient of the nominal and the real value of η. In case of the horizontal component $|H_\phi|$, the VEL is systematically shifted to larger values for all zenith angles and frequencies due to the octocopter misalignment and misplacement. The correction factor ϵ is used to determine the horizontal VEL $|H_\phi|$. In both meridional subcomponents, the VEL becomes small at large zenith angles and strongly dependent on the antenna alignments. Therefore, in the meridional

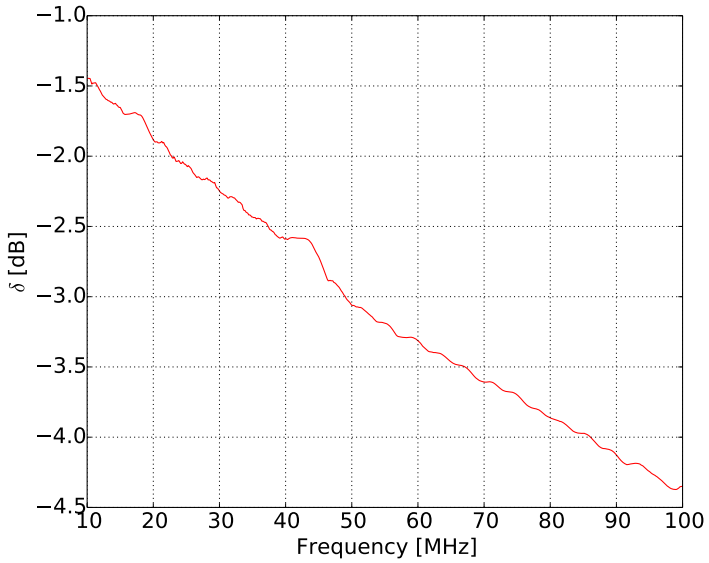

Figure 8.6: *Cable attenuation factor δ of the additional cables used in the $|H_\phi|$ example flight as function of the frequency in logarithmic units.*

subcomponents $|H_{\theta,\mathrm{hor}}|$ and $|H_{\theta,\mathrm{vert}}|$, the effects of the octocopter misalignment and misplacement are included in the systematic uncertainties.

Octocopter Flight Height

The octocopter flight height is determined by a barometer measuring the change of air pressure Δp during the flight. The octocopter software assumes a linear dependency of Δp and the octocopter flight height over ground h_{raw}. Two corrections have been applied to the raw flight height. Firstly, it was observed that the flight height differs between take off and landing. Therefore, a linear time dependent correction is applied which constrains the flight height over ground at take off and landing to zero. Secondly, AERA is located at a height of about $1550\,\mathrm{m}$ above sea level. Therefore, such a linear relation between Δp and h_{raw} used by the octocopter software is not precise enough. A more realistic calculation considering an exponential model of the barometric formula [248] as well as the height and latitude dependent gravitation is used to determine the more precise octocopter height h_{octo}. An inverse quadratic relation between gravitation and the height above sea level with a value at sea level of $g(0) = 9.797\,\frac{\mathrm{m}}{\mathrm{s}^2}$ at the latitude of AERA is taken into account. The raw octocopter height from the barometer as well as the height after all corrections of the $|H_\phi|$ example flight are shown on the left side of Fig. 8.9 in comparison to the octocopter height determined with the optical method. The quotient of the octocopter height measured by the camera method and by the full corrected barometer method is shown in the histogram on the right side of Fig. 8.9. Both methods agree at the level of $1.1\,\%$ in the median. In the following, the optical method is used to correct for the small difference.

Octocopter Position Shift from Optical Method Position Reconstruction

While the octocopter position measured by the built-in sensors (air pressure, GPS) is recorded nearly

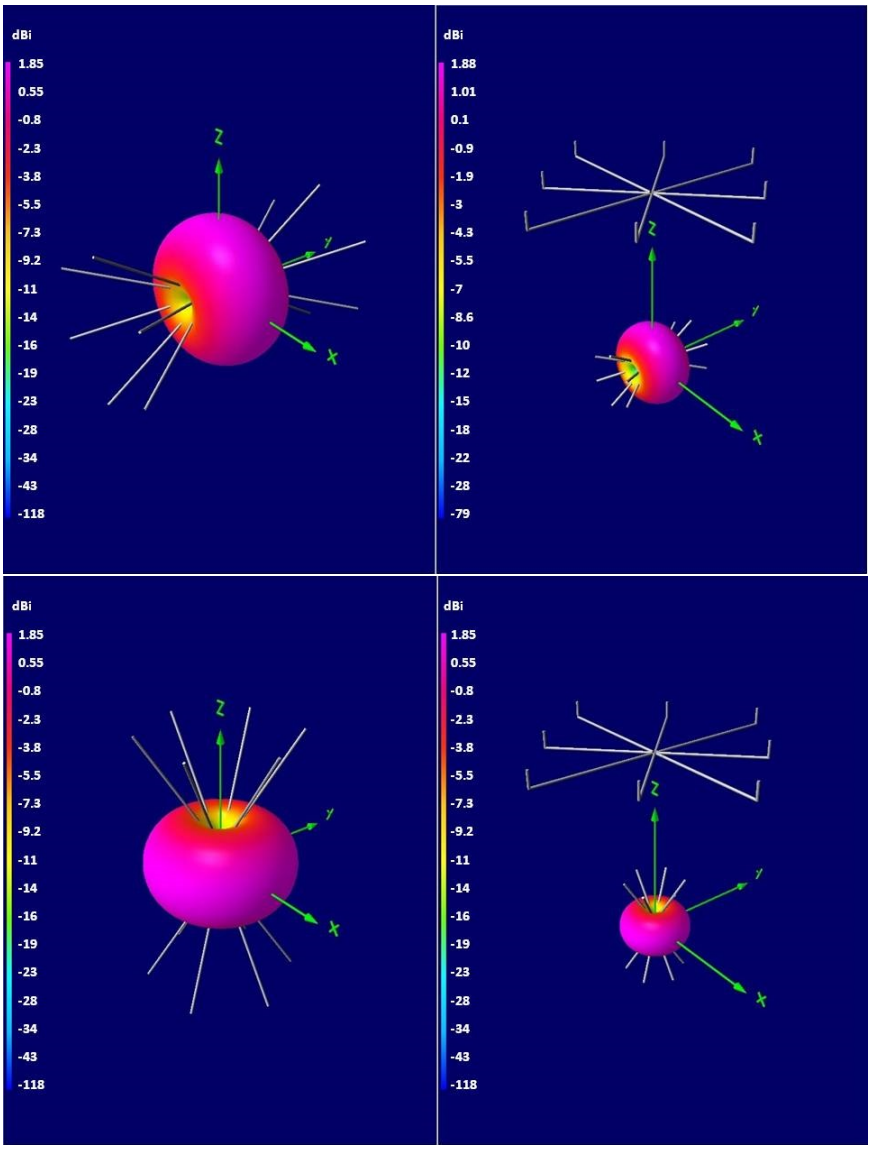

Figure 8.7: *Total antenna gain at $f = 55\,\mathrm{MHz}$ of the transmitting antenna in free space **(left)** and when mounted beneath a model of the octocopter **(right)** in the case of a horizontally **(top)** and vertically **(bottom)** aligned antenna obtained from NEC-2 simulations. The total antenna gain is color coded in logarithmic units. The pinker the color, the higher is the antenna sensitivity to this direction.*

each second, the cameras used in the optical method take pictures of the flight every $3\,\mathrm{s}$. Furthermore, it turned out that the fluctuations of the built-in sensors are smaller in comparison to the optical method. Nevertheless, the systematic uncertainties of the octocopter position reconstruction using the optical method are still much smaller. The uncertainties are described in detail in the following subsection. To combine both advantages of high statistics and small uncertainties, the octocopter position measured by the built-in sensors is taken and then shifted towards the position measured with the optical method. Therefore, the octocopter position in the XY-plane is shifted by the median distance and the octocopter height measured by the barometer is shifted by the median factor between both methods. For the $|H_\phi|$ example flight, the octocopter XY-position measured by GPS is shifted by $0.83\,\mathrm{m}$ to the west and

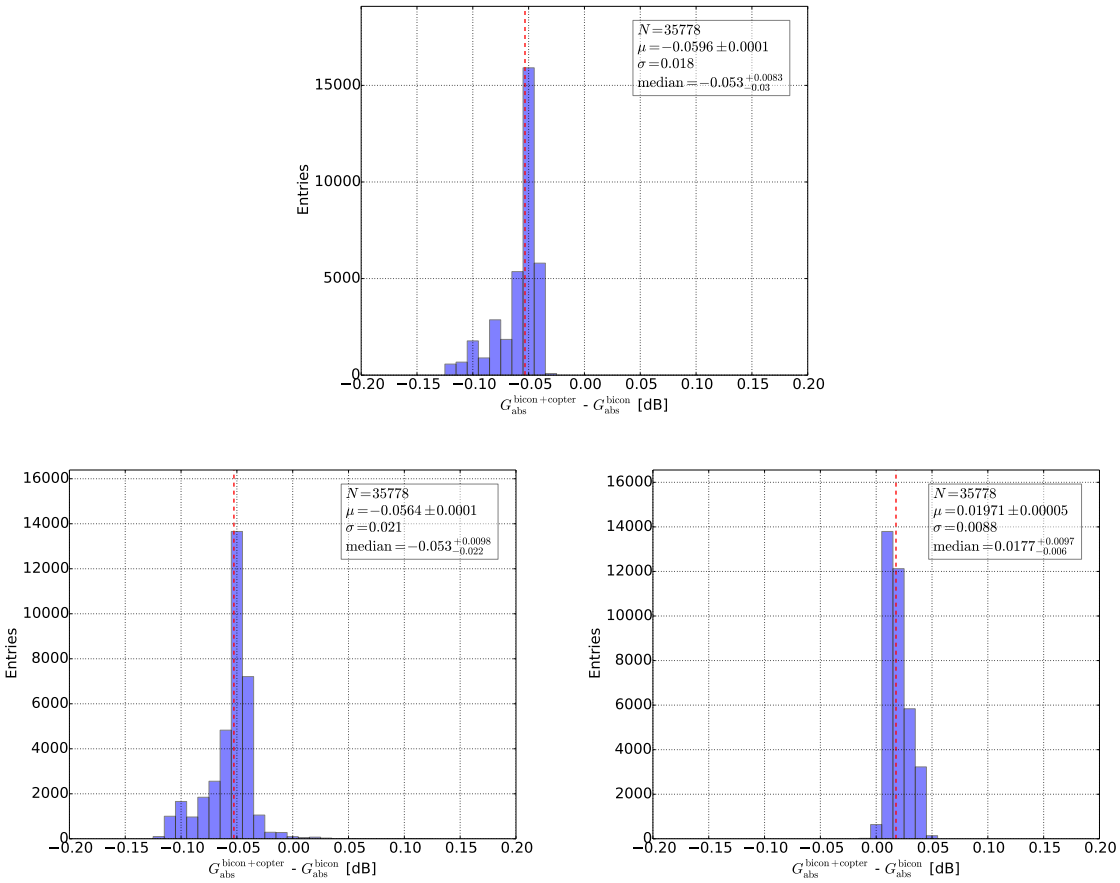

Figure 8.8: *Influence of the octocopter on the absolute antenna gain of a horizontally aligned transmitting antenna in the direction perpendicular to the antenna alignment* ***(top)*** *which is needed for the measurements of the* $|H_\phi|$ *component and in the direction parallel to the antenna alignment* ***(bottom left)*** *which is needed for the* $|H_{\theta,hor}|$ *component. The influence of the octocopter on the absolute antenna gain of a vertically aligned transmitting antenna which is needed for the* $|H_{\theta,vert}|$ *component is shown in the* ***(bottom right)*** *diagram. The simulation contains zenith angles from* $91\,^\circ$ *to* $179\,^\circ$ *in steps of* $1\,^\circ$ *and a frequency range from* $30\,\mathrm{MHz}$ *to* $80\,\mathrm{MHz}$ *in steps of* $0.25\,\mathrm{MHz}$*. The red dashed lines indicate the median values.*

$3.22\,\mathrm{m}$ to the south. The full corrected flight height measured by the barometer is shifted by $1.1\,\%$.

8.2.3 Uncertainties

In this subsection, the statistical and systematic uncertainties are discussed using the $|H_\phi|$ example flight at a middle frequency of $f = 55\,\mathrm{MHz}$ and a zenith angle bin of $(\Theta = 42.5 \pm 2.5)\,^\circ$ as mentioned above. This zenith angle is chosen as most events at AERA are reconstructed coming from this direction. While some systematic uncertainties are stable between flights, e.g., measurement of the power injected to the transmitting antenna or the transmitting antenna response pattern, others are flight dependent, e.g., the octocopter position and the measurement of the receiving power at the AUT. The VEL relative uncertainties are listed in Tab. 8.3. These individual uncertainties are described in detail in the following subsections. The global systematic uncertainties add quadratically to $6.3\,\%$ and

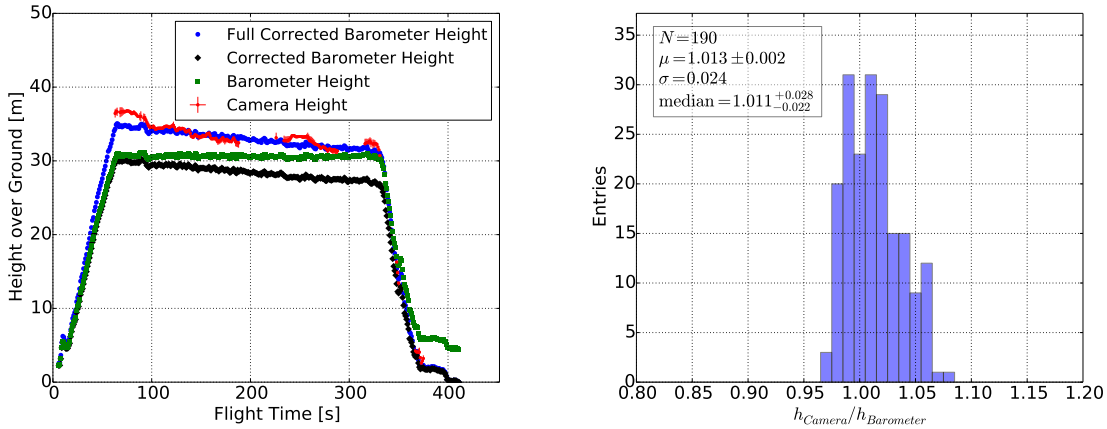

Figure 8.9: ***(left)*** *Corrections for the measured octocopter height with the raw data denoted by the green rectangles. The black diamonds refer to the height after linear correction for the start and end positions. The blue circular symbols show the corrections for the linear barometric formula used in the octocopter electronics. The octocopter height determined by the optical method is denoted by the red dots. All measurements are shown as a function of the flight time.* ***(right)*** *Histogram of the quotient of the full corrected barometer height and measured height from the optical method.*

the flight-dependent systematic uncertainty is $6.9\,\%$.

Transmitting Antenna Position

The systematic uncertainty of the position reconstruction of the optical method was determined by comparing the reconstructed octocopter position with the position measured by a DGPS which gives an accurate position determination. The combined mass of the transmission antenna and the additional DGPS exceeds the maximal payload capacity of the octocopter. Therefore, a separate flight with DGPS but without transmitting antenna and source generator was performed. The octocopter positions measured with the optical method and the DGPS are compared in Fig. 8.10. The systematic uncertainty of the octocopter position in the XY-plane is calculated using the quadratic sum of both median values (red dashed lines) in the X and Y direction which is smaller than $1\,\mathrm{m}$. Equally, the systematic uncertainty of the octocopter height is $\sigma_h = 0.06\,\mathrm{m}$. The influence on the VEL is determined by shifting the reconstructed octocopter position by these uncertainties and redoing the VEL calculation given in Eq. (3.26) of each zenith angle bin separately for the XY-plane and the height. The VEL systematic uncertainty is given by half the difference of the upper and lower shift of the VEL. The systematic uncertainty on the VEL at a zenith angle of $\Theta = 42.5^\circ (2.5^\circ, 72.5^\circ) \pm 2.5^\circ$ due to the octocopter's XY-position is $1.5\,\%$ ($0.2\,\%$, $2.9\,\%$) and due to the octocopter's height is $0.1\,\%$ ($0.2\,\%$, $< 0.1\,\%$).

The statistical uncertainty of the octocopter's built-in sensors is determined in the following way: The flight height measured by the barometer has to be corrected as described in section 8.2.2 which causes further uncertainties during the flight. The statistical uncertainty of the octocopter height measured with the barometer is then determined by comparing the measured height with the height measured by the DGPS (lower right panel of Fig. 8.11). The statistical uncertainty are found to be $\sigma = 0.33\,\mathrm{m}$

source of uncertainty / %	systematic	statistical
flight-dependent uncertainties	**6.9**	**2.7**
transmitting antenna XY-position	1.5	1.0
transmitting antenna height	0.1	0.6
transmitting antenna tilt	< 0.1	< 0.1
size of antenna under test	1.4	-
uniformity of ground	< 0.1	-
RSG1000 output power	2.9	2.3
influence of octocopter	< 0.1	-
electric-field twist	0.4	0.2
LNA temperature drift	1.0	0.6
receiving power	5.8	-
background	0.4	-
global uncertainties	**6.3**	**<0.1**
injected power	2.5	< 0.1
transmitting antenna gain	5.8	-
cable attenuation	0.5	< 0.1
all / %	**9.3**	**4.7**

Table 8.3: Uncertainties of the horizontal component of the vector effective length $|H_\phi|$ of the example flight at $55\,\mathrm{MHz}$ and $(42.5 \pm 2.5)\,^\circ$. While the overall systematic uncertainty is the quadratic sum of each single systematic uncertainty, the overall statistical uncertainty is described by the observed signal fluctuation during the measurement. The statistical uncertainty of each source of uncertainty describes the expected uncertainty, e.g., from the manufacturer's information.

which results in a $0.6\,\%$ uncertainty in the VEL. The horizontal position uncertainties are determined in a measurement where the octocopter remains stationary on the ground. The measurement is presented in Fig. 8.11. The diagrams show a statistical uncertainty of $\sigma = \sqrt{0.48^2 + 0.39^2}\,\mathrm{m} = 0.6\,\mathrm{m}$ in the XY-plane which results in a $1.0\,\%$ uncertainty in the VEL. All these uncertainties are smaller than those of the optical method described by the widths of the distributions shown in Fig. 8.10 where the octocopter positions measured with DGPS and the camera method are compared.

The transmission antenna is mounted at a distance of $s_{Ant} = 0.7\,\mathrm{m}$ beneath the octocopter. Hence, a tilt of the octocopter, described by the pitch and the roll angle, changes the position in the XY-plane of the transmission antenna as well as its height over ground. In the case of the example flight, the average pitch (roll) angle of the octocopter is -0.6° (0.9°) which lead to a systematic uncertainty smaller than $0.1\,\%$ at $55\,\mathrm{MHz}$ and $(42.5 \pm 2.5)\,^\circ$.

Size of AUT

The size of the LPDA in the z-direction is $1.7\,\mathrm{m}$. The interaction point of the signal at each frequency is set to the center of the LPDA. Therefore, there is a systematic uncertainty in the height interval between transmitting antenna and AUT which is conservatively estimated to be $0.85\,\mathrm{m}$. For the example flight, this systematic results in a VEL systematic uncertainty of $1.4\,\%$ at $55\,\mathrm{MHz}$ and $(42.5 \pm 2.5)\,^\circ$.

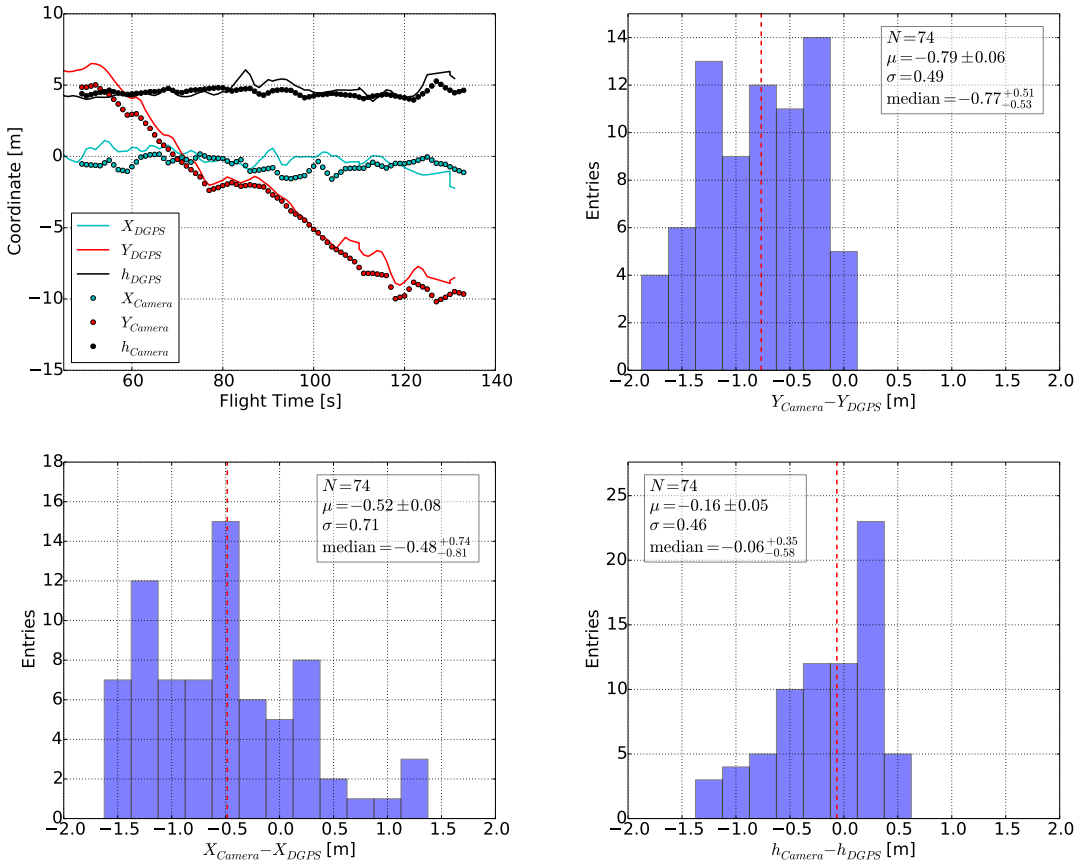

Figure 8.10: *Comparison of the octocopter position measured with the optical method and with an additional differential GPS (DGPS) mounted at the octocopter during one flight.* ***(upper left)*** *Raw position data measured with DGPS (lines) and the optical method (dots) as function of the flight time. The distance between the reconstructed octocopter position measured by optical method and DGPS in X and Y direction are shown in the* ***(upper right)*** *and* ***(lower left)*** *figure. The difference of the octocopter height measured by the barometer and DGPS is shown in the* ***(lower right)*** *figure. The systematic uncertainty in the XY-plane of the octocopter position is calculated by the quadratic sum of both median values (red dashed lines) in X and Y direction. Similarly, the median of the height difference of both measurement setups is taken as systematic uncertainty of the octocopter height.*

Uniformity of Ground Height

The ground height above sea level at the octocopter starting position and at the LPDA is measured by DGPS. The ground is not completely flat but varies at the level of a few cm over a distance of $5\,\mathrm{m}$ which is incorporated as additional uncertainty on the height. The resulting influence on the VEL is less than $0.1\,\%$.

Emitted Signal towards the Antenna Under Test

The uncertainty of the emitted signal contains effects from the power output of the RSG1000, the injected power into the transmission antenna, the transmission response pattern, the influence of the octocopter on the pattern as well as the misalignment and misplacement of the transmitting antenna which changes the emitted power transmitted towards the AUT and lead to a twist of the signal polar-

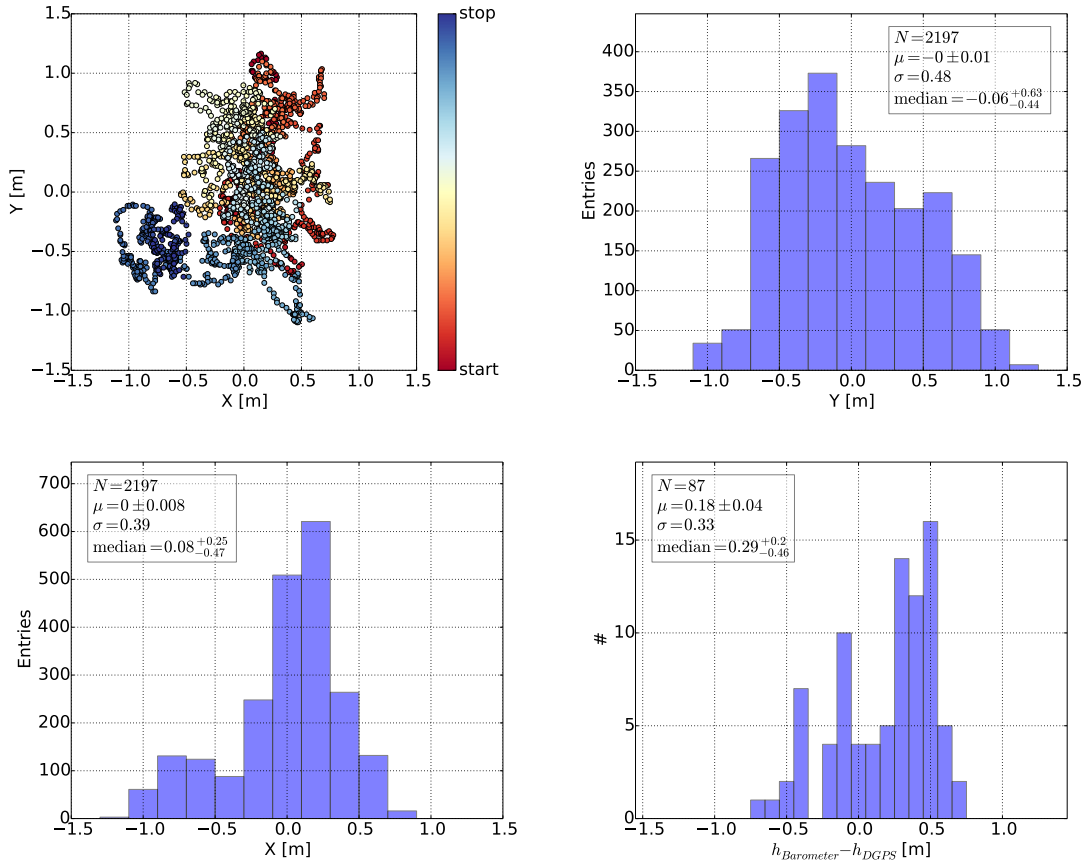

Figure 8.11: *The statistical uncertainties of the octocopter position reconstruction using the built-in sensors. The uncertainty of the horizontal position is determined in a measurement while the octocopter is on ground and does not move.* ***(upper left)*** *Measured octocopter GPS-position with respect to the average position at* $(0, 0)$*. Color coded is the time.* ***(upper right)*** *Histogram of the distance between measured and average position in Y direction.* ***(lower left)*** *Histogram of the distance between measured and average position in X direction.* ***(lower right)*** *The statistical uncertainty of the octocopter height measured with the barometer is determined by comparing the measured flight height with the height measured using a DGPS. Then, uncertainties arising from the height corrections are taken into account. The histogram of the octocopter height difference over ground measured with the barometer compared to the DGPS measurement is shown.*

ization at the AUT.

The manufacturer of the RSG1000 states a signal stability of $0.2\,\mathrm{dB}$ measured at a constant temperature of $20\,^\circ$ which results in a statistical uncertainty of $2.3\,\%$ in the VEL. The calibration measurements were performed at temperatures between $15\,^\circ\mathrm{C}$ and $25\,^\circ\mathrm{C}$. Here, the manufacturer denotes a systematic uncertainty of $0.25\,\mathrm{dB}$ due to temperature shifts which results in $2.9\,\%$ in the VEL.

The injected power from the RSG1000 to the transmission antenna is measured twice in the lab using the FSH4 spectrum analyzer averaged over 100 samples and an Agilent N9030A ESA spectrum analyzer averaged over 1000 samples. The systematic uncertainty of the FSH4 measurement is $0.5\,\mathrm{dB}$ and the systematic uncertainty of the Agilent N9030A ESA measurement is $0.24\,\mathrm{dB}$. Both are combined yielding a total systematic uncertainty of $0.22\,\mathrm{dB}$ in the VEL. As there is a quadratic relation between injected power and the VEL (cf. Eq. (3.26)) the systematic uncertainty on the VEL is $2.5\,\%$.

The statistical uncertainties of these measurements are small due to the number of samples and can be neglected.

The antenna manufacturer specifies a systematic uncertainty of the transmitting antenna pattern of $0.5\,\mathrm{dB}$ which results in a systematic uncertainty on the VEL of $5.8\,\%$. The influence of the octocopter on the transmission antenna pattern investigated with simulations is small and, therefore, a systematic uncertainty due to the octocopter influence on the transmission antenna pattern can be neglected.

Misalignment and misplacement of the transmitting antenna lead to a twist of the signal polarization and furthermore, altered the signal strength at the AUT. The AUT sensitivity to an electric field is given by $\eta = \sin(\alpha)\cos(\beta)$ with the angles α and β as described in section 8.2.2. Both angles, and therefore η, depend on the octocopter rotation angles as well as on the octocopter position. The angle β linearly depends on α and on the AUT orientation which is known with a precision of 1°. The uncertainty of all three octocopter rotation angles is estimated to be 1°. In the case of the horizontal VEL, the uncertainty of α is given by the quadratic sum of two octocopter rotation angles and the angle which arises from the octocopter position uncertainties as well as the size of the AUT. For the example flight, the resulting influence on the VEL is $0.4\,\%$ at $55\,\mathrm{MHz}$ and $(42.5 \pm 2.5)^\circ$. In contrast, both meridional subcomponents are not corrected for the octocopter misalignment and misplacement. Here, the octocopter misalignment and misplacement is completely included in the systematic uncertainty. Therefore, the systematic uncertainty of the VEL due to an octocopter misalignment and misplacement is larger for both meridional subcomponents than in the case of the horizontal component. The systematic uncertainty on the VEL is calculated in the same way but using the nominal values of α and β in each zenith angle bin of 5° instead. As β linearly depends on α, only a further uncertainty on α given by the difference between the measured median values and nominal values of α is needed, quadratically added and then propagated to the systematic uncertainty on the VEL. In case of both meridional subcomponents, both angles α and β depend on the zenith angle. Hence, this systematic uncertainty is strongly zenith angle dependent for both meridional subcomponents.

The uncertainties of the injected power to the transmitting antenna and the transmitting antenna pattern limit the overall calibration accuracy. In comparison to other calibration campaigns at LOFAR or Tunka-Rex, a RSG1000 were used as signal source as well but a different transmitting antenna. Both RSG1000 signal sources differ on a percent level only. However, the manufacturer of the transmitting antenna used at LOFAR and Tunka-Rex states a systematic uncertainty of the transmitting antenna pattern of $1.25\,\mathrm{dB}$ [249]. Hence, the AERA calibration has a significantly smaller systematic uncertainty due to the more precise calibration of the transmitting antenna.

Received Signal at the Antenna Under Test

Within the uncertainty of the received signal all uncertainty effects of the received power at the AUT including the full signal chain from the LPDA to the spectrum analyzer as well as the LNA and cables are considered. In the following, a drift of the LPDA LNA gain due to temperature fluctuations, the uncertainty of the received power using the FSH4 and the influence of background noise as well as the uncertainty of the cable attenuation measurements are discussed.

The LPDA LNA power gain depends on the temperature. The temperature drift was measured in the laboratory and was determined to $0.017\,\mathrm{dB/K}$ using the FSH4 in the vector network analyzer mode

(refer to Chap. 5). The calibration measurements were performed at temperatures between $15\,^{\circ}\mathrm{C}$ and $25\,^{\circ}\mathrm{C}$ which results in a systematic uncertainty of $1\,\%$ in the VEL due to temperature drifts of the LNA. The measurements of the LPDA LNA power gain due to temperature fluctuations using the FSH4 show fluctuations of typically less than $0.1\,\mathrm{dB}$ which results in an expected statistical uncertainty of $0.6\,\%$ in the VEL.
The event power is measured using the FSH4 spectrum analyzer. The manufacturer states a systematic uncertainty of $0.5\,\mathrm{dB}$. The systematic uncertainty in the VEL is then $5.8\,\%$. Also the background noise is measured using the FSH4 in spectrum analyzer mode. The systematic uncertainty of the VEL considering event power (P) and background noise (B) is $\sqrt{\frac{P^2+B^2}{P^2-B^2}}\frac{0.5}{2}\,\mathrm{dB}$. If the background noise is of the same order of magnitude as the measured event power for more than $50\,\%$ of events in a 5° zenith angle bin, the systematic uncertainty for this zenith angle bin is set to $100\,\%$. For the example flight, the systematic due to background noise results in an additional VEL systematic uncertainty of $0.4\,\%$ at $55\,\mathrm{MHz}$ and $(42.5 \pm 2.5)\,^{\circ}$. A further background influence on the measured signal at the LPDA due to the communication between the remote control and the octocopter is not expected, as they communicate at $2.4\,\mathrm{GHz}$ and the LPDA is sensitive in the frequency range from $30\,\mathrm{MHz}$ to $80\,\mathrm{MHz}$.
The attenuation of the cable is measured with the FSH4 in network analyzer mode, transmitting a signal with a power of $0\,\mathrm{dBm}$, and averaged over 100 samples. Therefore, the statistical uncertainty can be neglected. The manufacturer states a systematic uncertainty of $0.04\,\mathrm{dB}$ for transmission measurements with a transmission higher than $-20\,\mathrm{dB}$ which applies in case of the cables. This results in a systematic uncertainty of $0.5\,\%$ in the VEL.

8.2.4 Simulation of the Experimental Setup

The calibration measurement is simulated using the NEC-2 simulation code. Here, the LPDA, the transmission antenna and realistic ground properties are taken into account. At standard ground conditions the ground conductivity is set to be $1.4\,\mathrm{mS/m}$ and the standard ground permittivity is set to be 5.5 in the simulation. The distance between both antennas is set to be $30.3\,\mathrm{m}$. The VEL is calculated using Eq. (3.32) modified with Eq. (3.49) considering the manufacturer information for the response pattern of the transmitting antenna as well as the transfer function from the LPDA output to the system consisting of the transmission line from the LPDA footpoint to the LNA and the LNA itself. To investigate the simulation stability, several simulations with varying antenna separations and changing ground conditions were performed. Antenna separations ranging from $25\,\mathrm{m}$ to $50\,\mathrm{m}$ were simulated and the resulting VEL as function of the zenith angle at $55\,\mathrm{MHz}$ are shown in Fig. 8.12. The resulting VEL at $35\,\mathrm{MHz}$ and $85\,\mathrm{MHz}$ are shown in the appendix D.1. The simulations exhibit only small changes of the resulting LPDA VEL. Hence, the simulations confirm that the measurement is being done in the far-field region. Furthermore, the influence of different ground permittivities on the LPDA VEL in a transmission simulation is investigated. Measurements of the ground permittivity at the AERA site yield values between 2 and 10 depending on the soil humidity (refer to Chap. 6) and thus, the LPDA VEL is simulated using ground permittivities ranging from 2 to 10. The ground permittivity is identified as the main uncertainty of the original simulation compared to the influence of different ground conductivities or an additional box beneath the LPDA (refer to Chap. 7). In Fig. 8.13,

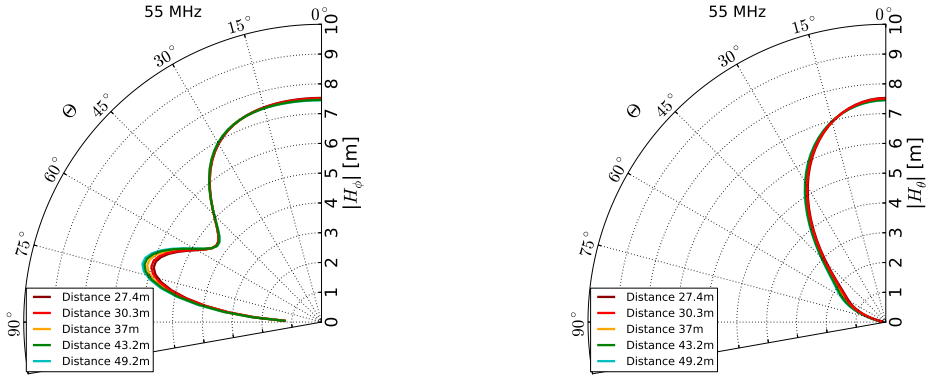

Figure 8.12: *Simulations of the LPDA vector effective length (VEL) for different distances of the transmitting antenna to the LPDA. In the **(left)** diagram, the horizontal VEL $|H_\phi|$ and in the **(right)** diagram the meridional VEL $|H_\theta|$ as function of the zenith angle Θ at $55\,\mathrm{MHz}$ are shown.*

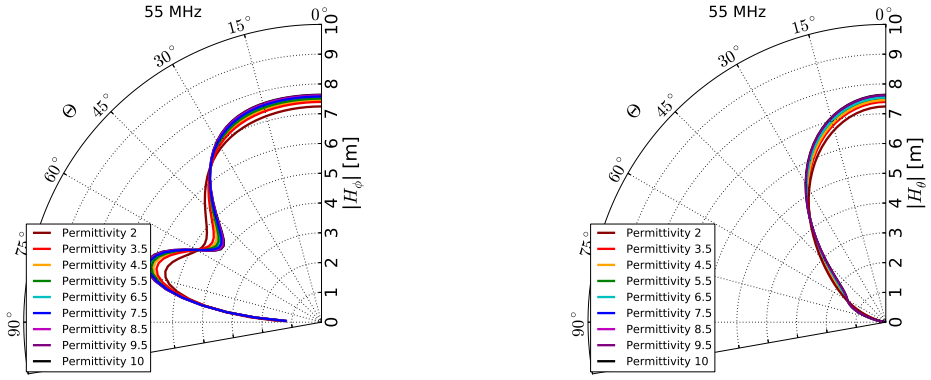

Figure 8.13: *Simulations of the LPDA vector effective length (VEL) for different ground permittivities. In the **(left)** diagram, the horizontal VEL $|H_\phi|$ and in the **(right)** diagram the meridional VEL $|H_\theta|$ as function of the zenith angle Θ at $55\,\mathrm{MHz}$ are shown.*

the simulations of the horizontal and meridional VEL for these different ground permittivities as function of the zenith angle at $55\,\mathrm{MHz}$ are shown. The resulting VEL at $35\,\mathrm{MHz}$ and $75\,\mathrm{MHz}$ are shown in the appendix D.3. In the case of an applied ground permittivity of 2 and of 10, the influence on the horizontal VEL is at the level of $1\,\%$ averaged over all frequencies and zenith angles with a scatter of less than $6\,\%$. The influence of the ground permittivity on the electric-field reconstruction is further discussed in section 8.4.2.

8.3 Measurement of the LPDA Vector Effective Length

In this section, the reproducibility and the combination of all measurements performed on different days and under different environmental conditions are discussed. Furthermore, the combined results of the LPDA VEL are compared to the values obtained from the NEC-2 simulation.

8.3.1 Horizontal Vector Effective Length

Here, the results of the measurements of the horizontal VEL $|H_\phi|$ are presented. In total, five independent measurements were performed to determine $|H_\phi|$ as a function of the zenith angle Θ. The horizontal VEL $|H_\phi|$ in zenith angle intervals of 5° for three different measurements at 35 MHz, 55 MHz, and 75 MHz is shown on the left side of Fig. 8.14. The global systematic uncertainties of each flight are denoted by the light colored band and the flight dependent systematic uncertainties are indicated by the dark colored band.

On the left side of Fig. 8.15, the ratio $\sigma_{\mathrm{VEL}}/\overline{\mathrm{VEL}}$ is shown where σ_{VEL} denotes the fluctuation and $\overline{\mathrm{VEL}}$ is the average VEL from five measurements in each zenith angle bin and for each frequency. Compared to the average $\overline{\mathrm{VEL}}$, the median value of the ratio $\sigma_{\mathrm{VEL}}/\overline{\mathrm{VEL}}$ is 6 % which is well compatible with the estimated uncertainties presented in Tab. 8.3.

The compatibility of each measurement compared with the other measurements is described by the compatibility parameter p which denotes the difference between the measurement i and the weighted average $\overline{\mathrm{VEL}}_4$ of the other four measurements in numbers of the combined flight-dependent uncertainties σ:

$$p_i = \frac{|VEL_i - \overline{\mathrm{VEL}}_4|}{\sigma}. \tag{8.2}$$

The combined flight-dependent uncertainty σ is determined by the quadratical combination of the flight-dependent uncertainties of $\overline{\mathrm{VEL}}_4$ with the flight-dependent systematics and the statistical uncertainties of the measurement i. On the right side of Fig. 8.15, the compatibility parameter p of the example flight for all frequency and all zenith angles with $\Theta < 90^\circ$ (blue histogram) and $\Theta < 60^\circ$ (green histogram) is shown. In the median, the example measurement and the average of the other four measurements agree within one standard deviation. This is also the case for all other measurements. The respective comparisons are shown in the appendix D.3. The measurements agree within its uncertainties and thus, they are weighted by its uncertainties and then combined in the following.

At the right side of Fig. 8.14, all performed measurements to determine $|H_\phi|$ are combined in zenith angle intervals of 5°, weighted by the quadratic sum of the systematic and the statistical uncertainties of each flight. The gray band describes the constant systematic uncertainties whereas the statistical and flight-dependent systematic uncertainties are combined within the error bars. The constant systematic uncertainty of the combined horizontal VEL is 6.3 % and the uncertainties considering flight dependent systematic and statistical uncertainties for the combined horizontal VEL result in 4.7 % at a zenith angle of $(42.5 \pm 2.5)^\circ$ and a frequency of 55 MHz. The overall uncertainty of the determined LPDA VEL in the horizontal polarization adds quadratically to 7.9 %. The overall uncertainty of all other arrival directions and frequencies are shown on the left side of Fig. 8.16. On the right side of Fig. 8.16, a histogram of the overall uncertainties for all frequencies and zenith angle bins up to 85° is shown. For larger zenith angles, the LPDA loses sensitivity and the systematic uncertainty

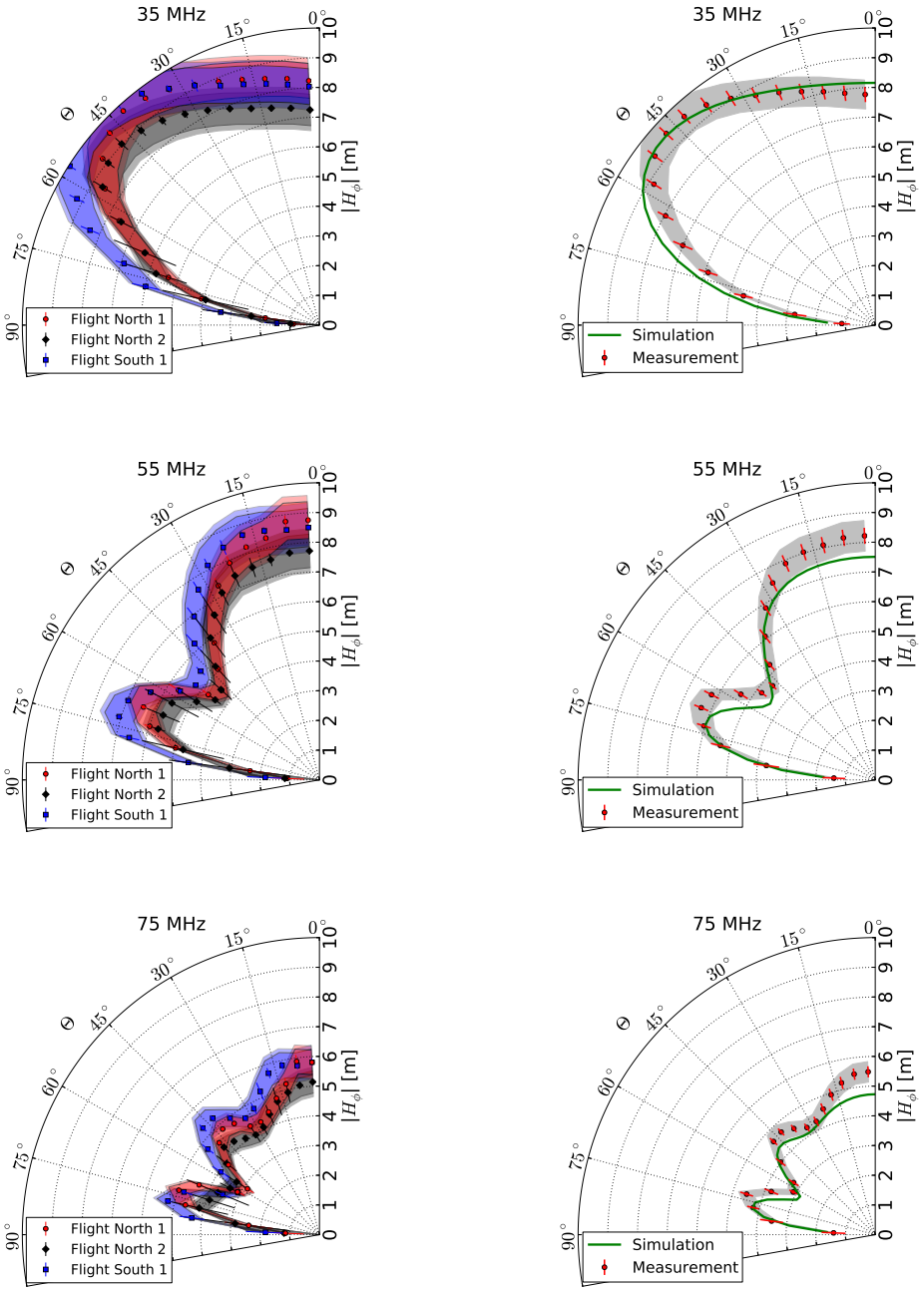

Figure 8.14: ***(left)*** *Mean horizontal vector effective length* $|H_\phi|$ *(dots) and standard deviation (error bars) of three different measurements and* ***(right)*** *the overall combinations in comparison to the simulation (green curve) as a function of the zenith angle in* 5° *bins at* ***(from top to bottom)*** $35\,\mathrm{MHz}$, $55\,\mathrm{MHz}$ *and* $75\,\mathrm{MHz}$. *The colored bands in the left diagrams describe the global (light color) and flight-dependent (dark color) systematic uncertainties of each flight. The gray band in the right diagrams describes the global systematic uncertainties whereas the statistical and flight-dependent systematic uncertainties are combined within the error bars.*

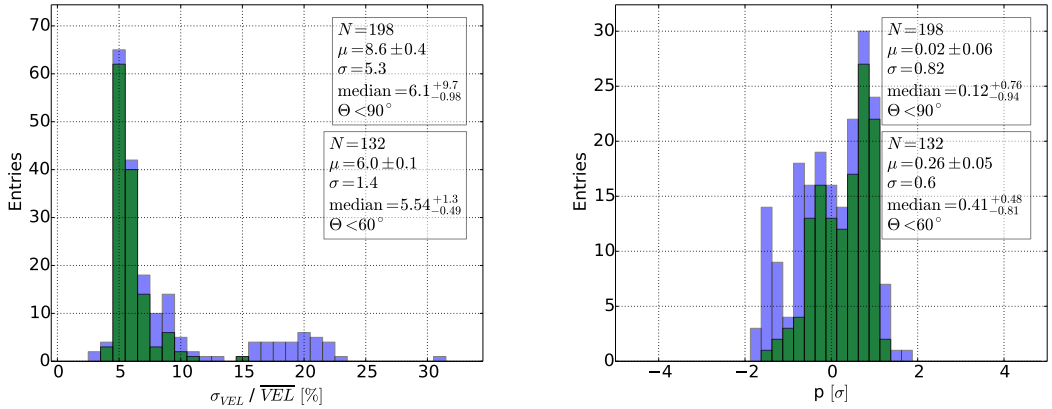

Figure 8.15: ***(left)*** *Histogram of the ratio $\sigma_{\mathrm{VEL}}/\overline{\mathrm{VEL}}$ of all frequencies and zenith angles with $\Theta < 90^\circ$ (blue histogram) and $\Theta < 60^\circ$ (green histogram). Here, σ_{VEL} denotes the fluctuation and $\overline{\mathrm{VEL}}$ is the average vector effective length (VEL) from five measurements of each zenith angle in bins of 5° and of each frequency.* ***(right)*** *Histogram of the compatibility parameter p of the example flight in numbers of the combined flight-dependent uncertainties σ of all frequencies and zenith angles with $\Theta < 90^\circ$ (blue histogram) and $\Theta < 60^\circ$ (green histogram). The combined flight-dependent uncertainty σ is determined by the quadratic combination of the flight-dependent uncertainties of $\overline{\mathrm{VEL}}_4$ with the flight-dependent systematics and the statistical uncertainties of the example flight.*

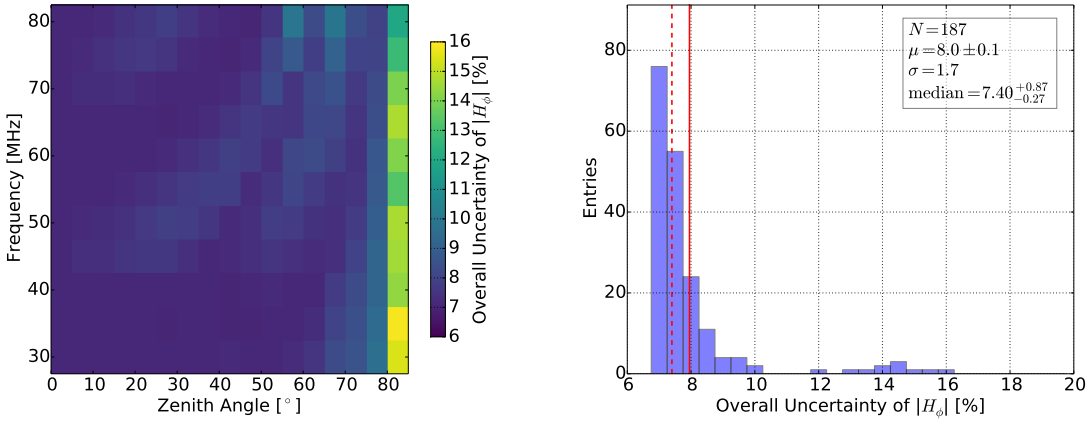

Figure 8.16: ***(left)*** *Overall uncertainty of the horizontal vector effective length $|H_\phi|$ including statistical and systematic uncertainties for all frequencies as a function of the zenith angle Θ up to 85° in 5° bins.* ***(right)*** *Histogram of all overall uncertainties for all frequencies and all zenith angle bins previously mentioned. The median (average value μ) is marked as red dashed line (red solid line).*

exceeds $20\,\%$. Therefore, angles beyond 85° are not considered in the following discussion. Taking all intervals of the frequencies and zenith angles with equal weight, the median overall uncertainty including statistical and systematic uncertainties is $7.4^{+0.9}_{-0.3}\,\%$. The green curve in Fig. 8.14 marks the simulation of $|H_\phi|$. The agreement between the combined measurements and the simulation of $|H_\phi|$ is illustrated in the diagram of their ratio versus zenith angle Θ and frequency f in the upper left panel of Fig. 8.17. In the upper right panel of Fig. 8.17, all ratios are filled into a histogram with entries

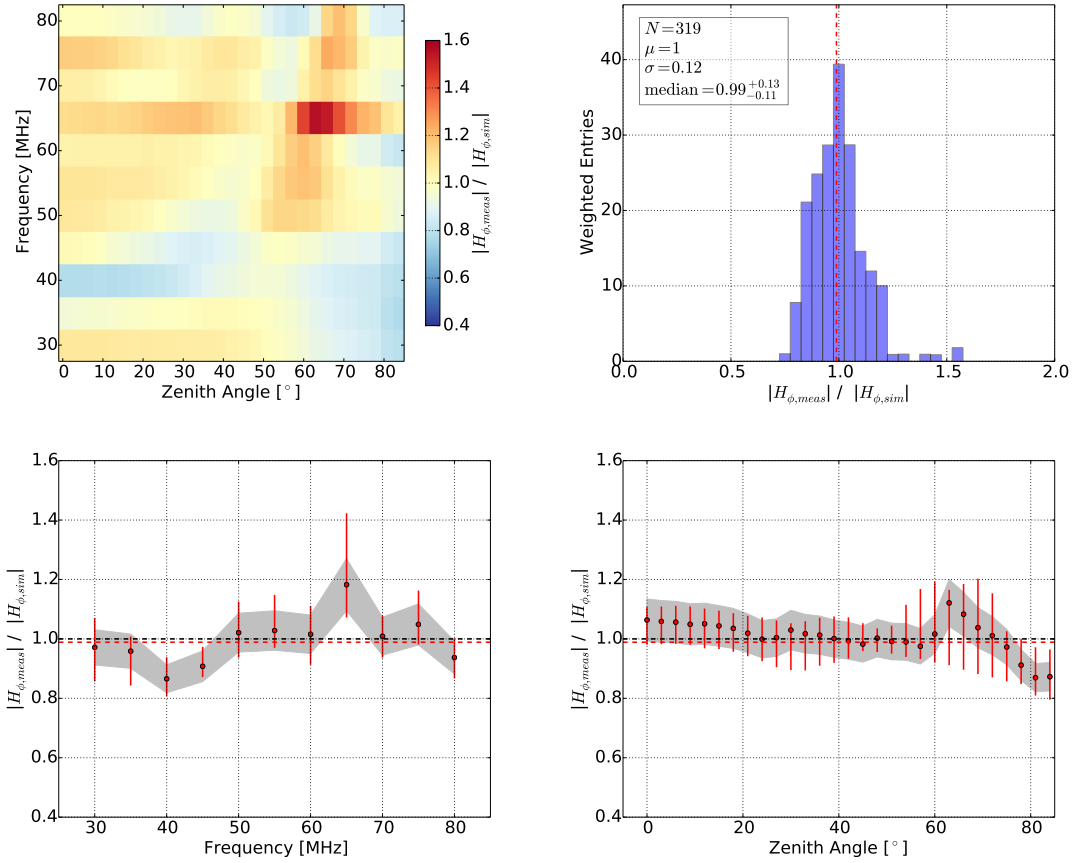

Figure 8.17: *Combined horizontal vector effective length $|H_\phi|$ compared to the simulation.* ***(top left)*** *Ratio of the combination of all measurements and simulation for all frequencies as a function of the zenith angle Θ up to 84° in 3° bins.* ***(top right)*** *Histogram of the ratios of the combination of all measurements and simulation for all frequencies and all zenith angle bins previously mentioned weighted with $\sin(\Theta)$. The median value is marked as the red dashed line.* ***(bottom left)*** *Median (red dots) and the $68\,\%$ quantile (red error bars) of the zenith angle weighted ratio distribution as a function of the frequency.* ***(bottom right)*** *Median (red dots) and the $68\,\%$ quantile (red error bars) of the ratio distribution as a function of Θ. The gray band indicates the global systematic uncertainty of the measurement and the red dashed lines mark the overall zenith angle weighted median in both lower diagrams.*

weighted by $\sin(\Theta)$ in consideration of the decrease in field of view at small zenith angles. The combined measurement and the simulation agree to within $1\,\%$ in the median. The fluctuation described by the $68\,\%$ quantile is at the level of $\frac{0.13+0.11}{2} = 0.12$. The two lower panels of Fig. 8.17 show the median ratio as a function of the frequency (left) and as a function of the zenith angle (right). In both cases, the red error bars mark the $68\,\%$ quantile of the distributions.

8.3.2 Meridional Vector Effective Length

In this subsection, the results of the meridional VEL $|H_\theta|$ are discussed. For both subcomponents $|H_{\theta,\mathrm{hor}}|$ and $|H_{\theta,\mathrm{vert}}|$, three independent measurements were taken and averaged. The averaged components are combined to determine $|H_\theta|$ as a function of the zenith angle Θ using Eq. (8.1). In

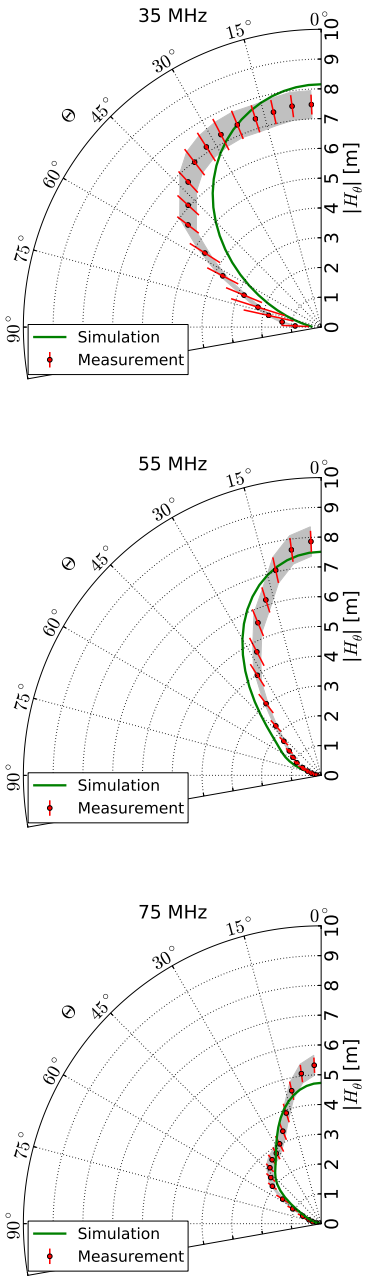

Figure 8.18: *Combination of all measurements of the meridional vector effective length $|H_\theta|$ (red dots) as a function of the zenith angle Θ in comparison to the simulation (green curve) for three different frequencies* ***(from top to bottom)*** $35\,\mathrm{MHz}$, $55\,\mathrm{MHz}$ *and* $75\,\mathrm{MHz}$. *The gray band describes the global systematic uncertainties whereas the statistical and flight-dependent systematic uncertainties are combined within the error bars.*

Fig. 8.18, all performed measurements of $|H_\theta|$ are combined in zenith angle intervals of 5°, weighted by the quadratic sum of the systematic and the statistical uncertainties of each flight. The gray band describes the global systematic uncertainties whereas the statistical and flight-dependent systematic uncertainties are combined within the red error bars. The global systematic uncertainty of the combined VEL is $6.3\,\%$. The uncertainties considering flight-dependent systematic and statistical uncer-

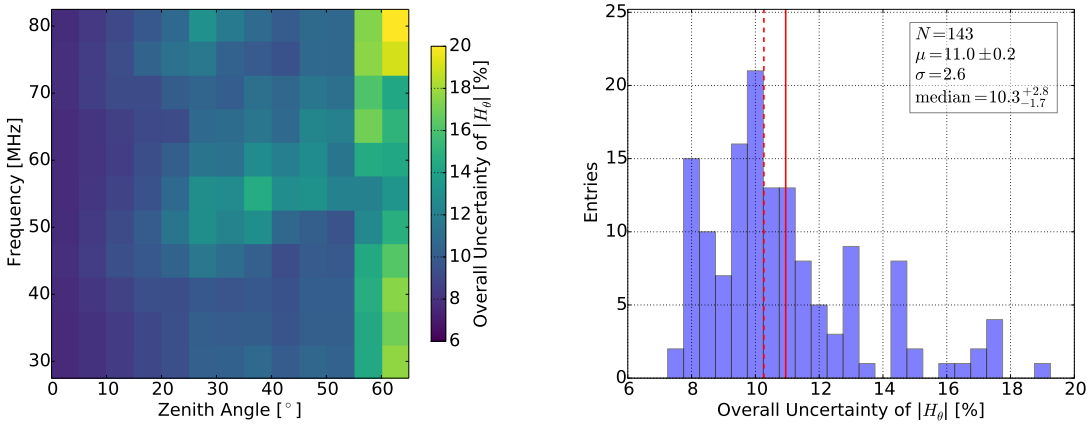

Figure 8.19: ***(left)*** *Overall uncertainty of the meridional component of the LPDA vector effective length* $|H_\theta|$ *including statistical and systematic uncertainties for all frequencies as a function of the zenith angle* Θ *up to* $65°$ *in* $5°$ *bins.* ***(right)*** *Histogram of all overall uncertainties for all frequencies and all zenith angles up to* $65°$*. The median (average value* μ*) is marked as red dashed line (red solid line).*

tainties of the combined VEL result in $11.2\,\%$ at a zenith angle of $(42.5 \pm 2.5)°$ and a frequency of $55\,\mathrm{MHz}$. The overall uncertainty of the determined LPDA VEL in the meridional polarization adds quadratically to $12.9\,\%$. The overall uncertainty of all other arrival directions and frequencies are shown on the left side of Fig. 8.19. On the right side of Fig. 8.19, a histogram of the overall uncertainties for all frequencies and zenith angle bins up to $65°$ is shown. For larger zenith angles, the LPDA loses sensitivity and the systematic uncertainty exceeds $20\,\%$. Therefore, these angles are not considered in the following discussion. Taking all intervals of the frequencies and zenith angles with equal weight, the median overall uncertainty including statistical and systematic uncertainties is $10.3^{+2.8}_{-1.7}\,\%$. This is larger than the uncertainty of the horizontal component $|H_\phi|$. The reasons are that firstly, the meridional component $|H_\theta|$ is a combination of two measurements of $|H_{\theta,\mathrm{hor}}|$ and $|H_{\theta,\mathrm{vert}}|$ whereas $|H_\phi|$ is directly measured. Secondly, the number of measurements is smaller than in the case of $|H_\phi|$ and thirdly, the horizontal component is corrected for the octocopter misplacement and misalignment in comparison to the meridional subcomponents where this effect is included in the systematic uncertainties. The green curve in Fig. 8.18 indicates the simulation of $|H_\theta|$. The agreement between the combination of all measurements and the simulations of $|H_\theta|$ is illustrated by the diagram of their ratio versus zenith angle Θ and frequency f shown in the upper left panel of Fig. 8.20. In the upper right panel, all ratios for all zenith angles and frequencies are filled into a histogram with entries weighted by $\sin(\Theta)$ in consideration of the decrease in field of view at small zenith angles. The combined measurement and the simulation agree to within $5\,\%$ in the median. The fluctuation described by the $68\,\%$ quantile is at the level of $\frac{0.29+0.22}{2} = 0.26$. The two lower panels of Fig. 8.20 show the median ratio as a function of the frequency (left) and as a function of the zenith angle (right). In both cases, the red error bars mark the $68\,\%$ quantile of the distributions.

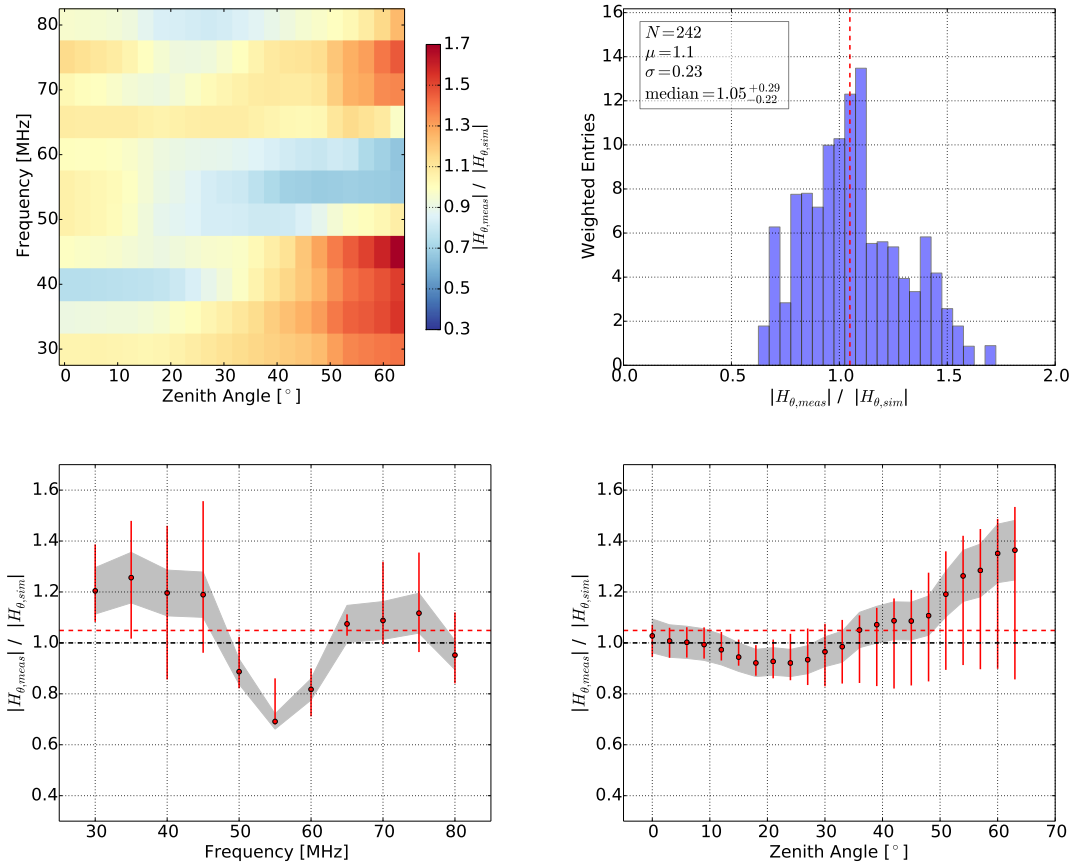

Figure 8.20: *Combined meridional vector effective length $|H_\theta|$ compared to the simulation.* ***(top left)*** *Ratio of combination of all measurements and simulation for all frequencies as a function of the zenith angle Θ up to 63° in 3° bins.* ***(top right)*** *Histogram of all ratios of the combination of all measurements and simulation for all frequencies and all zenith angle bins previously mentioned weighted with $\sin(\Theta)$. The median value is marked as the red dashed line.* ***(bottom left)*** *Median (red dots) and the $68\,\%$ quantile (red error bars) of the zenith angle weighted correction factor distribution as a function of the frequency.* ***(bottom right)*** *Median (red dots) and the $68\,\%$ quantile (red error bars) of the ratio distribution as a function of Θ. The gray band indicates the global systematic uncertainty of the measurement and the red dashed lines mark the overall zenith angle weighted median in both lower diagrams.*

8.3.3 Interpolation to all Arrival Directions and Frequencies

The horizontal and meridional VEL magnitudes are measured in the LPDA axis with highest sensitivity to the respective VEL component (cf. Sec. 8.1) and in frequency bins of $5\,\mathrm{MHz}$. To achieve an overall LPDA calibration for all incoming directions and frequencies the measurement is combined with the standard original simulation of the LPDA VEL pattern. In contrast to the simulations presented in this chapter, only the LPDA with the following amplifier stage but without the transmitting antenna are taken into account as discussed in Chap. 7. This original simulation of the LPDA pattern is then combined with the results from the calibration campaign. The calibrated LPDA VEL pattern is obtained by multiplying the full pattern of the simulated VEL with the ratio of measured to simulated VEL magnitudes shown in Figs. 8.17 and 8.20. The ratios are linearly interpolated between

the measurements at each zenith angle and each frequency bin. The respective frequency and zenith angle dependent ratios are applied at all azimuth angles. With this method, the magnitude of the VEL is normalized to the calibration measurements, while the VEL phase comes entirely from the original simulation.

8.4 Influence on Cosmic-Ray Signal Reconstruction

In this section, the influence of the modified LPDA pattern on the cosmic-ray signal reconstruction is discussed. In the first part of this section, the influence of the differences between simulated and measured VEL on the electric field as well as on the radiation energy for one event with a specific arrival direction are presented. In the second part, the influence of the uncertainty of both components of the VEL on the electric-field is discussed.

8.4.1 Influence of Modified Pattern on one Example Event

To reconstruct the electric field of a measured radio signal induced by an air shower, the Auger software framework $\overline{\text{Off}}\,\underline{\text{line}}$ [219, 220] is used (cf. Sec. 4.3.6). To show the influence of the improved VEL, an air shower measured in 9 stations at AERA with a zenith angle of 30° and an azimuth angle of 14° south of east is presented as an example. The energy of the primary cosmic ray is reconstructed to $1.1 \cdot 10^{18}\,\mathrm{eV}$ using information from the surface detector. In Fig. 8.21, the electric field reconstructed at the station with highest signal-to-noise ratio (SNR) is shown once using the simulated antenna response with and once without the corrections owing to the measurements of the VEL magnitude in both components. For clarity, only one polarization component of the electric field is shown. The general shape of the electric-field trace is the same for both reconstructions. The trace of the modified LPDA pattern exhibits an up to $7\,\%$ larger amplitude. The measured energy fluence that scales with the amplitude squared in the east-west polarization at this station with highest SNR changes from $100\frac{\mathrm{eV}}{\mathrm{m}^2}$ to $112\frac{\mathrm{eV}}{\mathrm{m}^2}$. The total energy fluence of all polarizations changes from $141\frac{\mathrm{eV}}{\mathrm{m}^2}$ using the simulated antenna response pattern to $156\frac{\mathrm{eV}}{\mathrm{m}^2}$ using the modified antenna response pattern which is an effect at the level of $9\,\%$. The reconstructed radiation energy of the full event changes from $7.96\,\mathrm{MeV}$ to $8.54\,\mathrm{MeV}$. The ratio of these radiation energies is 0.93.

8.4.2 Uncertainty of the Cosmic-Ray Signal Reconstruction

In this subsection, the systematic uncertainty of the cosmic-ray signal reconstruction that results from the overall uncertainty of the calibration and from the uncertainty due to different ground permittivities is determined. In the first case, the VEL magnitude is shifted up and down by one standard deviation of the overall uncertainty. The VEL phase remains unchanged. In the case of the uncertainty due to different ground permittivities, the antenna pattern with a ground permittivity of 2 and of 10 are used (see Fig. 8.13) which is based on the permittivity measurements discussed in Chap. 6. The respective VEL is denoted as H^{down} and H^{up}. The antenna response is applied to a simulated electric-field pulse using once H^{up} and once H^{down} to obtain the corresponding voltage traces $\mathcal{U}^{\mathrm{up}}$ and $\mathcal{U}^{\mathrm{down}}$ according to Eq. (3.21). Then, the original VEL is used to reconstruct the electric-field pulse once from $\mathcal{U}^{\mathrm{up}}$ and once from $\mathcal{U}^{\mathrm{down}}$. From the difference of the two resulting electric-field pulses, the systematic

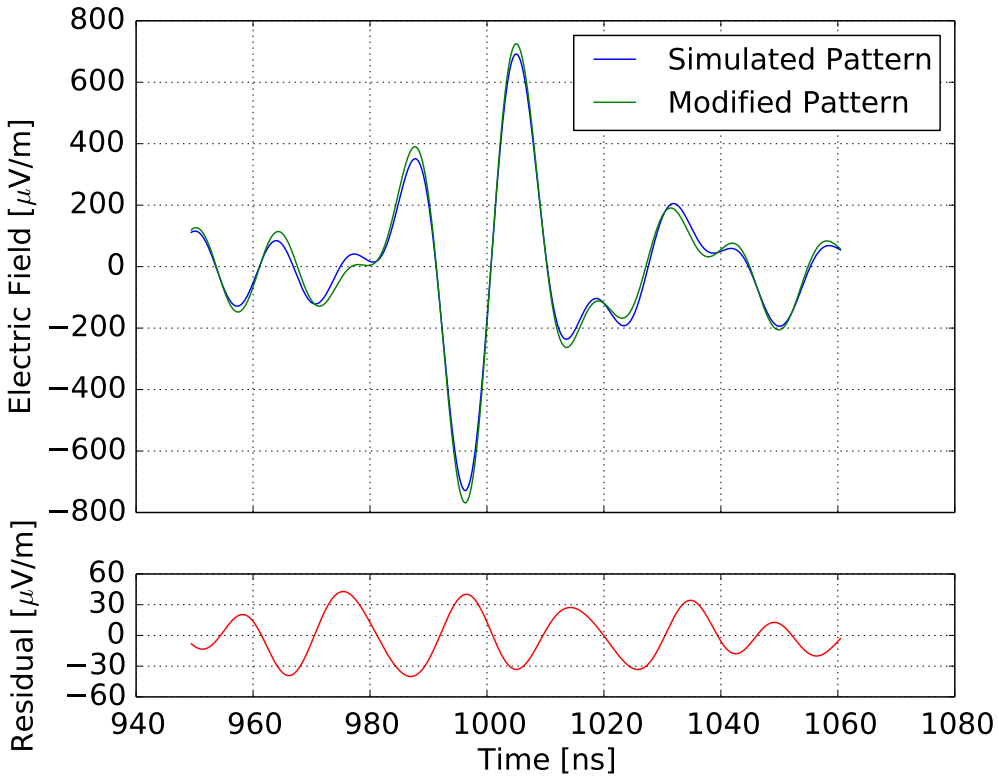

Figure 8.21: ***(top)*** *Reconstructed electric-field trace at the station with highest signal-to-noise ratio in the east-west polarization of a signal measured at AERA with a zenith angle of* 30° *and an azimuth angle of* 14° *south of east using the simulated LPDA pattern (blue line) and using the modified pattern considering the correction factors between measurement and simulation (green line). The residual between both reconstructed traces as function of the time is shown in the* ***(lower)*** *diagram. The measured energy fluence in the east-west polarization changes from* $100\,\frac{\mathrm{eV}}{\mathrm{m}^2}$ *to* $112\,\frac{\mathrm{eV}}{\mathrm{m}^2}$.

uncertainty of the amplitude or the energy fluence can be determined. Both uncertainties, resulting from the calibration campaign and resulting from different ground permittivities, are then combined quadratically.

An additional uncertainty on the electric-field trace can arise due to an uncertainty on the VEL phase. An uncertainty in the VEL phase leads to a signal distortion of the radio pulse resulting in an increased signal pulse width and a smaller electric-field amplitude or vice versa. However, the energy fluence of the signal pulse which is given by the integral over the electric-field trace remains constant. Hence, a VEL phase uncertainty propagates to an additional uncertainty in the electric-field amplitude whereas the energy fluence does not change due to a VEL phase uncertainty. Therefore, the systematic uncertainty of the energy fluence due to the VEL uncertainty is discussed in the following.

The radio pulse is approximated with a bandpass-limited Dirac pulse and the polarization is adjusted according to the dominant geomagnetic emission process. As the uncertainty of the VEL and the polarization of the electric-field pulse depend on the incoming signal direction, different directions in bins of 10° in the azimuth angle and in bins of 5° in the zenith angle are simulated. Due to the

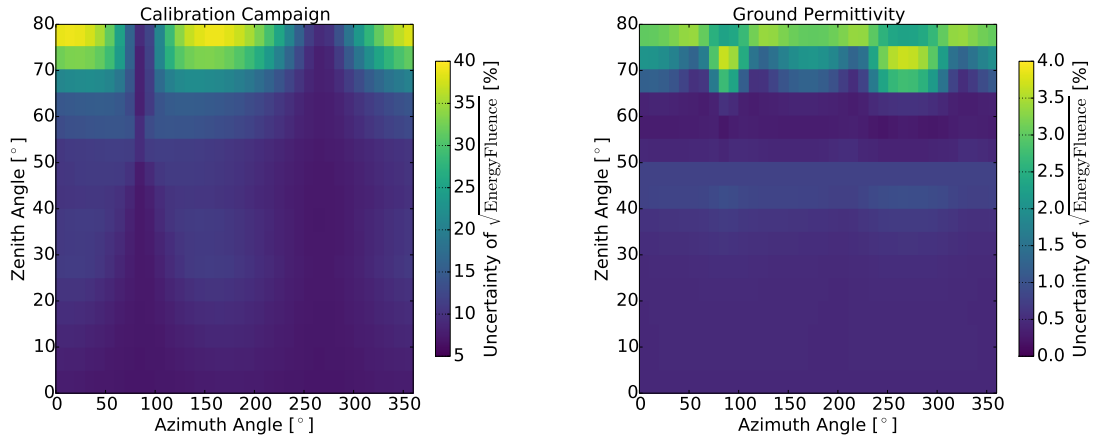

Figure 8.22: *Systematic uncertainty of the square root of the energy fluence resulting from the calibration campaign* ***(left)*** *and resulting from different ground permittivities* ***(right)*** *for all arrival directions taking into account a signal polarization due to the dominant geomagnetic emission process. The calibration uncertainty is the dominant uncertainty in the energy fluence reconstruction.*

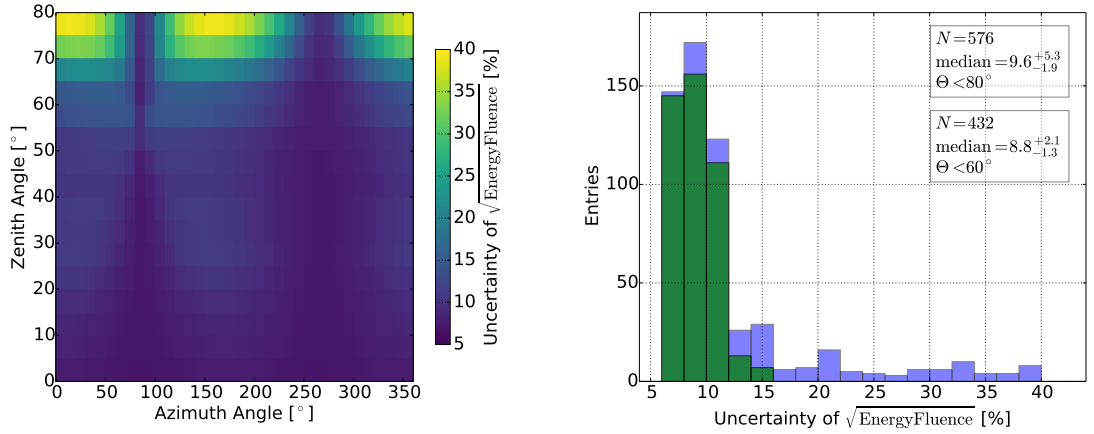

Figure 8.23: ***(left)*** *Combined systematic uncertainty of the square root of the energy fluence resulting from the calibration campaign and resulting from different ground conditions for all arrival directions taking into account a signal polarization due to the dominant geomagnetic emission process.* ***(right)*** *Histogram of the systematic uncertainty of the square root of the energy fluence of signals with zenith angles smaller than* $80°$ *(blue) and of signals with zenith angles smaller than* $60°$ *(green).*

changing polarization also the relative influences of the $|H_\phi|$ and $|H_\theta|$ components change with direction. The resulting systematic uncertainties of the energy fluence from the calibration campaign and resulting from different ground permittivities are shown in Fig. 8.22 and the quadratic combination of these uncertainties is presented in Fig. 8.23. The square root of the energy fluence is shown because the energy fluence scales quadratically with the electric-field amplitude and the cosmic-ray energy. Hence, the systematic uncertainty of the square root of the energy fluence is the relevant uncertainty in most analyses. The systematic uncertainty is dominated by the calibration uncertainty and for most regions, the systematic uncertainty is at the level of $10\,\%$. The uncertainty increases only at large

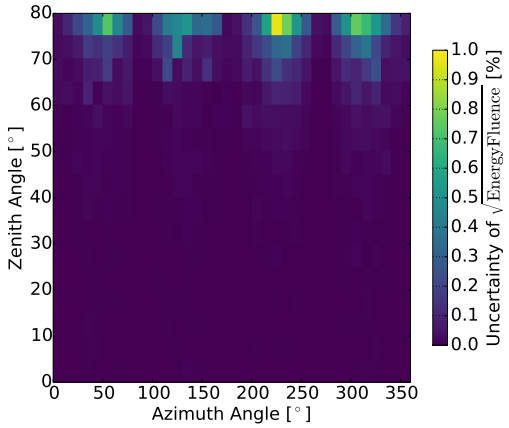

Figure 8.24: *Systematic uncertainty of the square root of the energy fluence due to an additional phase offset normally distributed around $\mu = 0\,^\circ$ with a standard deviation of $\sigma = 3\,^\circ$ for all arrival directions taking into account a signal polarization due to the dominant geomagnetic emission process.*

zenith angles ($\theta > 60^\circ$) due to the increased uncertainty of $|H_\theta|$. An azimuthal pattern appears at 90° and 270°. At these azimuth angles, the uncertainty is smaller because the electric-field pulse is polarized in the $\vec{e}_\phi$ component and only the more precise $|H_\phi|$ component contributes. For incoming signal directions with zenith angles smaller than 60°, the systematic uncertainty of the square root of the energy fluence owing to the antenna calibration and different ground permittivities is at most $14.2\,\%$ with a median of $8.8^{+2.1}_{-1.3}\,\%$.

As an additional cross check, simulation studies with changed VEL phase have been performed to investigate the influence of the phase on the energy fluence. It is found that there is no influence in case of a constant phase offset. A frequency-dependent offset which changes the phase derivation with respect to the frequency just move the signal in time without any differences in the signal pulse shape. In the case of adding an offset normally distributed around $\mu = 0\,^\circ$ with a standard deviation of $\sigma = 3\,^\circ$ for all arrival directions and frequencies, an influence far below $0.1\,\%$ for all zenith angles smaller than $60\,^\circ$ is observed. The influence increase to the level of $1\,\%$ at higher zenith angles which is negligible compared to the uncertainties from the calibration. The uncertainty of the square root of the energy fluence due to this additional phase offset is shown in Fig. 8.24.

9 Development of a 3D Radio Station at AERA

Typically, radio stations in air shower experiments consist of two perpendicular polarized antennas which are usually aligned horizontally. The third component, in this case the vertical polarization of the electric field, is not measured directly but is important for the data analysis of radio signals from air showers. The third component is then calculated from observations in the two other components, the arrival direction, and exploiting the property of electromagnetic waves that they are polarized only perpendicular to the propagation direction (cf. Chap. 3).
Radio stations consisting of three separated antennas with different antenna orientations are called 3D radio stations. They enable a direct measurement of all components of the electric field in contrast to the conventional 2D radio stations. The additional measurement of the third component potentially reduces the uncertainties of the electric-field reconstruction and thus improves the data quality. Furthermore, the measurement of the third component enables measuring radio signals from extensive air showers in regions where the 2D radio station is not sensitive and thus potentially extends the field of view of the radio detector.
For AERA, a new 3D radio station was developed. A subset of Butterfly radio stations is extended with a vertical antenna called Wifivert antenna forming a 3D radio station. In this chapter, the antenna design and first data analysis of data recorded with 3D radio stations are presented.
The chapter is structured as follows. First, the motivation of 3D radio stations at AERA is pointed out in detail. In Sec. 9.2, the mechanical design of the Wifivert antenna is discussed. Then, the antenna is electrically characterized in Sec. 9.3. Afterwards, the antenna response pattern of the Wifivert antenna is presented in Sec. 9.4 based on simulations using the NEC-2 simulation code. The Wifivert antennas have been deployed at AERA and take data since 2015. In Sec. 9.5, a first data analysis is performed and the functionality of the antenna is proven. Furthermore, based on this data analysis a first conclusion about the physics goals of 3D radio stations is given.

9.1 Physics Goals of 3D Radio Stations

In several analyses, it was shown that AERA enables the investigation of cosmic-ray and extensive air shower physic using 2D radio station consisting of two horizontally but perpendicular to each other oriented antennas, e.g., [15, 20, 24, 25]. Nevertheless, there are good reasons for developing 3D radio stations with an additional vertical antenna to observe radio signals from extensive air showers. In the following, the motivation of such 3D radio stations is pointed out.
One reason to develop a 3D radio station is that they enable measuring the full radio signal produced in extensive air showers in all three coordinates with one radio station only. Thus, three measurements of the radio signal are performed from which the electric field can be reconstructed. In the case of a 3D

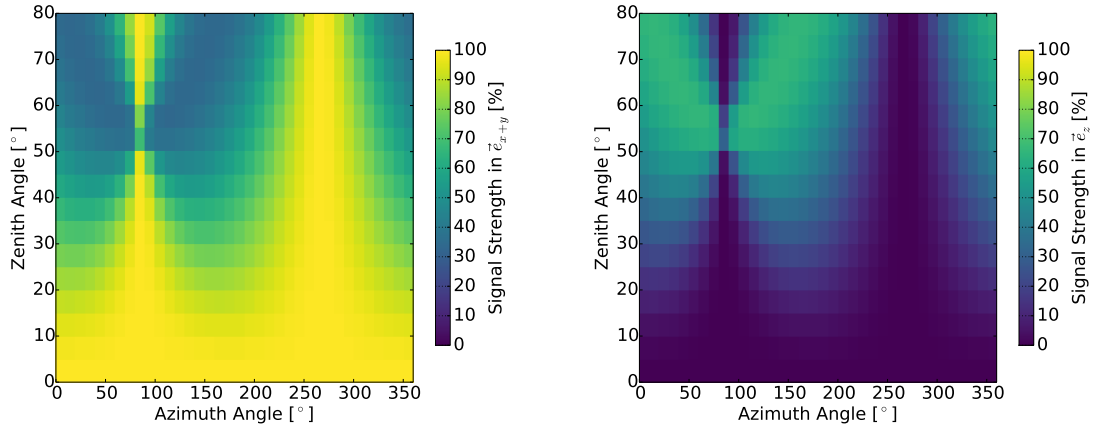

Figure 9.1: *The expected signal polarization for all arrival directions. The radio pulse is approximated with a bandpass-limited Dirac pulse and the polarization is adjusted according to the dominant geomagnetic emission process.* ***(left)*** *Color coded is the signal fraction of the signal horizontally polarized in* $\vec{e}_{x+y}$. ***(right)*** *Color coded is the signal fraction of the signal vertically polarized in* $\vec{e}_z$ *direction.*

radio station the system of equation as discussed in Sec. 3.8 is mathematically over-determined. There are three permutations of two measurements which can be used for the electric field reconstruction. These permutations can be combined and thus potentially reduces the uncertainties of the electric-field reconstruction.

Another reason becomes visible when calculating the expected radio signal strength from extensive air showers. In Fig. 9.1, the relative strength of the radio signal in the horizontally oriented XY-component (left) and in the vertical component (right) is visualized for all arrival directions in bins of 10° in the azimuth angle and in bins of 5° in the zenith angle. The radio pulse is approximated with a bandpass-limited Dirac pulse and the polarization is adjusted according to the dominant geomagnetic emission process. As can be seen, an azimuthal pattern appears at 90° and 270°. At these azimuth angles and for the regions with small zenith angles, the electric-field signal is mostly horizontally polarized. For all other regions, the vertical component of the signal gets more important, especially at large zenith angles. In general, the larger the zenith angle, the larger is the percentage fraction of the radio signal polarized into the vertical direction. As typically 2D radio stations consist of two horizontally aligned antennas, an additional vertical antenna extends the field of view of such radio stations to large zenith angles.

Extensive air showers coming from large zenith angles are called inclined showers or horizontal air showers (HAS). HAS have an increased flight path through the Earth's atmosphere resulting in a die-out of the hadronic and electromagnetic shower components before they are detectable at ground level. The shower information of HAS is then saved in the muonic and radio component of the shower only. In contrast to the muonic component, the radio emission primarily originates from the electromagnetic shower component. It is detectable on ground because the atmosphere is transparent to radio waves. Information provided by separate measurements of both components are directly connected to the primary cosmic-ray mass (cf. Sec 2.4.1). Furthermore, the area of the radio-emission footprint is extended to several square kilometers which shows great potential for future large-scale radio arrays

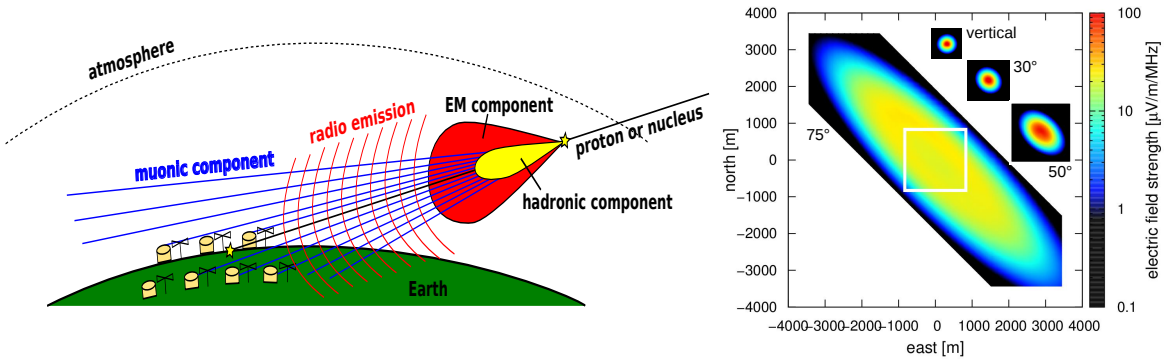

Figure 9.2: ***(left)*** *Region of the components of a horizontal air shower which has an increased flight path through the Earth's atmosphere. The hadronic and electromagnetic shower component die out before reaching the ground. The shower information is saved in the muonic and radio component of the shower only. Picture adapted from [35].* ***(right)*** *The footprint of the radio emission of a proton induced extensive air shower with an energy of* 10^{18} eV *for different zenith angles. The respective electric-field strength is color coded and obtained by CoREAS simulations [9, 28, 250]. The larger the zenith angle the larger is the footprint on ground. The white box marks the change of antennas distance from* 40 m *to* 100 m *in the simulation to save computing time [35, 251]. Plot taken from [35].*

(refer to [35, 36]). The principle of inclined air showers and their footprint on ground are illustrated in Fig. 9.2. As the fraction of the vertically polarized radio signal increases with the zenith angle, 3D radio stations potentially improve HAS research.

Moreover, an additional vertical antenna is useful for investigating extensive air showers with arrival directions from the north or south. In these cases, from Fig 9.1, a purely horizontally polarized signal is expected. According to the dominant geomagnetic emission process and the Earth's magnetic field pointing into the north direction [221], the radio signal is then fully polarized in the east-west component and produces a signal in the east-west antenna but no signal in the north-south antenna. However, small signal strengths are created in the north-south antenna due to noise. Even such small signals measured in the north-south antenna result in a large overestimation of the vertical electric-field component. The principle is illustrated in Fig. 9.3 for a signal coming from the south direction. For such arrival directions, an additional measurement of the radio signal using a vertical antenna enables constraining the signal reconstruction: If no signal pulse is measured in the vertical antenna, then the signal measured in the north-south antenna can be identified as noise and thus, can be rejected from the signal reconstruction.

9.2 Design of the Wifivert Antenna

A simple and economic solution of a 3D radio station at AERA is to extend the already used standard 2D radio stations at AERA with an additional vertical antenna. Compared with the LPDA, the Butterfly radio stations have a simpler antenna structure and therefore, they are chosen to test an additional vertical antenna. The most important design criterion is, that the influence of the vertical antenna on the Butterfly antenna is as little as possible. In this case, the reconstruction of the radio signal using the horizontal aligned Butterfly antennas is not negatively influenced and moreover, an additional

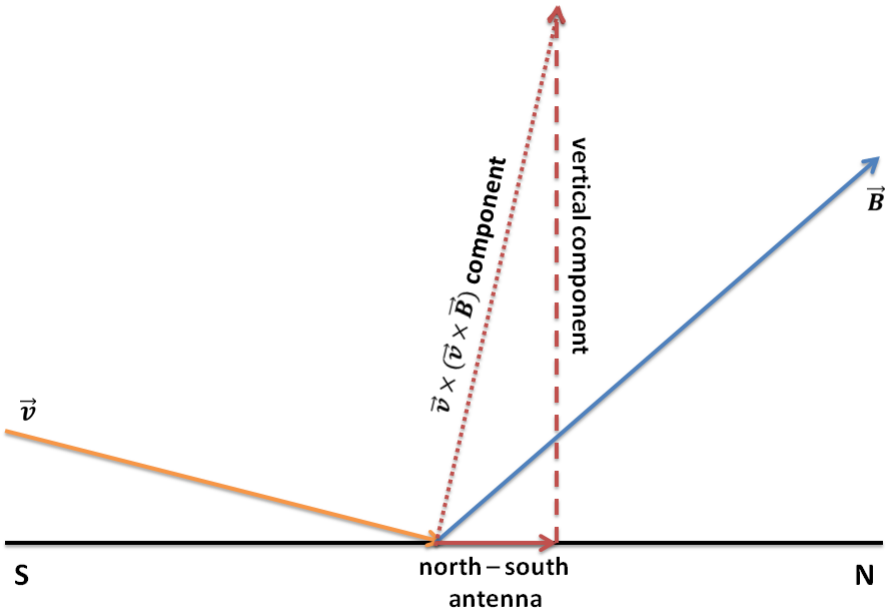

Figure 9.3: *Shower components of a radio signal with an incoming direction $\vec{v}$ (orange arrow) coming from south (S). The Earth's magnetic field $\vec{B}$ (blue arrow) points to the north direction. Then, the signal is expected to be polarized in the east-west direction due to the dominant geomagnetic effect. However, a small signal due to noise measured in the north-south antenna (red solid line) results in a large overestimation of the vertical electric-field component (red dashed line). Picture adapted from [252].*

information of the radio signal recorded with the vertical antenna is available. The influence of an additional vertical antenna on the Butterfly antenna is small if already existing components of the radio station are used as vertical antenna instead of implementing a further separated antenna. On the other hand, the structure of the additional antenna is then limited by the already existing structure of the radio station and thus, the antenna properties are not optimized for measuring radio signals from extensive air showers. Nevertheless, in the case of the Butterfly-equipped radio stations such antennas enables measuring the vertically polarized signal of radio signals from extensive air showers which is discussed later in this chapter.

The design of the Butterfly-equipped radio stations is described in detail in Sec. 4.3.1 and Sec. 4.3.3. The station pole and the wifi mast consist of aluminum - a conductive material - and are vertically aligned. Therefore, they are suited best as a vertical orientated antenna. On the other hand, the station pole and the wifi mast have fixed sizes and they are located at fixed positions. Moreover, the station pole is grounded. Hence, such antennas are not optimized to be sensitive in the frequency range 30 MHz and 80 MHz. Furthermore, an asymmetry in the antenna response pattern is expected because both, the station pole and the wifi mast, are displaced in the XY-plane and have an overlay in the z-axis. The combination of wifi mast and station pole to a vertical antenna is called Wifivert antenna. The whole Butterfly array can easily be extended with such Wifivert antennas. A 3D sketch of the Butterfly-equipped radio station extended with a Wifivert antenna is shown in Fig. 9.4. Color coded is

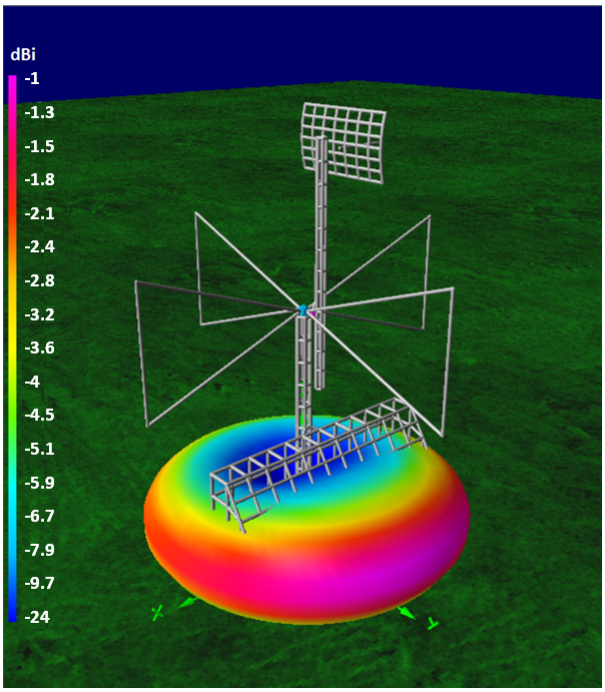

Figure 9.4: *Model of the 3D radio station equipped with two horizontally aligned Butterfly antennas and a vertically aligned Wifivert antenna used in the NEC-2 simulations. The wifi mast and the station pole form the Wifivert antenna. The Wifivert antenna footpoint (pink dot) is located in the middle of the Butterfly antennas close to their footpoints (blue dots). Color coded is the total Wifivert antenna gain in logarithmic units at* 55 MHz. *The pinker the color, the higher is the antenna sensitivity to this direction. At this frequency, the Wifivert antenna is most sensitive to the horizon, especially in the y-axis which corresponds to the north direction.*

the total Wifivert antenna gain for all arrival directions at 55 MHz obtained from NEC-2 simulations. The pinker the color, the higher is the antenna sensitivity to the respective arrival direction.

For the 3D radio station, the most components of the 2D radio station can be used without any modifications. Nevertheless, there are some modifications which have to be considered. The Wifivert antenna dipole arms have to be insulated from each other. Therefore, the wifi mast has to be electronically insulated from the wifi antenna as well as from the station pole. The aluminum clamp holding the wifi antenna and the clamp part used to fix the wifi mast are replaced with clamps made of non-conductive material. Moreover, both Wifivert dipole arms are connected to an additional low-noise amplifier (LNA). This LNA is located within the nut close to the Butterfly LNAs. The station pole is connected to the LNA via the screws fixing the Butterfly nut. The wifi mast is connected using an aluminum clamp at the wifi mast and an additional aluminum hat on top of the nut which is further connected to the LNA. All new components which are needed to extend the 2D radio station to a 3D radio station equipped with a Wifivert antenna are shown in Fig. 9.5.

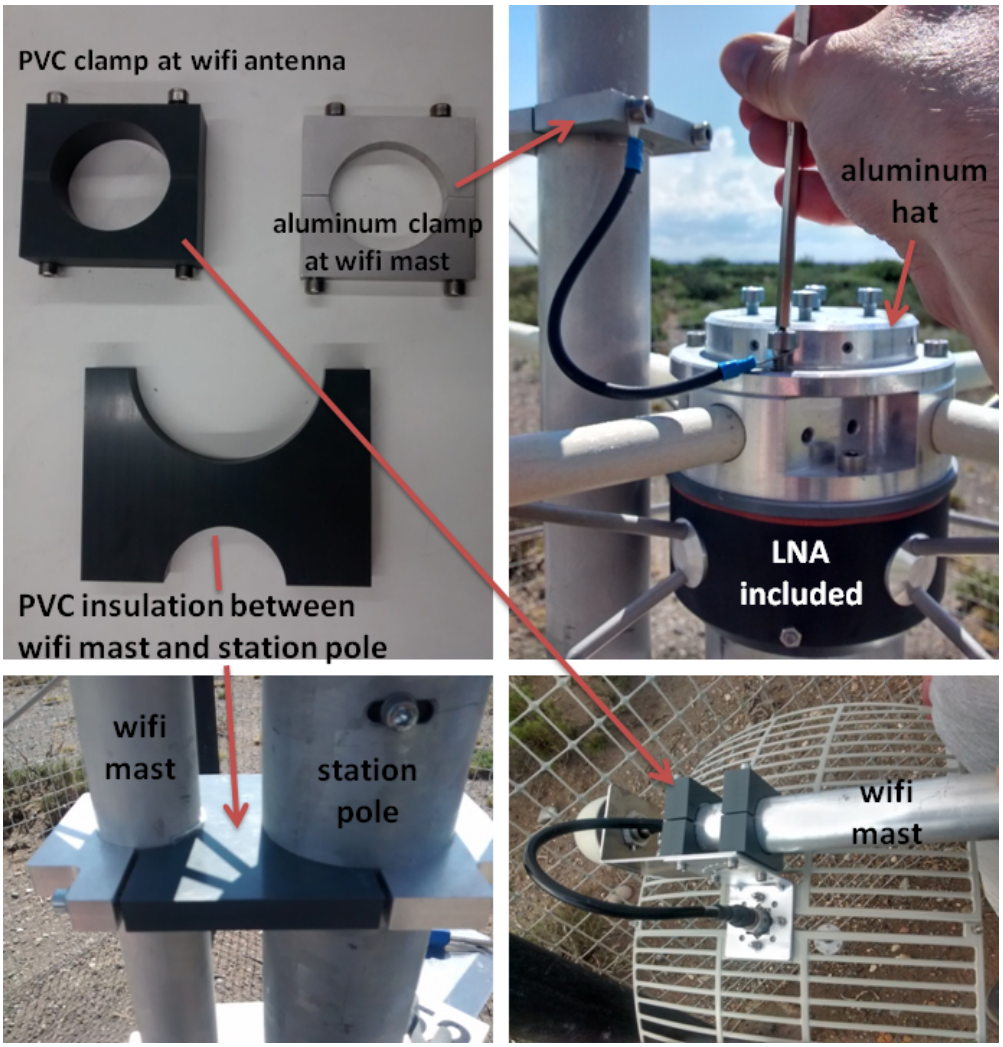

Figure 9.5: *Pictures of the modified antenna components needed to extend the Butterfly-equipped radio station at AERA to a 3D radio station equipped with the Wifivert antenna. The clamps of the Butterfly radio station holding the wifi mast and the wifi antenna are replaced with clamps made of PVC. An aluminum hat is added on top of the Butterfly hat to which the low-noise amplifier (LNA) is connected. The wifi mast is connected via an UV-resistant cable with the new aluminum hat and thus to the LNA.*

9.3 Electrical Characterization of the Wifivert Antenna

In this section, the Wifivert antenna is electrically characterized in terms of the antenna impedance and the antenna standard wave ratio (SWR). Afterwards, the electrical properties of the LNA connected to the Wifivert antenna are discussed. The LNA impedance as well as the LNA amplification described by the S-parameters are presented.

The NEC-2 simulation code is used to determine the antenna impedance and the antenna SWR. The model of the Wifivert antenna used in the simulation accounts for the full 3D radio station equipped with Butterfly antennas. The standard simulation model of the 2D radio station is modified with the additional Wifivert antenna as discussed in the previous section. Therefore, the wifi antenna and the station pole are electrically insulated from the wifi mast. The Wifivert antenna footpoint is set close

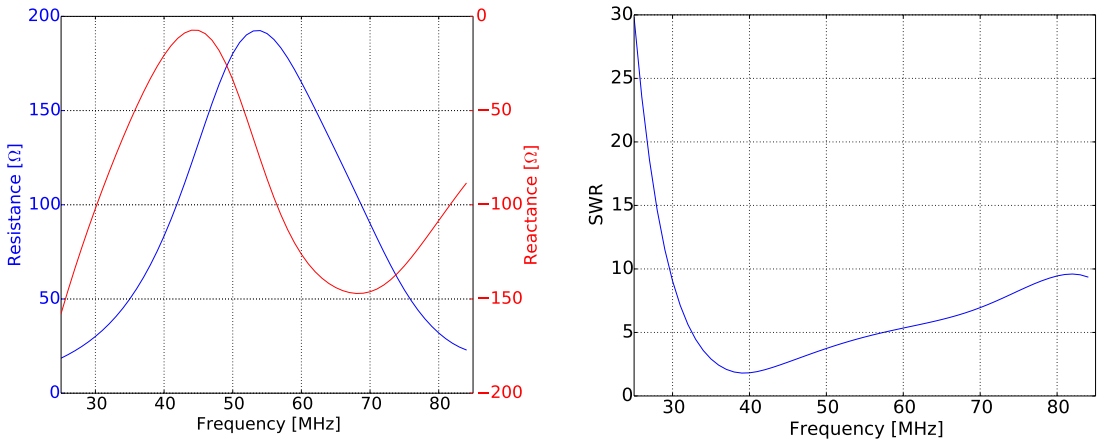

Figure 9.6: ***(left)*** *The Wifivert antenna impedance described by the antenna resistance (blue) and the antenna reactance (red) as well as* ***(right)*** *the resulting antenna standing wave ratio (SWR) as functions of the frequency obtained from NEC-2 simulations.*

to the Butterfly antenna footpoint connecting the wifi mast and the station pole as dipole arms with each other. The Wifivert antenna impedance and the corresponding SWR obtained from the NEC-2 simulation is shown in Fig. 9.6. The SWR reveals a minimum of below 2 at 40 MHz marking the antenna resonance frequency and which is well inside the sensitive frequency range of AERA of 30 MHz to 80 MHz. Hence, although the Wifivert antenna structure is not optimized, the Wifivert antenna fulfills the frequency requirement to be sensitive in the frequency range between 30 MHz to 80 MHz.

At the Wifivert antenna footpoint, an LNA is connected. A picture of the LNA is shown in Fig. 9.7. The LNA characteristics are described by the four amplifier S-parameters, most importantly by the power gain $|S21|^2$ and the power reflection at the LNA input port $|S11|^2$ which are related to the LNA impedance (cf. Sec. 3.6.5). The LNA impedance is shown on the left side of Fig. 9.8. The LNA power gain and the LNA power reflection at the input port are presented on the right side of Fig. 9.8. The LNA amplifies the recorded signal by a nearly constant value of about 24 dB in the whole frequency range from 30 MHz to 80 MHz. The LNA is originally developed to be used in the Butterfly antenna. Thus, the LNA impedance is optimized and matched to the Butterfly antenna impedance. In future, a new LNA has to be developed to reduce signal losses due to impedance mismatch between the Wifivert antenna and the LNA and to improve the Wifivert antenna sensitivity.

9.4 Simulation of the 3D Radio Station Response Pattern

In this section, the frequency and directional-dependent antenna sensitivity of the Wifivert antenna and its influence on the response pattern of the Butterfly antenna in terms of the VEL based on simulations is discussed. The simulations of the Wifivert antenna as well as of the Butterfly antenna account for the antenna itself as well as the following amplifier stage connected directly at the antenna footpoint in both cases. The simulation of the passive part considers the antenna response pattern at the antenna

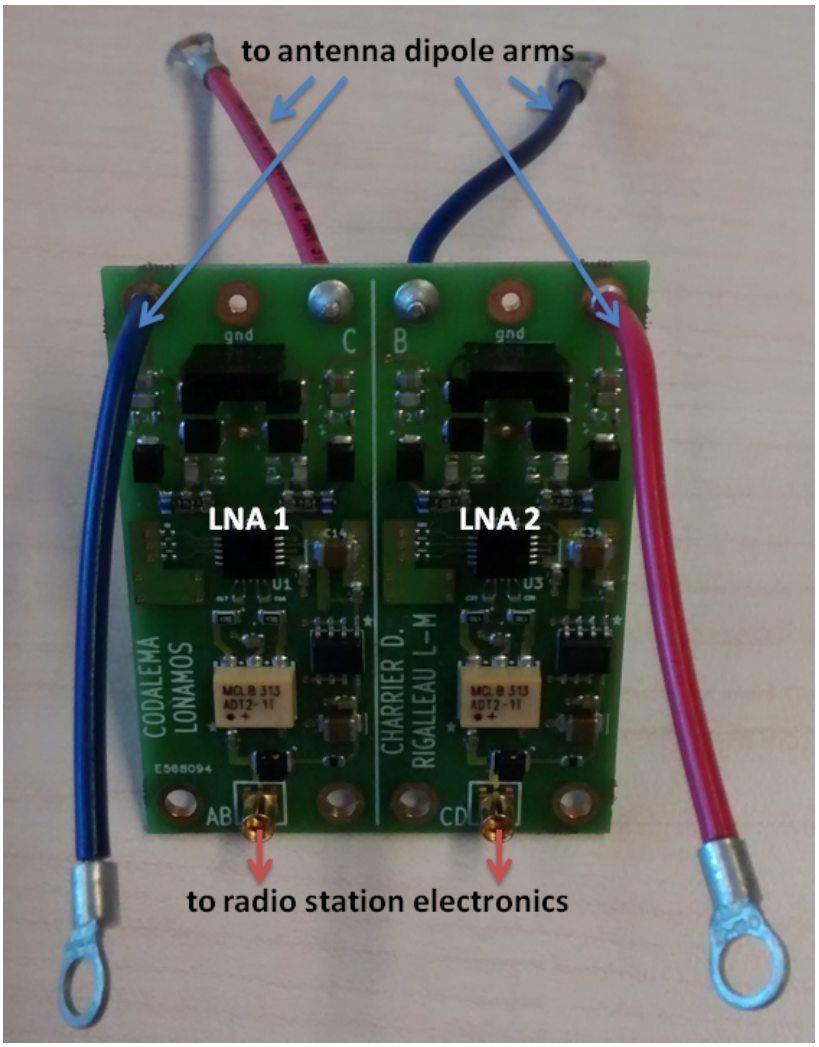

Figure 9.7: *Picture of the low-noise amplifier (LNA) used for the Wifivert antenna. Here, two LNAs are combined on one board. The red and blue cables are connected to the antenna dipole arms which are the station pole and the wifi mast in the case of the Wifivert antenna. The LNA output is located at the bottom of the LNA. A coaxial cable is needed to connect the LNA to the electronics of the radio station.*

footpoint and is performed using the NEC-2 simulation code. The LNA constitutes the active part of the antenna and its own influence on the antenna response pattern as well as reflection effects due to impedance mismatch between antenna and LNA which have to be considered separately.

For the simulation, realistic ground properties are taken into account. At standard ground conditions the ground conductivity is set to be $1.4\,\mathrm{mS/m}$ and the standard ground permittivity is set to be 5.5 (cf. Sec. 6 and Sec. 7.1).

The antenna VEL is calculated using Eq. (3.31) in a frequency range from $30\,\mathrm{MHz}$ to $80\,\mathrm{MHz}$ in steps of $1\,\mathrm{MHz}$, for zenith angles from $0\,^\circ$ to $90\,^\circ$ in steps of $3\,^\circ$, and for azimuth angles from $0\,^\circ$ to $360\,^\circ$ in steps of $7.5\,^\circ$. Then, the obtained VEL is modified with Eq. (3.49) considering the transfer function from the antenna footpoint to the output of the LNA. The respective antenna and LNA impedances used in the calculation are discussed in Sec. 9.3 in the case of the Wifivert antenna and in Sec. 4.3.3 in the case of the Butterfly antenna. The LNA is directly connected to the antenna footpoint for both an-

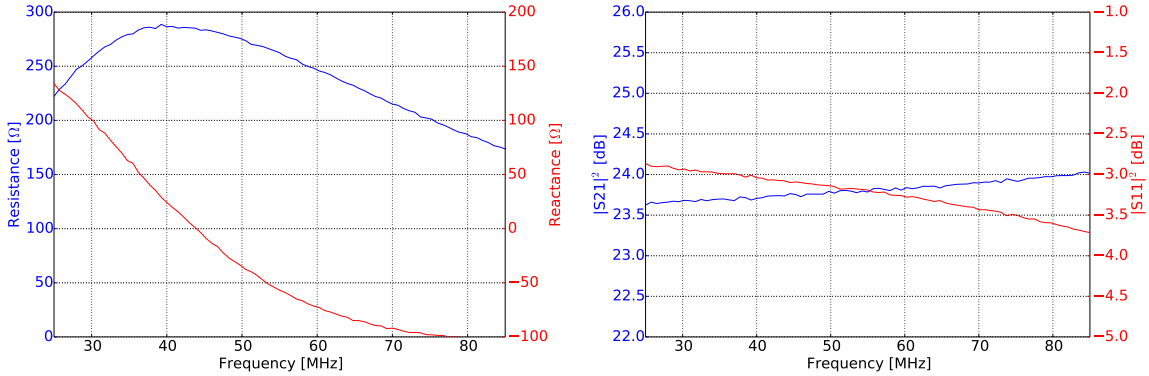

Figure 9.8: ***(left)*** *The low-noise amplifier (LNA) impedance described by the resistance (blue) and by the reactance (red).* ***(right)*** *The power gain $|S21|^2$ (blue) and the power reflection at the LNA input port $|S11|^2$ (red) as functions of the frequency.*

tenna types. Furthermore, no impedance transformer is used. Hence, to switch off their influences in Eq. (3.49), the transmission line length l_{tl} is set to zero and the transfer parameter r of the impedance transformer is set to 1.

In Fig. 9.9, the horizontal component $|H_\phi|$ and the meridional component $|H_\theta|$ as a function of the arrival direction for three different frequencies of 35 MHz, 55 MHz, and 75 MHz of vertically polarized Wifivert antenna are presented. The simulations exhibit that the Wifivert antenna is mainly sensitive for vertically polarized signals and only at higher frequencies sensitive in the horizontal component which is expected as the Wifivert antenna is vertically aligned. Thus, it is focused on the meridional component of the Wifivert antenna VEL $|H_\theta|$ in the following. In general, the Wifivert antenna is mainly sensitive at large zenith angles around 60 ° to 70 ° and decreases to small zenith angles close to 0 ° as well as to large zenith angles close to 90 °. For a better comparison of the antenna VEL between different arrival directions, in the following, it is focused on the four cardinal directions: north, south, east and west. In Fig. 9.10, the meridional component of the Wifivert VEL $|H_\theta|$ is presented as function of the zenith angle for the four cardinal directions and at three different frequencies of 35 MHz, 55 MHz, and 75 MHz. The simulation reveals an azimuthal asymmetry of the Wifivert antenna response pattern. This asymmetry is caused by the asymmetric setup of the Wifivert antenna as explained in Sec. 9.2 and the electronics box made of conductive material located north of the radio station.

Furthermore, in Fig. 9.11, the respective Wifivert antenna VEL is shown as a function of the frequency at a constant zenith angle of 15 °, 45 °, and 75 °. The simulations yield a larger Wifivert antenna sensitivity at frequencies up to about 50 MHz and a decrease to larger frequencies.

The most important requirement of the additional antenna in the Butterfly-equipped radio stations is that its influence on the Butterfly antenna is small. Then, the reconstruction of the radio signal using the horizontal aligned Butterfly antennas is not negatively influenced. As the Wifivert antenna consists of the structure of the radio station itself, only small influences on the Butterfly antenna response pattern are expected. These influences are investigated by comparing the response pattern of the Butterfly antenna obtained from the standard simulation with those obtained from the modified simulation considering the additional Wifivert antenna. In the standard simulation model of the Butterfly antenna,

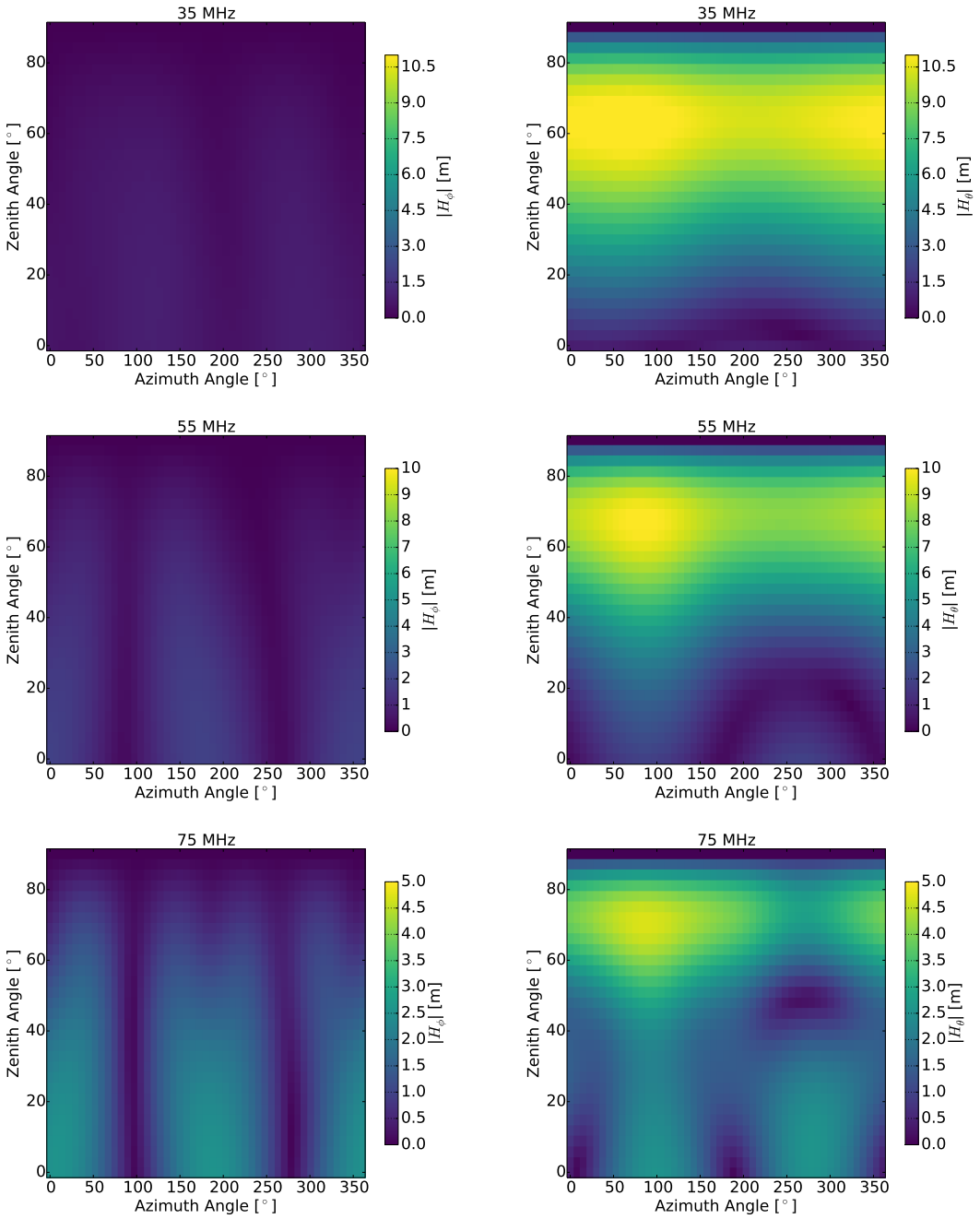

Figure 9.9: *Antenna response pattern of the vertically polarized Wifivert antenna.* ***(left)*** *Horizontal component of the Wifivert antenna vector effective length (VEL)* $|H_\phi|$ *and* ***(right)*** *meridional component of the Wifivert antenna VEL* $|H_\theta|$ *obtained from NEC-2 simulations as a function of the zenith angle* Θ *and the azimuth angle* Φ *counted from east anti clock wise at three different frequencies of* ***(from top to bottom)*** $35\,\mathrm{MHz}$, $55\,\mathrm{MHz}$, *and* $75\,\mathrm{MHz}$. *Note that the range of the color bar changes with the frequency for a better visualization of the respective VEL characteristics.*

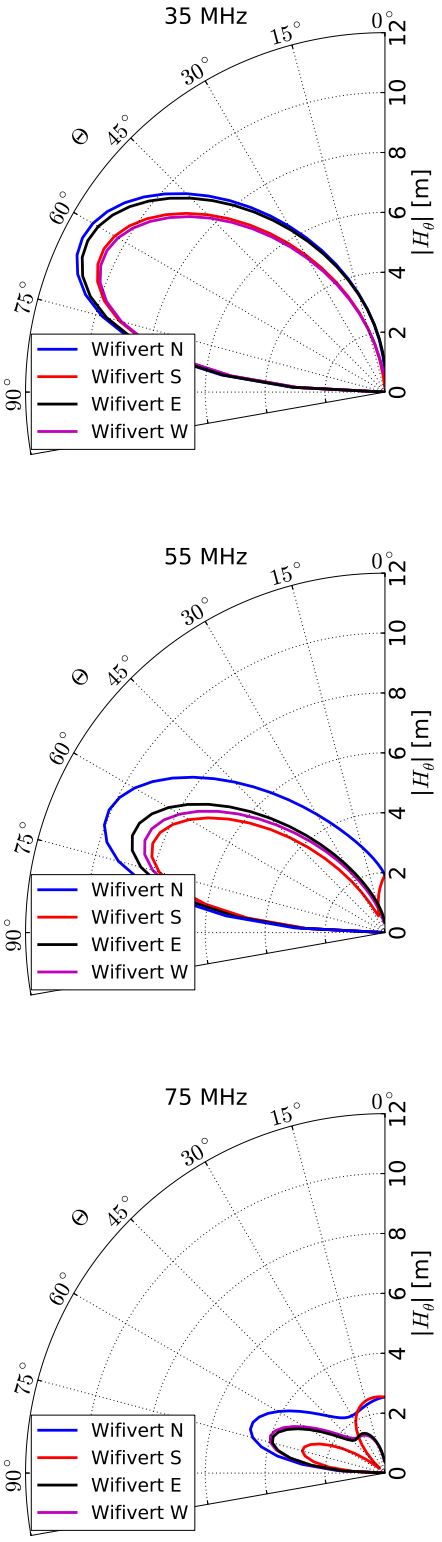

Figure 9.10: *Meridional component of the Wifivert antenna vector effective length* $|H_\theta|$ *obtained from NEC-2 simulations for the four different azimuthal directions: north (N), south (S), east (E) and west (W) as a function of the zenith angle* Θ *at a frequency of* ***(from top to bottom)*** $35\,\mathrm{MHz}$*,* $55\,\mathrm{MHz}$*, and* $75\,\mathrm{MHz}$*.*

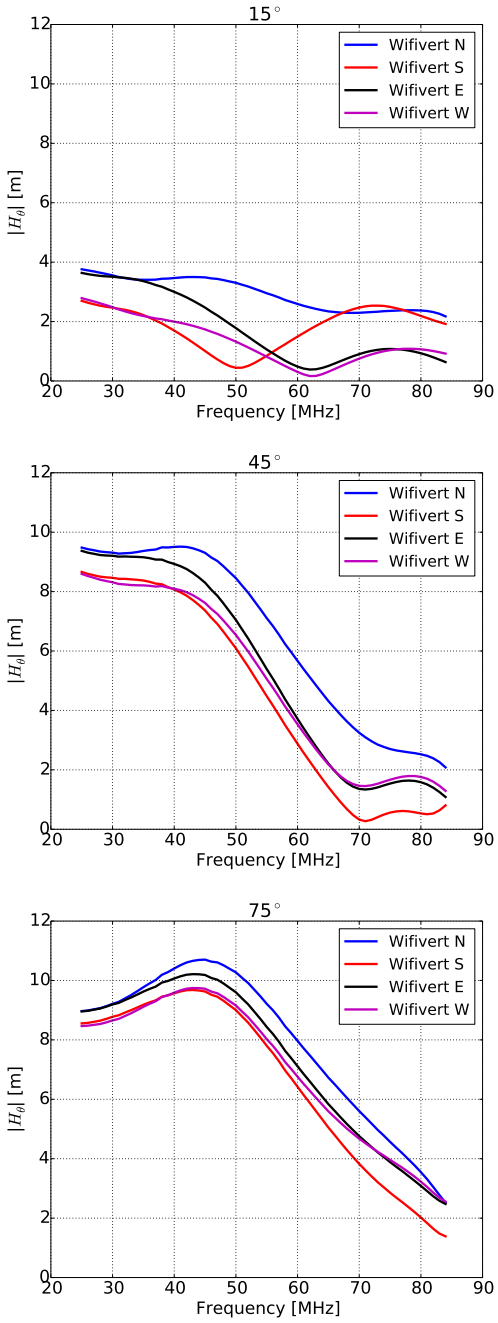

Figure 9.11: *Meridional component of the Wifivert antenna vector effective length $|H_\theta|$ obtained from NEC-2 simulations at four different azimuthal directions: north (N), south (S), east (E) and west (W) as a function of the frequency at a zenith angle of* ***(from top to bottom)*** $15\,^\circ$, $45\,^\circ$, *and* $75\,^\circ$.

both antennas of the radio station are considered and the model follows the real antenna specifications as discussed in Sec. 4.3.3. In Fig. 9.12, the horizontal component $|H_\phi|$ and the meridional component $|H_\theta|$ of the Butterfly antenna VEL as function of the zenith angle are compared to those using the modified Butterfly antenna model including the Wifivert antenna at three different frequencies of 35 MHz, 55 MHz, and 75 MHz. The Wifivert antenna marginally change the horizontal response pattern of the Butterfly antenna $|H_\phi|$. In the meridional component $|H_\theta|$, the influence is larger. All in all, the simulation confirms that the influence of the Wifivert on the Butterfly antenna is expected to be small and the Wifivert antenna is chosen to extend the Butterfly radio stations to 3D radio stations.

9.5 Measurements at AERA

To test the Wifivert antenna under realistic conditions, five Butterfly-equipped radio stations located in the east of the AERA array have been extended with the Wifivert antenna in 2015 (station ID: 85, 145, 146, 152, and 157). A map of AERA is shown in Fig. 9.13 where the 3D radio stations are indicated by the black squares. These stations are deployed with a grid distance of 375 m and are internally triggered by a small scintillator (refer to Sec.4.3.4) inside the station electronics box. The Wifivert antenna is tested in the regular case of data taking. This means that the scintillator is adjusted to observe signals coming from the zenith direction and thus is optimized for the well-understood case of cosmic-ray candidates observed in the horizontally aligned Butterfly antenna. In the following, the antenna functionality is tested by measuring the frequency spectra at AERA. Afterwards, the data set recorded with 3D radio stations is classified and first results are presented.

9.5.1 Measured Frequency Spectra

To test the antenna functionality, the frequency spectra of all three components of each 3D radio station are measured. The respective frequency spectra are shown in Fig. 9.14. The sensitive frequency range of AERA from 30 MHz to 80 MHz is well identifiable for all stations except for the station which is indicated by the green line in Fig. 9.14 (station ID: 85). Here also in both Butterfly antennas, noisy frequency spectra are observed. Therefore, this station is excluded from the further data analysis. The station is located in the south-west of the subsample of the five 3D radio stations at AERA. The other stations have a smooth frequency spectra and exhibit clear signals in all three polarizations, e.g., the four horizontally aligned beacon signals [202] at 59 MHz, 62 MHz, 69 MHz, and 71 MHz are clearly identifiable. In the frequency spectrum of the Wifivert antenna, the signals around 10 MHz to 20 MHz as well as at high frequencies above 55 MHz are visible. Compared to those of the Butterfly antenna, the frequency spectrum of the Wifivert antenna exhibits a smaller magnitude which is expected as the antenna response including LNA amplification and impedance mismatch is smaller. Furthermore, the frequency spectra of the Wifivert antenna exhibit larger fluctuations and more signals are observed. Human-made noise is often vertically polarized and mainly comes from the horizon. Thus, strong fluctuations in the frequency spectra of the Wifivert antennas are expected as the Wifivert antenna is vertically aligned and mainly sensitive towards the horizon. The measured spectra confirm the functionality of the Wifivert antenna in principle.

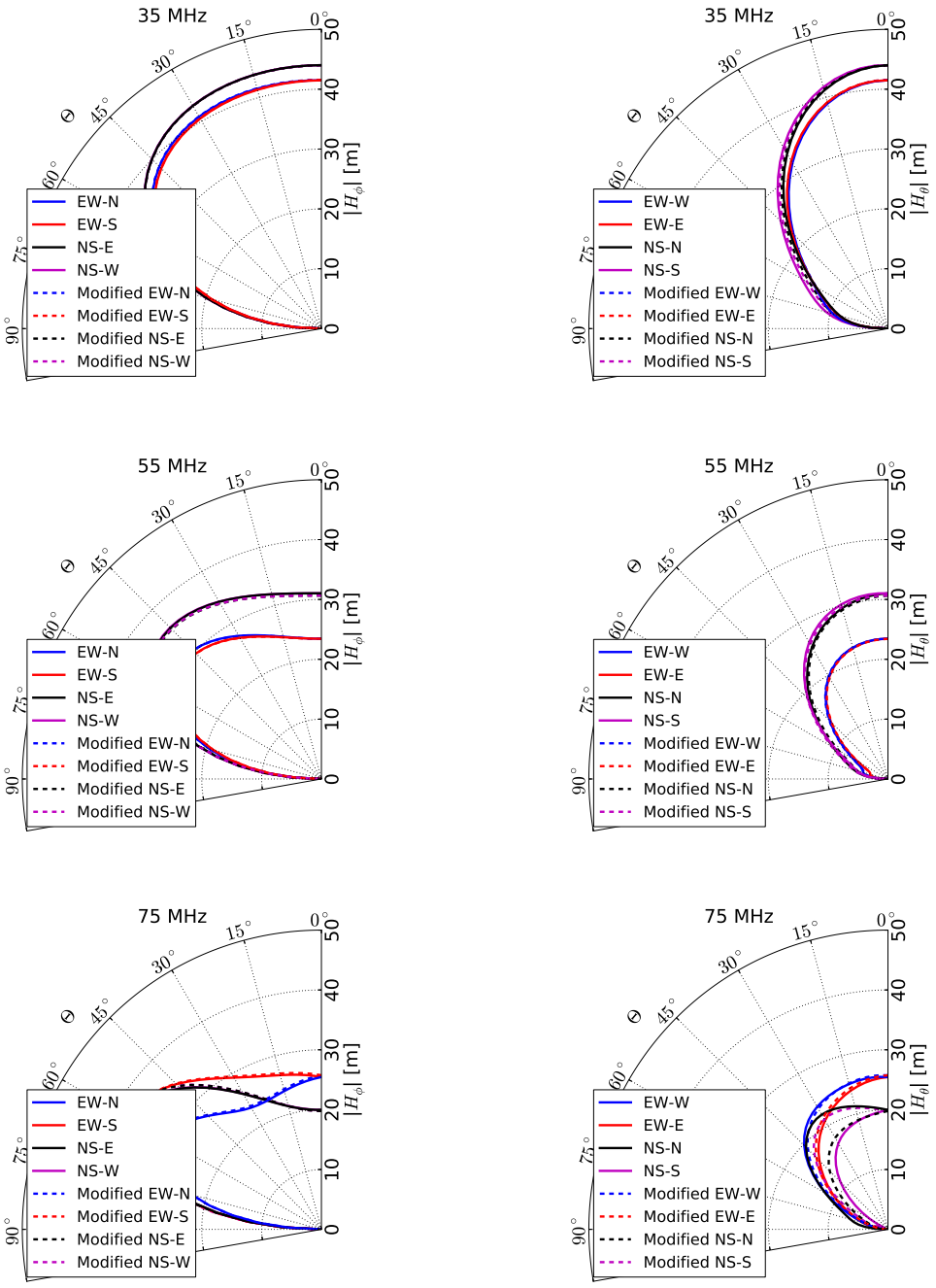

Figure 9.12: *Influence of the Wifivert antenna on the antenna response pattern of the east-west (EW) and north-south (NS) polarized Butterfly antennas for three different frequencies of* ***(from top to bottom)*** 35 MHz, 55 MHz, 75 MHz. ***(left)*** *The horizontal component of the Butterfly antenna* $|H_\phi|$ *and* ***(right)*** *the meridional component* $|H_\theta|$ *as a function of the zenith angle* Θ *in the main sensitive axes which corresponds to the four different azimuthal directions: north (N), south (S), east (E) and west (W). The lines indicate the standard simulation of the Butterfly antenna while the dashed lines mark the modified simulation including the Wifivert antenna.*

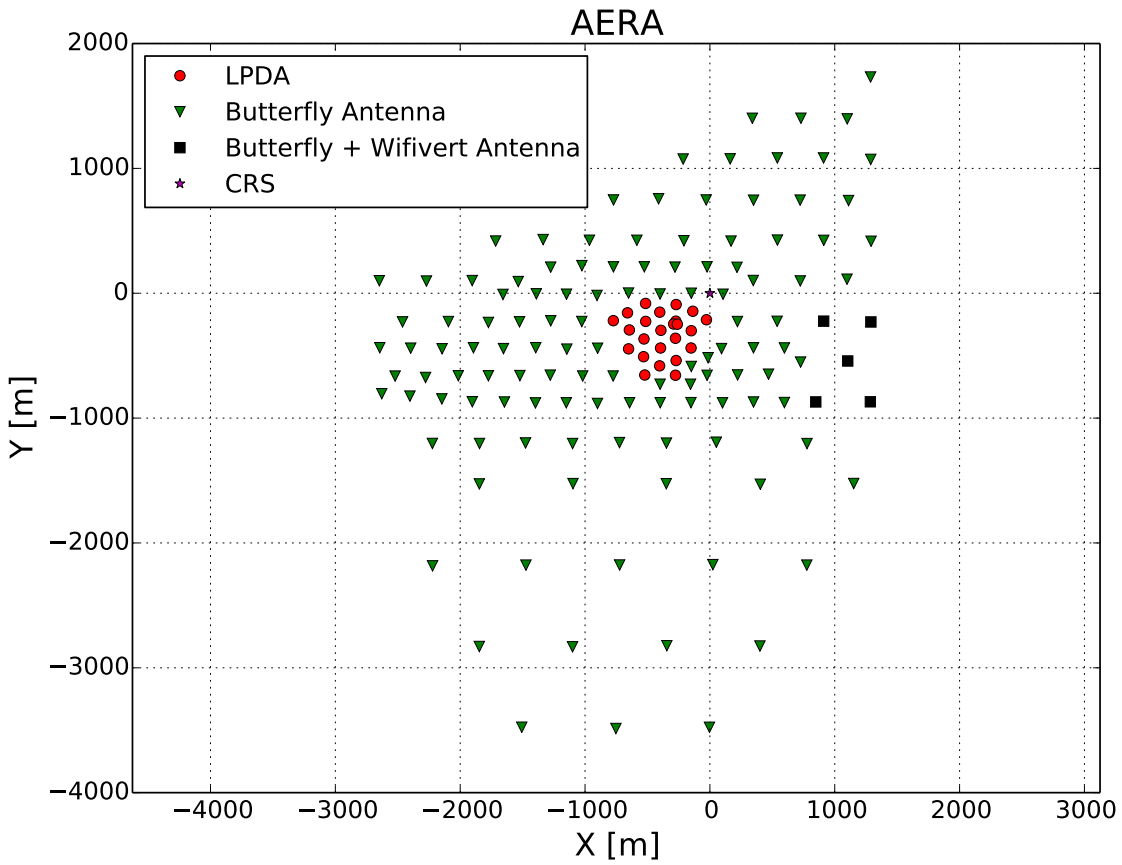

Figure 9.13: *Map of AERA. The central radio station (CRS) is marked as purple star and is set to the origin. The radio stations are set up on a regular grid in spacings of* 144 m, 250 m, 375 m *and* 750 m. *The LPDA-equipped radio stations are indicated by red dots and the Butterfly radio stations are marked by green triangles. The five Butterfly-equipped radio stations extended with the Wifivert antenna are deployed in the eastern part of the array and are indicated by the black squares.*

9.5.2 Data Set and Cuts

In this subsection, the data recorded using the 3D radio stations is described. An event is called 3D-event if at least three radio stations with signal are involved and at least one of them is a 3D radio station. A station is called station with signal if the respective scintillator was triggered. At first, no further signal-to-noise ratio (SNR) cuts are applied to achieve a larger data set. As no SNR cut is applied, also station with no cosmic-ray signal but noise are taken into account if the scintillator triggers which can lead to a wrong reconstruction of the arrival direction and the electric field from radio data. Therefore, instead of the electric field the following analysis is based on the recorded voltage trace.

In the following, 3D-events recorded from March to July 2015 are analyzed. In this time period, more than 2800 3D-events were measured in coincidence with the surface detector of the Pierre Auger Observatory. Hence, the shower information can be taken from the surface detector. The position of the scintillator signal coincidences with the radio signal which is typically later than 2000 ns within

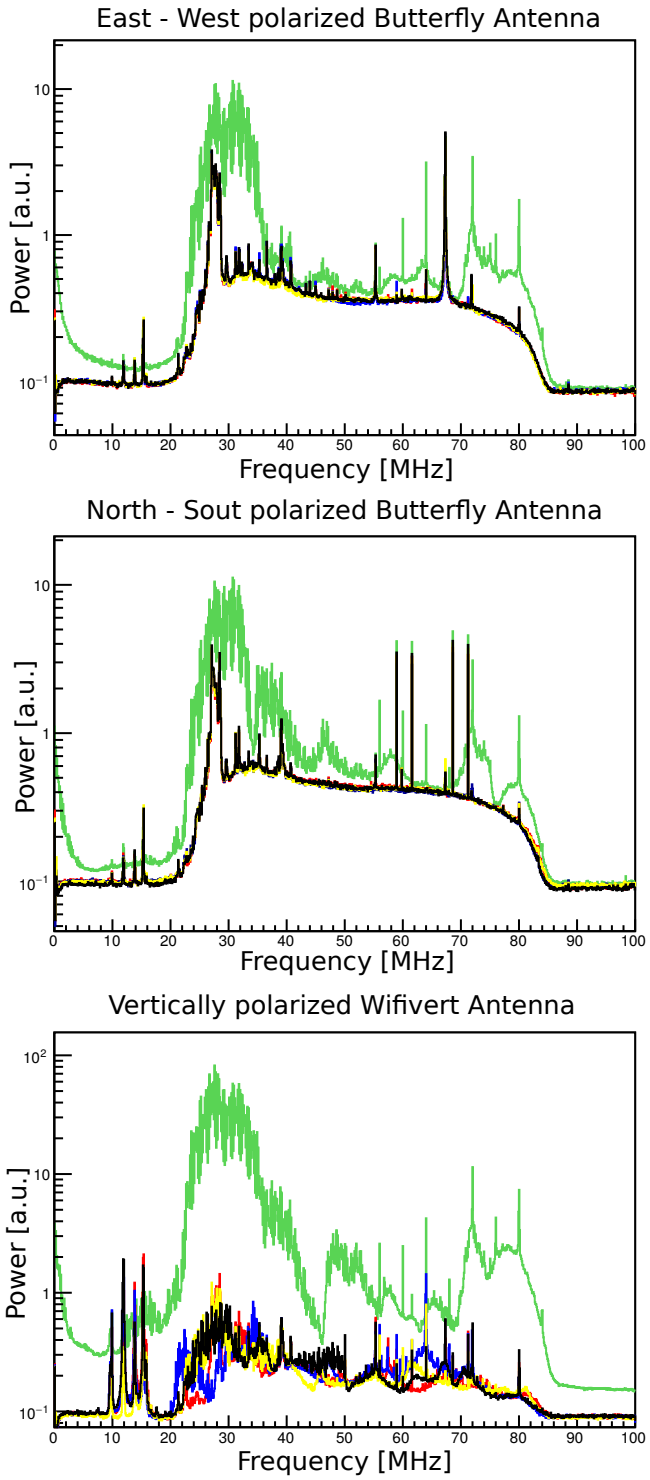

Figure 9.14: *Measured frequency spectra of all 3D radio stations at AERA equipped with an east-west* ***(top)****, and north-south* ***(middle)*** *aligned Butterfly antenna as well with the vertically aligned Wifivert antenna* ***(bottom)****. The different colors mark the respective station ID (85: green, 145: red, 146: blue, 152: yellow, 157: black). The spectra indicated by the green line reveals a broken station so that this station is excluded from further analysis.*

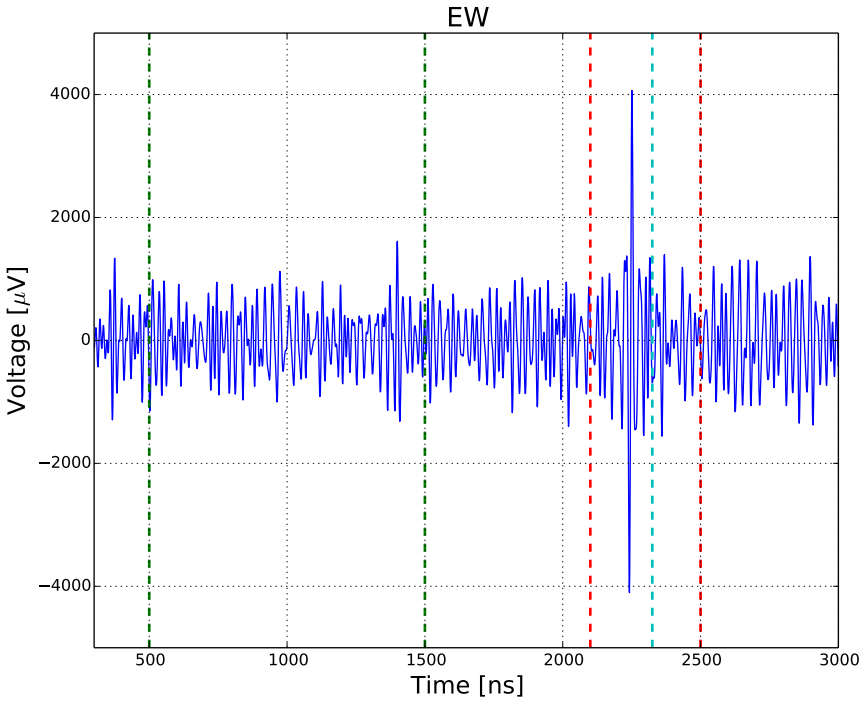

Figure 9.15: *Example of a voltage trace recorded in the east-west polarized Butterfly antenna. The signal time given by the scintillator is illustrated as a turquoise dashed line. The signal time is surrounded by the signal window (red dashed line) in which the signal pulse is expected in the voltage traces of the antenna. The noise expectation is calculated in the noise window (green dashed line).*

the recorded trace. The signal windows of $400\,\mathrm{ns}$ defines the time range in which the signal pulse is expected in the recorded voltage traces of each antenna and is defined by the scintillator signal time. The noise level is determined in the noise window defined from $500\,\mathrm{ns}$ to $1500\,\mathrm{ns}$ of the recorded trace which is well outside of the signal. To illustrate the definitions of signal time, signal window, and noise window, a measured voltage trace is shown exemplary in Fig. 9.15. The radio signal is classified calculating a SNR from the recorded voltage trace. The SNR in each antenna is then determined by the ratio of the maximum of the absolute value of the voltage trace measured in the signal window and the root mean square (RMS) of the noise window:

$$\mathrm{SNR} = \frac{\max(|\mathrm{U_{signal}}|)}{\mathrm{RMS(U_{noise})}}. \tag{9.1}$$

The coincident measurement of the scintillator, of the surface detector of the Pierre Auger Observatory and a large signal strength recorded using the Butterfly antennas are strong evidences for a radio signal originating from an extensive air shower. Events measured using the 3D radio stations are called cosmic-ray candidates if the combined SNR of both horizontally aligned Butterfly antennas of at least one 3D radio station fulfills $SNR_{\mathrm{hor}} = \sqrt{SNR^2_{\mathrm{EW}} + SNR^2_{\mathrm{NS}}} \geqslant 10$. From the 3D-events, 45 events were identified as cosmic-ray candidates. If additionally the SNR of the Wifivert antenna holds $SNR_{\mathrm{vert}} \geqslant 5$, the event is then called a golden 3D-event. In total, 13 3D-events are identified

as golden 3D-events in the given data set.

In Fig. 9.16, the voltage traces of two golden 3D events recorded in all three antennas of a 3D radio station are presented exemplary. The voltage trace reveals strong and narrow pulses within the Butterfly antennas. Due to the wider pulse recorded with the Wifivert antenna, the antenna group delay seems to be larger than those of the Butterfly antenna.

In Fig. 9.17, the cosmic-ray candidates and the golden 3D-events are classified using the shower information given by the surface detector of the Pierre Auger Observatory. The typical cosmic-ray energy is reconstructed to be in between $10^{17}\,\mathrm{eV}$ and $5 \cdot 10^{18}\,\mathrm{eV}$. Most events have an incoming zenith angle of $40\,^{\circ}$ to $60\,^{\circ}$. Larger zenith angles are suppressed due to the horizontally aligned scintillator. The reconstructed arrival directions reveal a north-south asymmetry which is expected from the dominant geomagnetic emission process as the Earth's magnetic field at AERA points close to the north direction [221], resulting in a larger signal strength if the cosmic ray is coming from a southern direction.

9.6 Data Analysis

In this section, the radio signals recorded using the 3D antennas of the 3D-events are analyzed in more detail. The aim is to confirm that the Wifivert antenna measures signals from cosmic-ray induced air showers and the recorded data are not produced by noise only. Here, the parameter of interest is the signal-to-noise ratio measured in the vertical antenna: $\mathrm{SNR}_{\mathrm{vert}}$.

The larger the measured SNR, the larger the probability that the recorded signal is really a cosmic ray and not noise. The measured radio signal of a Wifivert antenna is called cosmic-ray like if the requirement $\mathrm{SNR}_{\mathrm{vert}} \geqslant 5$ is fulfilled. Nevertheless, signals with $\mathrm{SNR}_{\mathrm{vert}} \geqslant 5$ can be produced by noise. To exclude that the 3D-events contain noise signals measured using the Wifivert antenna only, the expectation of the $\mathrm{SNR}_{\mathrm{vert}}$ distribution considering noise only is calculated and then compared with those of the measured radio signals. Therefore, the signal window itself plus half the width of the signal window before and after the signal window is removed from each trace of the 3D-events measured with the Wifivert antenna. The remaining voltage trace is then split in several noise areas which are of the same size as the signal window. The noise window remains constant. The $\mathrm{SNR}_{\mathrm{vert}}$ of each remaining voltage trace of each 3D radio station is then calculated using Eq. (9.1). The $\mathrm{SNR}_{\mathrm{vert}}$ distribution is shown in Fig. 9.18. A fraction of $(7.1 \pm 0.1)\,\%$ of the noise is classified as cosmic-ray-like signals. This value and its uncertainty is obtained by calculating the estimator of an efficiency and its standard deviation using a binomial distribution. Then, the real $\mathrm{SNR}_{\mathrm{vert}}$ distribution of the 3D-events measured in the Wifivert antenna is calculated and is presented in Fig. 9.19. It is differentiated between radio signals coming from regions with mostly horizontally polarized signals (left) and radio signals with a signal fraction of at least $10\,\%$ polarized into the vertical direction (right) as stated in Fig. 9.1. Furthermore, in the lower diagrams, an additional cut of $\mathrm{SNR}_{\mathrm{hor}} \geqslant 5$ in the traces measured with both Butterfly antennas is implemented whereas in the upper diagrams no further cut is taken into account.

In all cases, the fraction of cosmic-ray-like signals is higher than the expectation from pure noise. Moreover, the fraction increases if an additional cut in the $\mathrm{SNR}_{\mathrm{hor}}$ parameter of the horizontal antennas is implemented. These fractions are obtained by calculating the estimator of an efficiency using a

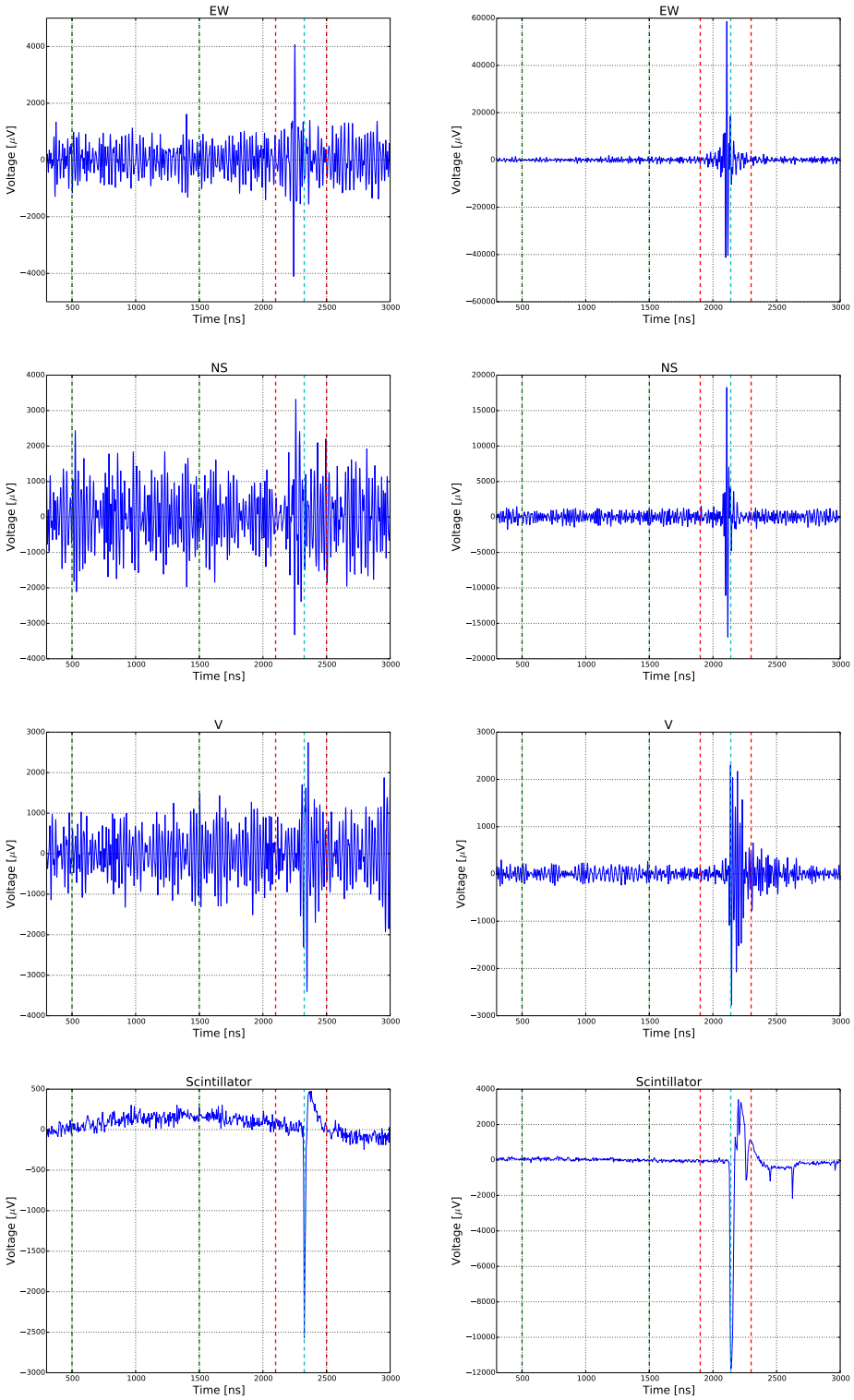

Figure 9.16: *Example events of two cosmic-ray candidates observed in coincidence with the surface detector, arriving at a zenith angle of* 61° *and from* 46° *east of south* ***(left)****, and arriving at a zenith angle of* 61° *and from* 24° *west of south* ***(right)****. The voltage traces recorded with* ***(from top to bottom)*** *the east-west aligned Butterfly antenna, the north-south aligned Butterfly antenna, the vertically aligned Wifivert antenna, and the corresponding scintillator. The minimum of the trace recorded in the scintillator defines the signal time (turquoise dashed line). The signal time is surrounded by the signal window (red dashed line) in which the signal pulse is expected in the voltage traces of the antenna. The noise expectation is calculated in the noise windows (green dashed line).*

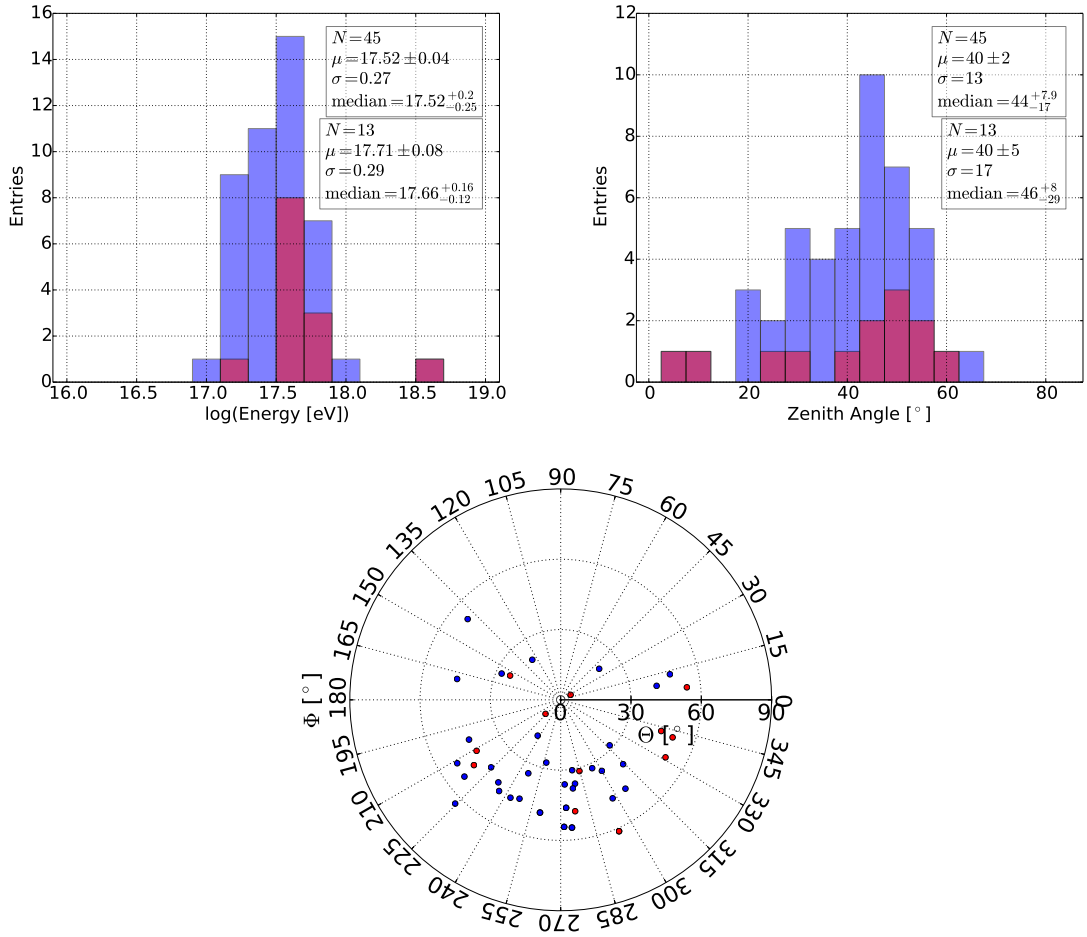

Figure 9.17: *Classification of the cosmic-ray candidates (blue) as well as the golden 3D events (red). The energy distribution is presented in the **(upper left)** diagram and the zenith angle distribution is shown in the **(upper right)** diagram. In the **(lower)** diagram, the arrival direction as function of the zenith angle and of the azimuth angle is presented. The data reveals a strong north-south asymmetry.*

binomial distribution. The given uncertainties of the efficiencies indicate the confidence intervals with confidence level $CL = 68\,\%$ [1]. In the case of a binomial distributed measurement, the confidence interval is based on the Fisher-Snedecor distribution (refer to [253]) and is calculated as given in [254]. For more details about calculating the confidence interval on the efficiency for the case of binomially distributed measurements refer to [255].

In Fig. 9.20, the fraction of cosmic-ray-like signals of the regions with expected horizontally polarized signal as well as of the regions with a vertically polarized signal of at least $10\,\%$ are presented. The expectation from noise is indicated by the black dashed line. The fraction of cosmic-ray-like signals measured in the signal windows is larger than those created from noise only. Hence, the analysis confirms that the Wifivert antenna enables measuring radio signals of cosmic-ray induced extensive

[1] In the case of full efficiency, the standard deviation of the binomial distribution is calculated to be zero. Nevertheless, it does not mean that the true efficiency is equal to unity and thus, it is not useful to describe the uncertainty. Instead, the confidence interval around the estimated efficiency is calculated.

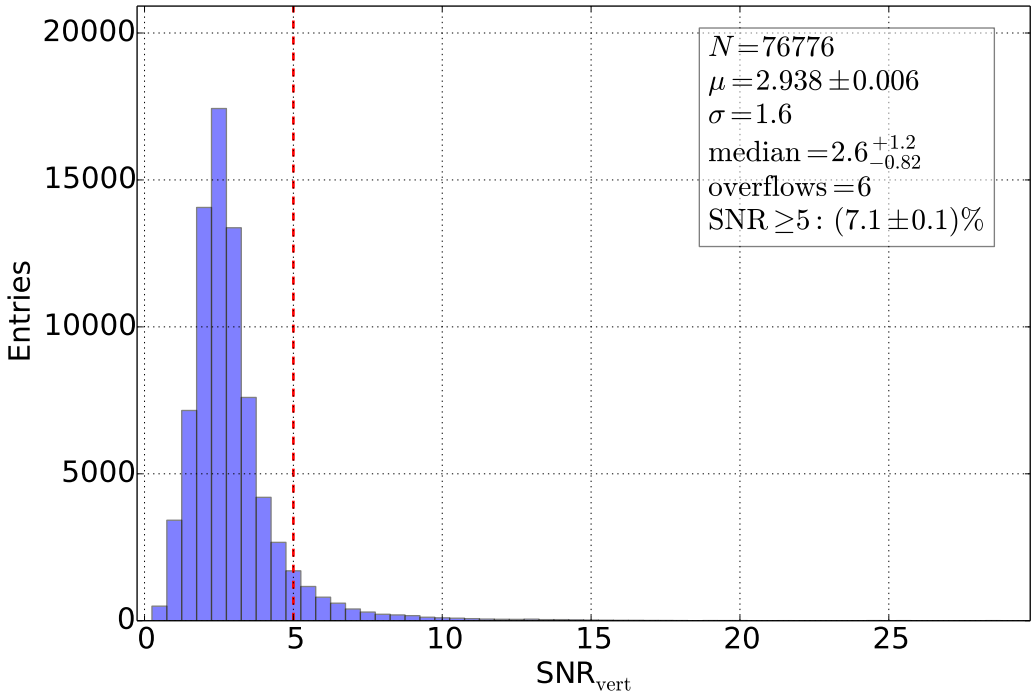

Figure 9.18: *The signal-to-noise (SNR) distribution of the noise expectation calculated from the voltage traces measured of all Wifivert antennas in the data set of the 3D events. In a fraction of* $(7.1 \pm 0.1)\,\%$*, the noise is identified as a cosmic-ray-like signal with a* $\mathrm{SNR}_{\mathrm{vert}} \geqslant 5$*.*

air showers. Furthermore, the fraction of cosmic-ray-like signals increases with the SNR cut applied in the horizontal polarization. The larger the radio signal strength in the horizontal polarization, the larger is the measured signal strength recorded in the Wifivert antenna especially for regions with larger expected vertically polarized signals. For these regions, the fraction of cosmic-ray-like signals is higher than for those with purely horizontally polarized signals which confirms the expected signal polarization from the dominant geomagnetic effect. It confirms that the Wifivert antenna is more sensitive into the respective region and thus potentially extends the field of view of the radio station especially to larger zenith angles.

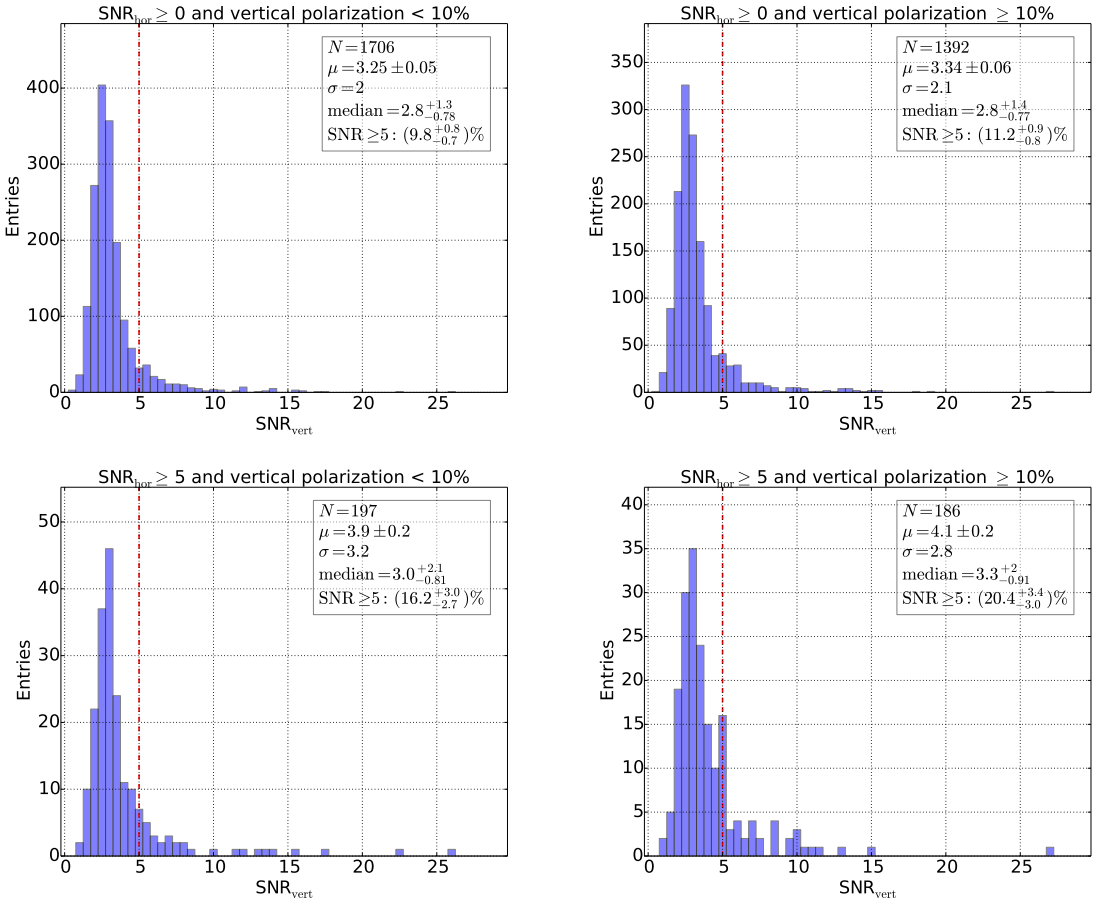

Figure 9.19: *The signal-to-noise (SNR) distribution calculated from the voltage traces measured in all Wifivert antennas in the data set of the 3D events. It is differentiated between radio signals coming from regions with mostly horizontally polarized signals* ***(left)*** *and with a signal fraction of at least* $10\,\%$ *polarized into the vertical direction* ***(right)****. In the* ***(lower)*** *diagrams, an additional cut of* $\mathrm{SNR}_{\mathrm{hor}} \geqslant 5$ *of the signal measured in the horizontally aligned antennas is implemented whereas in the* ***(upper)*** *diagrams no further cut is applied.*

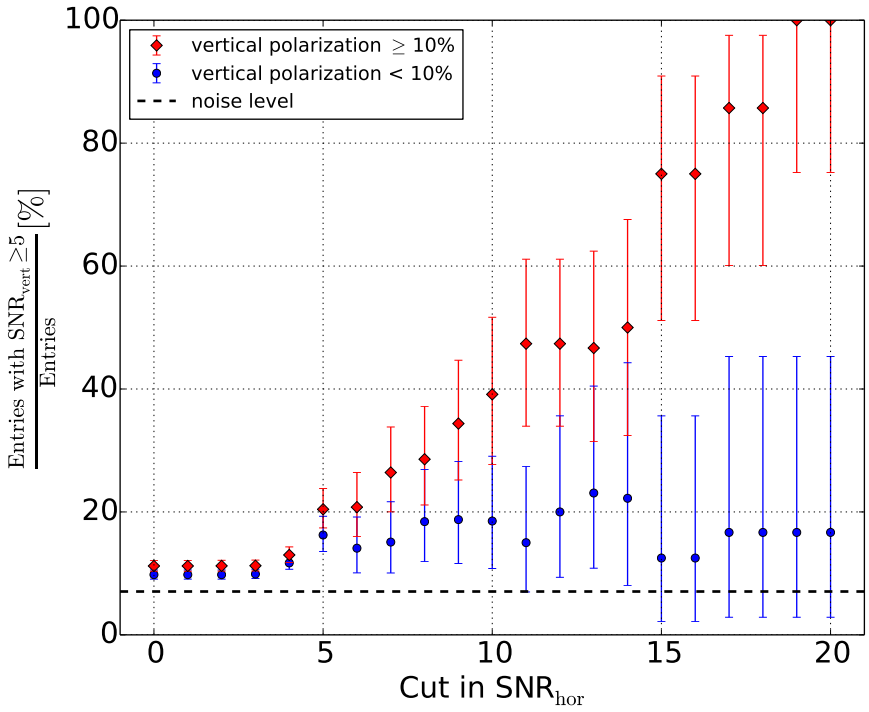

Figure 9.20: *Fraction of cosmic-ray-like signals using the Wifivert antennas as a function of a signal-to-noise (SNR) cut in the voltage traces measured in the horizontally aligned Butterfly antennas:* $\mathrm{SNR}_{\mathrm{hor}}$. *It is differentiated between radio signals coming from regions with mostly horizontally polarized signals (blue dots) and with a signal fraction of at least* $10\,\%$ *polarized into the vertical direction (red diamonds). The error bars indicate the respective* $68\,\%$ *confidence interval. The expectation from noise is indicated by the black dashed line. The radio signals recorded using the Wifivert antenna exhibit a larger fraction of cosmic-ray-like signals as expected from pure noise.*

10

Conclusion

Cosmic rays are messengers from far-away objects, e.g., active galactic nuclei, super novae, or star forming galaxies. With energies of more than $10^{20}\,\mathrm{eV}$, they are the most energetic particles in the universe, propagate through it, and some of them reach Earth which enables investigating fundamental questions of astro- and astroparticle physics.

In the atmosphere, high-energy cosmic rays interact with air molecules and create air showers of secondary particles. The cosmic-ray properties, e.g., its energy, can be determined by observing such air showers by stochastic measurements of secondary particles at the ground as well as directly by measuring fluorescence light emitted from air showers. Both detection techniques are established at the Pierre Auger Observatory. The measurement of radio emission is a complementary detection technique to investigate cosmic rays. The Auger Engineering Radio Array (AERA) is the radio detector of the Pierre Auger Observatory. Here, cosmic rays are observed with a duty cycle close to $100\,\%$. The atmosphere is transparent to radio waves which enables measuring the cosmic-ray energy potentially with reduced uncertainties compared to those made with the fluorescence detection technique.

The radio antennas used in the measurements and an accurate description of their frequency and directional-dependent sensitivities are of central importance for observing radio emission of air showers and for reconstructing cosmic-ray properties accurately. This so-called antenna response pattern is described by the formalism of the vector effective length (VEL) and is decomposed in a horizontal component H_ϕ and meridional component H_θ. The antenna VEL is obtained through an absolute antenna calibration. The uncertainty of the antenna calibration has been identified as the dominant uncertainty in reconstructing the cosmic-ray energy and thus, a reduction of the uncertainties is most desirable. In this thesis, an absolute antenna calibration of the radio stations equipped with logarithmic-periodic dipole antennas (LPDAs) has been performed.

Challenges of measuring cosmic-ray induced air showers at AERA are the variations in local weather conditions. During the day, temperature fluctuations of more than $20\,^\circ\mathrm{C}$ are not uncommon. These fluctuations have a direct influence on the signal processing of the radio station electronics, e.g., the low-noise amplifier (LNA) connected to the antenna. The LNA and the antenna form a technical unit and thus, it is included in the antenna response pattern. An accurate description of the LNA and its dependency on the temperature is therefore of great interest concerning the antenna calibration as well as data reconstruction. To measure the temperature dependency of the LNAs implemented in LPDA-equipped radio stations, an LNA was positioned in a temperature-adjustable and PC-controlled fridge. The LNA power gain has been measured as function of the frequency for several different temperatures. A temperature dependency of the LNA power gain of $-0.017\,\mathrm{dB/K}$ in the median with nearly no dependency on the frequency has been found. These results have been reproduced in a further measurement of a second LNA.

The ground conditions in the field described by the ground permittivity and ground conductivity and their variations, e.g., due to rainfall are further important environmental conditions influencing the

antenna response pattern. Both, ground permittivity and ground conductivity, have a direct influence on the signal reflection on ground and thus impact the antenna response pattern. It was found that the signal reflection on ground with typical ground conditions at AERA is mostly dependent on the ground permittivity. A measurement setup has been developed to measure the frequency-dependent permittivity of soil from the AERA site using a capacitor. Two measurements campaigns have been performed to obtain typical values of the ground permittivity at AERA. In the first campaign, soil samples from the AERA site have been collected and the ground permittivity has been measured in the laboratory with respect to the soil humidity. It was found that the ground permittivity is typically larger than 2 and increases with the soil humidity. In the second campaign, the ground permittivity has been measured directly at different positions within AERA to investigate the ground homogeneity at the site. For the majority of the positions, the measurements exhibit values from 6 to 7. Only in the very west and in the very east of AERA the permittivity differs which can be attributed to the fact that in the west of AERA the soil consistency is sandy whereas in the east the soil consistency is more earth like. From the measurement campaigns, typical values of the permittivity between 2 and 10 have been found depending on the soil humidity.

Using the NEC-2 simulation code, an overall LPDA response pattern in terms of the respective VEL component with standard environmental conditions for all arrival directions and frequencies ranging from $30\,\mathrm{MHz}$ to $80\,\mathrm{MHz}$ has been simulated. From multiple simulations the influence of changing environmental conditions such as changing ground conditions, conductive elements close to the antenna and an antenna misalignment on the LPDA response pattern have been investigated. In the case of an applied ground permittivity of 2 and of 10, which is based on the permittivity-measurements campaigns, the influence on the horizontal (meridional) LPDA VEL component $|H_\phi|$ ($|H_\theta|$) is at the level of $1.3\,\%$ ($0.5\,\%$) in the median and impacts the whole phase space defined by the frequency and zenith angle. Simulations of an electronics box beneath the LPDA exhibit an influence at the level of $0.3\,\%$ ($1\,\%$) on the horizontal (meridional) VEL component of the LPDA. In the case of the meridional component, especially the regions with large zenith angles are affected where the LPDA is less sensitive. The simulations yield that a misalignment of the LPDA of $1\,^\circ$ as well as different ground conductivities do not change the LPDA response pattern neither in the horizontal component $|H_\phi|$ nor in the meridional component $|H_\theta|$.

In a calibration campaign, the LPDA response pattern has been measured at the AERA site using a remotely piloted octocopter. The octocopter was used to place a calibrated source at different positions around an LPDA. The calibrated LPDA is representative for all LPDAs as they are mechanically and electrically identical on the percent level. All devices used in the measurements have been quantified concerning their uncertainties. Special focus was put on the accuracy of the position reconstruction of the calibrated source. The accuracy has been increased by combining the position information measured by the octocopter build-in sensors such as GPS, barometer, and inclination sensors with a newly developed optical method consisting of two cameras. To ensure reproducibility, the measurements have been repeated at different days with different environmental conditions. The measurements have been finally combined according to their uncertainties resulting in an overall uncertainty for the horizontal component of the LPDA VEL of $7.4^{+0.9}_{-0.3}\,\%$, and for the meridional component of $10.3^{+2.8}_{-1.7}\,\%$. These uncertainties are to compared with the uncertainty of a previously performed balloon-based calibration in which a smaller phase space was measured and an uncertainty of $12.5\,\%$ for the horizontal

component was achieved. The accurate measurements have been compared with NEC-2 simulations considering the antenna, the LNA as well as the transmission antenna. Correction factors, which are defined as the ratio between measured and simulated patterns for each frequency and arrival direction, have been calculated and the median of all correction factors has been found to be close to unity varying about 0.12 (0.26) for the horizontal (meridional) component. The influence of the modified LPDA response pattern on the data reconstruction has been demonstrated on one example event with a zenith angle of 30° and an azimuth angle of 14° south of east. The trace of the modified LPDA pattern exhibits an up to $7\,\%$ larger amplitude. The total energy fluence of all polarizations increase at the level of $9\,\%$. The reconstructed radiation energy of the full event changes from $7.96\,\mathrm{MeV}$ to $8.54\,\mathrm{MeV}$. Finally, the antenna calibration uncertainties of the horizontal and meridional antenna VEL as well as the uncertainties due to different ground permittivites are propagated to the square root of the energy fluence. The square root of the energy fluence is taken because the energy fluence scales quadratically with the electric-field amplitude and the cosmic-ray energy. Hence, the uncertainty of the square root is the relevant uncertainty in most analyses of radio data. It is found that for arrival directions with zenith angles smaller than $60\,^\circ$, the uncertainty in the square root of the energy fluence due to the calibration uncertainties and due to changing ground conditions is $8.8^{+2.1}_{-1.3}\,\%$ in the median.

Typically, radio stations in air shower experiments consist of two perpendicular polarized antennas which are usually aligned horizontally. The third component, the vertical polarization of the radio signal, is not measured directly but is important for the data analysis of radio signals from cosmic ray induced air showers. So, 3D radio stations are motivated as the simultaneous measurement of all three components potentially reduces the uncertainties of the electric-field reconstruction. Furthermore, such radio stations have an increased field-of-view towards the horizon. For AERA, a new 3D radio station has been developed. The mechanical and electrical properties of the antenna are presented. In 2015, a subset of five Butterfly radio stations was extended with a vertical antenna called Wifivert antenna forming 3D radio stations. Within three month of data taking, more than 2800 events have been observed using the 3D radio stations in coincidence with the surface detector of the Pierre Auger Observatory. From these events, 45 events are identified as cosmic-ray candidates with a signal-to-noise ratio (SNR) of 10 or more measured in the horizontally aligned antennas of at least one of the 3D stations. If additionally an $\mathrm{SNR} \geqslant 5$ in the vertical antenna is measured, the event is classified as a golden 3D-event. In total, 13 events are identified as golden 3D-events in the given data set. Using the Wifivert antenna, radio emission of air showers in the vertical polarization has been measured. It is shown that the antenna is especially sensitive on air showers at large zenith angles which is a focus topic of current research.

Future work will profit from the results presented in this thesis. The accurate measurements of the calibration campaign will improve the reconstruction of cosmic-ray properties using data measured with AERA, e.g., the primary cosmic-ray energy. With the reduced uncertainties of the calibration, the energy scale for air shower measurements from radio detectors is directly impacted. Using 3D radio stations, the vertical polarization of the radio signal is additionally measured compared to conventional 2D radio stations which reduces the uncertainties of the electric-field reconstruction. Furthermore, the field-of-view of these radio stations is extended towards the horizon and thus, 3D radio stations improve the research of horizontal air showers.

A

Measurement of the LPDA LNA Temperature Dependency

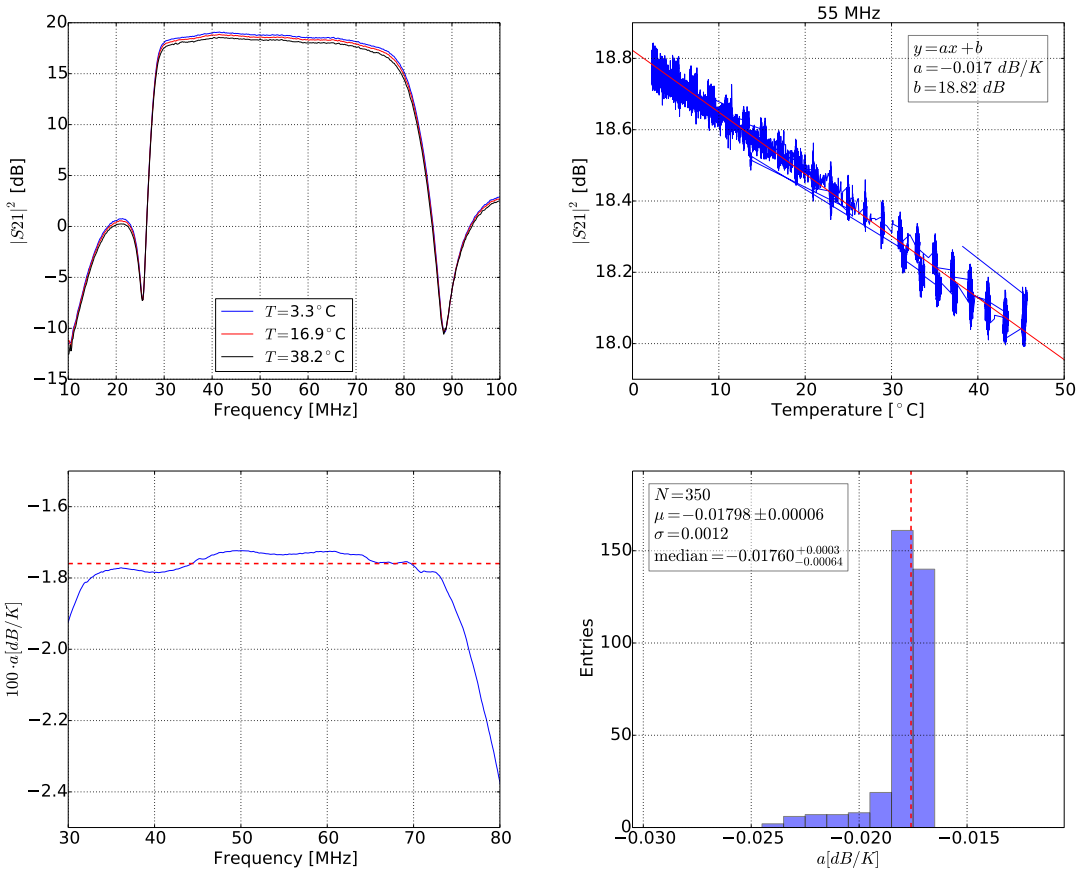

Figure A.1: *Temperature drifts of the LPDA LNA power gain.* ***(top left)*** *LNA power gain $|S21|^2$ as a function of the frequency for three different temperatures of $T = 3.3\,^{\circ}\mathrm{C}$, $T = 16.9\,^{\circ}\mathrm{C}$, and $T = 38.2\,^{\circ}\mathrm{C}$.* ***(top right)*** *LNA power gain $|S21|^2$ as a function of the temperature at $55\,\mathrm{MHz}$ (blue line). The red line indicates a linear fit to the measured data.* ***(bottom left)*** *Slope a of the temperature dependency of the LNA power gain as a function of the frequency.* ***(bottom right)*** *Histogram of a in the frequency range from $30\,\mathrm{MHz}$ to $80\,\mathrm{MHz}$. The red dashed line marks the median value in both lower plots.*

B

Relative Permittivity Measurements of Soil from the AERA Site

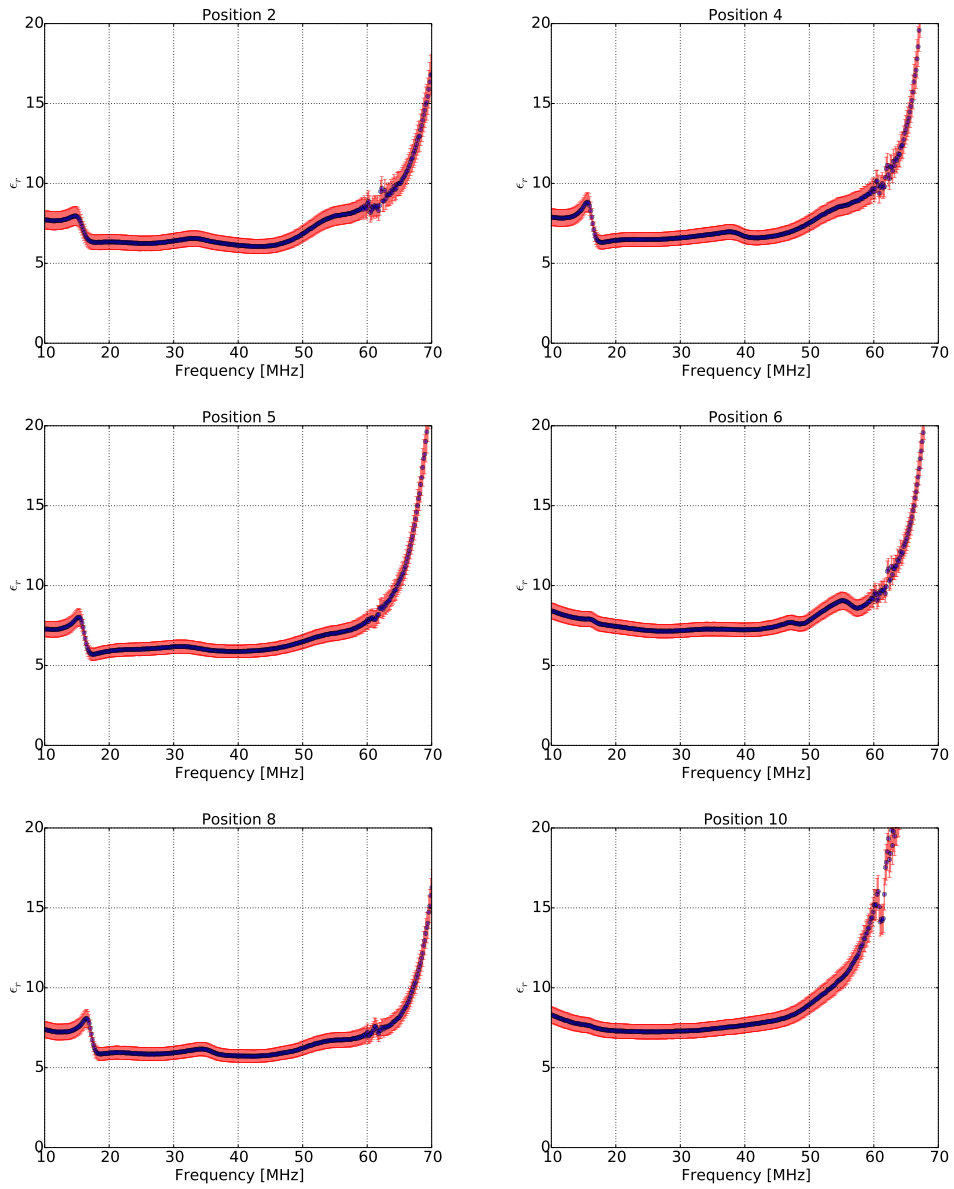

Figure B.1: *The relative permittivity (blue dots) as a function of the frequency measured at different positions at the AERA site. The red error bars indicate the uncertainty arising from the distance measurements between the capacitor plates and the black area marks the combined uncertainty arising from the vector network analyzer and arising from the measurements of the parasitic inductance of the setup.*

C

Simulation of the LPDA Response Pattern

C.1 Influence of Ground Conditions

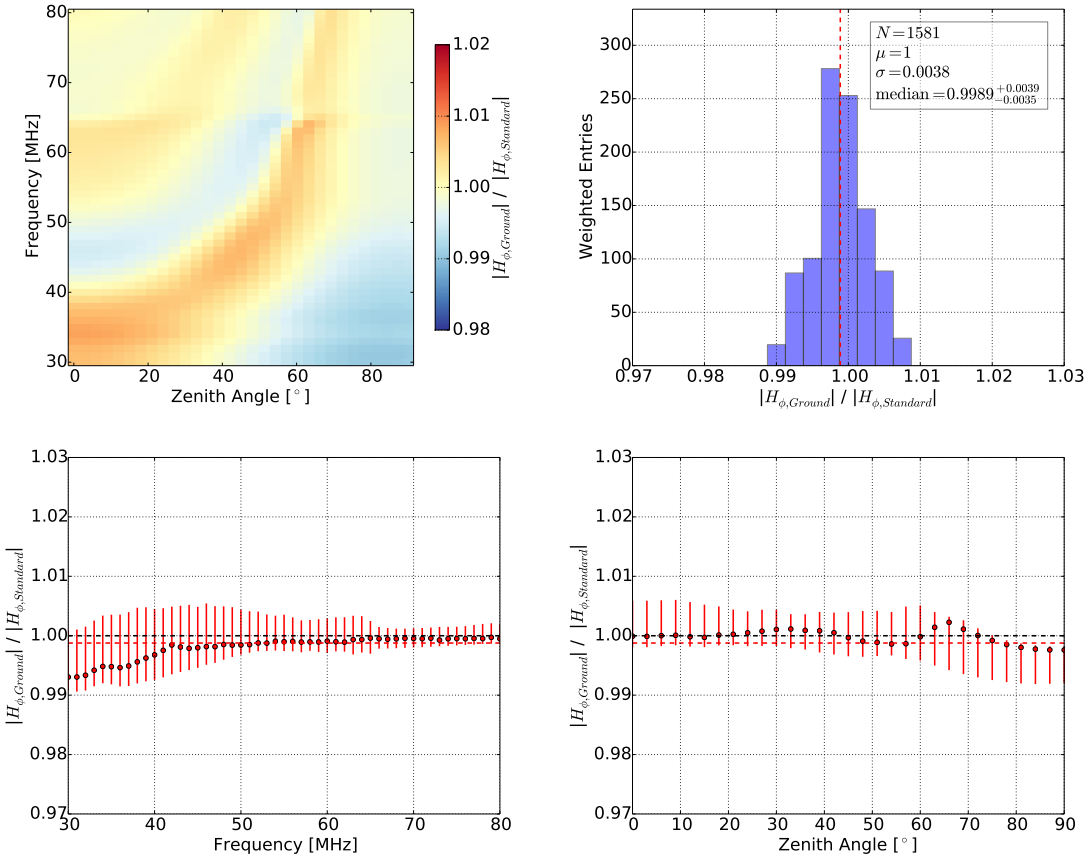

Figure C.1: *Horizontal component of the LPDA vector effective length $|H_\phi|$ obtained from the modified simulation with a ground conductivity of $0.5\ \frac{\mathrm{mS}}{\mathrm{m}}$ compared to those obtained from the standard simulation.* ***(top left)*** *Ratio of the modified simulation and standard simulation for all frequencies as a function of the zenith angle Θ.* ***(top right)*** *Histogram of all ratios of the modified simulation and standard simulation for all frequencies and all zenith angles weighted with $\sin(\Theta)$. The median value is marked as the red dashed line.* ***(bottom left)*** *Median (red dots) and the $68\,\%$ quantile (red error bars) of the zenith angle weighted ratio distribution as a function of the frequency.* ***(bottom right)*** *Median (red dots) and the $68\,\%$ quantile (red error bars) of the ratio distribution as a function of Θ. The red dashed lines mark the overall zenith angle weighted median in both lower diagrams.*

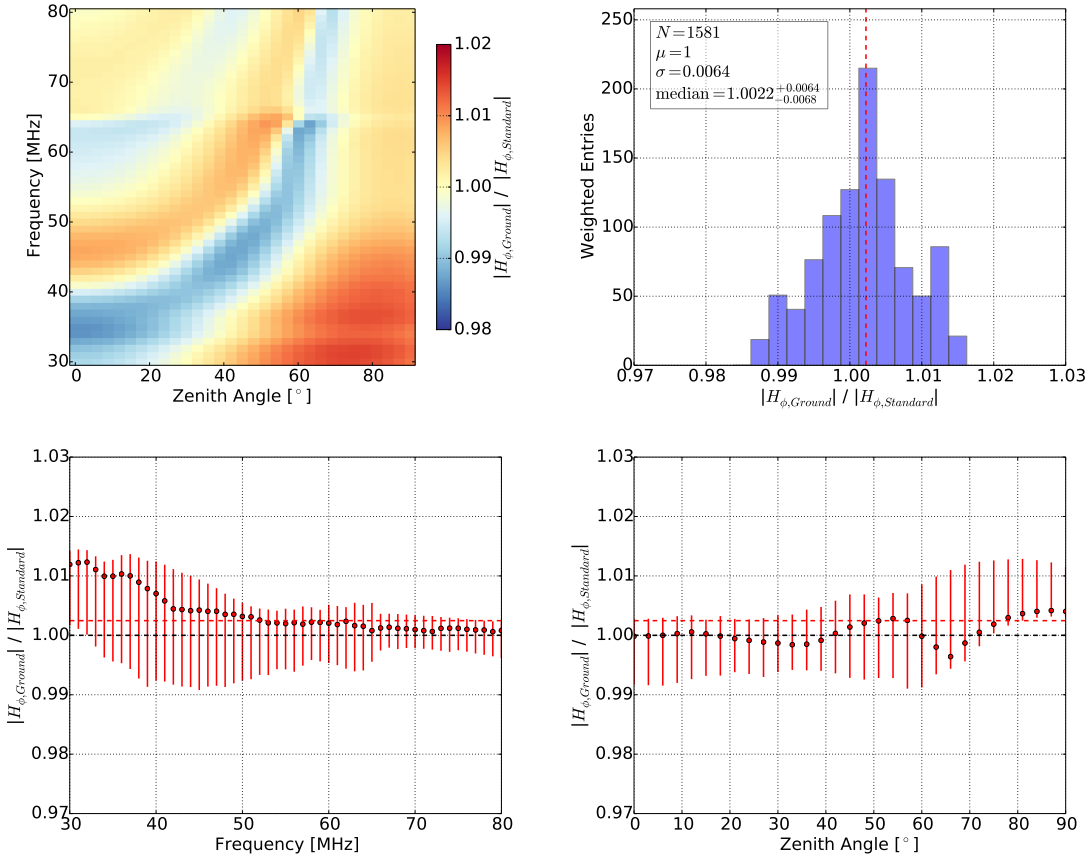

Figure C.2: *Horizontal component of the LPDA vector effective length $|H_\phi|$ obtained from the modified simulation with a ground conductivity of $3\,\frac{\mathrm{mS}}{\mathrm{m}}$ compared to those obtained from the standard simulation.* ***(top left)*** *Ratio of the modified simulation and standard simulation for all frequencies as a function of the zenith angle Θ.* ***(top right)*** *Histogram of all ratios of the modified simulation and standard simulation for all frequencies and all zenith angles weighted with $\sin(\Theta)$. The median value is marked as the red dashed line.* ***(bottom left)*** *Median (red dots) and the $68\,\%$ quantile (red error bars) of the zenith angle weighted ratio distribution as a function of the frequency.* ***(bottom right)*** *Median (red dots) and the $68\,\%$ quantile (red error bars) of the ratio distribution as a function of Θ. The red dashed lines mark the overall zenith angle weighted median in both lower diagrams.*

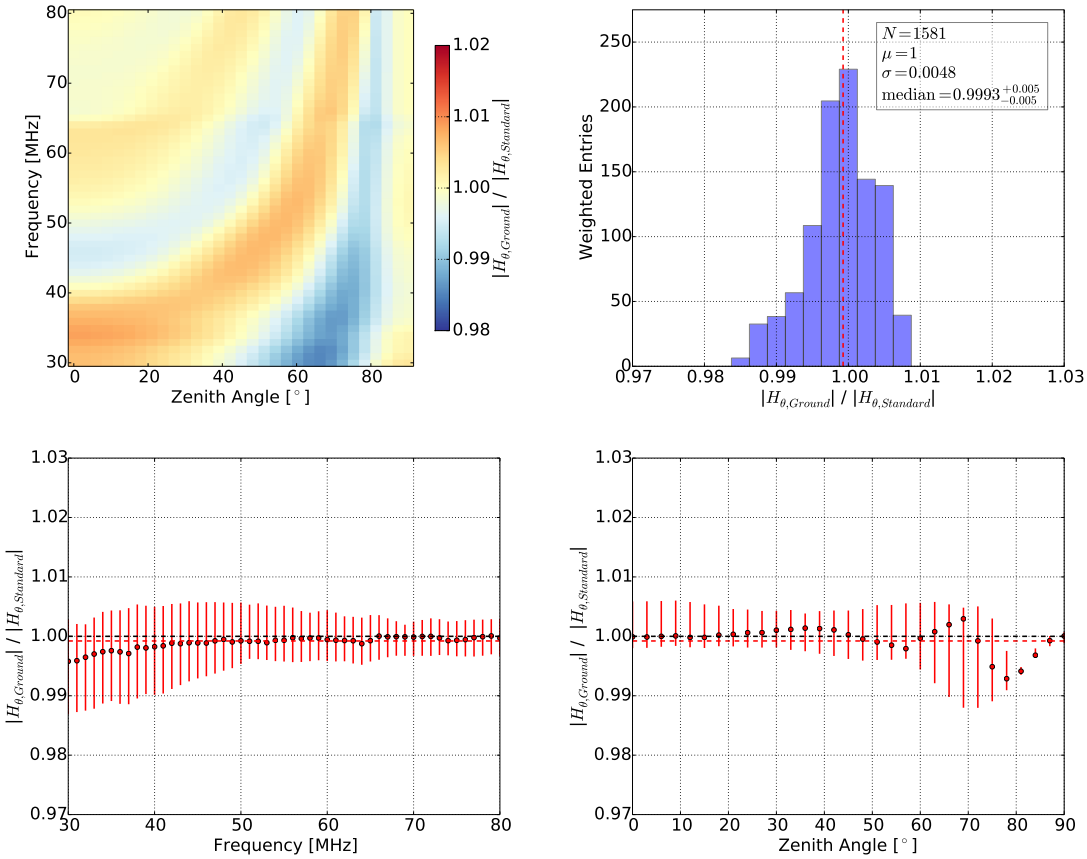

Figure C.3: *Meridional component of the LPDA vector effective length $|H_\theta|$ obtained from the modified simulation with a ground conductivity of $0.5\,\frac{\mathrm{mS}}{\mathrm{m}}$ compared to those obtained from the standard simulation.* ***(top left)*** *Ratio of the modified simulation and standard simulation for all frequencies as a function of the zenith angle Θ.* ***(top right)*** *Histogram of all ratios of the modified simulation and standard simulation for all frequencies and all zenith angles weighted with $\sin(\Theta)$. The median value is marked as the red dashed line.* ***(bottom left)*** *Median (red dots) and the $68\,\%$ quantile (red error bars) of the zenith angle weighted ratio distribution as a function of the frequency.* ***(bottom right)*** *Median (red dots) and the $68\,\%$ quantile (red error bars) of the ratio distribution as a function of Θ. The red dashed lines mark the overall zenith angle weighted median in both lower diagrams.*

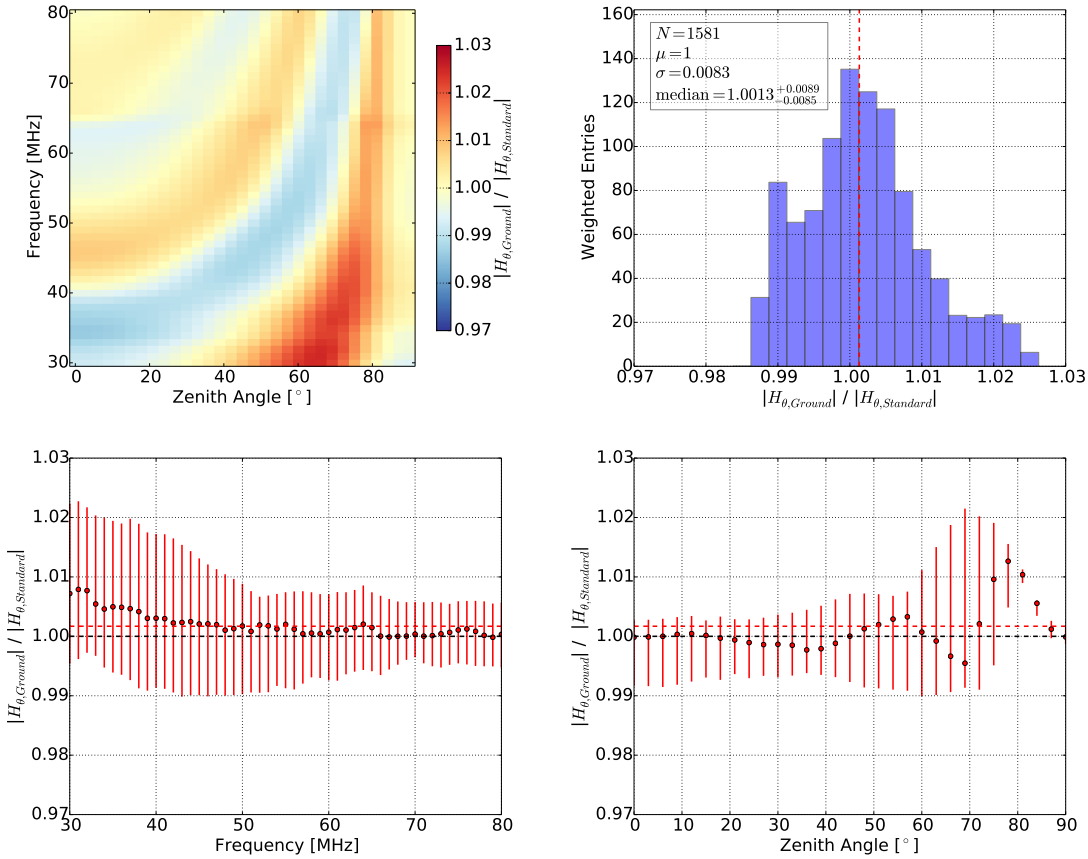

Figure C.4: *Meridional component of the LPDA vector effective length $|H_\theta|$ obtained from the modified simulation with a ground conductivity of $3\,\frac{\mathrm{mS}}{\mathrm{m}}$ compared to those obtained from the standard simulation.* ***(top left)*** *Ratio of the modified simulation and standard simulation for all frequencies as a function of the zenith angle Θ.* ***(top right)*** *Histogram of all ratios of the modified simulation and standard simulation for all frequencies and all zenith angles weighted with $\sin(\Theta)$. The median value is marked as the red dashed line.* ***(bottom left)*** *Median (red dots) and the $68\,\%$ quantile (red error bars) of the zenith angle weighted ratio distribution as a function of the frequency.* ***(bottom right)*** *Median (red dots) and the $68\,\%$ quantile (red error bars) of the ratio distribution as a function of Θ. The red dashed lines mark the overall zenith angle weighted median in both lower diagrams.*

C.2 Influence of the Electronics Box

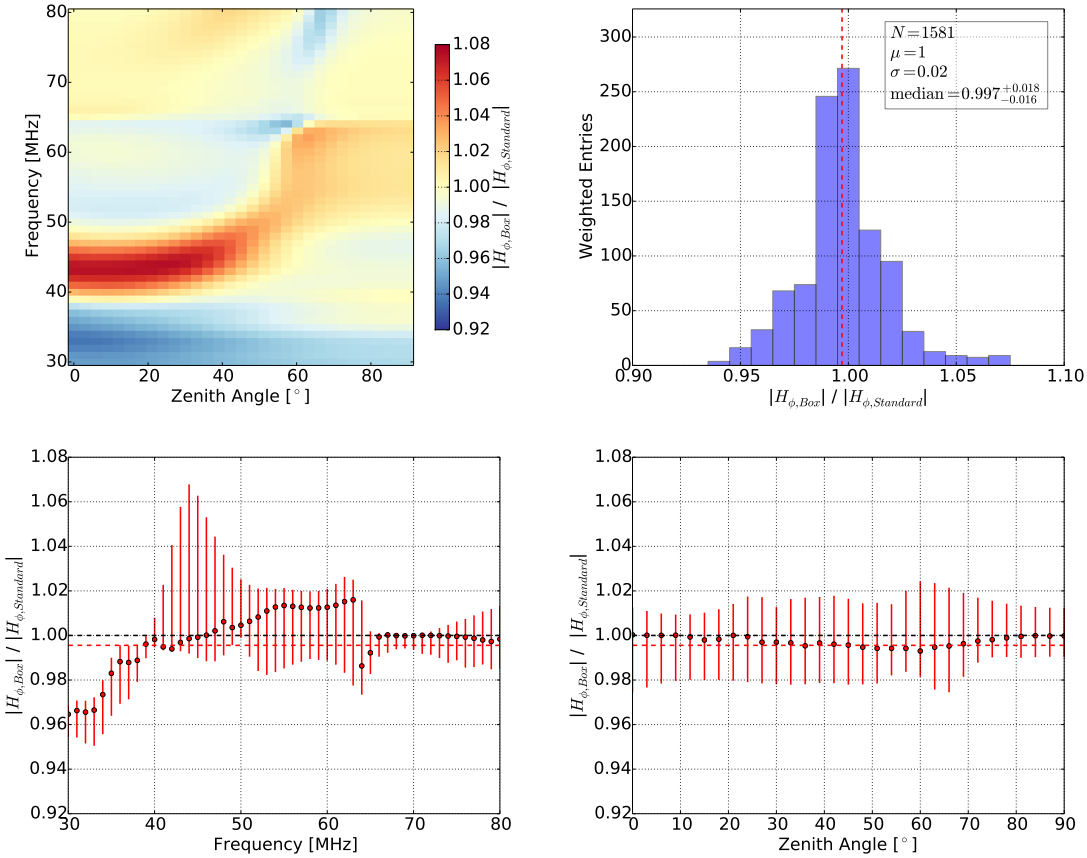

Figure C.5: *Horizontal component of the LPDA vector effective length $|H_\phi|$ obtained from the modified simulation with an electronics box of an east-west polarized LPDA in the south direction compared to those obtained from the standard simulation.* ***(top left)*** *Ratio of the modified simulation and standard simulation for all frequencies as a function of the zenith angle Θ.* ***(top right)*** *Histogram of all ratios of the modified simulation and standard simulation for all frequencies and all zenith angles weighted with $\sin(\Theta)$. The median value is marked as the red dashed line.* ***(bottom left)*** *Median (red dots) and the $68\,\%$ quantile (red error bars) of the zenith angle weighted ratio distribution as a function of the frequency.* ***(bottom right)*** *Median (red dots) and the $68\,\%$ quantile (red error bars) of the ratio distribution as a function of Θ. The red dashed lines mark the overall zenith angle weighted median in both lower diagrams.*

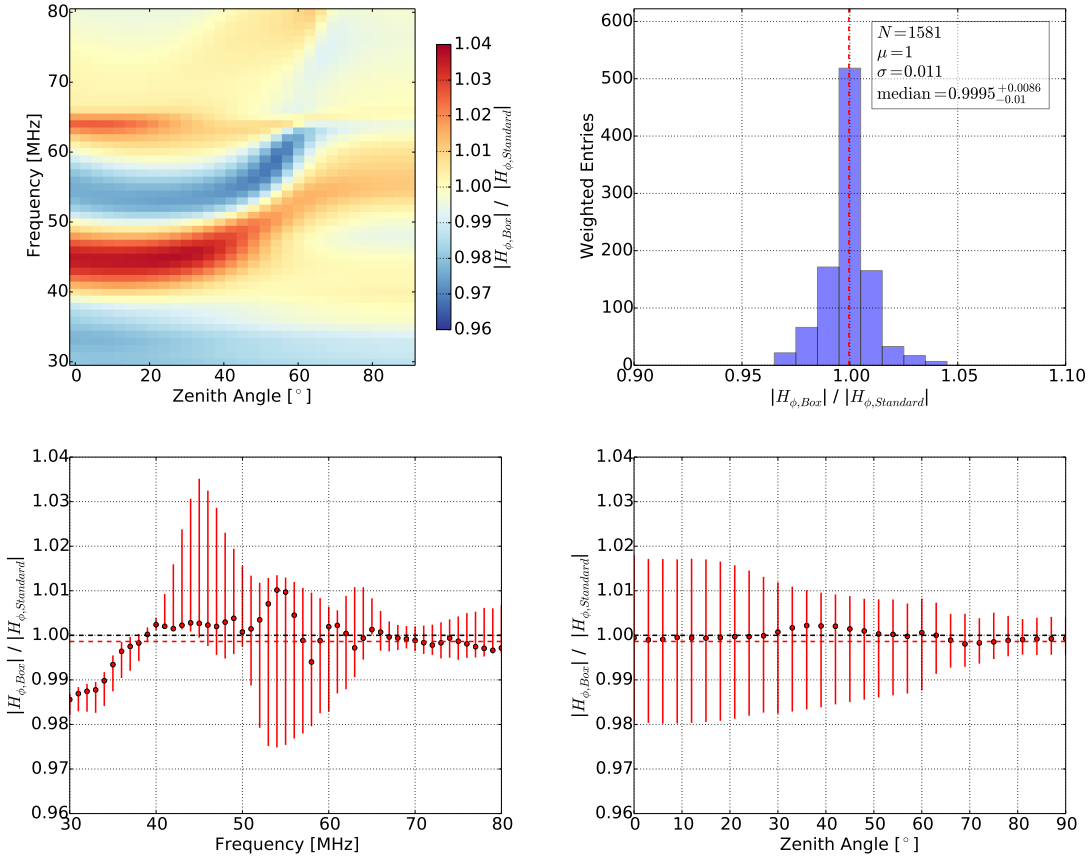

Figure C.6: *Horizontal component of the LPDA vector effective length $|H_\phi|$ obtained from the modified simulation with an electronics box of a north-south polarized LPDA in the east direction compared to those obtained from the standard simulation.* ***(top left)*** *Ratio of the modified simulation and standard simulation for all frequencies as a function of the zenith angle Θ.* ***(top right)*** *Histogram of all ratios of the modified simulation and standard simulation for all frequencies and all zenith angles weighted with $\sin(\Theta)$. The median value is marked as the red dashed line.* ***(bottom left)*** *Median (red dots) and the $68\,\%$ quantile (red error bars) of the zenith angle weighted ratio distribution as a function of the frequency.* ***(bottom right)*** *Median (red dots) and the $68\,\%$ quantile (red error bars) of the ratio distribution as a function of Θ. The red dashed lines mark the overall zenith angle weighted median in both lower diagrams.*

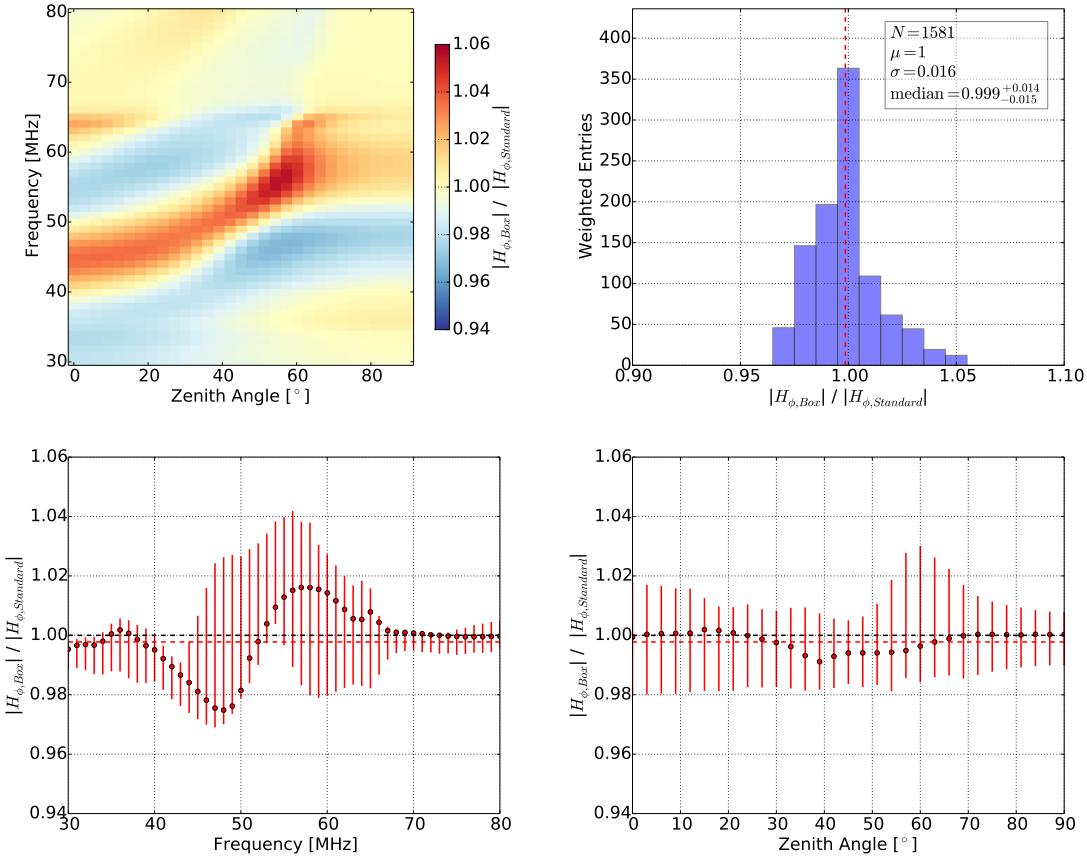

Figure C.7: *Horizontal component of the LPDA vector effective length $|H_\phi|$ obtained from the modified simulation with an electronics box of a north-south polarized LPDA in the west direction compared to those obtained from the standard simulation.* ***(top left)*** *Ratio of the modified simulation and standard simulation for all frequencies as a function of the zenith angle Θ.* ***(top right)*** *Histogram of all ratios of the modified simulation and standard simulation for all frequencies and all zenith angles weighted with $\sin(\Theta)$. The median value is marked as the red dashed line.* ***(bottom left)*** *Median (red dots) and the $68\,\%$ quantile (red error bars) of the zenith angle weighted ratio distribution as a function of the frequency.* ***(bottom right)*** *Median (red dots) and the $68\,\%$ quantile (red error bars) of the ratio distribution as a function of Θ. The red dashed lines mark the overall zenith angle weighted median in both lower diagrams.*

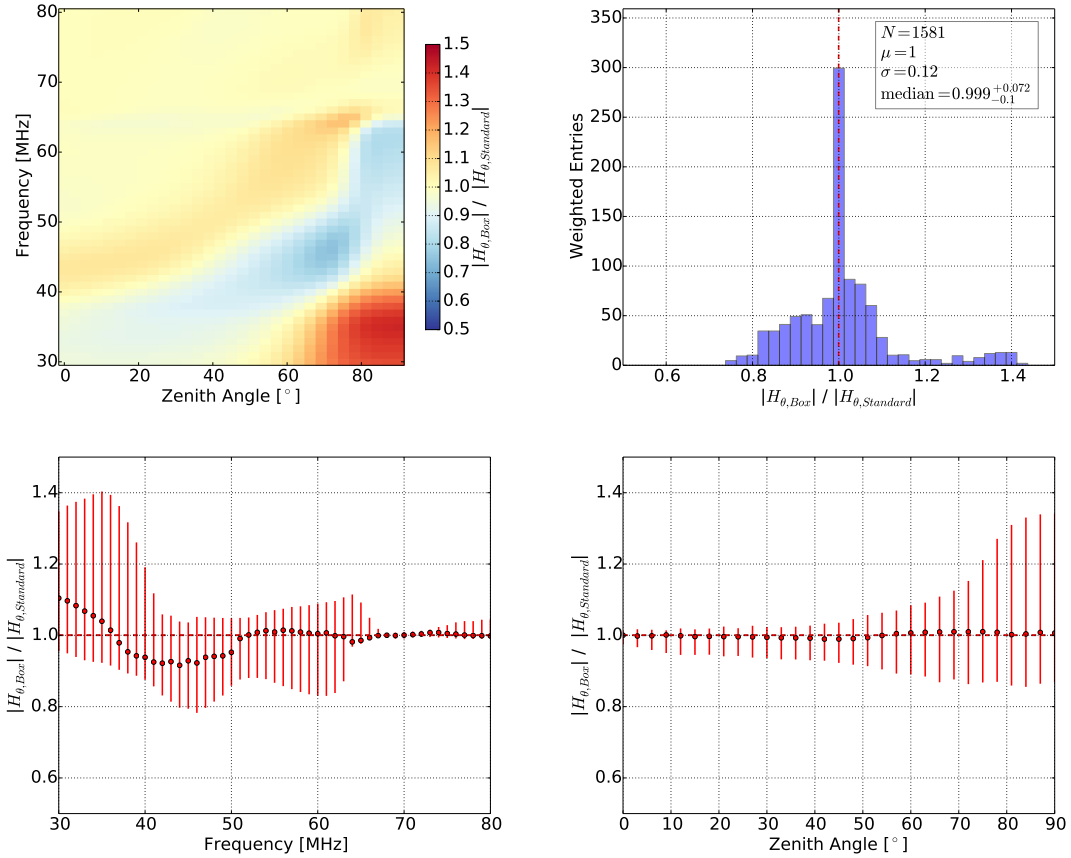

Figure C.8: *Meridional component of the LPDA vector effective length $|H_\theta|$ obtained from the modified simulation with an electronics box of an east-west polarized LPDA in the west direction compared to those obtained from the standard simulation.* ***(top left)*** *Ratio of the modified simulation and standard simulation for all frequencies as a function of the zenith angle Θ.* ***(top right)*** *Histogram of all ratios of the modified simulation and standard simulation for all frequencies and all zenith angles weighted with $\sin(\Theta)$. The median value is marked as the red dashed line.* ***(bottom left)*** *Median (red dots) and the $68\,\%$ quantile (red error bars) of the zenith angle weighted ratio distribution as a function of the frequency.* ***(bottom right)*** *Median (red dots) and the $68\,\%$ quantile (red error bars) of the ratio distribution as a function of Θ. The red dashed lines mark the overall zenith angle weighted median in both lower diagrams.*

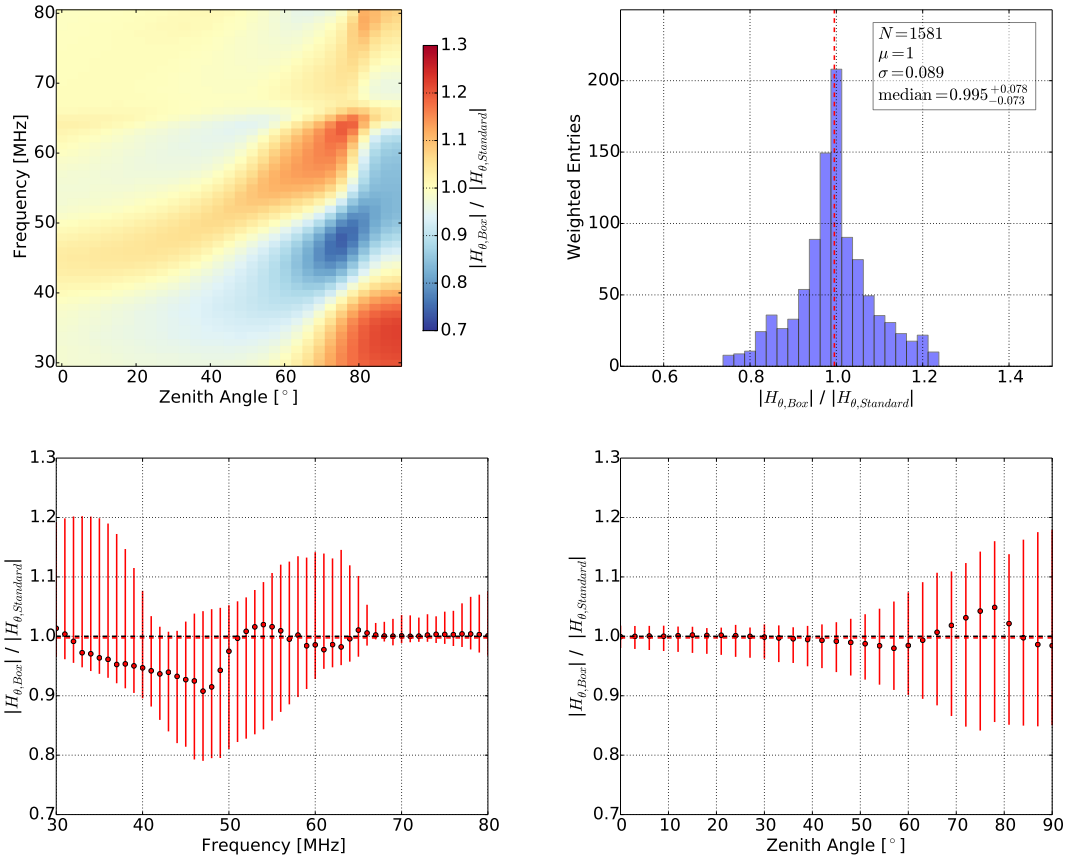

Figure C.9: *Meridional component of the LPDA vector effective length $|H_\theta|$ obtained from the modified simulation with an electronics box of a north-south polarized LPDA in the north direction compared to those obtained from the standard simulation.* ***(top left)*** *Ratio of the modified simulation and standard simulation for all frequencies as a function of the zenith angle Θ.* ***(top right)*** *Histogram of all ratios of the modified simulation and standard simulation for all frequencies and all zenith angles weighted with $\sin(\Theta)$. The median value is marked as the red dashed line.* ***(bottom left)*** *Median (red dots) and the $68\,\%$ quantile (red error bars) of the zenith angle weighted ratio distribution as a function of the frequency.* ***(bottom right)*** *Median (red dots) and the $68\,\%$ quantile (red error bars) of the ratio distribution as a function of Θ. The red dashed lines mark the overall zenith angle weighted median in both lower diagrams.*

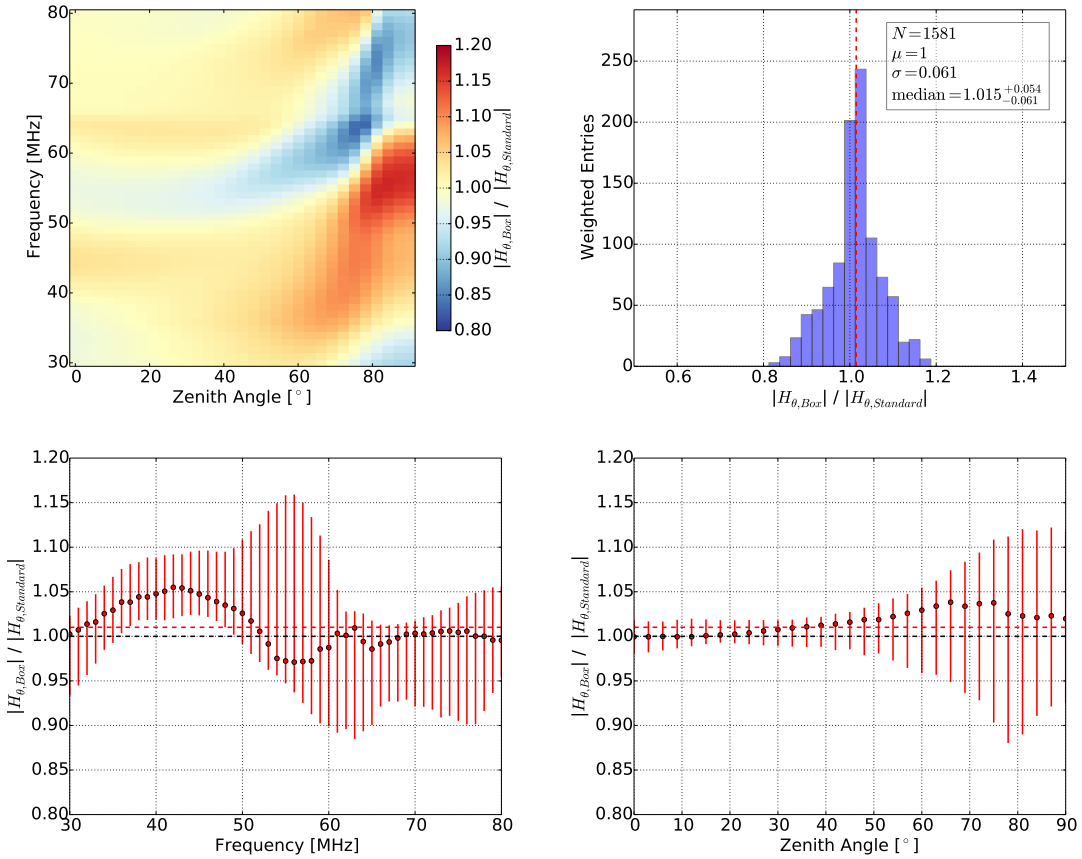

Figure C.10: *Meridional component of the LPDA vector effective length $|H_\theta|$ obtained from the modified simulation with an electronics box of a north-south polarized LPDA in the south direction compared to those obtained from the standard simulation.* ***(top left)*** *Ratio of the modified simulation and standard simulation for all frequencies as a function of the zenith angle Θ.* ***(top right)*** *Histogram of all ratios of the modified simulation and standard simulation for all frequencies and all zenith angles weighted with $\sin(\Theta)$. The median value is marked as the red dashed line.* ***(bottom left)*** *Median (red dots) and the $68\,\%$ quantile (red error bars) of the zenith angle weighted ratio distribution as a function of the frequency.* ***(bottom right)*** *Median (red dots) and the $68\,\%$ quantile (red error bars) of the ratio distribution as a function of Θ. The red dashed lines mark the overall zenith angle weighted median in both lower diagrams.*

D

Measurement of the LPDA Response Pattern

D.1 Simulation Antenna Separation

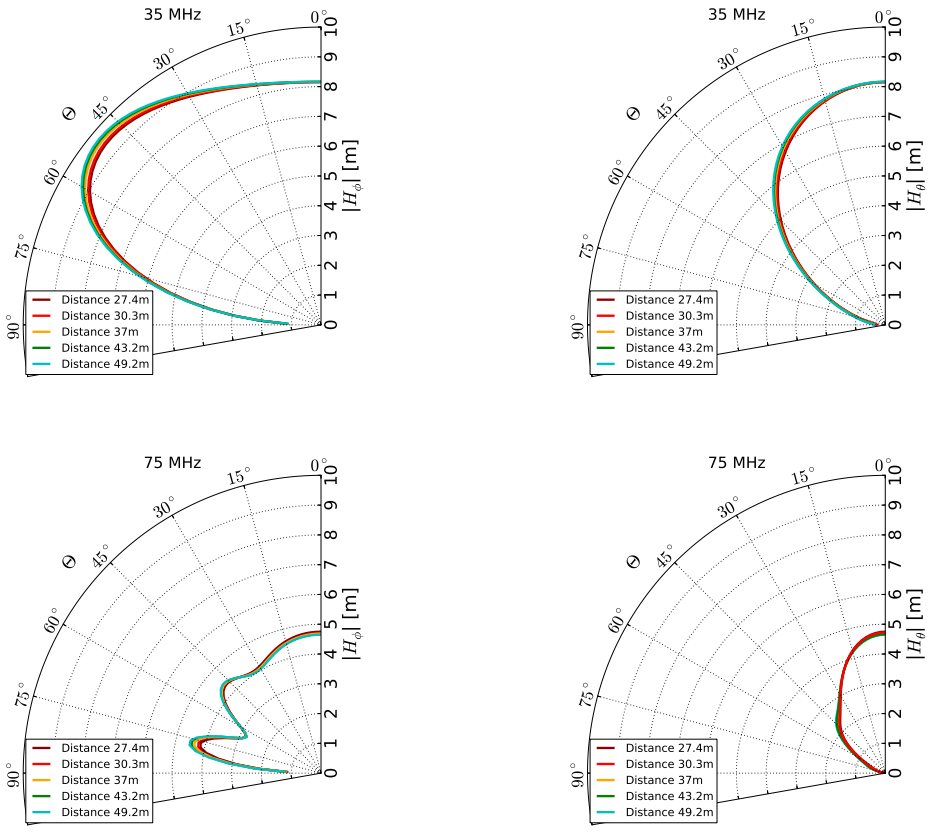

Figure D.1: *Simulations of the LPDA vector effective length (VEL) for different distances of the transmitting antenna to the LPDA. In the **(left)** diagrams, the horizontal VEL $|H_\phi|$ and in the **(right)** diagrams the meridional VEL $|H_\theta|$ as function of the zenith angle Θ at 35 MHz **(top)** and at 75 MHz **(bottom)** are shown.*

D.2 Simulation Ground Conductivity

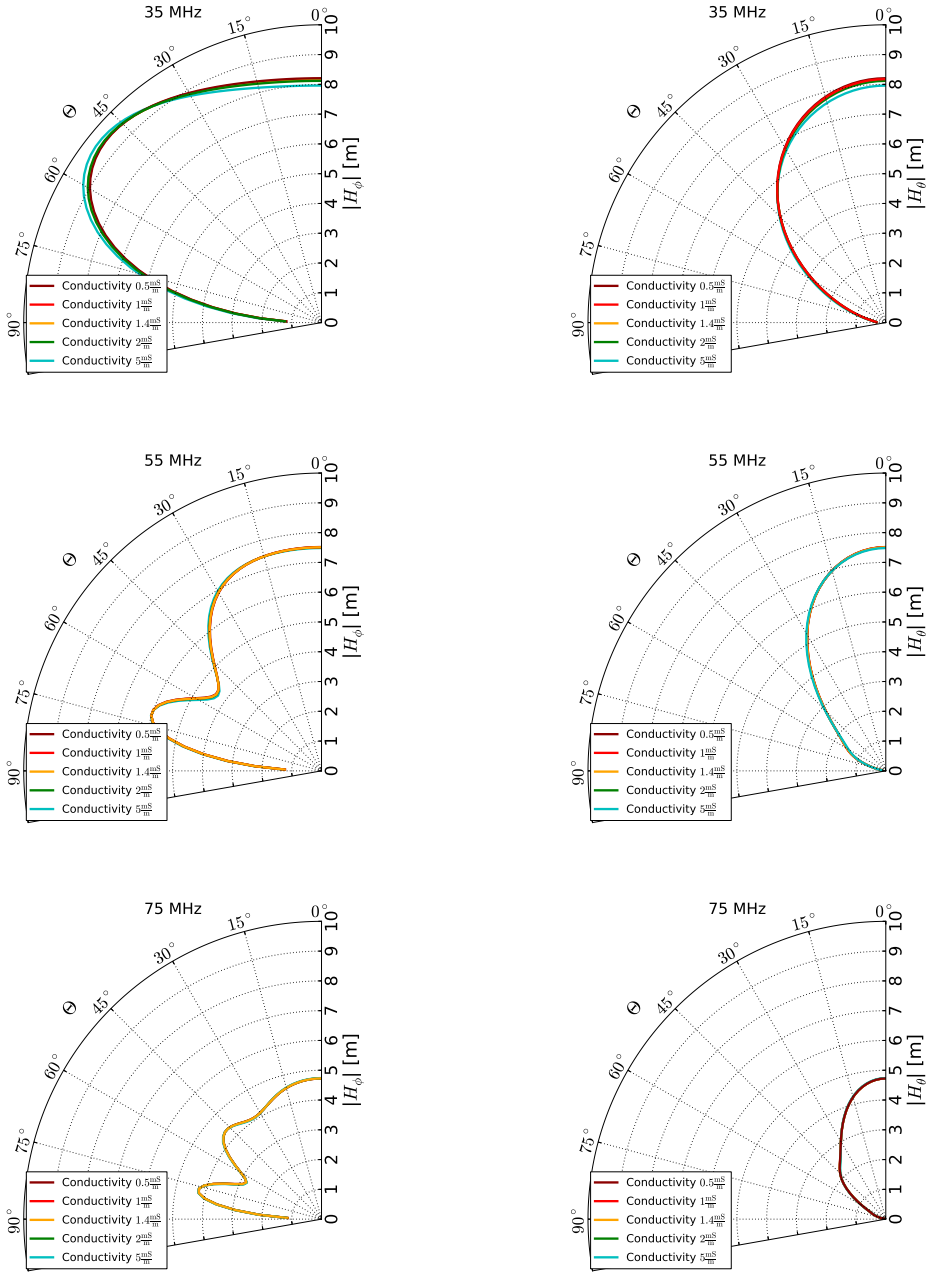

Figure D.2: *Simulations of the LPDA vector effective length (VEL) for different ground conductivities. In the* ***(left)*** *diagrams, the horizontal VEL* $|H_\phi|$ *and in the* ***(right)*** *diagrams the meridional VEL* $|H_\theta|$ *as function of the zenith angle* Θ *at* ***(from top to bottom)*** $35\,\mathrm{MHz}$*,* $55\,\mathrm{MHz}$*, and at* $75\,\mathrm{MHz}$*.*

D.3 Simulation Ground Permittivity

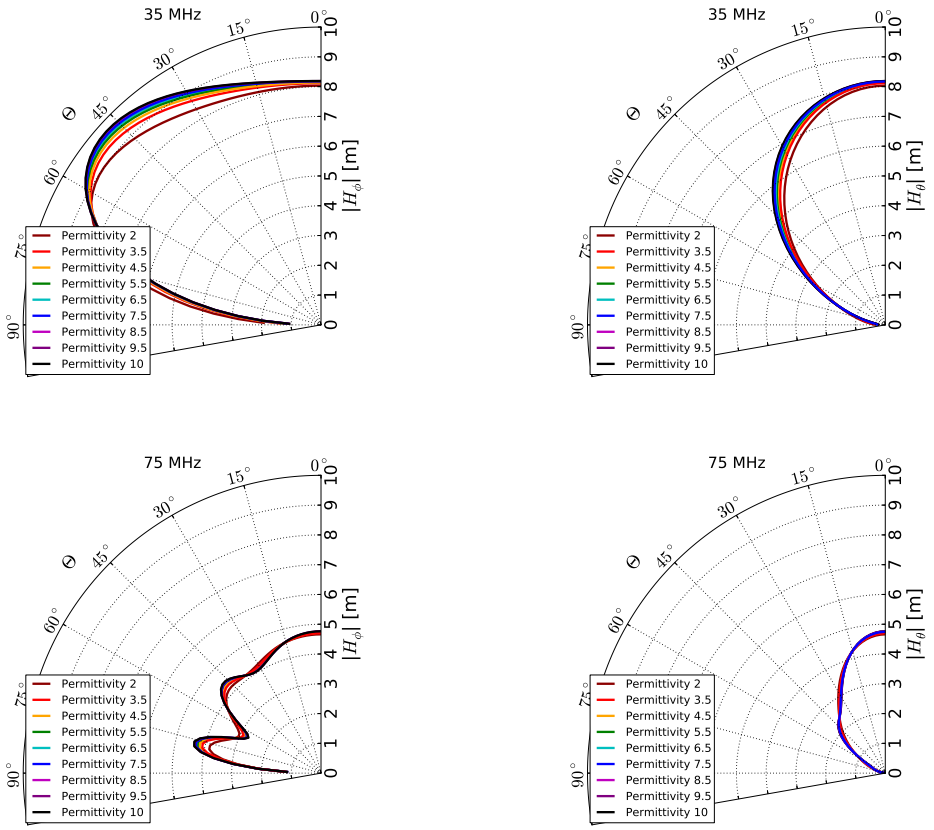

Figure D.3: *Simulations of the LPDA vector effective length (VEL) for different ground permittivities. In the **(left)** diagrams, the horizontal VEL $|H_\phi|$ and in the **(right)** diagrams the meridional VEL $|H_\theta|$ as function of the zenith angle Θ at 35 MHz **(top)** and at 75 MHz **(bottom)** are shown.*

D.4 Compatibility Parameter

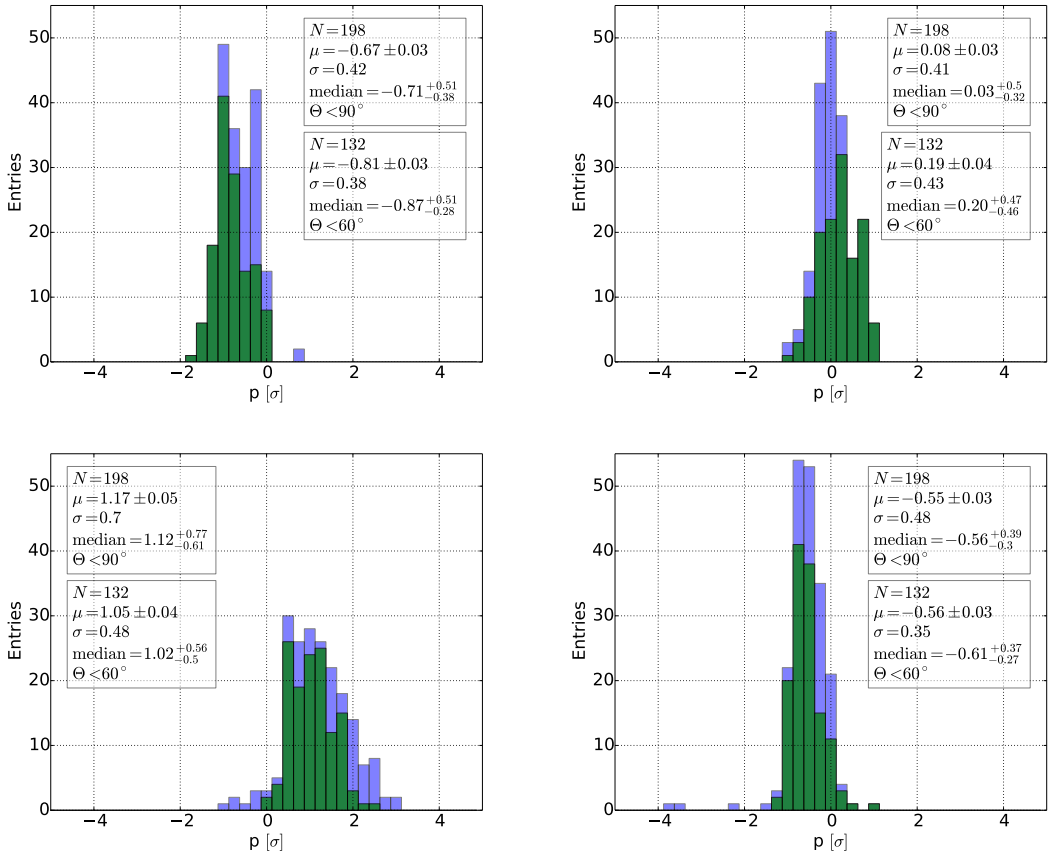

Figure D.4: *Histogram of the compatibility parameter p of four different measurements in numbers of the combined flight-dependent uncertainties σ of all frequencies and zenith angles with* $\Theta < 90^\circ$ *(blue histogram) and* $\Theta < 60^\circ$ *(green histogram). The combined flight-dependent uncertainty σ is determined by the quadratical combination of the flight-dependent uncertainties of* $\overline{\mathrm{VEL}_4}$ *with the flight-dependent systematics and the statistical uncertainties of the respective flight.*

Bibliography

[1] L. Evans and P. Bryant, „LHC Machine“, J. Instrum. **3** (2008).

[2] V.F. Hess, „Über Beobachtungen der durchdringenden Strahlung bei sieben Freiballonfahrten“, Phys. Zeitschr. **XIII**, 1084–1091 (1912).

[3] A. Aab et al. (Pierre Auger Collaboration), „The Pierre Auger Cosmic Ray Observatory“, Nucl. Instrum. Meth. A **798**, 172–213 (2015), arXiv:1502.01323.

[4] H. Falcke et al., „Detection and imaging of atmospheric radio flashes from cosmic ray air showers“, Nature **435**, 313–316 (2005), arXiv:astro-ph/0505383.

[5] D. Ardouin et al. (CODALEMA Collaboration), „Radioelectric field features of extensive air showers observed with CODALEMA“, Astropart. Phys. **26**, 341–350 (2006), arXiv:astro-ph/0608550.

[6] J. Schulz for the Pierre Auger Collaboration, „Status and prospects of the Auger Engineering Radio Array“, Proc. of the 34th ICRC, The Hague, The Netherlands, PoS(ICRC2015)615 (2015).

[7] P.A. Bezyazeekov et al. (Tunka-Rex Collaboration), „Measurement of cosmic-ray air showers with the Tunka Radio Extension (Tunka-Rex)“, Nucl. Instrum. Meth. A **802**, 89–96 (2015), arXiv:1509.08624.

[8] J.R. Hörandel et al., „Radio detection of Cosmic Rays with LOFAR“, Proc. of the 34th ICRC, The Hague, The Netherlands, PoS(ICRC2015)033 (2015).

[9] T. Huege, „Radio detection of cosmic ray air showers in the digital era“, Phys. Rep. **620**, 1–52 (2016), arXiv:1601.07426.

[10] F.G. Schröder, „Radio detection of cosmic-ray air showers and high-energy neutrinos“, Prog. Part. Nucl. Phys. **93**, 1–68 (2017), arXiv:1607.08781.

[11] F.D. Kahn and I. Lerche, „Radiation from cosmic ray air showers“, Proc. R. Soc. Lond. A **289**, 206–213 (1966).

[12] H.R. Allan, „Radio emission from extensive air showers“, Prog. Element. Part. Cosmic Ray Phys. **X**, 169–302 (1971).

[13] T. Huege and H. Falcke, „Radio emission from cosmic ray air showers: coherent geosynchrotron radiation“, Astron. Astrophys. **412**, 19–34 (2003), arXiv:astro-ph/0309622.

[14] D. Ardouin et al. (Codalema Collaboration), „Geomagnetic origin of the radio emission from cosmic ray induced air showers observed by CODALEMA“, Astropart. Phys. **31**, 192–200 (2009), arXiv:0901.4502.

[15] P. Abreu et al. (Pierre Auger Collaboration), „Results of a self-triggered prototype system for radio-detection of extensive air showers at the Pierre Auger Observatory“, J. Instrum. **7**, P11023 (2012), arXiv:1211.0572.

[16] G. Askaryan, „Excess negative charge of an electron-photon shower and its coherent radio emission“, Soviet Phys. JETP Lett. (USSR) **14**, 441–443 (1962).

[17] J.H. Hough J.R. Prescott and J.K. Pidcock, „Mechanism of Radio Emission from Extensive Air Showers“, Nature Phys. Sci. **223**, 109–110 (1971).

[18] A. Bellétoile et al., „Evidence for the charge-excess contribution in air shower radio emission observed by the CODALEMA experiment“, Astropart. Phys. **69**, 50–60 (2015).

[19] P. Schellart et al., „Polarized radio emission from extensive air showers measured with LOFAR“, J. Cosmol. Astropart. Phys. 10(2014)014 , arXiv:1406.1355.

[20] A. Aab et al. (Pierre Auger Collaboration), „Probing the radio emission from air showers with polarization measurements“, Phys. Rev. D **89**, 052002 (2014), arXiv:1402.3677.

[21] W.D. Apel et al. (LOPES Collaboration), „Reconstruction of the energy and depth of maximum of cosmic-ray air-showers from LOPES radio measurements“, Phys. Rev. D **90**, 062001 (2014), arXiv:1408.2346.

[22] A. Nelles et al., „The radio emission pattern of air showers as measured with LOFAR - a tool for the reconstruction of the energy and the shower maximum“, J. Cosmol. Astropart. Phys. 05(2015)018 , arXiv:1411.7868.

[23] P.A. Bezyazeekov et al. (Tunka-Rex Collaboration), „Radio measurements of the energy and the depth of the shower maximum of cosmic-ray air showers by Tunka-Rex“, J. Cosmol. Astropart. Phys. 01(2016)052 , arXiv:1509.05652.

[24] A. Aab et al. (Pierre Auger Collaboration), „Measurement of the Radiation Energy in the Radio Signal of Extensive Air Showers as a Universal Estimator of Cosmic-Ray Energy“, Phys. Rev. Lett. **116**, 241101 (2016), arXiv:1605.02564.

[25] A. Aab et al. (Pierre Auger Collaboration), „Energy estimation of cosmic rays with the Engineering Radio Array of the Pierre Auger Observatory“, Phys. Rev. D **93**, 122005 (2016), arXiv:1508.04267.

[26] D. Heck et al., „CORSIKA: A Monte Carlo code to simulate extensive air showers“, FZKA-6019 (1998).

[27] W.R. Carvalho Jr. J. Alvarez-Muñiz and E. Zas, „Monte Carlo simulations of radio pulses in atmospheric showers using ZHAireS“, Astropart. Phys. **35**, 325–341 (2012), arXiv:1107.1189.

[28] M. Ludwig T. Huege and C.W. James, „Simulating radio emission from air showers with CoREAS“, Proc. of the AIP Conf. **1535**, 128–132 (2013), arXiv:1301.2132.

[29] J.C. Glaser et al., „Simulation of radiation energy release in air showers“, J. Cosmol. Astropart. Phys. 09(2016)024 , arXiv:1606.01641.

[30] J.C. Glaser, „Absolute Energy Calibration of the Pierre Auger Observatory using Radio Emission of Extensive Air Showers“, PhD thesis (RWTH Aachen University, 2016).

[31] R. Krause for the Pierre Auger Collaboration, „A new method to determine the energy scale for high-energy cosmic rays using radio measurements at the Pierre Auger Observatory“, Proc. of the 35th ICRC, Busan, South Korea, PoS(ICRC2017)528 (2017).

[32] K. Link for the LOPES Collaboration, „Revised absolute amplitude calibration of the LOPES experiment“, Proc. of the 34th ICRC, The Hague, The Netherlands, PoS(ICRC2015)311 (2015), arXiv:1508.03471.

[33] R. Hiller for the Tunka-Rex Collaboration, „Calibration of the absolute amplitude scale of the Tunka Radio Extension (Tunka-Rex)“, Proc. of the 34th ICRC, The Hague, The Netherlands, PoS(ICRC2015)573 (2015).

[34] A. Nelles et al., „Calibrating the absolute amplitude scale for air showers measured at LOFAR“, J. Instrum. **10**, P11005 (2015), arXiv:1507.08932.

[35] O. Kambeitz, „Radio Detection of Horizontal Extensive Air Showers“, PhD thesis (Karlsruhe Institute of Technology (KIT), 2016).

[36] E.M. Holt for the Pierre Auger Collaboration, „Recent Results of the Auger Engineering Radio Array (AERA)“, Proc. of the 35th ICRC, Busan, South Korea, PoS(ICRC2017)492 (2017).

[37] G.J. Burke and A.J. Poggio, *Numerical Electromagnetics Code (NEC) Method of Moments*, tech. rep. (Lawrence Livermore National Laboratory, 1981).

[38] M. Motoki et al., „Precise Measurements of Atmospheric Muon Fluxes with the BESS Spectrometer“, Astropart. Phys. **19**, 113–126 (2003), arXiv:astro-ph/0205344.

[39] E.S. Seo et al. (CREAM Collaboration), „Cosmic-ray energetics and mass (CREAM) balloon project“, Adv. Space Res. **33**, 1777–1785 (2004).

[40] M. Ave et al., „The TRACER instrument: A balloon-borne cosmic-ray detector“, Nucl. Instrum. Meth. A **654**, 140–156 (2011).

[41] W.R. Binns et al., „The SuperTIGER instrument: measurement of elemental abundances of ultra-heavy galactic cosmic rays“, Astrophys. J. **788**, 18 (2014).

[42] M. Casolino and P. Picozza on behalf of the PAMELA collaboration, „The PAMELA experiment: A space-borne observatory for heliospheric phenomena“, Adv. Space Res. **41**, 2043–2049 (2008).

[43] A.A. Abdo et al. (Fermi LAT Collaboration), „Measurement of the Cosmic Ray $e^+ + e^-$ Spectrum from 20 GeV to 1 TeV with the Fermi Large Area Telescope“, Phys. Rev. Lett. **102**, 181101 (2009), arXiv:0905.0025.

[44] M. Aguilar et al. (AMS Collaboration), „First Result from the Alpha Magnetic Spectrometer on the International Space Station: Precision Measurement of the Positron Fraction in Primary Cosmic Rays of 0.5–350 GeV“, Phys. Rev. Lett. **110**, 141102 (2013).

[45] E.S. Seo et al., „Cosmic Ray Energetics And Mass for the International Space Station (ISS-CREAM)“, Adv. Space Res. **53**, 1451–1455 (2014).

[46] T. Antoni et al. (KASCADE Collaboration), „The cosmic-ray experiment KASCADE“, Nucl. Instrum. Meth. A **513**, 490–510 (2003).

[47] G. Navarra et al., „KASCADE-Grande: a large acceptance, high-resolution cosmic-ray detector up to 1018 eV“, Nucl. Instrum. Meth. A **518**, 207–209 (2004).

[48] H. Kawai et al. (Telescope Array Collaboration), „Telescope Array Experiment“, Nucl. Phys. B - Proc. Suppl. **175–176**, 221–226 (2008).

[49] K. Olive et al. (Particle Data Group), „Review of particle physics“, Chin. Phys. C **38**, 090001 (2014).

[50] J.J. Engelmann et al., „Charge composition and energy spectra of cosmic-ray nuclei for elements from Be to NI - Results from HEAO-3-C2“, Astron. Astrophys. **233**, 96–111 (1990).

[51] D. Müller et al., „Energy spectra and composition of primary cosmic rays“, Astrophys. J. **374**, 356–365 (1991).

[52] K. Asakimori et al. (JACEE Collaboration), „Cosmic-Ray Proton and Helium Spectra: Results from the JACEE Experiment“, Astrophys. J. **502**, 278–283 (1998).

[53] J. Alcaraz et al. (AMS Collaboration), „Cosmic protons“, Phys. Lett. B **490**, 27–35 (2000).

[54] J. Alcaraz et al. (AMS Collaboration), „Helium in Near Earth Orbit“, Phys. Lett. B **494**, 193–202 (2000).

[55] T. Sanuki et al., „Precise Measurement of Cosmic-Ray Proton and Helium Spectra with the BESS Spectrometer“, Astrophys. J. **545**, 1135–1142 (2000), arXiv:astro-ph/0002481.

[56] M. Boezio et al., „The cosmic-ray proton and helium spectra measured with the CAPRICE98 balloon experiment“, Astropart. Phys. **19**, 583–604 (2003), arXiv:astro-ph/0212253.

[57] S. Haino et al., „Measurements of primary and atmospheric cosmic-ray spectra with the BESS-TeV spectrometer“, Phys. Lett. B **29**, 35–46 (2004).

[58] V.A. Derbina et al., „Cosmic-Ray Spectra and Composition in the Energy Range of 10-1000 TeV per Particle Obtained by the RUNJOB Experiment“, Astrophys. J. **628**, L41–L44 (2005).

[59] F. Aharonian et al. (HESS Collaboration), „First ground-based measurement of atmospheric Cherenkov light from cosmic rays“, Phys. Rev. D **75**, 042004 (2007), arXiv:astro-ph/0701766.

[60] A. D. Panov et al., „Elemental energy spectra of cosmic rays from the data of the ATIC-2 experiment“, Bulletin of the Russian Academy of Sciences: Physics **71**, 494–497 (2007).

[61] M. Ave et al., „Composition of Primary Cosmic-Ray Nuclei at High Energies“, Astrophys. J. **678**, 262–273 (2008), arXiv:0801.0582.

[62] H.S. Ahn et al., „Energy spectra of cosmic-ray nuclei at high energies“, Astrophys. J. **707**, 593–603 (2009), arXiv:0911.1889.

[63] N.L. Grigorov et al., „Study of energy spectrum of primary cosmic-ray particle of high and ultrahigh energy on proton satellites“, Sov. J. Nucl. Phys. **11**, 588 (1970).

[64] N.L. Grigorov et al., Proc. of the 12th ICRC **1**, Hobart, Australia, 1746 (1971).
[65] N.L. Grigorov et al., Proc. of the 12th ICRC **1**, Hobart, Australia, 1752 (1971).
[66] T.V. Danilova et al., „The Energy Spectrum of the Primary Cosmic Rays in the Range 10^{13} - 10^{16} eV“, Proc. of the 15th ICRC **8**, Plovdiv, Bulgaria, 129 (1977).
[67] M. Nagano et al., „Energy spectrum of primary cosmic rays between $10^{14.5}$ and 10^{18} eV“, J. Phys. G: Nucl. Part. Phys. **10**, 1295–1310 (1984).
[68] Y.A. Fomin et al., „Energy Spectrum of Cosmic Rays at Energies of 5 x 10^{15} - 5 x 10^{17} eV“, Proc. of the 22th ICRC **2**, Dublin, Ireland (1991).
[69] K. Asakimori et al. (JACEE Collab.), „Energy spectra and composition of cosmic rays above 1 TeV per nucleon“, Proc. of the 22th ICRC **2**, Dublin, Ireland, 57–60 (1991).
[70] K. Asakimori et al. (JACEE Collab.), „Energy spectra of protons and helium nuclei above 5 TeV/nucleon“, Proc. of the 22th ICRC **2**, Dublin, Ireland, 97–100 (1991).
[71] K. Asakimori et al. (JACEE Collab.), Proc. of the 22th ICRC **2**, Calgary, Canada, 25–28 (1993).
[72] M. Amenomori et al., „The cosmic-ray energy spectrum between $10^{14.5}$ and $10^{16.3}$ eV covering the "knee"region“, Astrophys. J. **461**, 408–414 (1996).
[73] M.A.K. Glasmacher et al., „The cosmic ray energy spectrum between 10^{14} and $10^{16.}$ eV“, Astropart. Phys. **10**, 291–302 (1999).
[74] et al (HEGRA Collaboration) F.Arqueros, „Energy Spectrum and Chemical Composition of Cosmic Rays between 0.3 and 10 PeV determined from the Cherenkov-Light and Charged-Particle distributions in Air Showers“, Astron. Astrophys. **359**, 682–694 (2000), arXiv:astro-ph/9908202.
[75] T. Antoni et al. (KASCADE Collaboration), „KASCADE measurements of energy spectra for elemental groups of cosmic rays: Results and open problems“, Astropart. Phys. **24**, 1–25 (2005), arXiv:astro-ph/0505413.
[76] R.U. Abbasi et al. (High Resolution Fly's Eye Collaboration), „First Observation of the Greisen-Zatsepin-Kuzmin Suppression“, Phys. Rev. Lett. **100**, 101101 (2008), arXiv:astro-ph/0703099.
[77] J. Abraham et al. (Pierre Auger Collaboration), „Observation of the Suppression of the Flux of Cosmic Rays above 4 x 10^{19} eV“, Phys. Rev. Lett. **101**, 061101 (2008), arXiv:0806.4302.
[78] M. Amenomori et al., „The All-Particle Spectrum of Primary Cosmic Rays in the Wide Energy Range from 10^{14} to 10^{17} eV Observed with the Tibet-III Air-Shower Array“, Astrophys. J. **678**, 1165–1179 (2008).
[79] W.D. Apel et al. (KASCADE-Grande Collaboration), „Kneelike Structure in the Spectrum of the Heavy Component of Cosmic Rays Observed with KASCADE-Grande“, Phys. Rev. Lett. **107**, 171104 (2011), arXiv:1107.5885.
[80] M.G. Aartsen et al. (IceCube Collaboration), „Measurement of the cosmic ray energy spectrum with IceTop-73“, Phys. Rev. D **88**, 042004 (2013), arXiv:1307.3795.
[81] D. Ivanov for the Telescope Array Collaboration, „TA Spectrum Summary“, Proc. of the 34th ICRC, The Hague, The Netherlands, PoS(ICRC2015)349 (2015).
[82] I. Valiño for the Pierre Auger Collaboration, „The flux of ultra-high energy cosmic rays after ten years of operation of the Pierre Auger Observatory“, Proc. of the 34th ICRC, The Hague, The Netherlands, PoS(ICRC2015)271 (2015).
[83] G.V. Kulikov and G.B. Khristiansen, „On the size spectrum of extensive air showers“, J. Exp. Theor. Phys. **35**, 635–640 (1958).
[84] M.Aglietta et al. (EAS-TOP Collaboration), „The cosmic ray primary composition in the "knee" region through the EAS electromagnetic and muon measurements at EAS-TOP“, Astropart. Phys. **21**, 583–596 (2004).
[85] H. Ulrich et al. (KASCADE Collaboration), „Indirect Measurements around the Knee — Recent Results from KASCADE“, Int. J. Mod. Phys. A **20**, 6774–6777 (2005).

[86] K.H. Kampert et al. (KASCADE-Grande Collaboration), „Cosmic Rays in the 'Knee'-Region - Recent Results from KASCADE -“, Acta Phys. Polon. B **35**, 1799–1812 (2004), arXiv:astro-ph/0405608.

[87] V. Verzi, „Cosmic Rays: air showers from low to high energies - Rapporteur Report“, Proc. of the 34th ICRC, The Hague, The Netherlands, PoS(ICRC2015)015 (2015).

[88] K. Greisen, „End to the cosmic ray spectrum?“, Phys. Rev. Lett. **16**, 748–750 (1966).

[89] G.T. Zatsepin and V.A. Kuzmin, „Upper limit of the spectrum of cosmic rays“, J. Exp. Theor. Phys. Lett. **4**, 78–80 (1966).

[90] T. Pierog et al., „EPOS LHC : test of collective hadronization with LHC data“, Phys. Rev. C **92**, 034906 (2015), arXiv:1306.0121.

[91] S.S. Ostapchenko N.N. Kalmykov and A.I. Pavlov, „Quark-Gluon String Model and EAS Simulation Problems at Ultra-High Energies“, Nucl. Phys. B - Proc. Suppl. **52B**, 17–28 (1997).

[92] S.S. Ostapchenko, „QGSJET-II: towards reliable description of very high energy hadronic interactions“, Nucl. Phys. B - Proc. Suppl. **151**, 143–146 (2006), arXiv:hep-ph/0412332.

[93] S.S. Ostapchenko, „Status of QGSJET“, AIP Conf. Proc. **928**, 118–125 (2007), arXiv:0706.3784.

[94] S.S. Ostapchenko, „Monte Carlo treatment of hadronic interactions in enhanced Pomeron scheme: QGSJET-II model“, Phys. Rev. D **83**, 014018 (2011), arXiv:1010.1869.

[95] E.-J. Ahn et al., „Cosmic ray interaction event generator SIBYLL 2.1“, Phys. Rev. D **80**, 094003 (2009).

[96] R. Abbasi for the Pierre Auger Collaboration and the Telescope Array Collaboration, „Report of the Working Group on the Composition of Ultra-High Energy Cosmic Rays“, JPS Conf. Proc. **9**, 010016 (2016), arXiv:1503.07540.

[97] A. Aab et al. (Pierre Auger Collaboration), „Depth of maximum of air-shower profiles at the Pierre Auger Observatory. I. Measurements at energies above $10^{17.8}$eV“, Phys. Rev. D **90**, 122005 (2014).

[98] R.U. Abbasi et al. (Telescope Array Collaboration), „Study of Ultra-High Energy Cosmic Ray composition using Telescope Array's Middle Drum detector and surface array in hybrid mode“, Astropart. Phys. **64**, 49 (2014), arXiv:1408.1726.

[99] J. Abraham et al. (Pierre Auger Collaboration), „An upper limit to the photon fraction in cosmic rays above 10^{19}eV from the Pierre Auger Observatory“, Astropart. Phys. **27**, 155–168 (2007), arXiv:astro-ph/0606619.

[100] J. Abraham et al. (Pierre Auger Collaboration), „Upper limit on the cosmic-ray photon flux above 10^{19}eV using the surface detector of the Pierre Auger Observator“, Astropart. Phys. **29**, 243–256 (2008).

[101] J. Abraham et al. (Pierre Auger Collaboration), „Upper limit on the cosmic-ray photon fraction at EeV energies from the Pierre Auger Observatory“, Astropart. Phys. **31**, 399–406 (2009), arXiv:0903.1127.

[102] T. Winchen, „The Principal Axes of the Directional Energy Distribution of Cosmic Rays Measured with the Pierre Auger Observatory“, PhD thesis (RWTH Aachen University, 2013).

[103] A.M. Hillas, „The origin of ultrahigh-energy cosmic rays“, Ann. Rev. Astron. Astrophys. **22**, 425–444 (1984).

[104] K. Kotera and A.V. Olinto, „The Astrophysics of Ultrahigh-Energy Cosmic Rays“, Annu. Rev. Astron. Astrophys. **49**, 119–153 (2011), arXiv:1101.4256.

[105] K.V. Ptitsyna and S.V. Troitsky, „Physical conditions in potential sources of ultra-high-energy cosmic rays: Updated Hillas plot and radiation-loss constraints“, Phys. Usp. **53**, 691–701 (2010), arXiv:0808.0367.

[106] E. Fermi, „On the Origin of the Cosmic Radiation“, Phys. Rev. **75**, 1169–1174 (1949).

[107] V. Bosch-Ramon F.M. Rieger and P. Duffy, „Fermi acceleration in astrophysical jets“, Ap&SS **309**, 119–125 (2007), arXiv:astro-ph/0610141.

[108] R. Durrer and A. Neronov, „Cosmological magnetic fields: their generation, evolution and observation“, Astron. Astrophys. Rev. **21**, 62 (2013), arXiv:1303.7121.

[109] D. Walz, „Constraining models of the extragalactic cosmic-ray origin with the Pierre Auger Observatory“, PhD thesis (RWTH Aachen University, 2016).

[110] S. Hackstein et al., „Propagation of ultrahigh energy cosmic rays in extragalactic magnetic fields: a view from cosmological simulations“, Mon. Not. R. Astron. Soc. **462**, 3660–3671 (2016).

[111] Rainer Beck and Richard Wielebinski, „Magnetic Fields in Galaxies“, in *Planets, stars and stellar systems: volume 5: galactic structure and stellar populations*, edited by Terry D. Oswalt and Gerard Gilmore (Springer Netherlands, Dordrecht, 2013), pp. 641–723.

[112] P.P. Kronberg M.S. Pshirkov P.G. Tinyakov and K.J. Newton-McGee, „Deriving global structure of the Galactic Magnetic Field from Faraday Rotation Measures of extragalactic sources“, Astrophys. J. **738**, 192 (2011), arXiv:1103.0814.

[113] R. Jansson and G.R. Farrar, „A new model of the galactic magnetic field“, Astrophys. J. **757**, 13 (2012), arXiv:1204.3662.

[114] R. Jansson and G.R. Farrar, „The galactic magnetic field“, Astrophys. J. **761**, L11 (2012), arXiv:1210.7820.

[115] M.C. Beck et al., „New constraints on modelling the random magnetic field of the MW“, J. Cosmol. Astropart. Phys. 05(2016)056 , arXiv:1409.5120.

[116] M. Urban M. Erdmann G. Müller and M. Wirtz, „The nuclear window to the extragalactic universe“, Astropart. Phys. **85**, 54–64 (2016), arXiv:1607.01645.

[117] E. Regener, „Der Energiestrom der Ultrastrahlung“, Zeit. f. Phys. **80** (1933).

[118] A.A. Penzias and R.W. Wilson, „A Measurement of Excess Antenna Temperature at 4080 Mc/s“, Astrophys. J. **142**, 419–421 (1965).

[119] J.W. Cronin, „Cosmic rays: the most energetic particles in the universe“, Rev. Mod. Phys. **71**, 165–172 (1999).

[120] R.U. Abbasi et al. (Telescope Array Collaboration), „Indications of Intermediate-scale Anisotropy of Cosmic Rays with Energy Greater Than 57 EeV in the Northern Sky Measured with the Surface Detector of the Telescope Array Experiment“, Astrophys. J. **790**, L21 (2014), arXiv:1404.5890.

[121] K. Kawata for the Telescope Array Collaboration, „Ultra-High-Energy Cosmic-Ray Hotspot Observed with the Telescope Array Surface Detectors“, Proc. of the 34th ICRC, The Hague, The Netherlands, PoS(ICRC2015)276 (2015).

[122] M. Fukushima et al. for the Telescope Array Collaboration, „Telescope Array anisotropy summary“, Proc. of the 35th ICRC, Busan, South Korea, PoS(ICRC2017)548 (2017).

[123] O. Deligny for the Pierre Auger and the Telescope Array Collaboration, „Large-Scale Distribution of Arrival Directions of Cosmic Rays Detected at the Pierre Auger Observatory and the Telescope Array“, Proc. of the 34th ICRC, The Hague, The Netherlands, PoS(ICRC2015)395 (2015).

[124] P. Abreu et al. (Pierre Auger Collaboration), „Anisotropy and chemical composition of ultra-high energy cosmic rays using arrival directions measured by the Pierre Auger Observatory“, J. Cosmol. Astropart. Phys. 06(2011)022 .

[125] U. Giaccari for the Pierre Auger Collaboration, „Arrival directions of the highest-energy cosmic rays detected by the Pierre Auger Observatory“, Proc. of the 35th ICRC, Busan, South Korea, PoS(ICRC2017)483 (2017).

[126] M.-P. Véron-Cetty and P. Véron, „A catalogue of quasars and active nuclei: 12th edition“, Astron. Astrophys. **455**, 773–777 (2006).

[127] J. Aublin for the Auger Collaboration, „Arrival directions of the highest-energy cosmic rays detected with the Pierre Auger Observatory“, Proc. of the 34th ICRC, The Hague, The Netherlands, PoS(ICRC2015)310 (2015).

[128] A. Aab et al. (Pierre Auger Collaboration), „Searches for Anisotropies in the Arrival Directions of the Highest Energy Cosmic Rays Detected by the Pierre Auger Observatory“, Astrophys. J. **804**, 15 (2015), arXiv:1411.6111.

[129] M. Ackermann et al., „2FHL: the second catalog of hard FERMI-Lat sources“, Astrophys. J. **222**, 5 (2016), arXiv:1508.04449.

[130] A. Aab et al. (Pierre Auger Collaboration), „Large scale distribution of ultra high energy cosmic rays detected at the Pierre Auger Observatory with zenith angles up to 80°“, Astrophys. J. **802**, 111 (2015), arXiv:1411.6953.

[131] I. Al Samarai for the Pierre Auger Observatory, „Indications of anisotropy at large angular scales in the arrival directions of cosmic rays detected at the Pierre Auger Observatory“, Proc. of the 34th ICRC, The Hague, The Netherlands, PoS(ICRC2015)372 (2015).

[132] A. Aab et al. (Pierre Auger Collaboration), „Multi-resolution anisotropy studies of ultrahigh-energy cosmic rays detected at the Pierre Auger Observatory“, J. Cosmol. Astropart. Phys. 06(2017)026 .

[133] A. Aab et al. (Pierre Auger Collaboration), „Observation of a Large-scale Anisotropy in the Arrival Directions of Cosmic Rays above $8x10^{18}$eV“, Science **357**, 1266 (2017), arXiv:1709.07321.

[134] D. Heck R. Engel and T. Pierog, „Extensive air showers and hadronic interactions at high energy“, Ann. Rev. Nucl. Part. S. **61**, 467–489 (2011).

[135] D. Kümpel, „Multivariate Search for a Directional Excess of EeV Photons with the Pierre Auger Observatory“, PhD thesis (Bergische Universität Wuppertal, 2011).

[136] D. Heck and T. Pierog, „Extensive Air Shower Simulations with CORSIKA: A User's Guide“, (2017).

[137] J.F. Carlson and J.R. Oppenheimer, „On Multiplicative Showers“, Phys. Rev. **51**, 220–231 (1937).

[138] W. Heitler, *The Quantum Theory of Radiation*, third (Oxford University Press, 1954).

[139] J. Matthews, „A Heitler model of extensive air showers“, Astropart. Phys. **22**, 387–397 (2005).

[140] J. Hörandel, „Cosmic Rays from the Knee to the second Knee: 10^{14}eV to 10^{18}eV“, Mod. Phys. Lett. A **22**, 1533–1551 (2007), arXiv:astro-ph/0611387.

[141] T.K. Gaisser, *Cosmic Rays and Particle Physics* (Cambridge University Press, 1990).

[142] M.J. Tueros, „Estimate of the non-calorimetric energy of showers observed with the fluorescence and surface detectors of the Pierre Auger Observatory“, Proc. of the 33rd ICRC, Rio de Janeiro, Brazil (2013).

[143] „IEEE Standard Definitions of Terms for Antennas“, IEEE **145-1993** (2004).

[144] K. Rothammel and A. Kirschke, *Rothammels Antennenbuch*, 12th ed. (DARC Verlag GmbH, 2001).

[145] C. Balanis, *Antenna Theory - Analysis and Design*, third edition (John Wiley & Sons, Inc., 2005).

[146] W.L. Stutzman and G.A. Thiele, *Antenna Theory and Design*, 3rd ed. (John Wiley & Sons, Inc., 2012).

[147] U.A. Bakshi and A.V. Bakshi Bakshi, *Antennas & Wave Propagation* (Technical Publications Pune, 2008).

[148] J.D. Kraus, *Antennas* (McGraw-Hill, 1988).

[149] H.A. Wheeler, „The Radiansphere Around a Small Antenna“, Proc. IRE **47**, 1325–1331 (1959).

[150] R. Bansal, „The Far-Field: How Far is Far Enough?“, Applied Microwave & Wireless **60**, 58 (1999).

[151] K. Weidenhaupt, „LPDA-Antennas for Large Scale Radio Detection of Cosmic Rays at the Pierre-Auger-Observatory“, MA thesis (RWTH Aachen University, 2009).
[152] P. Abreu et al., „Antennas for the Detection of Radio Emission Pulses from Cosmic-Ray induced Air Showers at the Pierre Auger Observatory“, J. Instrum. **7**, P10011 (2012), arXiv:1209.3840.
[153] H.T. Friis, „A note on a simple transmission formula“, Proc. IRE **34**, 254 (1946).
[154] *NEC2++*, http://elec.otago.ac.nz/w/index.php/Necpp (2017).
[155] A.J. Poggio and E.K. Miller, *Integral Equation Solutions of Three-dimensional Scattering Problems* (MBA technical memo: MBAssociates, 1970).
[156] W.C. Gibson, *The Method of Moments in Electrodynamics* (Champman & Hall/CRC, 2008).
[157] R.F. Harrington, *Field Computation by Moment Methods* (IEEE/OUP Series on Electromagnetic Wave Theory, 1993).
[158] A. Voors, *4NEC2*, http://www.qsl.net/4nec2/ (2017).
[159] S. Fliescher, „Antenna Devices and Measurement of Radio Emission from Cosmic Ray induced Air Showers at the Pierre Auger Observatory“, PhD thesis (RWTH Aachen University, 2011).
[160] W.A. Davis and K. Agarwal, *Radio Frequency Circuit Design* (Wiley series in microwave and optical engineering, 2001).
[161] H. Carlin, „The Scattering Matrix in Network Theory“, IRE Transactions on Circuit Theory **3**, 88–97 (1956).
[162] M. Bass et al., *Handbook of Optics*, Vol. 1: Geometrical and Physical Optics, Polarized Light, Components and Instruments (McGraw-Hill Professional Publishing, 2009).
[163] ITU Recommendation, „Electrical Characteristics of the Surface of the Earth“, ITU-R Recommendations & Reports, 527–3 (1992).
[164] W.G. Fano and V. Trainotti, IEEE Ann. Rept. Conf. Electr. Insul. Dielectr. Phenom. **2001**, 75 (2011).
[165] I.Allekotte et al. (Pierre Auger Collaboration), „The Surface Detector System of the Pierre Auger Observatory“, Nucl. Instrum. Meth. A **586**, 409–420 (2008), arXiv:0712.2832.
[166] J. Abraham et al. (Pierre Auger Collaboration), „The Fluorescence Detector of the Pierre Auger Observatory“, Nucl. Instrum. Meth. A **620**, 227–251 (2010), arXiv:0907.4282.
[167] P. Abreu et al. (Pierre Auger Collaboration), „The exposure of the hybrid detector of the Pierre Auger Observatory“, Astropart. Phys. **34**, 368–381 (2011), arXiv:1010.6162.
[168] P. Sommers, „Capabilities of a giant hybrid air shower detector“, Astropart. Phys. **3**, 349–360 (1995).
[169] P. Sommers B. Dawson H. Dai and S. Yoshida, „Simulations of a giant hybrid air shower detector“, Astropart. Phys. **5**, 239–247 (1996).
[170] I. Mariş for the Pierre Auger Collaboration, „The AMIGA infill detector of the Pierre Auger Observatory: performance and first data“, Proc. of the 32th ICRC **1**, Beijing, China, 267 (2011).
[171] A. Aab et al. (Pierre Auger Collaboration), „Prototype muon detectors for the AMIGA component of the Pierre Auger Observatory“, J. Instrum. **11**, P02012 (2016), arXiv:1605.01625.
[172] H.-J. Mathes for the Pierre Auger Collaboration, „The HEAT telescopes of the Pierre Auger Observatory status and first data“, Proc. of the 32th ICRC **3** (2011).
[173] J. Abraham et al. (Pierre Auger Collaboration), „Trigger and aperture of the surface detector array of the Pierre Auger Observatory“, Nucl. Instrum. Meth. A **613**, 29–39 (2010), arXiv:1111.6764.
[174] B. Wundheiler for the Pierre Auger Collaboration, „The AMIGA muon counters of the Pierre Auger Observatory: performance and studies of the lateral distribution function“, Proc. of the 34th ICRC, The Hague, The Netherlands, PoS(ICRC2015)324 (2015).

[175] J. Abraham et al. (Pierre Auger Collaboration), „Properties and performance of the prototype instrument for the Pierre Auger Observatory“, Nucl. Instrum. Meth. A **523**, 50–95 (2004).

[176] B. Schmidt, „Ein lichtstarkes komafreies Spiegelsystem“, Mitteilungen der Hamburger Sternwarte in Bergedorf **7**, 15–17 (1938).

[177] H. Reis M. de Oliveira V. de Souza and R. Sato, „Manufacturing the Schmidt corrector lens for the Pierre Auger Observatory“, Nucl. Instrum. Meth. A, 360–370 (2004).

[178] J.T. Brack et al., „Absolute calibration of a large-diameter light source“, J. Instrum. **8**, P05014 (2013), arXiv:1305.1329.

[179] V. Verzi for the Pierre Auger Collaboration, „The energy scale of the Pierre Auger Observatory“, Proc. of the 33rd ICRC, Rio de Janeiro, Brazil (2013).

[180] J. Bäuml for the Pierre Auger Collaboration, „Measurement of the Optical Properties of the Auger Fluorescence Telescopes“, Proc. of the 33rd ICRC, Rio de Janeiro, Brazil (2013).

[181] L. Tomankova, „Optical Properties and Calibration of the Pierre Auger Fluorescence Detector“, PhD thesis (Karlsruhe Institute of Technology (KIT), 2016).

[182] J. Schulz, „Cosmic radiation - reconstruction of cosmic-ray properties from radio emission of extensive air showers“, PhD thesis (Radboud University Nijmegen, 2016).

[183] M. Giller et al., „Energy spectra of electrons in the extensive air showers of ultra-high energy“, J. Phys. G: Nucl. Part. Phys. **30**, 97–105 (2004).

[184] R. Engel F. Nerling J. Blümer and M. Risse, „Universality of electron distributions in high-energy air showers-description of cherenkov light production“, Astropart. Phys. **24**, 421–437 (2006).

[185] M. D. Roberts, „The role of atmospheric multiple scattering in the transmission of fluorescence light from extensive air showers“, J. Phys. G: Nucl. Part. Phys. **31**, 1291–1301 (2005).

[186] B. Wilczyńska J. Pekala P. Homola and H. Wilczyński, „Atmospheric multiple scattering of fluorescence and cherenkov light emitted by extensive air showers“, Nucl. Instrum. Meth. A **605**, 388–398 (2009), arXiv:0904.3230.

[187] M. Giller and A. Śmiałkowski, „An analytical approach to the multiply scattered light in the optical images of the extensive air showers of ultra-high energies“, Astropart. Phys. **36**, 166–182 (2012), arXiv:1201.4052.

[188] M. Ave et al. (Airfly Collaboration), „Spectrally resolved pressure dependence measurements of air fluorescence emission with AIRFLY“, Nucl. Instrum. Meth. A **597**, 41–45 (2008).

[189] M. Ave et al. (Airfly Collaboration), „Precise measurement of the absolute fluorescence yield of the 337nm band in atmospheric gases“, Astropart. Phys. **42**, 90–102 (2013).

[190] F. Blanco J. Rosado and F. Arqueros, „On the absolute value of the air-fluorescence yield“, Astropart. Phys. **55**, 51–62 (2014), arXiv:1401.4310.

[191] T.K. Gaisser and A.M. Hillas, „Reliability of the method of constant intensity cuts for reconstructing the average development of vertical showers“, Proc. of the 15th ICRC **8**, Plovdiv, Bulgaria, 353 (1977).

[192] M. Unger et al., „Reconstruction of Longitudinal Profiles of Ultra-High Energy Cosmic Ray Showers from Fluorescence and Cherenkov Light Measurements“, Nucl. Instrum. Meth. A **588**, 433–441 (2008), arXiv:0801.4309.

[193] B.G. Keilhauer, „Investigation of Atmospheric Effects on the Development of Extensive Air Showers and their detection with the Pierre Auger Observatory“, PhD thesis (KIT, 2003).

[194] X. Bertou et al. (The Pierre Auger Collaboration), „Calibration of the surface array of the Pierre Auger Observatory“, Nucl. Instrum. Meth. A **568**, 839–846 (2006).

[195] C. Bonifazi for the Pierre Auger Collaboration, „The angular resolution of the Pierre Auger Observatory“, Nucl. Phys. B - Proc. Suppl. **190**, 20–25 (2009), arXiv:0901.3138.

[196] K. Kamata and J. Nishimura, „The Lateral and the Angular Structure Functions of Electron Showers“, Prog. Theor. Phys. Supp. **6**, 93–155 (1958).

[197] K. Greisen, „The extensive air showers“, Prog. in Cosmic Ray Phys. **3**, 1 (1956).

[198] J. Knapp D. Newton and A. Watson, „The optimum distance at which to determine the size of a giant air shower“, Astropart. Phys. **26**, 414–419 (2007), arXiv:astro-ph/0608118.

[199] J. Hersil et al., „Observations of Extensive Air Showers near the Maximum of Their Longitudinal Development“, Phys. Rev. Lett. **6**, 22–23 (1961).

[200] A. Aab et al. (Pierre Auger Collaboration), „Reconstruction of inclined air showers detected with the Pierre Auger Observatory“, J. Cosmol. Astropart. Phys. 08(2014)019 , arXiv:1407.3214.

[201] H.P. Dembinski et al., „A likelihood method to cross-calibrate air-shower detectors“, Astropart. Phys. **73**, 44–51 (2016), arXiv:1503.09027.

[202] A. Aab et al. (Pierre Auger Collaboration), „Nanosecond-level time synchronization of autonomous radio detector stations for extensive air showers“, J. Instrum. **11**, P01018 (2016), arXiv:1512.02216.

[203] K. Weidenhaupt, „Antenna Calibration and Energy Measurement of Ultra-High Energy Cosmic Rays with the Auger Engineering Radio Array“, PhD thesis (RWTH Aachen University, 2014).

[204] J. Kelley for the Pierre Auger Collaboration, „Data acquisition, triggering, and filtering at the Auger Engineering Radio Array“, Nucl. Instrum. Meth. A **725**, 133–136 (2013), arXiv:1205.2104.

[205] M. Stephan for the Pierre Auger Collaboration, „Antennas, Filters and Preamplifiers designed for the Radio Detection of Ultra-High-Energy Cosmic Rays“, in Proc. of the Asia-Pacific-Microwave Conf., Yokohama Japan, 1455–1458 (2010).

[206] C. Rühle, „Entwicklung eines schnellen eingebetteten Systems zur Radiodetektion kosmischer Strahlung“, PhD thesis (Karlsruher Instituts für Technologie (KIT), 2014).

[207] D. Charrier (for the CODALEMA Collaboration), „Antenna development for astroparticle and radioastronomy experiments“, Nucl. Instrum. Meth. A **662**, 142–145 (2012).

[208] C. Timmermans et al., „Description of the scintillator triggered AERA-II stations“, Internal note of the Pierre Auger Observatory, GAP 2013-074 (2013).

[209] D.M. Varnav A.M. van den Berg and G. Zarza, „Fiber communication system for the Auger Engineering Radio Array at the Southern Auger Observatory“, Internal note of the Pierre Auger Observatory, GAP-2011-035 (2011).

[210] T. Winchen, „Measurements of the Continuos Radio Background and Comparison with Simulated Radio Signals from Cosmic Ray Air Showers at the Pierre Auger Observatory“, MA thesis (RWTH Aachen University, 2007).

[211] *coaxial cable specifications*, https://www.bundesnetzagentur.de (2017).

[212] R. Krause, „Octocopter based Calibration of the Butterfly Antenna for the Pierre Auger Observatory“, MA thesis (RWTH Aachen University, 2012).

[213] D. Charrier, *Butterfly Antenna LNA*, private communication.

[214] B. Revenu for the AERA Central DAQ group, „AERA central trigger“, Internal note of the Pierre Auger Collaboration, GAP 2012-115 (2012).

[215] L. Mohrmann M. Erdmann S. Fliescher and K. Weidenhaupt, „A novel method of selecting cosmic ray candidates“, Internal note of the Pierre Auger Collaboration, GAP 2011-108 (2011).

[216] S. Grebe, „Finger on the pulse of ccosmic-ray - depedence of the radio pulse shape on the air shower geometry“, PhD thesis (Radboud University Nijmegen, 2013).

[217] T. Karskens, „An absolute calibration of the antennas at LOFAR“, MA thesis (Radboud University Nijmegen, 2015).

[218] M. Zöcklein, *Calibration of the Auger Engineering Radio Array using the Galactic Radio Background*, BA thesis (RWTH Aachen University, 2016).

[219] S. Argirò et al., „The offline software framework of the Pierre Auger Observatory“, Nucl. Instrum. Meth. A **580**, 1485–1496 (2007), arXiv:0707.1652.

[220] P. Abreu et al. (Pierre Auger Collaboration), „Advanced functionality for radio analysis in the Offline software framework of the Pierre Auger Observatory“, Nucl. Instrum. Meth. A **635**, 92–102 (2011), arXiv:1101.4473.

[221] E. Thébault et al., „International Geomagnetic Reference Field: the 12th generation“, Earth, Planets and Space **67**, 79 (2015).

[222] S. Jansen S. Grebe and C. Timmermans, „Suppression of self-introduced narrowband RFI in the time domain“, Internal note of the Pierre Auger Collaboration, GAP 2013-012, 2013 (2013).

[223] S. Jansen, „Radio for the masses - cosmic ray mass composition masurements in the radio frequency domain“, PhD thesis (Radboud University Nijmegen, 2016).

[224] L. Mohrmann, „Measurement of radio emission from cosmic ray induced air showers at the Pierre Auger Observatory with a spherical wave reconstruction“, MA thesis (RWTH Aachen University, 2011).

[225] A. Leurs, „Measurement of cosmic ray induced air showers using a conical wave form reconstruction of radio emission signals at the Pierre Auger Observatory“, MA thesis (RWTH Aachen University, 2013).

[226] W. Apel et al. (LOPES Collaboration), „The wavefront of the radio signal emitted by cosmic ray air showers“, J. Cosmol. Astropart. Phys. (2014)025 , arXiv:1404.3283.

[227] A. Corstanje et al., „The shape of the radio wavefront of extensive air showers as measured with LOFAR“, Astropart. Phys. **61**, 22–31 (2015), arXiv:1404.3907.

[228] A. Nelles et al., „A parameterization for the radio emission of air showers as predicted by CoREAS simulations and applied to LOFAR measurements“, Astropart. Phys. **60**, 13–24 (2015), arXiv:1402.2872.

[229] J.C. Glaser for the Auger Collaboration, „Analytic description of the radio emission of air showers based on its emission mechanisms“, Proc. of the 35th ICRC, Busan, South Korea, PoS(ICRC2017)529 (2017).

[230] D. Stange, „Entwicklung und Inbetriebnahme eines Testkühlstands für Messungen an Silizium-Photomultipliern“, MA thesis (RWTH Aachen University, 2012).

[231] *Rohde & Schwarz FSH4 Spectrum and Network Analyzer*, https://www.rohde-schwarz.com/de/produkt/fsh-produkt-startseite_63493-8180.html (2017).

[232] *Digital Humidity Sensor SHT1x (RH/T)*, https://www.sensirion.com/en/environmental-sensors/humidity-sensors/digital-humidity-sensors-for-accurate-measurements/, Sensirion AG (2017).

[233] *Anritsu MS46522A Vector Network Analyzer*, https://www.anritsu.com/en-US/test-measurement/products/ms46522a (2017).

[234] J. Eichler P. Kurzweil B. Frenzel and B. Schiewe, *Physik Aufgabensammlung* (Vieweg + Teubner, 2008).

[235] *The Engineering ToolBox - Relative Permittivity*, http://www.engineeringtoolbox.com/relative-permittivity-d_1660.html (2017).

[236] *Dielektrizitätszahlen verschiedener Werkstoffe*, http://www.forum-sondermaschinenbau.de/seiten/Dielektrizitaetszahl.htm (2017).

[237] *RF Cafe - Dielectric Constant, Strength, & Loss Tangent*, http://www.rfcafe.com/references/electrical/dielectric-constants-strengths.htm (2017).

[238] S. Bender and M. Schaller, *Vergleichendes Lexikon Wichtige Definitionen, Schwellenwerte und Indices aus den Bereichen Klima, Klimafolgenforschung und Naturgefahren* (Climate Service Center, 2014).

[239] *HiSystems GmbH, Mikrokopter Octo XL*, http://www.mikrokopter.de (2017).

[240] R. Šmída et al., „First experimental characterization of microwave emission from cosmic ray air showers“, Phys. Rev. Lett. **113**, 221101 (2014), arXiv:1410.8291.

[241] *Canon Ixus 132*, http://www.canon.de/for_home/product_finder/cameras/digital_camera/ixus/ixus_132/ (2017).

[242] F. Briechle, „Octocopter Position Reconstruction for Calibrating the Auger Engineering Radio Array“, MA thesis (RWTH Aachen University, 2015).

[243] F. Briechle for the Pierre Auger Collaboration, „In-situ absolute calibration of electric-field amplitude measurements with the radio detector stations of the Pierre Auger Observatory“, EPJ Web of Conferences **135**, Groningen, The Netherlands, 01014 (2017), arXiv:1609.01511.

[244] *Hiper V*, https://www.topconpositioning.com/gnss/integrated-gnss-receivers/hiper-v (2017).

[245] *RSG1000 Signal Generator*, http://www.teseq.de/produkte/RSG-1000.php (2017).

[246] *Agilent N9030A ESA Spectrum Analyzer*, http://literature.cdn.keysight.com/litweb/pdf/5990-3952EN.pdf?id=1759326 (2017).

[247] *Schwarzbeck Mess-Elektronik, Ultra Light BBOC 9217 Biconical Antenna with UBAA 9114 4:1 Balun*, http://schwarzbeck.de/Datenblatt/91149217.pdf (2017).

[248] *MikroKopter, air pressure sensor as altitute meter*, http://wiki.mikrokopter.de/en/heightsensor (2017).

[249] R. Hiller, „Radio measurements for determining the energy scale of cosmic rays“, PhD thesis (Karlsruhe Institute of Technology (KIT), 2016).

[250] T. Huege and C. W. James, „Full Monte Carlo simulations of radio emission from extensive air showers with CoREAS“, Proc. of the 33rd ICRC, Rio de Janeiro, Brazil (2013), arXiv:1307.7566.

[251] E.M. Holt, „Simulationsstudie für ein großskaliges Antennenfeld zur Detektion von Radioemission ausgedehnter Luftschauer“, MA thesis (Karlsruhe Institute of Technology (KIT), 2013).

[252] C. Welling, „Identification of radio signals from cosmic ray induced air showers with the auger engineering radio array“, MA thesis (RWTH Aachen University, 2017).

[253] F.E. James, *Statistical Methods in Experimental Physics*, 2nd edition (World Scientific Publishing Company, 2006).

[254] G. Cowan, „Error analysis for efficiency“, RHUL Physics (2008).

[255] W.-M. Yao et al., „Review of particle physics“, J. Phys. G: Nucl. Part. Phys. **33**, 1 (2006).

Zusammenfassung

Bei kosmischer Strahlung handelt es sich um Teilchen, deren Ursprung außerhalb der Erde liegt wie z.B. aktive Galaxienkernen, Supernovae oder Starburstgalaxien. Mit Energien von mehr als $10^{20}\,\mathrm{eV}$ stellen kosmische Teilchen die höchst-energetischen Teilchen im Universum dar, propagieren durch dieses und einige können, trotz der großen Distanzen, auf der Erde nachgewiesen werden. Die Messung von kosmischen Teilchen ermöglicht somit die Untersuchung fundamentaler Fragen der Astro- und Astroteilchenphysik.
Treffen hochenergetische Teilchen auf die Erde, interagieren diese mit Luftmolekülen der Atmosphäre. Bei dieser Interaktion werden Kaskaden von Sekundärteilchen produziert und bilden sogenannte Luftschauer. Die Eigenschaften des primären kosmischen Teilchens, z.B. dessen Energie, kann durch stochastische Messungen der Sekundärteilchen am Boden bestimmt werden. Eine weitere Methode ist die direkte Messung von Fluoreszenzlicht. Sekundärteilchen regen Luftmoleküle energetisch an, welche anschließend Energie in Form von Fluoreszenzlicht wieder abgeben. Beide Methoden werden am Pierre Auger Observatorium zur Messung von Luftschauern eingesetzt. Die Messung von Radioemission von Luftschauern ist eine komplementäre Methode um Luftschauer zu untersuchen. Das Auger Engineering Radio Array (AERA) ist der Radiodetektor des Pierre Auger Observatoriums. Da die Atmosphäre transparent für Radiowellen ist, ermöglicht die Radiodetektion die Bestimmung der Energie des kosmischen Teilchens potentiell mit reduzierten Unsicherheiten im Vergleich zur Fluoreszenzmethode.
Um die Radioemission von Luftschauern zu detektieren, als auch für eine genaue Rekonstruktion der Eigenschaften des primären Teilchens, spielen die Radioantennen sowie eine akkurate Beschreibung dessen frequenz- und richtungsabhängigen Antennensensitivität eine zentrale Rolle. Dieses sogenannte “antenna response pattern” wird durch den Formalismus der “vector effective length” (VEL) beschrieben, welche in zwei Komponenten unterteilt ist, einen horizontalen Anteil H_ϕ sowie in einen meridionalen Anteil H_θ. Die VEL wird durch eine absolute Antennenkalibration ermittelt. Die Ungenauigkeit der Kalibration wurde als dominante Unsicherheit innerhalb der Energierekonstruktion des kosmischen Teilchens identifiziert. Eine Reduktion der Unsicherheit ist daher von besonderem Interesse. In dieser Arbeit wurde eine absolute Antennenkalibration der Radiostationen durchgeführt, welche mit logarithmisch-periodischen Dipolantennen (LPDAs) ausgestattet sind.
Eine der Herausforderungen zur Messung von Luftschauern mit AERA sind die variierenden lokalen Wetterbedingungen. Diese Fluktuationen haben einen direkten Einfluss auf die Signalverarbeitung der Elektronik, welche in den Radiostationen verwendet wird, z.B. auf den eigenbauten Verstärker (LNA), welcher direkt mit der Antenne verbunden ist. Die Eigenschaften des LNAs sind auf die der Antenne abgestimmt. LNA und Antenne bilden daher eine technische Einheit und der LNA ist in der Beschreibung des “antenna response patterns” zu berücksichtigen. Eine akkurate Beschreibung des LNAs als auch die Temperaturabhängigkeit der Signalverstärkung sind daher von großem Interesse bei der Antennenkalibration sowie bei der Rekonstruktion von Radiodaten. Zur Bestimmung der Temperaturabhängigkeit

des LPDA LNAs wurde dieser in einem regelbaren und PC-gesteuerten Kühlschrank positioniert. Die frequenzabhängige Leistungsverstärkung des LNAs wurde für verschiedene Temperaturen gemessen. Die Temperaturabhängigkeit der Leistungsverstärkung wurde im Median zu $-0.017\mathrm{dB/K}$ ermittelt und es wurde nahezu keine Frequenzabhängigkeit festgestellt. Diese Ergebnisse konnten in einer weiteren Messung eines zweiten LNAs bestätigt werden.
Die Bodenbedingungen vor Ort, welche durch die Bodenleitfähigkeit sowie der Bodenpermittivität beschrieben werden, als auch deren Variation, z.B. aufgrund von Regen, sind weitere wichtige Umweltbedingungen, welche das "antenna response pattern" beeinflussen. Beides, Leitfähigkeit und Permittivität, beeinflussen die Signalreflektion elektromagnetischer Wellen am Boden. Es wurde gezeigt, dass die Signalreflektion bei einer Bodenbeschaffenheit wie sie bei AERA vorkommt vor allem von der Permittivität abhängt. Daher wurde ein Messaufbau entwickelt, um die Bodenpermittivität bei AERA und ihre Frequenzabhängigkeit zu messen. Zwei Messkampagnen wurden durchgeführt. Zum einen wurden Bodenproben genommen und die Permittivität bei verschiedener Feuchtigkeit im Labor gemessen. Die Messungen ergaben, dass die Permittivität typischerweise größer als 2 ist und mit der Bodenfeuchte steigt. Um die Homogenität der Bodenbeschaffung zu untersuchen wurden außerdem Messungen direkt vor Ort an verschiedenen Positionen durchgeführt. Bei der Mehrzahl an Positionen wurden Permittivitäten zwischen 6 und 7 gemessen. Nur an den Rändern von AERA ganz im Westen als auch ganz im Osten weichen die Werte nach unten bzw. oben ab. Dies kann daher rühren, dass im Westen von AERA die Bodenkonsistenz sandiger und im Osten erdiger ist. Innerhalb der Messkampagnen wurden typische Werte der Bodenpermittivität zwischen 2 und 10 ermittelt.
Im Rahmen von Simulationen wurde die LPDA Sensitivität für alle Richtungen und Frequenzen zwischen $30\,\mathrm{MHz}$ und $80\,\mathrm{MHz}$ in Einheiten der VEL charakterisiert. Für die Simulationen wurde der NEC-2 Simulationscode verwendet und Standardumweltbedingungen definiert. Mit Hilfe der Simulationen wurde der Einfluss von verschiedenen Umweltbedingungen wie variierende Bodenbeschaffenheit, leitende Elemente in der Nähe der Antenne oder auch eine Verdrehung der Antenne untersucht und abgeschätzt. Der Einfluss auf die horizontal (meridionale) Komponente der LPDA VEL H_ϕ (H_θ) aufgrund variierender Bodenpermittivitäten zwischen 2 und 10 ist im Median von der Größe von $1.3\,\%$ ($0.5\,\%$) und der gesamte Phasenraum definiert durch Frequenz und Zenitwinkel ist beeinflusst. Simulationen einer Box aus leitendem Material, welche unterhalb der Antenne positioniert ist, zeigen einen Einfluss von $0.3\,\%$ ($1\,\%$) auf die horizontale (meridionale) Komponente der LPDA VEL. Im Falle der meridionalen Komponente sind vor allem Regionen mit großen Zenitwinkeln betroffen in denen die LPDA kaum sensitiv ist. Simulationen der Antennenverdrehung um 1° als auch von verschiedenen Bodenleitfähigkeiten zeigen, dass die LPDA Sensitivität dadurch nicht beeinflusst wird.
Innerhalb einer Kalibrationskampagne wurde das LPDA pattern mittels eines ferngesteuerten Oktokopters im Feld gemessen. Der Oktokopter wurde benutzt, um eine kalibrierte Signalquelle an verschiedenen Stellen um eine LPDA zu positionieren. Die kalibrierte LPDA

ist repräsentativ für alle LPDAs, da diese auf dem Pozentlevel mechanisch wie elektrisch identisch sind. Die in der Kalibration genutzten Geräte wurden anhand ihrer Ungenauigkeiten quantifiziert. Besonderer Fokus wurde auf die Genauigkeit der Positionsrekonstruktion der Signalquelle gelegt. Die Genauigkeit wurde verbessert indem die Informationen der im Oktokopter eingebauten Sensoren wie GPS, Barometer und Neigungssensoren mit einer neu entwickelten optischen Methode basierend auf zwei Kameras kombiniert wurden. Um Reproduzierbarkeit sicherzustellen, wurden die Messungen an verschiedenen Tagen und bei verschiedenen Umweltbedingungen wiederholt. Diese Messungen wurden schließlich anhand ihrer Unsicherheiten kombiniert. Die kombinierte Unsicherheit der horizontalen Komponente der LPDA VEL wurde zu $7.4^{+0.9}_{-0.3}\,\%$ und die der meridionale Komponente zu $10.3^{+2.8}_{-1.7}\,\%$ bestimmt. Diese Unsicherheiten sind zu vergleichen mit der Unsicherheit der bisherigen Kalibration in welcher ein kleinerer Phasenraum gemessen und eine Unsicherheit der horizontalen Komponente von $12.5\,\%$ erreicht wurde. Diese genauen Messungen wurden mit NEC-2 Simulationen verglichen in denen der gesamte Aufbau bestehend aus LPDA, LNA sowie der transmittierenden Antenne berücksichtigt wurde. Korrekturfaktoren, welche durch das Verhältnis zwischen Messung und Simulation definiert sind, wurden für alle Frequenzen und Ankunftsrichtungen berechnet. Der Median aller Korrekturfaktoren liegt nahe bei eins und weist eine Variation von 0.12 (0.26) innerhalb der horizontalen (meridionalen) Komponente auf. Der Einfluss des modifizierten LPDA patterns wurde anhand eines Beispielereignisses (Zenitwinkel = $30\,^\circ$; Azimutwinkel = $14\,^\circ$ südlich von Osten) demonstriert. Bei Verwendung des modifizierten Pattern wurde das elektrische Feld mit einer $7\,\%$ höheren Amplitude rekonstruiert. Die "energy fluence" aller Polarisationen steigt um $9\,\%$ und die rekonstruierte "radiation energy" ändert sich von $7.96\,\mathrm{MeV}$ zu $8.54\,\mathrm{MeV}$. Des Weiteren wurden die Unsicherheiten aufgrund der Kalibration als auch aufgrund variierender Bodenpermittivitäten auf die Wurzel der "energy fluence" fortgepflanzt. Die Wurzel, weil die "energy fluence" quadratisch mit der Amplitude des elektrischen Feldes als auch quadratisch mit der Energie des Primärteilchens skaliert und somit die Unsicherheit der Wurzel der "energy fluence" die relevante Unsicherheit der meisten Analysen darstellt. Für Ankunftsrichtungen mit einem Zenitwinkel kleiner $60\,^\circ$ wurde die Unsicherheit der Wurzel der "energy fluence" aufgrund der Kalibration sowie variierender Bodenpermittivitäten im Median zu $8.8^{+2.1}_{-1.3}\,\%$ ermittelt.
Typischerweise bestehen Radiostationen in Luftschauerexperimenten aus zwei senkrecht zueinander polarisierten Antennen, welche herkömmlicher Weise horizontal ausgerichtet sind. Die dritte Komponente, die vertikale Polarisation des Radiosignals, wird dann nicht direkt gemessen. Sie ist jedoch wichtig für die Analyse von Radiodaten. Sogenannte 3D Radiostationen sind daher motiviert, da die gleichzeitige Messung aller drei Komponenten potenziell die Unsicherheiten der Rekonstruktion des elektrischen Feldes reduziert. Des Weiteren haben 3D Radiostationen einen erweitertes Blickfeld zum Horizont. Innerhalb dieser Arbeit wurde eine neue 3D Radiostation für AERA entwickelt. Die mechanischen und elektrischen Eigenschaften dieser Radiostation wurden diskutiert. Insgesamt wurden 5 Butterfly Radiostationen mit der Wifivert Antenne, eine vertikal ausgerichtete Antenne, zu einer 3D Radiostation er-

weitert. Innerhalb von drei Monaten der Datennahme wurden mehr als 2800 Ereignisse in Koinzidenz mit dem Oberflächendetektor des Pierre Auger Observatoriums aufgezeichnet. Von diesen Ereignisse erfüllen 45 Ereignisse die Bedingung eines "signal-to-noise ratio" (SNR) von mehr als 10 in den horizontalen Antennen von mindestens einer der 3D Radiostationen. Diese Ereignisse sind als Kandidaten für kosmische Teilchen klassifiziert. Wenn zusätzlich ein SNR $\geqslant 5$ in der Wifivert Antenne gemessen wurde, wird das Ereignis ein goldenes 3D Ereignis genannt. In dem Datensatz wurden insgesamt 13 Ereignisse als goldene 3D Ereignis identifiziert. Mit der Wifivert Antenne wurden Radiosignale von Luftschauern in der vertikalen Polarisation gemessen. Es wurde gezeigt, dass die Antenne besonders sensitiv ist, wenn der Luftschauer einen großen Zenitwinkel aufweist. Solche sogenannten horizontalen Luftschauer liegen im Fokus aktueller Forschung.
Zukünftige Untersuchungen werden von den Ergebnissen dieser Arbeit profitieren. Die akkuraten Messungen der Kalibration wird die Rekonstruktion der Eigenschaften des primären kosmischen Teilchens, wie z.B. die Teilchenenergie, verbessern. Aufgrund der reduzierten Unsicherheiten der Kalibration wird die Unsicherheit der Energieskala für Luftschauermessungen von Radiodetektoren direkt beeinflusst. Bei Verwendung von 3D Radiostationen werden alle drei Polarisationen des Radiosignals gleichzeitig gemessen, was die Unsicherheit der Rekonstruktion des elektrischen Feldes im Vergleich zu herkömmlichen 2D Radiostationen verringert. Des Weiteren ist das Sichtfeld von 3D Radiostationen zum Horizont hin erweitert, so dass 3D Radiostationen eine verbesserte Erforschung von horizontalen Luftschauern ermöglichen.

Danksagung

Viele verschiedene Personen haben mit ihrer Hilfe und Unterstützung zur Erstellung dieser Thesis beigetragen und ohne sie wäre diese Arbeit in dieser Form nicht möglich gewesen. Deshalb möchte ich nun die Gelegenheit wahrnehmen und an dieser Stelle einige persönliche Worte äußern und meinen Dank aussprechen.
Ein besonderer Dank gilt Prof. Dr. Martin Erdmann. Er hat mir die Möglichkeit gegeben dieses Thema zu bearbeiten und hat mich während der Promotion betreut. Die Arbeit im Team von Prof. Erdmann hat mir viel Spaß gemacht und ermöglichte mir einen tiefen Einblick in die Grundlagenforschung, besonders im Bereich Astroteilchenphysik sowie Hardwarearbeiten und Datenanalyse. Vielen Dank für die sehr gute Betreuung und das tolle gebotene Arbeitsumfeld.
Prof. Dr. Christopher Wiebusch hat sich freundlicherweise dazu bereit erklärt meine Dissertation als Zweitgutachter zu lesen und zu bewerten. Vielen Dank.
Ebenfalls gilt der gesamten Arbeitsgruppe von Prof. Erdmann mein Dank. In regelmäßigen Meetings wurde der aktuelle Forschungsstand besprochen, die derzeitigen Herausforderungen diskutiert und Lösungsansätze erarbeitet. Darüber hinaus fand ein reger Austausch von Gedanken und Ideen auch außerhalb der Meetings themenübergreifend statt. Insgesamt herrschte durchgehend ein sehr angenehmes Arbeitsklima in der Arbeitsgruppe und ich bin froh Teil dieser Gruppe gewesen sein zu dürfen.
Aus der Arbeitsgruppe besonders hervorzuheben sind Florian Briechle, Christian Glaser und Klaus Weidenhaupt. Alle drei haben sich intensiv mit Radioantennen, dem Radiodetektor des Pierre Auger Observatoriums und der Aufnahme sowie Analyse von Radiodaten beschäftigt und waren somit die ersten Ansprech- und Diskussionspartner für mich. Klaus Weidenhaupt war mein Betreuer während meiner Masterarbeit und er hat mich in den Bereich der Radiodetektion von ausgedehnten Luftschauern eingeführt. Mit ihm zusammen habe ich das Oktokopterprojekt begonnen und die Messprozedur der Antennenkalibration unter Verwendung des Oktokopters erarbeitet. Mit Florian Briechle habe ich das Oktokopterprojekt weitergeführt und weiter optimiert. Er hat intensiv bei den Feldarbeiten z.B. den in dieser Arbeit präsentierten Permittivitätsmessungen sowie den Kalibrationsflügen in Argentinien mitgewirkt. Im Rahmen seiner Masterarbeit hat er die Positionsrekonstruktion des Oktokopters mit Hilfe der Kameramethode optimiert und somit signifikant zur Reduzierung der Kalibrationsunsicherheiten beigetragen. Christian Glaser ist Experte im Bereich $\overline{\text{Off}}$ $\underline{\text{line}}$ sowie der Eventrekonstruktion von Radiodaten. Er war direkter Diskussionspartner und hat stets mit guten Ratschlägen geholfen meine Forschungsarbeit zu optimieren.
Des Weiteren gilt mein Dank den Mitarbeitern der mechanischen und der elektronischen Werkstatt des III. Physikalischen Instituts A der RWTH Aachen. Hier besonders hervorzuheben sind die jeweiligen Werkstattleiter Herr Barthel Phillips sowie Herr Franz-Peter Zantis. Herr Philipps war der direkte Ansprechpartner für sämtliche Fragestellungen mit mechanischem Bezug. Er hat z.B. die Konstruktion und Realisierung der 3D Radio Stationen ermöglicht. Herr Zantis war mein Ansprechpartner für elektronische Fragestellungen. In etlichen

Besprechungen haben wir zusammen das Prinzip der Permittivitätsbestimmung der Bodenproben diskutiert. Außerdem hat er mich bei den Labormessungen der Bodenpermittivität unterstützt.
Auch muss ich mich bei der gesamten Auger Collaboration bedanken. Ich durfte die Collaboration auf mehreren Konferenzen vertreten und dort mich sowie meine Forschungsergebnisse einer großen internationalen Hörerschaft präsentieren. Sämtliche Präsentationen (Mündliche in Form von Talks sowie Schriftliche in Form von Proceedings) wurden im Vorfeld gründlich diskutiert. Dies hat letztendlich zur Optimierung der Forschungsergebnisse sowie der Präsentationen beigetragen. Im Rahmen meiner Publikationen sind besonders hervorzuheben: Carola Dobrigkeit Chinellato und Stephane Coutu vom Auger publication committee, aber auch viele weitere interne reviewer der Collaboration.
Die Mitglieder des editorial boards des LPDA Kalibrationspapiers waren Martin Erdmann, Brian Fick, Tim Huege, Lorenzo Perrone sowie Benoît Revenu. Vielen Dank für die guten Diskussionen und nützlichen Kommentare über mehrere Meetings hinweg, welche letztendlich mit zur erfolgreichen Veröffentlichung des Papiers geführt haben.
Ich bedanke mich bei der RWE Power AG und unseren lokalem Ansprechpartner von RWE, Herr Peter Weber. RWE hat uns einen Zugang zum Tagebau Inden ermöglicht und erlaubt dort eine Radiostation zu Testzwecken aufzubauen. Dadurch waren wir in der Lage die Oktokopterflüge zu proben und Testmessungen direkt an einer Radiostation mit ähnlichen Bedingungen wie in Argentinien durchzuführen. Dies hat maßgeblich zum Erfolg der Messungen in Argentinien beigetragen.
Zu guter Letzt möchte ich meiner Familie danken, besonders meinen Eltern Cordula und Wilfred Krause sowie meiner Frau Katharina Krause, welche mich in jeglicher Hinsicht unterstützt haben, mit mir geduldig waren und mir in schwierigeren und stressigen Situationen Halt gaben (und geben). Was wäre ich nur ohne euch? Diese Arbeit wäre ohne euch nicht möglich gewesen. Ebenfalls zu erwähnen sind meine Kinder Freya und Tristan Krause, welche mich mit Ihrer Lebensfreude Tag für Tag aufs Neue begeistern. Ich bin unendlich froh und glücklich darüber, dass ihr mir geschenkt wurdet.

List of Publications

Published Articles with Significant Personal Contribution

A. Aab et al. (Pierre Auger Collaboration)
"Calibration of the Logarithmic-Periodic Dipole Antenna (LPDA) Radio Stations at the Pierre Auger Observatory using an Octocopter"
J. Instrum. **12** (2017) T10005
The work presented in this publication was primarily performed by the author of this thesis. The text of the publication has been written by the author of this thesis and was revised and copy-edited by the co-authors of the publication.

A. Aab et al. (Pierre Auger Collaboration)
"Energy estimation of cosmic rays with the Engineering Radio Array of the Pierre Auger Observatory"
Physical Review D **93** (2016) 122005
The author of this thesis contributed to the absolute antenna calibration and to the parts of the analysis where the uncertainty of the electric-field amplitude is determined. The text of the publication has been revised and copy-edited by the author of this thesis.

A. Aab et al. (Pierre Auger Collaboration)
"Measurement of the Radiation Energy in the Radio Signal of Extensive Air Showers as a Universal Estimator of Cosmic-Ray Energy"
Phys. Rev. Lett. **116** (2016) 241101
The author of this thesis contributed to the absolute antenna calibration and to the parts of the analysis where the uncertainty of the electric-field amplitude is determined. The text of the publication has been revised and copy-edited by the author of this thesis.

A. Nelles et al.
"Calibrating the absolute amplitude scale for air showers measured at LOFAR"
J. Instrum. **10)** (2015) P11005
The author of this thesis has been involved in the calibration measurements of the LOPES antenna response pattern and has contributed to the parts of the analysis. The text of the publication has been revised and copy-edited by the author of this thesis.

M. Erdmann, R. Fischer, C. Glaser, D. Klingebiel, R. Krause et al.
"A field study of data analysis excercises in a bachelor physics course using the internet platform VISPA"
Eur. J. Phys. **35** (2014) 35018
The author of this thesis has participated in the field study. The text of the publication has been revised and copy-edited by the author of this thesis.

Conference Proceedings

R. Krause for the Pierre Auger Collaboration
"A new method to determine the energy scale for high-energy cosmic rays using radio measurements at the Pierre Auger Observatory"
Proc. of the 35th ICRC 2017, Busan, South Korea (2017)
PoS (ICRC2017) 528
Significant parts of the work presented in this publication have been performed by the author of this thesis. The text of the publication has been written by the author of this thesis and was revised and copy-edited by the co-authors of the publication.

R. Krause for the Pierre Auger Collaboration
"Detection of Ultrahigh-Energy Cosmic Rays with the Auger Engineering Radio Array"
Proc. of the VCI 2016, Vienna, Austria (2016)
Nucl. Instrum. Meth. A, **845C** (2017) 378-382
Significant parts of the work presented in this publication have been performed by the author of this thesis. The text of the publication has been written by the author of this thesis and was revised and copy-edited by the co-authors of the publication.

R. Krause for the Pierre Auger Collaboration
"AERA – The Auger Engineering Radio Array"
Proc. of the VULCANO Conf. 2014, Vulcano Island, Italy (2014)
Frascati Physics Series Vol. **58** (2014) 315-322
Significant parts of the work presented in this publication have been performed by the author of this thesis. The text of the publication has been written by the author of this thesis and was revised and copy-edited by the co-authors of the publication.

Internal Publications

D. Maschmann, M. Erdmann and R. Krause
"A Monitoring System for Motions of Butterfly Antennas for the Auger Engineering Radio Array"
Internal note of the Pierre Auger Collaboration (2014), GAP2014_113
The work presented in this publication is based on the Bachelor thesis of D. Maschmann which was supervised by the author of this thesis. The text of the publication has been revised and copy-edited by the author of this thesis.

F. Briechle, M. Erdmann, C. Glaser and R. Krause
Internal note of the Pierre Auger Collaboration (2015), GAP2015_081
The work presented in this publication is based on the Master thesis of F. Briechle which was supervised by the author of this thesis. The text of the publication has been revised and copy-edited by the author of this thesis.